Electrical and chemical mapping of silicon pn junctions using energy-filtered X-ray PhotoElectron Emission Microscopy

Maylis Lavayssiere

UNIVERSITÉ DE GRENOBLE

THÈSE

Pour obtenir le grade de

DOCTEUR DE L'UNIVERSITÉ DE GRENOBLE

Spécialité : **Micro et Nano Electronique**

Arrêté ministériel : 7 août 2006

Présentée par

Maylis LAVAYSSIÈRE

Thèse dirigée par **Nicholas BARRETT**

préparée au sein du **Laboratoire d'Electronique et des Technologies de l'Information (LETI) du CEA Grenoble**
dans **l'École Doctorale Electronique, Electrotechnique, Automatisme et Traitement du Signal**

Electrical and chemical mapping of silicon pn junctions using energy-filtered X-ray PhotoElectron Emission Microscopy

Thèse soutenue publiquement le **02 mars 2011**,
devant le jury composé de :

M. Roland MADAR
LMGP PHELMA (Grenoble) - Président
M. Jacques CAZAUX
GRESPI/Matériaux Fonctionnels (Reims) - Rapporteur
M. Gerd SCHÖNHENSE
Johannes Gutenberg University (Mainz) - Rapporteur
M. Jean-Charles JOUD
SIMAP PHELMA (Grenoble) - Examinateur
M. Pierre MÜLLER
CINaM-CNRS (Marseille) - Examinateur
M. François ROCHET
Université Paris VI (Paris) - Examinateur
M. Nicholas BARRETT
CEA DSM IRAMIS (Saclay) - Directeur de thèse
M. Olivier RENAULT
CEA-LETI MINATEC (Grenoble) - Encadrant de thèse

"Oh ! qu'ils sont beaux les feux de paille ! qu'ils sont fous,
Les albums ! et non incassables, mes joujoux !"
Jules Laforgue, Des Fleurs de bonne volonté

Acknowledgments

After three years and a couple of months learning, performing experiments, thinking and a lot of writing, this PhD work ends. It has been a fruitful experience both at a professional and a personal level which has afforded me interacting with lots of interesting people. I wish to express my deepest gratitude to all those who have contributed to this work, as well as to those who have contributed to making this period a pleasant and enjoyable time.

My gratitude goes to Jean-Claude Royer and Frédéric Laugier, who gave me the opportunity to work with them in the DPTS department and in the LCPO laboratory. I also would like to thank Narciso Gambacorti, Amal Chabli, François Bertin, for providing knowledgeable discussions.

I am grateful to Nick Barrett and Olivier Renault, who planned and launched the XPEEM project, for the opportunity they give me to do my PhD thesis in a great work environment. Without them, this thesis would not have been accomplished.

For this PhD, I would like to thank my reading committee members: Jacques Cazaux, and Gerd Schönhense for their interest in my studies, and their helpful comments. I would also like to thank the other members of my oral defense committee: Roland Madar, Jean-Charles Joud, Pierre Müller and François Rochet, for their time and their insightful questions.

I am thankful to the OMICRON and FOCUS teams, specially Konrad Winkler, Dietmar Funnemann, Burkhard Kroemker, Matthias Escher, and Nils Weber for their kind guidance and cooperation during the entire period of my study, and for the help they gave me on technical problems as well as simulation ones.

I am deeply indebted to Denis Mariolle, for his expert guidance, his patience and support at all levels; he helps me to move forward in my research.

I am also pleased to record my gratitude to Denis Renaud and Jean-Michel Hartmann, for the time they spent helping me at each process step of the epitaxial silicon doped sample fabrication.

I further would like to mention Véronique Robert and Thomas Ernst for all those scientific and friendly discussions, and specially Véronique for helping me in discovering the patent world.

There are many other people who also contributed to this thesis and I wish to thank all of them: Robert Baptist, David Cooper, Jean-Paul Barnes, Marc Veillerot, Pierrette Rivallin and Brigitte Florin which contributions, detailed comments and insights, have been of great value to me.

During this work I have collaborated with many colleagues for whom I have great regard, and I wish to extend my warmest thanks to those who have helped me with my chemistry work, specially for the cleaning steps and the numerous tests performed: Jean-Marc Fabbri at Grenoble and Jocelyne Leroy at Saclay and SOLEIL.

I'm highly obliged to Bruno Delomez, Julien Rault, Yanyu Mi, Giovanni Vanacore, Ingo Krug for all the nice moments spent together on synchrotron facility.

My gratitude also goes to all the people who helped performing my experiments in the SOLEIL synchrotron: Fausto Sirotti, Mathieu Silly, and Stéphanie Blanchandin. I'm also in debt of Claudine Chaleil, who gave me the opportunity to perform valuable experiments.

I am grateful to Alain Faure for his guidance and knowledgeable discussions not only about ultravacuum but also about food and cooking. It has been a real pleasure to work with you!

I wish to thank the whole laboratory for all the extra-work activities, specially the coffee breaks, and particularly all the colleagues with whom I have spent more time. Thank you all for those enjoyable moments gathered in the canteen for the lunch breaks: Christophe Licitra, Anne-Marie Papon, Robert Truche, Dominique Lafond, Cécile Provost, Eric De Vito, Eugénie Martinez, Névine Rochat and Nicolas Chevalier. I also want to thank specially the best secretary I have ever met: Marie-Andrée Lesbre, for her patience and kindness to assist me in many different ways anytime I needed.
My sincere thanks go to the old dream-team colleagues which have become true friends: Khaled Kaja, Clément Gaumer, Cyril Ailliot, Aude Bailly, Michaël Jublot, and Madeline Lambert. Thank you for all the nice and funny moments we shared together! Other fellows have also reinforced this team which now I would acknowledge: Edouard Deschaseaux, Olivier Desplats, Matthias Kühne, Hélène Rotella, Adeline Grenier, Matthieu Py, Sylvain Pierre, Victor Malgras, Yann Pitis, Charles Bourin, Pauline Calka, Rachid Boujamaa, Lin You and Lukasz Borowik. I owe specially Claire Mathieu since I have appreciated our inspirational discussions, with lots of great moments engraved in memory. Thank you for your warm support!

My sincere gratitude goes to special people which have guided me, helping me in my choices: my physics teachers Daniel and Marie-Christine Labernède, and my astronomer friends Philippe Dupouy, Jean Lecacheux, François Colas, Guillaume Blanchard, Françoise Colas, Martine Castets, Valérie Desnoux and Christian Buil. I am also thankful to my old friends for being a great company always present, and so patient with me: Sandrine M., Matthieu C., Cécile and Cyril D., Benjamin C., Jérôme D., Laurie C., Guillaume C., Hélène D., and Nicolas P..

Last but not least, I would like to thank my parents, my brother, my grandparents, and all my family for all their love and encouragement. I dedicate this work to them and to Papy Louis which is still present with us. I would like to finish these acknowledgments with two people who I consider belonging to my family: Pauline Rose, thank you for your support and your understanding at the most happy, but also the heavy moments during these years. Jean-Marc Navas thank you for your constant encouragements! And finally, my greatest regards and sincere thanks for my loving, supportive, and patient Eric throughout these years, I'm deeply indebted to you!

Table of Contents

List of Abreviations

AC	Alternative Current
AFM	Atomic Force Microscopy
ARXPS	Angle-Resolved XPS
ATP	Atom Probe Tomography
BSE	Backscattered Electrons
CA	Contrast Aperture
CAE	Constant Analyser Energy
CCD	Charge Coupled Device
CEA	Commissariat à l'Energie Atomique
CITS	Current Imaging Tunnelling Spectroscopy
CRR	Constant Retard Ratio
dc	Direct Current
DNA	DeoxyriboNucleic Acid
DOS	Density of States
DPTS	Departement Plate-forme Technologique Silicium
DRT	Direction de la Recherche Technologique
EA	Energy Aperture
ESCA	Electron Spectroscopy for Chemical Analysis
FE SEM	Field-Emission Scanning Electron Microscopy
FIB	Focused Ion Beam
FIT	Flexible Image Transport
FoV	Field of View
FTIR	Fourier Transform InfraRed spectroscopy
FXS	Focused X-ray Source
HDA	Hemispherical Double Analyzer
HF	HydroFluoric acid
HFET	Heterostructure Field Effect Transistor
HSA	Hemispherical Single Analyzer
IDEA	Imaging Double Energy Analyzer
IRAMIS	Institut Rayonnement Matière de Saclay
KFM	Kelvin Force Microscopy
LCPO	Laboratoire de Caracterisation Physique Off-line
LETI	Laboratoire d'Electronique et de Technologies de l'Information
LINAC	LINear ACcelerator
LURE	Laboratoire pour l'Utilisation du Rayonnement Electromagnetique
MEMS	Micromechanical systems

MCP	Multi Channel Plate
MIR	Multiple Internal Reflection
MOS	Metal-Oxide-Semiconductor
MOSFET	Metal-Oxide-Semiconductor Field-Effect Transistor
MXPS	Multi-Probe XPS
NEMS	Nanomechanical systems
NEXAFS	Near Edge X-ray Absorption Fine Structure
NanoESCA	Nano Electron Spectroscopy for Chemical Analysis
PEEM	PhotoElectron Emission Microscopy
PES	Photoelectron Spectroscopy
PNA	Peptide Nucleic Acid
RP	Resolving Power
SCM	Scanning Capacitance Microscopy
SCPIO	Service de la Caracterisation Physique In-line/Off-line
SCR	Space Charge Region
SE	Secondary Electron
SEM	Scanning Electron Microscopy
SIMS	Secondary Ion Mass Spectrometry
SLEEM	Scanning Low-Energy Electron Microscope
SMART	Spectro-Microscope with Aberration correction for many Relevant Techniques
SNR	Signal-to-Noise Ratio
SOLEIL	Source Optimisée de Lumière d'Energie Intermédiaire de LURE
SPEM	Scanning PhotoElectron Microscopy
SPHINX	Spectromicroscope for PHotoelectron Imaging of Nanostructures with X-rays
SPV	Surface Photovoltage
SRAM	Static Random Access Memory
SSRM	Scanning Spreading Resistance Microscopy
STM	Scanning Tunelling Microscopy
TEM	Transmission Electron Microscopy
TEMPO	Time resolved Experiments on Materials with Photoelectron Spectroscopy
ToF	Time-of-Flight
UHV	Ultra High Vacuum
UPS	Ultraviolet Photoelectron Spectroscopy
UV	Ultraviolet
VBM	Valence Band Maximum
XAS	X-ray Absorption Spectroscopy
XMCD	X-ray Magnetic Circular Dichroism
XMLD	X-ray Magnetic Linear Dichroism
XPEEM	X-ray PhotoElectron Emission Microscopy
XPS	X-ray Photoelectron Spectroscopy
1D	one-dimensional
2D	two-dimensional
3D	three-dimensional

Symbols

Avogadro's number	N_A	6.022×10^{23} atoms per mole
Boltzmann's constant	k	1.38×10^{-23} J.K^{-1} 8.62×10^{-5} eV.K^{-1}
Electronic charge	q	1.602×10^{-19} C
Vacuum permittivity	ϵ_0	8.854×10^{-12} F.m^{-1} 8.854×10^{-14} F.cm^{-1}
Silicon permittivity	ϵ_0	1.04×10^{-12} F.m^{-1} 1.04×10^{-14} F.cm^{-1}
Silicon gap	$E_{g,Si}$	1.12 eV
Silicon electron affinity	χ_{Si}	4.05 eV
Intrinsic carrier concentration for silicon	n_i	1.45×10^{10} atoms.cm^{-3}

General Introduction

This thesis reports on the application of energy filtered X-ray PhotoElectron Emission Microscopy (XPEEM) to analyze doped silicon patterns. It focuses on two important aspects:

- the electrical and chemical mapping of pn junctions as a function of the surface state,
- the influence of the junctions on PEEM imaging.

For the characterization of these materials a new concept of energy filtered PEEM was used, and experiments were performed in both laboratory and synchrotron environments. We have obtained complementary results to highlight our understanding of the pn junctions in terms of electrical and chemical characterization. Thanks to full field, energy-filtered electron imaging, this instrument directly measures spatial changes in work function, core-level and valence band depending on the silicon doping type and level and the surface state.

We have designed, produced and characterized optimised patterned silicon surfaces in order to probe the band bending in the depletion zone due to the pn junctions. However, because of the unavoidable presence of a native oxide on the surface, we have developed a dedicated passivation protocol to attain flat band conditions conditions.

The second issue is dedicated to the imaging conditions themselves, since, when imaging pn junctions, one has to take into account the inherent properties of the junction. We focus on the local lateral electrical field existing across pn junctions, which influences the photoelectron trajectories on their extraction from the surface. This field can alter lateral resolution in PEEM imaging. To better appreciate its influence, we compare simulations with experiments, varying different parameters.

This thesis work was done at the CEA LETI MINATEC in Grenoble, in collaboration with the IRAMIS institute at the CEA of Saclay and the SOLEIL synchrotron facility in Saint-Aubin.
The organisation of this manuscript is divided in five chapters:

- In chapter 1, a brief presentation of the physics governing silicon pn junctions is first made. We position then our study in the 2D dopant characterization techniques by reviewing the most important advantages and drawbacks of each of them. We give then the various interpretations in terms of secondary electron contrast in electron emission microscopy. We finish by reviewing the studies already performed by XPEEM on silicon samples, in order to highlight the peculiarities of our analysis.

- Chapter 2 introduces the physical principles of energy filtered PEEM. We present the two main laboratory and synchrotron X-ray sources used during this thesis. We then detail the performances of our instrument in terms of energy resolution, and the state-of-the-art lateral resolution achieved in laboratory.

- In chapter 3, the fabrication process of the different silicon doped samples is described. It is completed by an extensive characterization study of these patterned samples. We detail then the optimisation of a passivation protocol established to remove the native oxide from the sample surface, and thus, reach flat band conditions. We show the advantages and limitations of such a process thanks to XPS analysis of the Si $2p$ core-level and compare the results with the existing literature on the Si $2p$ spectra of passivated surfaces.

- Chapter 4 is dedicated to the presentation of the results acquired with this energy filtered PEEM, by microspectroscopy and spectromicroscopy at different energy range: secondary electrons, core-level and valence band photoelectrons. The characterization of the samples is done in terms of work function mapping, deconvolution of high-resolved core-level Si $2p$ spectra, and valence band maximum determination. We present core-level imaging integrated over the whole Si $2p$ peak.

- Chapter 5 addresses first the contrast observed in photoemission threshold PEEM at the junction. Secondly, we study in more detail the triple contrast observed for closed micron scale patterns. Modelling the closed regions as a diode provides a coherent explanation of the triple contrast. The chapter presents numerical simulations of modifications in the PEEM contrast due to the presence of a lateral electric field across the pn junction. Electrical and physical topography influence the apparent pattern size and junction position as observed in PEEM. A qualitative comparison with experiment provides a better understanding of the phenomena. Finally, the possibility of observing indirectly the local electrical fields using dark field imaging is explored.

Chapter 1

Imaging of silicon pn junctions

Contents

1.1 Needs for multiscale characterization of doping in devices

The scaling of integrated circuits for technological breakthrough forces improvements in terms of design and fabrication. To observe such structures requires the development capabilities of characterization at different scales, from few microns to a tenth of a nanometer. The fabrication processes must be fully understood since, for example, defects can create dopant diffusion. In 2010, process simulations are also still performed to describe in detail the interactions between implantation doping and defects [1]. The devices complexity in terms of technological steps grows with the needs of better performances. To improve indeed the fabrication of high-performance devices, it is necessary to understand the surface properties and dopant distribution, whatever the device scale.

In most cases, semiconducting materials are doped with impurity atoms to change their properties and create junctions. These junctions can be combined and exploited to form devices having a key role in integrated circuits. One of the most common use which can be cited is the Metal Oxide Semiconductor Field Effect Transistor (MOSFET) device: smaller and smaller transistor devices at the nano-scale are necessary for logic applications, with current research performed on the 22 nm node. However, the semiconductor device landscape also concerns larger scales: this is the case for transistors dedicated to power applications (Heterojunction field effect transistors HFETs) and for nano- and micro- electromechanical systems (NEMS and MEMS). HFET devices present gate lengths ranged from approximately 0.25 to 5 μm with gate widths between 50 and 800 μm to be high-efficiency and compact power amplifiers. Silicon nanowires are expected to have applications in field effect transistors, sensors, resonators and thermoelectric systems. Another example are microelectromechanical systems (MEMS) which refer to microscopic devices which have a characteristic length of less than 1 mm but more than 100 nm, and nanoelectromechanical systems (NEMS) refer to nanoscopic devices smaller than 100 nm, down to 10 nm. Both combine electrical and mechanical components.
The measurement of 2D carrier or dopant distribution across the junction is becoming more and more important, for example, locating dopants with ever-increasing precision at different scales. Achieving two dimensions (2D) characterization of electrical and chemical states requires multidisciplinary techniques at the micro- to nano- scales.

1.2 Structure of pn junction at thermodynamic equilibrium

1.2.1 The pn junction

When n-type and p-type silicon are joined together under equilibrium conditions, the Fermi level is flat through the entire structure, and corresponds to the straight horizontal dashed line in figure 1.1 a), a pn junction is formed. This is not possible by joining two materials mechanically, but by chemical processes allowing the existence of these two different regions within a single crystal.
The region on the left is p-type with an acceptor density N_a given by the holes which

are majority carriers, while the region on the right is n-type with a donor density N_d determined by the electrons concentration. The physical localisation where the different doping types are in contact is called the *metallic junction*. It is important to distinguish this notion from the *electrical junction* since, their positions do not always coincide. The latter parameter is defined as the zone inside the depletion region, where the electron concentration is equal to the hole one.

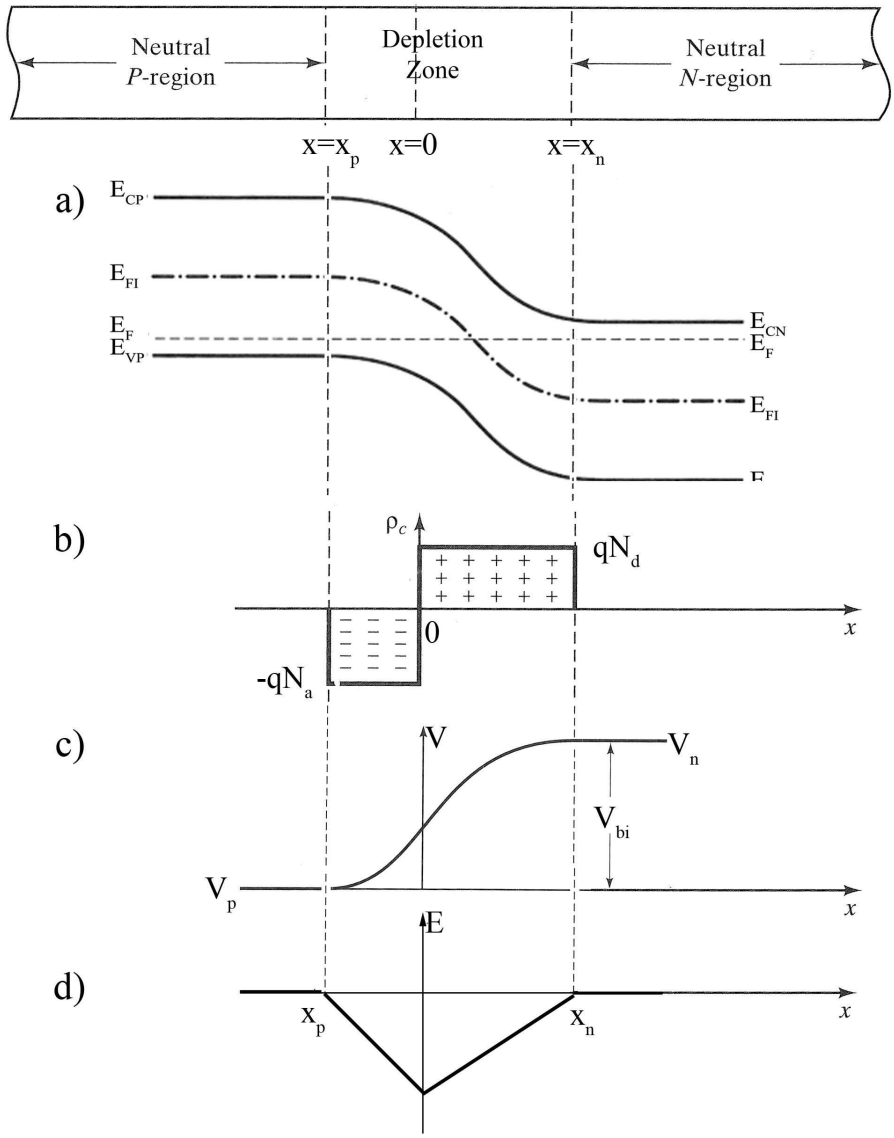

Figure 1.1: *a) Energy band diagram of a pn junction at equilibrium. b) Distribution of charges and c) representation of the potential in the space charge region at thermal equilibrium. Definition of the built-in potential V_{bi}. d) Representation of the electrical field in the space charge region at thermal equilibrium.*

1.2.2 Band bending and depletion zone

A physical system in equilibrium does not mean that everything is static: electrons and holes are indeed flowing in both directions across the junction. The electrons leave behind them ionized donors with a positive charge in the n-region of the junction, and the holes leave a negative charge in the p-one, given the presence of ionized acceptors. This process creates in the pn junction, a region around the junction where the free carriers density is negligible: the *depletion region* or *space charge zone*.
Even a semiconductor which possesses localized electronic surface states usually induces a perturbation of the local charge, creating a depletion zone. We will also study this kind of depletion zone occurring, for example, at the buried interface with an oxide and the sample surface which results in band bending.

The theory of the depletion zone at the surface of a semiconductor has been given by Schottky *et al.* [2] and Mott [3]. Garrett *et al.* [4] also considered the properties of the space charge region and the role of surface states at a semiconductor surface. The charge redistribution depends on the surface dopant type and on the position of the Fermi level at the surface. These surface states carry charge, which screens an opposite charge inside the semiconductor material. The higher the electron density, the shorter the range over which electrons have to rearrange in order to establish an effective shielding.

This depletion zone, is represented in figure 1.1. We consider two frontiers on the abscissa x_p and x_n respectively for the p-doped zone and for the n-doped zone. The charge density in the pn junction can be expressed as:

$$\rho(x) = \begin{cases} 0 & \text{for } x < x_p \text{ and } x > x_n \\ -qN_a & \text{for } x_p < x < 0 \\ qN_d & \text{for } 0 < x < x_n \end{cases}$$

where q is the electric charge.

Its width depends on the doping concentrations of the n-doped and p-doped layers. However, around x_n some electrons can penetrate into the depletion zone, and the same phenomenon appears for the holes around x_p. This leads to a perturbation of the potential on a certain distance called the *Debye length*, respectively L_{Dn} in n-type region and L_{Dp} in p-type region.

$$L_{Dn} = \sqrt{\frac{kT\epsilon}{2q^2N_d}} \, . \tag{1.1}$$

$$L_{Dp} = \sqrt{\frac{kT\epsilon}{2q^2N_a}} \, . \tag{1.2}$$

To determine the space charge width in the n-doped region, the use of the expression 1.1 of the built-in potential yields:

$$W_n = 2L_{Dn}\left(\frac{1}{1+N_d/N_a} ln\left(\frac{N_dN_a}{n_i^2}\right)\right)^{1/2} \, . \tag{1.3}$$

By the same way, using expression 1.2, the space charge width in the p-doped region is:

$$W_p = 2L_{Dp}\left(\frac{1}{1+N_a/N_d} ln\left(\frac{N_d N_a}{n_i^2}\right)\right)^{1/2} , \tag{1.4}$$

The depletion width is given by the sum of the space charge extension of the two regions: $W = W_n + W_p$. If the junction is strongly asymmetric, the space charge zone spreads over the less doped one.

1.2.3 The built-in potential

When, in thermal equilibrium, no external voltage is applied between the n-type and p-type regions, there is an internal potential of the conduction electron which varies from a value V_p in the p-doped region, to a value V_n in the n-type one. Since thermal equilibrium implies that the Fermi energy is constant through the entire pn structure, the difference between these two regions, is called the *built-in potential* V_{bi}. It is defined as the difference in energy between the n-type and the p-type semiconductor. Its value is clearly presented in figure 1.1 c) and is equal to the full band bending in equilibrium.

As a consequence, the built-in potential is given by:

$$V_{bi} = \frac{kT}{q} ln\left(\frac{N_d N_a}{n_i^2}\right) . \tag{1.5}$$

1.2.4 Lateral electric field across pn junction

According to Poisson's equation, the charge distribution occurring in the depletion zone results in an electric field which is accompanied by a band bending that can be interpreted as an energy barrier.
The presence of a space charge zone implies the existence of a potential variation across the barrier, and thus, the presence of an electrical field: it is high in the major part of the depletion zone, as presented in figure 1.1 d). The width of the depletion zone depends on the doping concentrations of the n-doped and p-doped layers.

The behavior of the electrical field on the x axis is given by $E = -dV/dx$ for the two doped regions:

$$E = -\frac{qN_a}{\epsilon}(x - x_p) \text{ for } x_p < x < 0 , \tag{1.6}$$

$$E = \frac{qN_d}{\epsilon}(x - x_n) \text{ for } 0 < x < x_n , \tag{1.7}$$

where ϵ is the vacuum dielectric permittivity.

1.3 2D dopant mapping of pn junctions: state of the art of existing techniques

As one of the most recent two-dimensional dopant mapping techniques, it is important to position energy-filtered PEEM within the field of existing techniques. The 2D carrier and

dopant profiling techniques the most relevant for silicon dopant imaging are presented with their present advantages and drawbacks. Techniques introduced have been classified in five categories:

- *Scanning ion probe techniques*, such as Secondary Ion Mass Spectrometry (SIMS) and Time of Flight (ToF) SIMS.
- *Scanning probe near-field microscopy-based techniques*, such as Kelvin Force Microscopy (KFM), Scanning Capacitance Microscopy (SCM) and Scanning Spreading Resistance Microscopy (SSRM).
- *Electron microscopy-based techniques*, such as Scanning Electron Microscopy (SEM) and electron holography.
- *Ion microscopy-based techniques* which corresponds to the Atom Probe Tomography (APT) technique.
- *Photoemission-based microscopy techniques*, such as Scanning PhotoElectron Microscopy (SPEM) and PhotoElectron Emission Microscopy (PEEM).

They are assessed on the basis of sensitivity, spatial resolution, nature of the information provided by the technique (which can be either chemical or electrical), and capacity to do non-destructive analysis of real devices [5].

1.3.1 Scanning ion probe techniques

1.3.1.1 2D Secondary Ion Mass Spectrometry and Imaging SIMS

SIMS can provide in-depth compositional information from materials. It can be extended to investigate two- and three-dimensions (3D) elemental distribution for trace elements. SIMS can be operated either in static or in dynamic mode.

An energetic primary ion beam of 1 keV to 20 keV sputters the sample, removing material from the surface. These primary particles are either reactive or inert. It is a destructive technique since the sample is damaged during the analysis [6]. Only a small fraction of the sputtered material corresponds to atoms or molecules ionized, either positively or negatively and are called secondary ions, the rest being ejected as neutral atoms or molecules. The secondary ions are collected and separated in energy and mass thanks to the combination of an energy analyzer and a magnetic analyzer, which forms a secondary ion mass spectrometer [7,8]. The energy analyzer can be a sector, a quadrupole or a time-of-flight. During the ablation, the surface is removed layer by layer, providing a highly sensitive chemical profile concentration of the material.
The sample studied can be either bulk, thin layer or powder. The crater size can vary from 100 nm to 500 μm. Sputter rates can be adjusted to analyse depths ranging from many microns to few nanometers. All elements and isotopes can be recorded, including hydrogen, with a high surface sensitivity from ppm down to ppb. The quantification requires reference samples to calibrate the instrument: for each atomic species present, concentration calibration with respect to the bulk matrix is established. This technique is one of the most used for dopant depth profiling, thanks to its high dynamic sensitivity range, from 10^{14} to 10^{21} atoms.cm^{-3}.

Static imaging SIMS Static SIMS investigates the chemical composition of the outermost atomic monolayers, providing rapid characterization of both organic and inorganic species present on the surface with a high sensitivity. In this configuration, a small number of primary ions are used to analyse the sample. It helps in studying phenomena such as corrosion or adsorption. It can be applied by using the Time of Flight ToF-SIMS configuration, where the secondary ions ejected are analyzed and separated thanks to the fact that ions lighter have higher velocities than the heavier ones, and then, reach the detector earlier. Figure 1.2 shows some negative secondary ion images obtained from a Peptide Nucleic Acid (PNA) biosensor chip which was hybridized with complementary deoxyribonucleic acid (DNA) [9]. The spatial distribution of specific chemical species can be clearly identified. By scanning a finely focused primary ion beam over the sample surface, and acquiring a mass spectrum at each pixel of the CCD detector, it is possible to carry out the chemical mapping. The lateral resolution can be down to 100 nm but it is limited by the ion beam diameter.

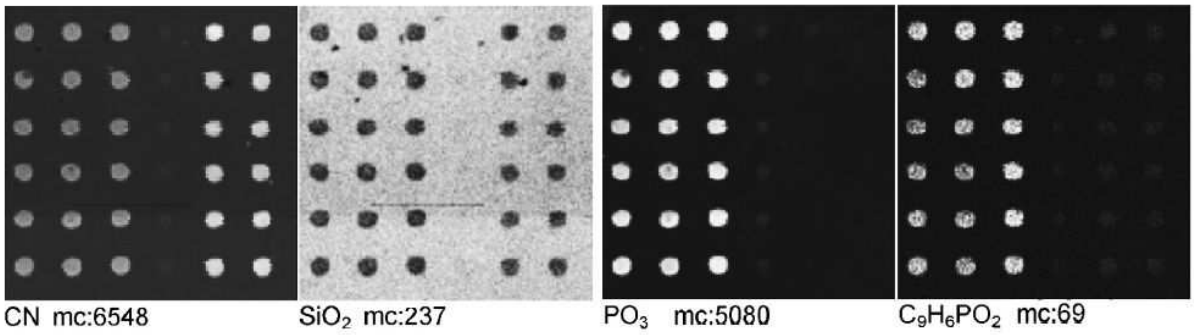

Figure 1.2: *Negative ToF-SIMS images of a Si wafer PNA/DNA biosensor chip. (25 keV Bi^{3+}, field of view (1500 × 1500) mm^2. Light gray corresponds to high intensity [9].*

Dynamic 2D SIMS Dynamic SIMS enables 2D depth-profiling analysis of thin layers and interfaces [10, 11]. It is more destructive than static SIMS, since it uses high intensity primary ion beams and prolonged exposure. Such conditions allow to remove much more material and to acquire a series of mass spectra at different depths.
In this mode, material removal and mass spectrometry are carried out either simultaneously or in an alternating mode, producing mass spectrometric images. In ToF-SIMS configuration, the entire mass spectrum can be stored at each cycle of the depth profile. Then, the 2D dopant distribution is obtained by recombination of these depth profiles thanks to algorithms. The major scientific impact of dynamic SIMS is the in-depth analysis of semiconductor materials, where low level dopants are analyzed in successive thin slices of materials down to 1 or 2 nm thick [12].

The 2D SIMS method was developed by Hill *et al.* but the technique remains complex [13]. Ukraintsev *et al.* demonstrated a simplest version where the SIMS lateral resolution can be decreased down to the photomask pixel size, i.e. 10 nm, for a dopant concentration sensitivity of 10^{17} atoms.cm^{-3} [10].
The major drawbacks of this technique are firstly that depth analysis is limited by the

capabilities of the primary ion beam to penetrate inside the sample. Moreover, the difficulties to combine high resolution with sensitivity in low doped areas limits the samples to be studied in such conditions. Secondly, spatial resolution is limited by the beam width, which can not be decreased under 50 nm. Finally, the stoichiometric and matrix properties of the sample must be known to interpret properly the data.

1.3.2 Scanning Probe Microscopy Techniques

Two reviews present the Atomic Force Microscopy (AFM)-based electrical characterization techniques [14,15]. Table 1.1 summarizes the various techniques which can be considered, displaying the type of probe used and the measured physical quantity. Duhayon *et al.* compared Scanning Capacitance Microscopy (SCM), Scanning Spreading Resistance Microscopy (SSRM) and Kelvin probe Force Microscopy (KFM) [16] and De Wolf *et al.* added Scanning Tunneling Microscopy (STM) to these three methods [17] for comparison. The basic characteristics of these four main techniques are now introduced.

Technique	Mode	Probe	Measured quantity
STM	STM	Metallic needle	No. Doping atoms I-V spectra
Selective etching +AFM	NC-AFM	Ultrasharp Si	Topography after chemical etching
SCM	C-AFM	Metal-coated Si or metallic	Depletion capacitance C-V spectra
SSRM	C-AFM	Diamond-coated Si or metallic	Electrical resistance I-V spectra
KFM	NC-AFM	Metal-coated Si or metallic	Electrostatic potential (electric field)
SSHM	STM	Metallic needle with microwave cavity	Depletion capacitance

Table 1.1: *Summary of the different scanning probe microscopy techniques which can be utilized for 2D carrier profiling. Column mode reflects the scanning mode (NC: non contact; C: contact) [17]. SSHM corresponds to Scanning Surface Harmonic Microscopy.*

Scanning Transmission Microscopy This technique probes the surface topographical and electrical structure with high lateral resolution of conductive samples, down to 1 Å. It is able to image atom arrangements on surfaces. STM is at the origin of the scanning probe microscopies. It was developed by Binnig and Rohrer who were awarded with the Nobel prize for physics in 1986.
The principle of STM consists in tunneling of electrons between two electrodes, corresponding respectively to the outer atoms of the sample surface and those of a tip, under an electric field. To keep a current constant, a piezoelectric feedback system enables small movements by applying a voltage V to the probe when the latter is scanned above the sample. Its movement is recorded and displayed as an image of the sample local density of states, as presented in figure 1.3 a).
STM can be used to image a depletion zone at a silicon pn junction surface [18,19]. Clear contrast was observed between electrically different regions: n-, p- and the depletion zone, shown in figure 1.3 b) [20].

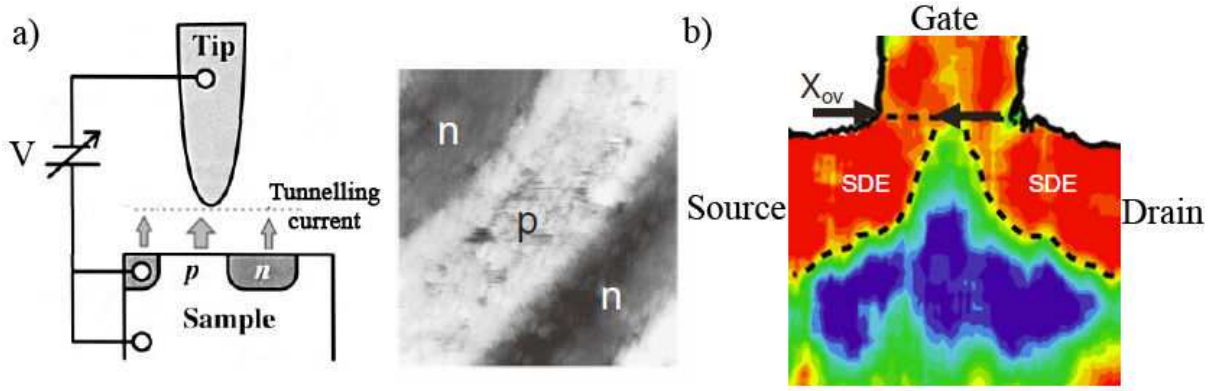

Figure 1.3: *a) Schematic illustration of STM measurement on a nanoscale pn junction and resulting image. b) cross-section of a MOSFET transistor with a gate length of 38 nm and STM 2D (CITS mode) carrier profile extracted [21, 22].*

This technique has some drawbacks: depending on the electrical conductivity in the sample, the force between the tip and this latter can vary, creating mechanical tip-sample interactions during the observations, which renders the ability to position the tunneling tip reliably and reproducibly more difficult [23].
Moreover, variations of the depletion layer observed by Fukutome [21] depending on STM bias voltage is considered to be due to the local band bending caused partially by the STM tip. This very surface sensitive technique must be performed under Ultra High Vacuum (UHV) to avoid contamination and native oxide on the samples surface since it requires a conductive surface. To measure bulk electronic structure, it is important to eliminate as much surface states or defects in the band gap as possible, since they cause the surface Fermi level pinning [24]. A possibility to avoid them is to passivate the surface, in order to obtain near flat band conditions [25].

Combining the spectroscopic capabilities and the scanning ability of an STM gives rise to the Current Imaging Tunneling Spectroscopy (CITS) technique. This latter enables to obtain 2D spatially resolved spectroscopic information from the tunneling current characteristics which are used to construct images that reveal atomic- to nanometer-scale variations in electronic structure on the sample surface.
Such a system works as follows: stabilizing the current at a fixed value for a given voltage, a constant-current topographic scan is performed over the sample surface. For each point, a current-voltage spectrum is measured, whose variations correspond to variations in electronic structure across the sample surface. Plotting the current measured at specific bias voltages is called a current image. In 2010, Fukutome [22] has realized a 2D view carrier profile as a tunneling current image with UHV-STM in CITS mode of p-type Metal-Oxide-Semiconductor Field-Effect Transistor (MOSFET), with a gate length of 38 nm presented in figure 1.3 b) which highlights this technique breakthrough in device characterization.

Scanning Capacitance Microscopy This technique measures the variation of the electric capacity dC of a MOS structure formed artificially between a tip and an oxide-covered surface, when applying an electrical modulation dV. It measures the doping concentration, and the carrier type of cross-section or planar samples [26]. For pn junction imaging, the technique is often utilized at constant voltage mode: the alternating current (ac) voltage is applied to the sample and the change in capacitance under the tip is recorded. SCM has a lateral resolution of 10-20 nm and the junction position is directly obtained [27–29].
The main drawback is the sample preparation: cross-section samples are difficult to obtain since it is very hard to control the attack speed and to stop at the exact required localization. One solution is to use Focused Ion Beam (FIB) preparation combined with plasma etching [30]. Moreover, the nature of the dielectric oxide coverage on the sample surface is of prime importance: high-quality surface oxide with constant thickness in the scanned region is required, otherwise artifacts can appear [31]. The 2 nm native oxide growing on the silicon is too thin whereas a thicker uniform oxide of 3 nm or more, grown by dry or wet oxidation enables SCM measurements. The combination of this oxide and diamond-coated probe is suitable for stable, reliable and reproducible measurements, but remains difficult challenging [32].

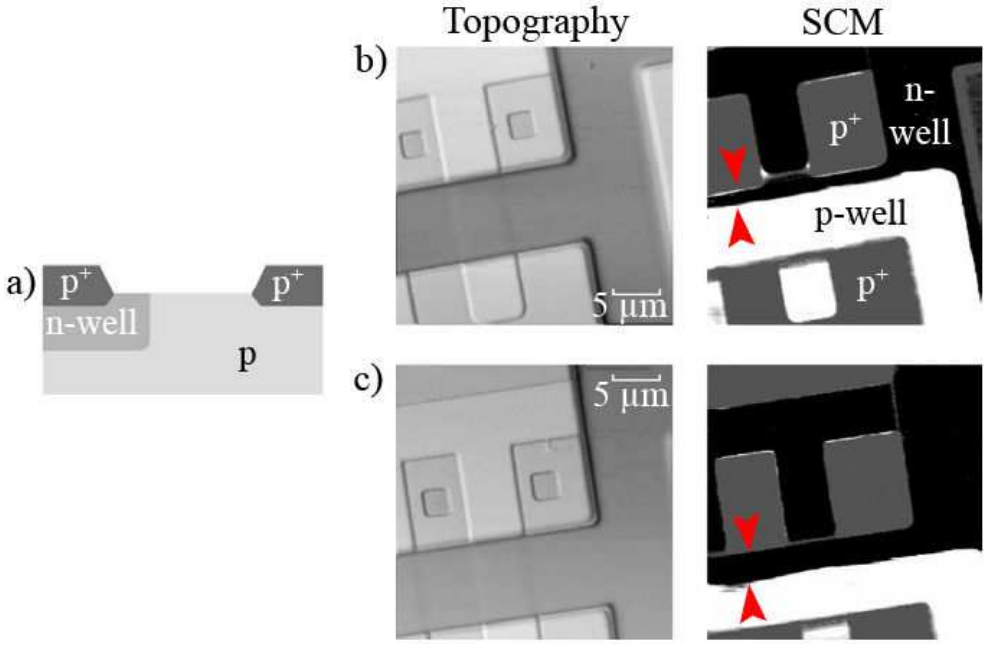

Figure 1.4: *a) Schematic cross-section of the wafer: AFM and SCM images of this wafer b) with mask misalignment and c) with correct mask alignment [33].*

The breakthrough in sample preparation has avoided the contrast reversal effect, characterized by the fact that the SCM output is not always a monotonically increasing signal with decreasing dopant concentration [34]. This drawback, which has prevented quantification for many years can be due to interface states, semiconductor work-function or interface trap density depending on the polishing quality and the oxide preparation [35]. New procedures based on the use of peak dC/dV at every spatial point, for dopant profile

extraction have improved the measurements [36]. Figure 1.4 shows that SCM visualizes and identifies the position of the dopant areas and can help for example, in the detection of wrong mask alignment during fabrication process: comparing b) and c) images of the n well adjacent to the P^+ areas represented by the two red arrows on a silicon wafer, one observe that this latter is too narrow in b) and that current leakage occurs [33].

SCM is sensitive to 10^{15} to 10^{20} atoms.cm^{-3}, and is almost non destructive. Its spatial resolution is limited by the sensitivity of the capacitance sensor and the tip-sample contact area, the tip geometry, and the dopant level and the topography of the sample surface. For this latter case, Buzzo *et al.* [37] compared a 2D dopant analysis of 4H silicon carbide pn junctions with SCM to quantify the influence of the surface roughness on the junction position.

Scanning Spreading Resistance Microscopy This technique consists in scanning a hard conductive diamond-coated silicon probe, in contact mode across the sample. It measures the electric resistance between a contact tip and the contact on the sample backside when applying a potential difference. The resistance depends on the doping level but it is not possible to determine the carrier type. On ultrashallow pn junction for the delineation of carriers within silicon devices, Zhang *et al.* [38] have achieved a 1 nm spatial resolution, as presented in figure 1.5 a).

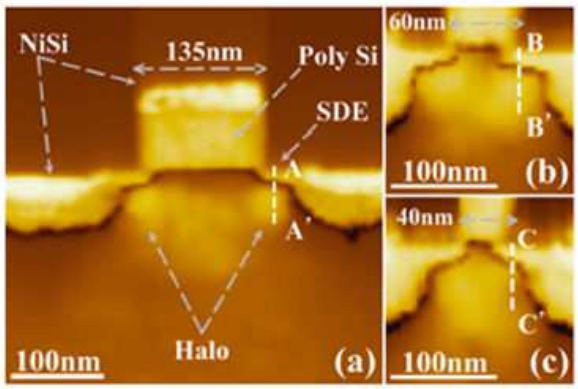

Figure 1.5: *a) SSRM images of ultrashallow junction p-type MOSFETs, gate lengths of a) 135 nm, b) 60 nm, and c) 40 nm [39].*

SSRM employs a strong tip pressure and thus, both the sample surface and the scanning tip are damaged [40, 41]. The technique is less dependent than SCM to surface preparation: it provides a better spatial resolution, sensitivity, quantification and reproducibility [42, 43]. The dopant gradient resolution is higher: 1-2 nanometers per decade, thanks to the resistance increase for small carrier concentrations [44]. SSRM also gives some complementary information about highly doped region, and enables, as seen in figure 1.5 b) and c) to distinguish an arsenic-halo corresponding to impurities within the p-type MOSFET device.
The limitations of this technique are the impossibility to distinguish n-type from p-type and, as for SCM, the tip shape which restrains the resolution. Hence, SCM and SSRM

are complementary ambient techniques for dopant characterization. Both are sensitive to the whole dynamic range between 5×10^{14} atoms.cm^{-3} and 2×10^{21} atoms.cm^{-3}.

Kelvin Force Microscopy This is a non contact and non destructive electrostatic force microscopy technique. Its principle consists in scanning a sample with an AFM cantilever excited electrically by applying a voltage (ac+dc) to the tip. The amplitude of vibration is proportional to the electrostatic restoring force between the tip and the conductive sample. This potential difference between the tip and the sample is obtained by varying the direct current voltage until the alternating current vibration of the tip at the frequency near the cantilever resonance becomes nil. The electrochemical potential of the sample surface is measured with respect to the tip one. This potential depends on the work-function difference, from which one can deduce the local carrier concentration. However, quantitative potential profiling is limited by surface charges and adsorbed molecules which induce band bending. Saraf *et al.* [45] have measured the 2D-potential distribution inside asymmetric pn junctions. Combining with a 3D analysis of the tip-sample electrostatic interaction, they are able to deduce the direct local measurement of surface charge and band bending in semiconductors.

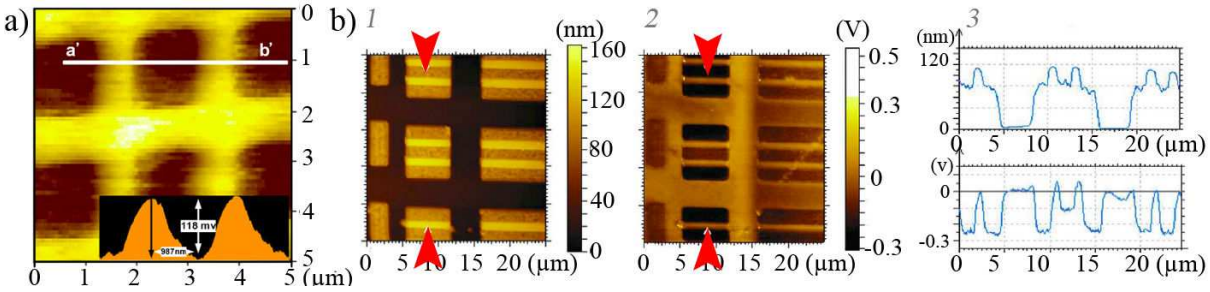

Figure 1.6: *a) Surface potential image of a pn junction array measured by KFM [46]. b) The topography 1- and surface potential 2- images of Static Random Access Memory (SRAM). The cross-section profiles along the directions indicated with red arrows in 1- and 2- are shown in the top and bottom parts of 3- [47].*

KFM is sensitive to variations in dopant concentration between 10^{15} to 10^{20} atoms.cm^{-3}. Tsui *et al.* have established correlations between surface potential difference of a pn junction and carrier-dopant concentration. Besides, the cross-sectional profile of a pn junction array extracted from its surface potential mapping has been successfully demonstrated by Tsui *et al.* [46], and is presented in figure 1.6 a). Figure 1.6 b) shows the clear contrast which can be obtained depending on the dopant type for Static Random Access Memory (SRAM) studies. The spatial resolution can attain 30 nm using a low humidity environment, such as nitrogen gas flushing.
A higher imaging resolution can be achieved by using a smaller probe tip, when modifying the Atomic Force Microscope cantilever with a Multi-Walled Carbon Nanotube (MWNT): it helps resolving the dopant distribution to within 10 nm in air [48]. The sample surface potential being very sensitive to surface changes and to adsorbed molecules, KFM encounters more difficulties in concentration quantification than SSRM [16].

1.3.3 Ion microscopy-based techniques

1.3.3.1 Atom Probe Tomography

Atom Probe Tomography (APT) provides real analytical atomic scale mapping of chemical species, including ultra-shallow and extremely highly-doped pn junctions, as well as MOS structures [49]. It utilizes a high voltage to evaporate atoms as charged ions one-by-one using, either a pulsed field, or a mass spectrometer, and is completed by a delay-line position-sensitive detector [50]. The original position from which the atom field evaporated can be determined, and data are then rearranged in a 3D reconstruction of the volume using computer calculation. An introduction to the history of this technique and the underlying physics is given by Miller and Forbes [51].

This technique is sensitive to field evaporated ion species in a field of view of typically 50 nm to 100 nm in diameter where it is possible to distinguish the physical variations in dopant distribution down to 0.5 nm in lateral resolution [52]. Figure 1.7 presents two atom maps of silicon devices: a) is a Si:SiGeB:Si multilayer test structure. Here APT spatial sensitivity for interface analysis is clearly seen and also helps in identifying areas of local Ge accumulation. Figure 1.7 b) shows the APT capabilities to provide atomic scale maps of chemical species, here when characterizing a metal-oxide-semiconductor (MOS) structure.

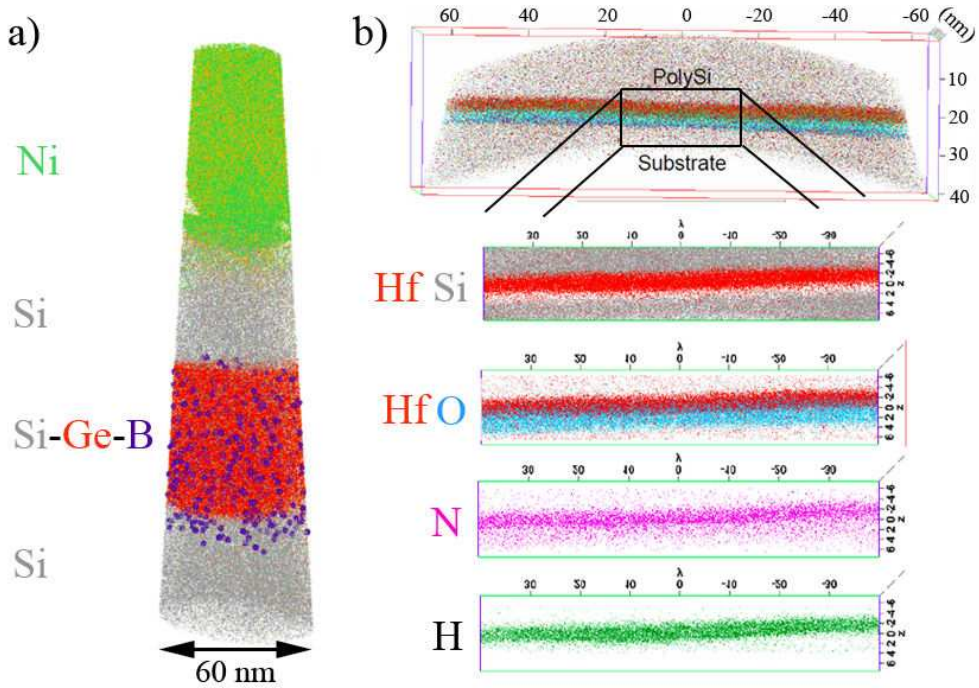

Figure 1.7: *a) Si:SiGeB:Si multilayer test structure [53]. b) Spatial distribution of elements within a polySi/Hafnia high k dielectric stack. Each point represents an atom [54].*

The major limitation of this technique is the sample preparation, which requires milling of sharp needle shaped specimens of several nanometers in diameter. Mechanical stresses in the specimen can provoke fractures. The sample must also have a good electrical conductivity for voltage pulsed field evaporation [55, 56]. Moreover, the information

is collected in 3D, the data acquisition is long and the zone probed stays small, around 10^6 nm^3. The lateral resolution is degraded for larger volumes. The detection level is 10^{19} atoms.cm^{-3} for arsenic and 5×10^{18} atoms.cm^{-3} for boron [52].
Laser pulsing to evaporate atoms have drastically improved the capabilities of the technique in terms of mass resolution and the Signal-to-Noise Ratio (SNR) increase, thus improving the spatial resolving power of the instrument [49, 57]. This leads to a better sensitivity to low concentrations, and an ultimate detection limit of tens of ppm.

Another limitation of the technique is the inclusion of materials with different kinetic of field evaporation in the same sample volume: when considering species with higher evaporation fields, they evaporate more slowly, complicating the depth reconstruction of the volume.

1.3.4 Electron microscopy-based techniques

1.3.4.1 Electron Holography

Electron holography is a high resolution coherent interferometric technique. It maps the local concentration of active dopants via electrostatic potential distribution [58,59]. This technique can be also used on reverse biased pn junctions or deep submicron transistor structures [60]. Recently, Yoo *et al.* [61] reported the quantitative analysis of a pn junction and estimated the built-in potential across the junction. Electron holography provides access to the phase of the electron wavefront which has crossed the sample. It is a technique allowing the combination of nanometer scale spatial resolution and sufficient sensitivity to detect the implanted dopants [62, 63] with doping levels from 10^{16} to 10^{21} atoms.cm^{-3} [16, 64] and a resolution of 10 nm [65].

The electron optical geometry for off-axis electron holography in Transmission Electron Microscope (TEM) is presented by Midgley [67]: highly coherent electrons emitted from a field emission gun are divided into a reference wave, traveling in vacuum, and an object wave, passing through the sample. Due to its inner potential which increases the electron kinetic energy, the electron wavelength becomes shorter in the specimen than in vacuum. An electrostatic biprism placed after the sample bends the two waves so that they form an interference pattern called hologram recorded by a 2D detector. This hologram contains the electron wave, as presented in figure 1.8 a): amplitude and phase informations. The phase shifts relative to the reference wave since the inner potential changes as a result of the built-in potential generated at the junction. Part b) of the same figure presents the reconstructed amplitude and phase image of the transistor, the phase images being proportional to the inner electrostatic potential distribution.
The sample preparation is difficult since this method requires specimen whose thickness should be in the range of 200 nm to 400 nm, in order to optimize the signal-to-noise ratio [68]. Several methods exist, such as tripod polishing, Ar ion beam milling and FIB milling but they induce electrically dead layers near surface regions. Damage induced by FIB can be of two types: amorphisation of the silicon surface and gallium implantation [69]. Their presence create interactions with the electron beam and affect the holography measurements [70–72]. Figure 1.8 c) illustrates this for FIB prepared samples, the theoretical phase profile being compared to the experimental one for differently doped pn junctions. For the lightly-doped specimens, the phase profile measured is less than theory, whereas for specimens with higher dopant concentrations the measured

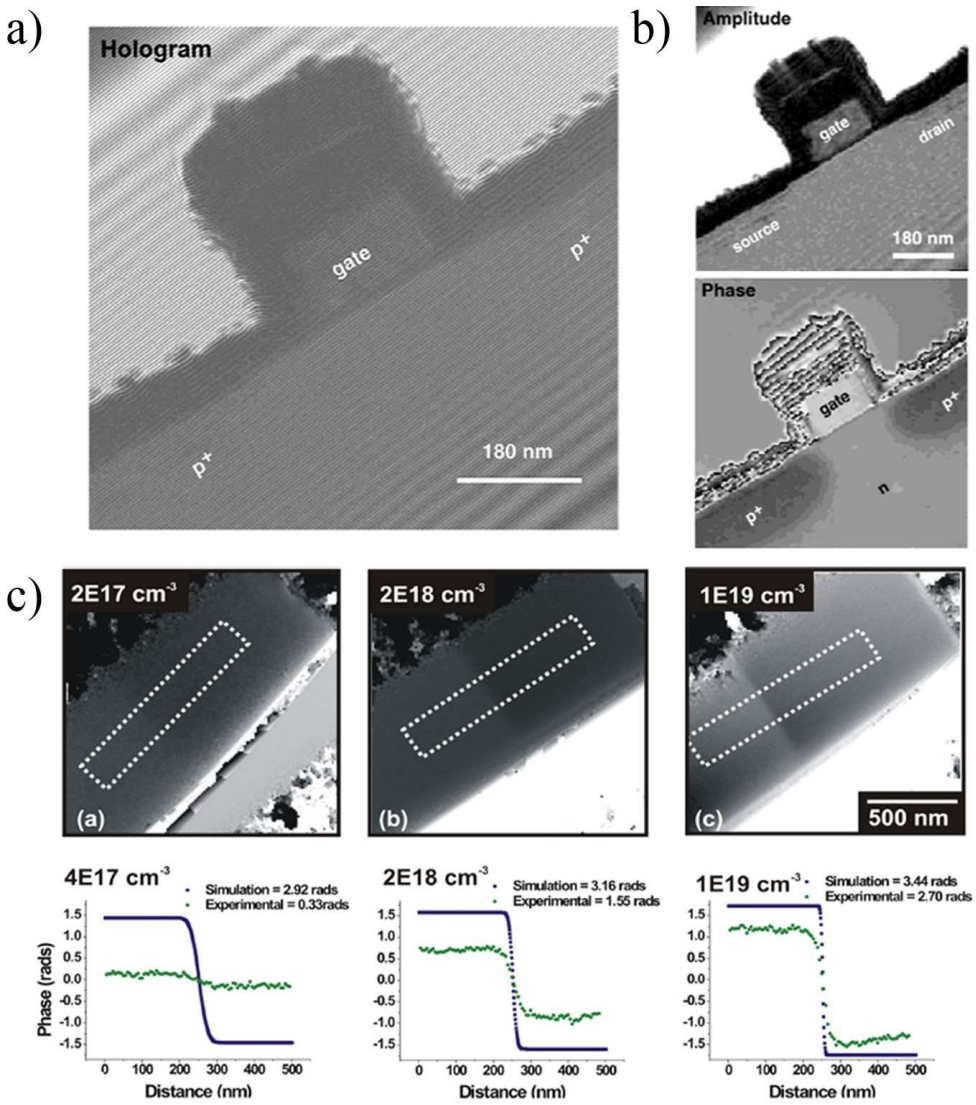

Figure 1.8: *a) Hologram of a 0.18 µm p-MOS transistor structure. b) Reconstructed amplitude and phase image of the transistor [60]. c) Top images represent phase images of 400 nm-thick-specimen for each of the pn junctions with different doping, and prepared by conventional FIB milling. Bottom images show the experimental phase profile extracted from the white rectangles, compared to the theoretical step in phase for perfect bulk-like specimens [66].*

profiles fit the theoretical one. Cooper *et al.* [66] deduced that the electrically inactive thickness is strongly dependent on the dopant concentration in the specimens.
Charging can also have a serious effect on electron holographic measurements of electrostatic potential, especially in sample regions close to the interface with vacuum. For low doped samples, the measurements are dependent on the strength of the electron beam due to the number of electron-hole pairs created in the sample which can be closed to the carrier concentration in the pn junction. Therefore, the relative effects of charging can be stronger for low doped samples, which implies this technique not to be used below 10^{17} atoms.cm^{-3} [73].

1.3.4.2 Electron Microscopy

Scanning Electron Microscopy This technique is the best known and the most widely used to study the surface of materials. The contrast in the Secondary Electron (SE) image reveals information about the sample composition and its surface topography and potential. Images in SEM are acquired by scanning a highly focused primary electron beam on the sample surface. Its energy varies in the range 5 keV to 30 keV. The SE emitted are then collected by a detector.
The implementation of field-emission electron guns helps in such studies. Field-Emission SEM (FE-SEM) is particularly well suited for the delineation of electrical junctions [74]: it improves resolution and reduces surface damages due to the radiation. It enables the direct observation of electrically active dopant distribution. It detects contrast with sensitivity to dopant concentration of 10^{15} to 10^{20} atoms.cm^{-3}, and a sub-10 nm spatial resolution with an accuracy of $\pm 10\%$ [75, 76], as can be seen in figure 1.9. Such resolution is possible thanks to the primary electron beam which can be highly focused down to very small spots. Contrary to conventional instrumentation, this technique has the advantage to provide narrower probe diameters with low voltages. It generates much smaller interaction volumes, i.e. lower penetration depths around 5 nm to 50 nm, hence giving rise to higher resolution imaging capabilities. The specimen is usually immersed in a relatively strong magnetic field in order to obtain high resolution of 1 nm or even less with a primary beam energy of 15 keV.

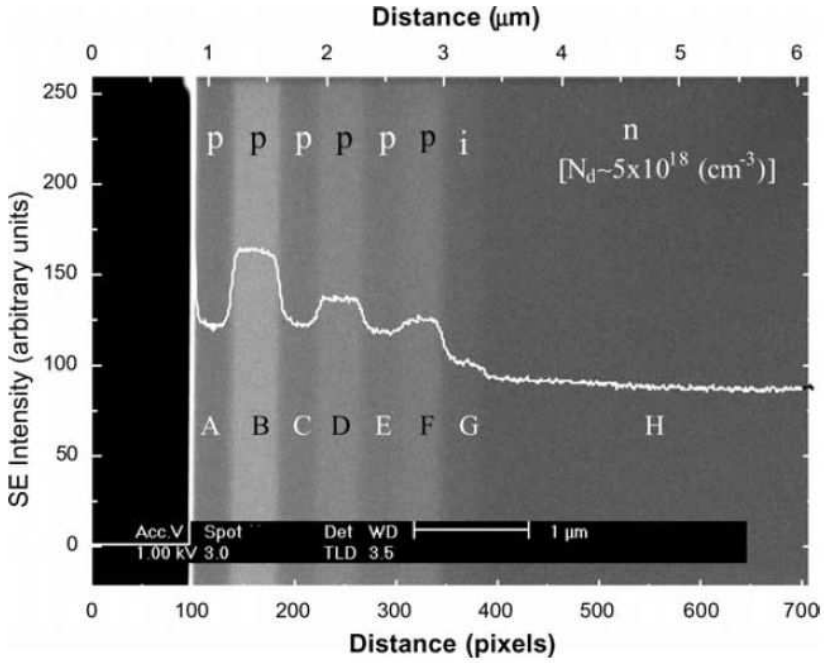

Figure 1.9: *SE image of cleaved silicon and the corresponding SEM intensity profile. The p-doped layers labeled* A, B, C, D, E, *and* F *are B-doped to* $2\times10^{15}, 1\times10^{19}$, 1×10^{15}, 1×10^{18}, 1×10^{15}, *and* 1×10^{17} *atoms.cm*$^{-3}$ *respectively. Layer* G *is an intrinsic layer, and layer H is an n-doped layer (Sb doped) with a doping concentration of* 5×10^{18} *atoms.cm*$^{-3}$ *[77].*

SEM can be used to observe silicon pn junctions but it is important to be careful

when interpreting the images, keeping in mind the sample surface quality influences the observations: contamination layer deposited on the surface affects indeed the intensity signal. Moreover, dopant profiling of devices can imply to prepare a cross section through the area of interest. Preparing samples with FIB, or by polishing, due to topography can also generate a thick damaged surface layer which brings difficulties to observe a good secondary electron dopant contrast with secondary electrons [30, 78]. It is better to observe cleaved samples, or FIB choosing conditions to reduce the damaged layer [79]. The image quality is also degraded in presence of native oxide. Hydrofluoric acid (HF) cleaning is often used to minimize this problem.

Though conventional SEM is sensitive to the doping level and its logarithmic dependence of contrast regarding the p-type carrier concentration being well known, it is not possible to distinguish differently n-doped zones. Schönjahn *et al.* [80] have got rid of this problem by using an energy-filtering detector. Conventional SEM remains qualitative whereas reliable quantitative analysis of the dopant concentration can be derived from the energy distribution of secondary electrons emitted per doped regions with this energy-filtering system.
SEMs can be operated with different kinds of filters, some of whom are presented in chapter 2, section 2.2. Liu *et al.* [81] showed that SEM is an excellent tool to characterize the leakage mechanisms in SRAM junctions. Kazemian *et al.* [82] measured the potential difference across pn junctions of different doping levels. They observed that filtered secondary electron imaging reveals and quantifies the dopant distributions. First application of the SE contrast on silicon carbide was realized, showing the possibilities of this technique to quantitatively delineate the electrical junction on both hetero- and homojunctions [83, 84]. Further investigations are still in progress to establish a quantitative conversion of this contrast into the local carriers density and then, into the dopant profile.

The growing use of secondary electron imaging to map dopant distributions has motivated investigation of the mechanisms that give rise to dopant contrast, a point which will be detailed in section 5.2.

Scanning Low-Energy Electron Microscope A SEM can easily be converted into a SLEEM. These acceleration voltages in the column are lowered, usually below 50 eV, by using a retarding-field optical element such as a cathode lens. The sample is biased at a high negative potential in order to retard the primary electrons before their impact [85]. This achieves nearly constant spatial resolution through the energy scale. A good review on this technique is given by Müllerová *et al.* [86].
SLEEM is a valuable addition to the standard SEM because it is sensitive to structure and orientation in crystalline materials. Moreover, since the incident electrons diffuse into a smaller interaction volume, it works at lower sampling depth and is able to image surfaces with high sensitivity, as can be seen in figures 1.10 a) and b). Regarding the lateral resolution, nearly the same as the SEM one can be achieved with an electron beam at 1 keV and a retarding field optics. Resolution of about 4 nm at 100 eV was thus obtained experimentally in such conditions.

An important drawback to both SEM or SLEEM is the carbon contamination layer formation of the sample surface irradiated. Contamination is created by the decomposi-

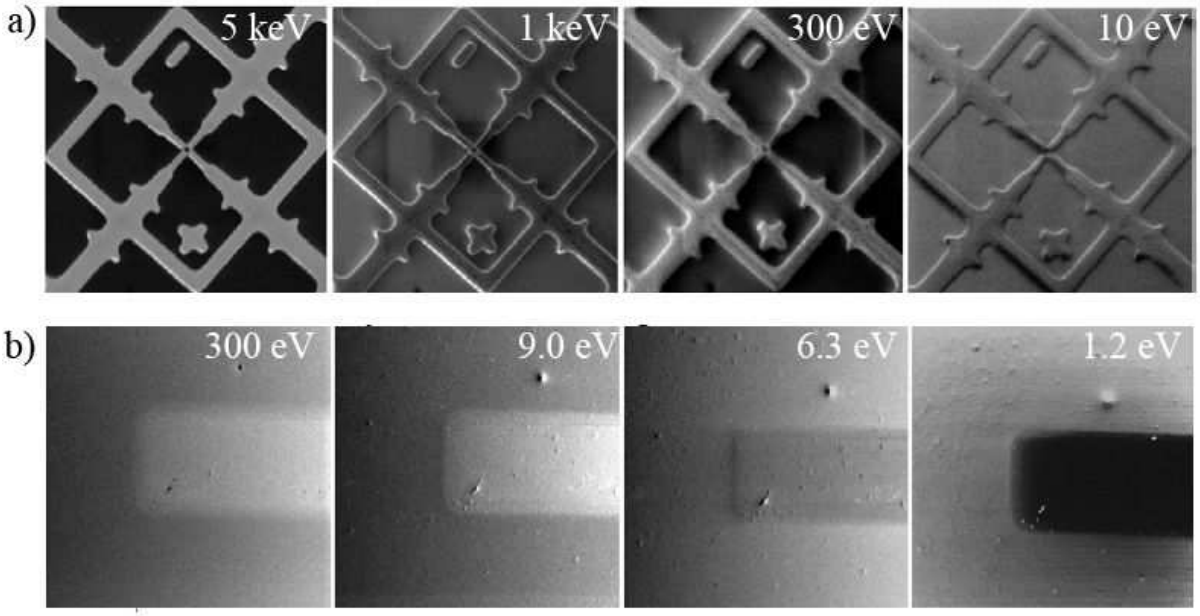

Figure 1.10: *SLEEM images: a) patterned 80 nm Pt layer on Si and b) P^+ type doped area on N type Si(111) for several electron energies [87].*

tion of adsorbed hydrocarbons under electron beam impact. Low primary energy beam, in the range 50 eV to 100 eV, corresponds for the secondary electrons to the minimum of the inelastic mean free path. This implies not taking into account the photoemitted electrons and the fast backscattered electrons [88]. The role of the different types of secondary electron SE_2 and SE_3 in Low Voltage SEM has been studied by Cazaux [89].

1.3.5 Photoemission-based microscopy

Photoemission electron microscopy is a powerful surface-sensitive technique suitable for imaging of doping-induced contrast in semiconductors. Two kinds of imaging methods are presented: the *microspectroscopy*, or Scanning PhotoElectron Microscopy (SPEM) and the *spectromicroscopy* or PhotoElectron Emission Microscopy (PEEM). These techniques are in reality spatially resolved photoelectron spectroscopy. The PEEM technique being the heart of this thesis, a more complete overview will be realized in chapter 2 section 2.1.2.

SPEM The SPEM requires a well focused photon beam which scans the sample surface as depicted in figure 1.11 a). The photoemitted electrons are collected by a detector. By scanning the sample with the photon beam, a 2D image of this surface is acquired. One can obtain a chemical map but this procedure can cause artifacts when following dynamical processes [90].

SPEM spatial resolution is only limited by the photon spot size. In laboratory conditions, the resolution is not better than several tens of microns due to the size of the focused X-ray spot. To obtain high resolution, SPEM is performed with synchrotron radiation and zone plates or mirror optics can focus spot sizes down to 100 nm [91, 92].

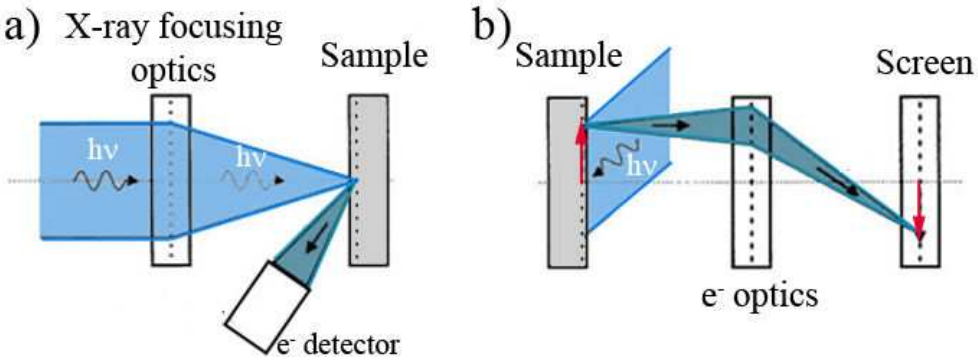

Figure 1.11: *Difference between a) SPEM and b) PEEM techniques.*

Reaching lateral resolution better than 50 nm remains difficult due to signal and working distance constraints [93].

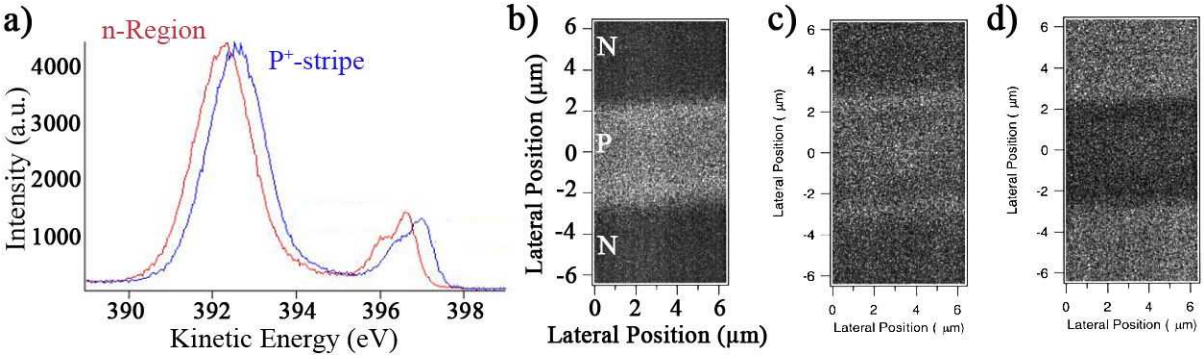

Figure 1.12: *a) Scanned Si 2p SPEM intensity maps showing energy dependent contrast across a silicon p-stripe, at electron energies of b) 397.22 eV, c) 396.98 eV, and d) 396.82 eV. Field of view (FoV) is (6.4±12.8) µm [94].*

PEEM In contrast to SPEM, PEEM does not use a scanned focused probe beam but the sample is uniformly illuminated, generally reducing beam induced damages on delicate surfaces. The data acquisition is full-field, as can be seen in figure 1.11 b). The surface magnified image can be observed directly and in real-time onto a fluorescent screen. This technique gives the electronic and chemical surface properties with spatial resolution only limited by the chromatic aberrations of the objective lens. It varies between 10 nm to 30 nm when considering SE imaging, these particles having thus a kinetic energy close to zero [92, 95, 96]. Spatial resolution down to 5 nm has been measured on biological specimen with a PEEM aberration corrected in synchrotron environment [97]. PEEM can perform real-time imaging, and is well adapted for real time observations. The time resolution can be decreased down to 180 ps using a PEEM combined with an imaging retarding field analyser [98].

The advantages of full-field microscopy with PEEM versus those of scanning microscopy with SPEM have been presented by Margaritondo, Renault *et al.* and Barinov *et al.* [93, 99, 100]. The major drawback of these techniques is that both are sensitive to

artifacts if the sample is not flat or conductive. Photoemission electron microscopy is a surface-sensitive probe providing dopant contrast in imaging.

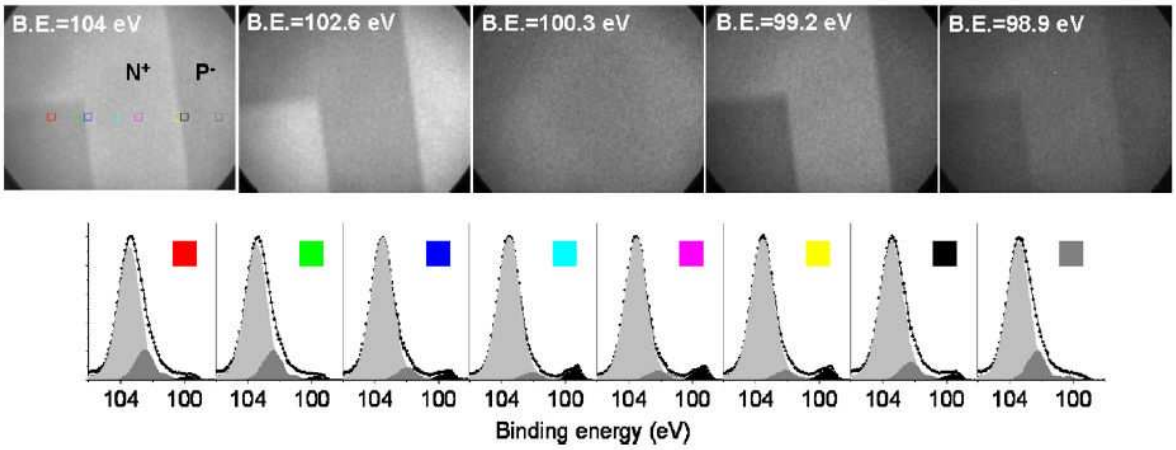

Figure 1.13: *Top: selected XPEEM images from the energy filtered image series across the Si 2p core level on sample N^+/P. Bottom: local Si 2p core level spectra and best least squares fits: the Si^{4+} component due to the native SiO_2 oxide is in light gray, the sub-oxide components gray and the Si^0 substrate component black. FoV is 25 μm [101].*

The combination of an energy filter and an electron microscope enables to obtain full spectral information available to characterize in detail the chemical and electrical properties of the imaged surface. Imaging the contrast variations across a silicon pn junction can be achieved in SPEM or in PEEM. Figures 1.12 and 1.13 respectively show contrast on core-level images of lateral silicon doped pn-junction, thus, variation in the energy bands across a device can be imaged directly. Core-level imaging with a sub-micron resolution is possible, and less than 500 nm have been reached with an X-ray laboratory source. Lateral resolution of 100 nm has been reached by Bailly *et al.* [102] using synchrotron radiation.
Combined with an electron analyser, the XPEEM can indirectly determine dopant concentrations from band lineup due to variations of the Fermi level. Ballarotto *et al.* have observed that differences in relative PEEM intensities show a systematic variation with p-type dopant concentration in the range of 1×10^{17} atoms.cm^{-3} to 2×10^{20} atoms.cm^{-3}, as seen in figure 1.14 a) [103]. Figure 1.14 b) presents the intensity on the PEEM image increase with doping concentration, at a rate of approximately 2 per decade, in good agreement with calculations based on photoemission from the valence band for a photon energies up to 0.18 eV above threshold.

1.3.6 Summary

The visualisation of 2D dopant mapping is still of importance nowadays, as the study of pn junction for devices at different scales. A non exhaustive list of the most used techniques has been done with their drawbacks and advantages that we have to be aware of for choosing the most suitable technique for the problem to be studied.

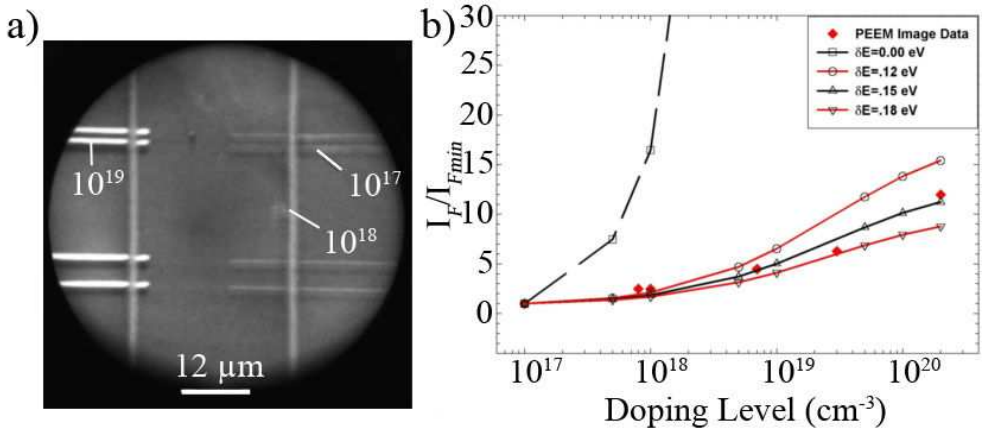

Figure 1.14: *a) PEEM image of lateral array of pn junctions. The doping concentrations are given in the image. b) Calculated threshold photoyields from Si(001) versus doping level at the sample surface. The red diamonds show the measured relative values of the PEEM intensities. δE corresponds to the position of the pinning states relative to the surface valence band [103].*

A comparison of different dopant profiling techniques using identical samples has been done by some laboratories [16, 17]. They provide a state-of-the-art preview of the techniques. Table 1.2 is extracted from reference [17], resuming well the last part of this chapter. Note that the improvements since these publications in sensitivity or resolution have not been taken into account.

Method	Resolution (nm)	Range (cm^{-3})	Concentration resolution	D/C	Quantification	Comments and problems
SCM	10	10^{15}-10^{20}	Power	C	Limited	Uncertainties at junctions, poor quantification procedure
SSHM	5	NA	Power	C	No	No quantification procedure
STM-atom counting	atomic	10^{18}-10^{20}	Linear	D	Yes	Only GaAs, not on Si
STM-STS/CITS	atomic	NA	Log.	C	Limited	Only junction delineation and type (n or p) identification
STM-STP	10	NA	Limited	C	Limited	Only junction delineation
KPM	100	10^{15}-10^{20}	Limited	C	Limited	Poor quantification procedure, stray-fields limit the resolution
SSRM	20	10^{15}-10^{20}	Linear	C	Yes	Availability diamond probes
Chemical etch + AFM/STM	1	10^{17}-10^{20}	Limited	C	Limited	Difficult to quantify, poor reproducibility
Imaging SIMS	100	NA	Linear	D	Yes	Sensitivity limited by target volume
2D-SIMS	30-50	10^{16}-10^{21}	Linear	D	Yes	Special structures required
2D-Tomography SIMS	50	NA	Linear	D	Yes	Special structures required. Complex sample preparation
Lateral SIMS	5-10	Done	Linear	D	Yes	Only the lateral dose Distribution is measured
2D-SRP	100	10^{15}-10^{21}	Linear	C	Yes	Special structures required
Chemical etch + SEM/STM	20	10^{17}-10^{21}	-	C	Limited	Only qualitative
FE-SEM	10-20	4.10^{16}-10^{20}	Limited		Limited	Robust model for quantification is not available
Electron Holography	1-10	10^{17}-10^{20}	Limited	C	Limited	
Inverse modeling with $C-V$	NA	NA	Inverse modeling techniques	C	Yes	Resolution and accuracy are unknown, long calculation times

Table 1.2: *Comparison of two-dimensional doping (D) and carrier (C) profiling methods (NA=not available) for direct measure of the dopants [16].*

1.4 Imaging of pn junctions with electron microscopies

1.4.1 Introduction to contrast

Contrast in electron microscopy corresponds to spatial variations in the image intensity. It depends on both local secondary photoemission yield and on the photothreshold energy distribution of the electrons photoemitted.
To quantify dopant contrast, we compare the averaged intensity values between two zones in an image. If we consider a doped layer deposited on a substrate, their intensities, respectively I_{dep} and I_{sub} are different and give rise to a contrast between the two doped zones. The dopant contrast value C can be extracted according to the relation:

$$C = \frac{I_{dep} - I_{sub}}{I_{dep} + I_{sub}} \, . \tag{1.8}$$

1.4.2 State-of-the-art of the interpretation of contrast when imaging pn junctions with an electron microscope

Chang and Nixon [104] were the first to observe in SEM that the SE yield changes across a pn junction: the p-type region emits more SE than the n-region, appearing brighter in the images. Venables *et al.* [76] highlight the sensitivity of PEEM to the dopant concentration. In addition, SE contrast on pn junctions depends on the doping level.
There are several possible contributions to the changes in the SE distribution [105]:

- band bending effects at the surface due to a change of the relative electron affinity in the presence of a built-in potential across pn junctions,
- the change of Schottky barrier at the surface due the presence of surface states, carbon contamination or native oxide,
- the change in the escape depth due to differences in the attenuation rate of hot electrons, i.e. photoexcited electrons, hence when reabsorbed, create electron/hole pairs with different yield,
- effects due to external electric fields influencing SE trajectories, from the p-doped towards the n- doped zone.

1.4.2.1 Schottky barrier and band bending

Surface states Band bending at the surface of a semiconductor with doped patterns has an effect on SE contrast. Contrast can be created by surface states present in differently doped zones which induce surface band bending [74]. The effective electron affinity being a potential barrier, the escape probability increases with decreasing the surface barrier [106, 107]. A smaller energy transfer is required to excite an electron from the valence band to the vacuum in p-type material, than in n-type.

Ballarotto [103, 108] considers SE contrast due to a difference of ionization energy, which has an impact on photoelectron generation, emitted above the surface barrier. This implies a modification in the photoemission yield. Surface states pin the Fermi level, which results in band bending. If the distribution is inhomogeneous, it leads to a

spatial variation of the effective photothreshold [109]. In their study, Ballarotto *et al.* used a PEEM without energy filtering, they concluded that both photoyield position and intensity contribute to contrast and depend on:

- The doping level (position).
- The position of surface states relative to the bulk Fermi level (position).
- The density of states (intensity).

Surface states hence change the surface potential and reduce the difference in escape energy for electrons coming from regions of different dopant concentration and type. A reduction in surface state density should increase the contrast.

Giesen *et al.*, in their paper [110] discuss contrast due to the Fermi level pinning between the valence and the conduction band edge at the surface since PEEM is a suitable technique to observe variations in the near-surface electronic structure induced by a high density of surface states.

Built-in potential Elliott *et al.* [75] have studied dopant contrast from silicon pn junctions with structures varying in doping level and width, and confirmed that contrast arises in SEM images due to the built-in junction potential V_{bi}. It can be expressed in terms of changes of the relative electron affinity in the presence of the built-in potential at the junction [111], resulting in different ionization energies for p- and n-type. In this way, Kazemian *et al.* [79] report quantification of the dopant profiles with energy filtered secondary electron imaging. They also show that at high magnifications with SEM, a large number of electron-hole pairs are generated, which reduce the built-in potential, and hence the contrast [77].

Dapor *et al.* [112] performed Monte Carlo modeling to match the experimental SE emission distribution from doped silicon, taking into account the dopant contrast appearing when observing different doped zones. To understand it, they calculate the SE emission from a doped silicon, taking into account the electron affinity which behaves like a potential barrier.

A recent study carried out by Volotsenko *et al.* [113] with a KFM, shows that SE contrast is governed by the SE escape depth and their escape probability, which is related to the SE distribution, and as seen before, to the effective electron affinity [113]. As can be seen in figure 1.15, surface states trap holes on the surface of the p-doped region, which results in a depletion zone in the n-doped region, the bands bending up by ΔV_p. In a symmetrical way, electrons are trapped in the n-doped zone and the band are bend down in the p-doped one ΔV_n. This behavior reduces the built-in voltage $\Delta V_{bi'}$ at the surface, comparing to its bulk value.

Müllerovà and Frank [86] give a role of the angular distribution of SE emission on the contrast mechanisms in SEM, and Sealy *et al.* [114] add that the higher the surface potential barrier, the narrower the emission angle of SE. In case of n-doped region, due to its higher surface barrier compared to p-doped one, its SE emission is lower. In their paper, Sealy *et al.* also present a range of experimental results used to demonstrate the wide applicability of the SE contrast for dopant mapping.

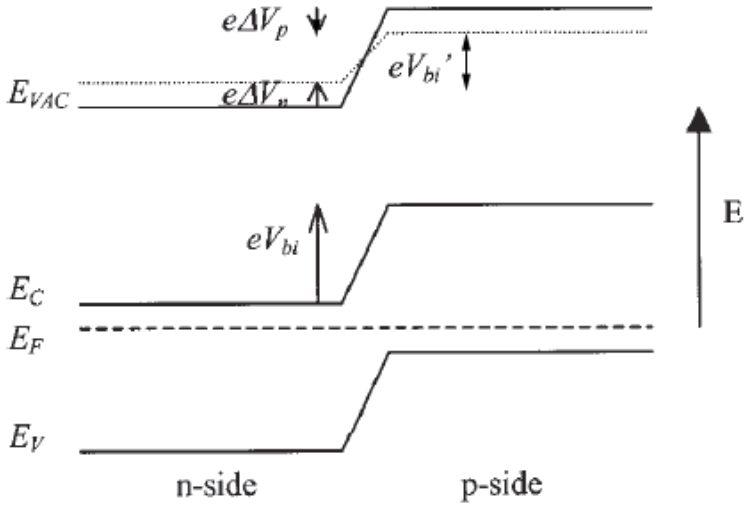

Figure 1.15: *Energy band diagram for a pn junction. The dotted line represents the vacuum level with modified built-in potential [75].*

Surface contamination The contrast in SE images is strongly affected by the presence of surface contamination. We can mention for example:

- native oxide,
- carbon,
- charging effects,

since all of these factors induce a modification of the Schottky barrier at the sample surface.

El Gomati *et al.* [115] have studied in low voltage SEM the effect of SE escape depth on their energy distribution. A carbon contamination layer created from adsorbed hydrocarbons deposited by the electron impact in SEM, 4-5 nm thick, can behave with the silicon surface as a metal-semiconductor contact. A Schottky contact is thus formed with the n-type whereas an ohmic contact is created with the p-doped zone. The electron transfer from the silicon to the contamination layer, increases the potential barrier for SE. Thus, the total SE yield from n-type is lower than the p-type one, which creates contrast in SE imaging.

Müllerovà [116] has shown that SLEEM mode is more sensitive to dopant contrast than SEM since the carbon contamination is smaller. Dapor *et al.* [112] in their Monte Carlo modeling also outline the influence of surface effects in dopant contrast imaging. Cazaux [117, 118] discuss the influence of changes in the work function or in the electron affinity of the SE escape probability. Surface cleanliness can affect the potential barrier of the surface when observing a metal in SEM. Though his calculations are done for electron beam sources, this approach can be applied in the case of other excitation sources, in our case, X-rays.

The native oxide on silicon can also induce band bending and modify the SE emission. Zaggout *et al.* [119] have shown that the oxide thickness influences the contrast in both

low voltage SEM and PEEM.
Device structures buried under ultrathin oxides can be probed by PEEM technique. This study performed by Ballarotto *et al.* [120] has shown the change in SE contrast with the oxide thickness: the thicker the oxide, the more the signal is attenuated. This is due to band bending in the depth direction perpendicular to the surface at the buried interface between the oxide and the semiconductor. However, due to a contrast reversal observed in the thicker oxide, the authors have added a contribution from the interface states within the gap.
Using a free electron laser excitation source, Ballarotto *et al.* [108] have investigated pn junctions buried under a native oxide and how different surface states due to this oxide affect doping-induced contrast. However, they have only studied p-type doped patterns. They showed that PEEM is sensitive to doping-induced contrast even when the surface is covered by an overlying oxide up to 15 nm [120]. A native oxide on the surface implies a change in the work function due to a band bending modification, itself depending on the surface state and the doping type and concentration.
A SPEM with energy filtering and synchrotron illumination was used for imaging Si $2p$ core-level variations across heavily doped p silicon patterns on n substrate. In this study, Phaneuf *et al.* have highlighted the role of the native oxide layer in the deduced band alignment and band bending at the pn junction interface as a function of the underlying doping level and type [94].

1.4.2.2 Electron-hole pair creation by hot electrons

Franck *et al.* [121] consider the role of hot electrons in the SE emission yield. They have worked with a high pass energy-filtered PEEM and demonstrated contrast inversion for faster electrons. They have shown that the contrast between p- and n- type silicon doped can be influenced by different absorptions of hot electrons capable of passing over the surface barrier potential. The hot electrons are likely to be scattered inelastically above the vacuum level, and can be returned below the surface barrier. This can create electron-hole pairs whose generation rate depends on the electron energy relatively to the valence band maximum, modifying thus the electron-hole pair creation yield with the doping type.

Electron energies required for SE to pass through the surface barrier potential of a semiconductor are different for n- and p- doped type. For a given energy, a photoelectron excited is more likely to be emitted from p-type than n-type. Thus, with respect to the energy levels governing inelastic events, the reabsorption of hot electrons is higher for n-doped regions. The more the electron absorption, the lower the spectra yield, since the electron-hole pair production requires an amount of energy. A difference in photoyield occurs, hence explaining that the n-type zone appears darker than the p-type.
Contrast variations can thus be explained by the differences in the absorption of these hot electrons on their way to the surface depending the type of semiconductors, since the surface barrier is different. However, Kazemian *et al.* [77] have shown that electron-hole pair generation has a negligible effect on the doping contrast in SEM, except when considering high magnifications and low scan frequencies.

1.4.2.3 Electrical contrast

The SE contrast can be modulated by electrical fields which appear above the sample surface, and are called external patch fields. They are generated in the vacuum by the built-in potential existing at the contact zone of different semiconductors, such as pn junctions.
Buzzo *et al.* [83] explain that close to the depletion zone, this built-in potential produces an electric field above the surface which deviates the SE. In the vicinity of the junction, they simulate the electric fields lines. If SE have low kinetic energy, these fields being closed loops, the electrons can be either attracted towards the surface, or highly deflected in the horizontal direction, as shown in figure 1.16. These effects reduce the number of SE reaching the detector. In this case, electrons emitted from the p-doped region are accelerated out of the surface while the ones emitted form the n-region are retarded. Variations in the photocurrent distribution occur then in the image plane.

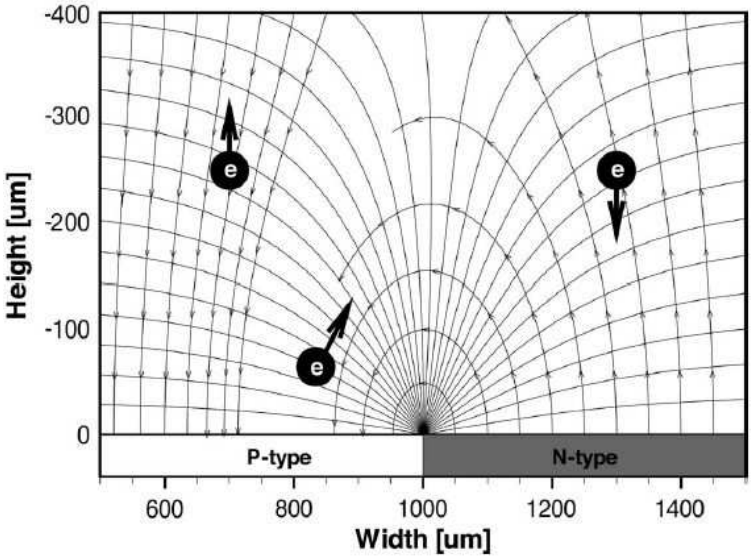

Figure 1.16: *Stray potential and stray electric field resulting at the surface of an abrupt unbiased SiC junction produced by the built-in potential (simulation by DESSIS). The vectors representing the electric field point in the opposite direction as the electrostatic force. The radial thin lines are equipotential lines, whereas the thick lines represent the field lines [84].*

In the same manner as subsurface electric fields can affect the measured photocurrent, surface electric fields can also deform the angular characteristics of electron emission.
The study of contrast formation due to electric fields on the sample surface was also performed by Nepijko *et al.* [122]. They have defined the main factor as being the difference of the emission current density due to the lateral electric field between different regions of the sample.

1.4.2.4 Conclusion

In conclusion, the secondary electrons have to deal with lots of interactions on their transport towards the surface, including surface states at the interface with vacuum. The basic explanation of SE contrast due to difference in doping is clearly too simplistic.

Other mechanisms can influence the SE intensity and thus, it is of interest to bear in mind the factors which can be responsible. One of the last study to date, lead by Chee *et al.* [78] provides a detailed understanding of the doping contrast mechanisms in a SEM. They have developed a quantitative numerical model for doping contrast, enabling the effects due to surface band bending depending on the density of states considered, surface external patch fields and external fields due to the detection system of the instrument, specially the detector solid collection angle. However, whatever theory is preferred, the sample surface state is a very important factor which influences the SE contrast on semiconductor surfaces either by SEM or by PEEM.
In the next section, we present the different interpretations advanced to explain the mechanisms leading to the formation of material and electrical contrast when imaging silicon doped patterns such as pn junctions with a PEEM.

1.4.3 Positioning of our study in PEEM imaging

A well-established way to obtain 2D images of dopant is to use electron microscopy, such as SEM or PEEM to map the spatial distribution of secondary electrons emitted from the surface. However, some factors can influence the contrast obtained on imaging at threshold. These latter are briefly introduced in the beginning of this section. We present then a state-of-the-art of the XPEEM studies performed on silicon doped samples, mostly at threshold.

1.4.3.1 Origin of contrast in XPEEM imaging

Contrast mechanisms can be divided into several categories, as graphically presented by Mutoro in figure 1.17.

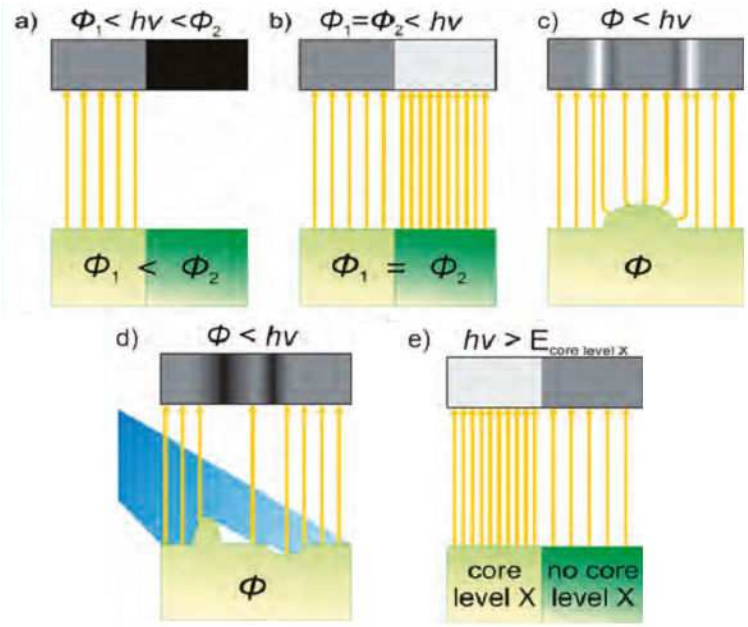

Figure 1.17: *Contrast mechanisms: a) Work function, b) Material, c) Topography, d) Shadow effect, e) Chemistry [123].*

It is important to understand the factors responsible of the imaging degradation to differentiate their effects from the physical mechanisms we are interested in.
Problems of charging hiding contrast have been avoided during this thesis since researches were focused on semiconductor samples and not insulating ones. However, some interesting papers on this topic can be quoted: [90, 124, 125].

Material contrast At threshold, contrast can be explained by the fact that regions with same work function appear with different brightnesses in the image, due to a difference in the photoemission yield: this is the *material contrast*. An other contrast, the *work function contrast* is observed from regions with different work function presenting different emission probabilities. If the work function of the observed region exceeds the photon excitation energy, no secondary electron emission appears. For more explanation, see the paper of Pryzchowski *et al.* [126] on the influence of work function differences on the photocurrent. Contrast due to work function variations depends on both the surface density and the crystalline orientation of the surface, as presented in the study of Renault *et al.* on copper grains [127].

Absorption contrast In *X-ray Absorption Spectroscopy*(XAS), the photon energy through absorption edges of elements in order to excite the core-level electrons up to the empty electronic states below the vacuum level. The resulting core-holes are filled by transition to allow the de-excitation of the system, creating fluorescence emission and Auger electrons. These electrons are collected as the total yield photocurrent, directly proportional to the absorption coefficient. The area on the surface containing the element of interest emits more photoelectrons and thus, at the given absorption edge X-ray energy, appears brighter.
Near Edge X-ray Absorption Fine Structure (NEXAFS) furnishes the *chemical contrast*: differences in images taken at several X-ray energies near a given absorption edge allow to determine the local bonding state of surface atom responsible for the fine structure modification of the absorption coefficient.

Magnetism contrast X-ray absorption is frequently dichroic and depends on the orientation of the electric field vector with respect to the sample magnetization.

- *X-ray Magnetic Linear Dichroism* (XMLD)is used to study the properties of antiferromagnetic systems.
- *X-ray Magnetic Circular Dichroism* (XMCD), the absorption of left or right handed circularly polarized light depends on the orientation of the magnetic moment in the sample and is used to study the properties of ferro or ferrimagnetic materials [128].

Since this thesis deals with studies on non magnetic semiconductor surfaces, we do not discuss further this contrast. It is well presented by Stöhr *et al.* [128] and by Schneider [95].

Topographic and shadow effect contrast Electron imaging is sensitive to the object topography. If this latter is not smooth, the electrical field created between the sample and the extractor lens is modified. Hence, the photoelectron trajectories in the vicinity

of this zone are deflected, giving brighter or darker zones within the images [95, 129].
It is possible to simulate the influence, for example, of step height on electron trajectories in an electron microscope column [129,130]. Chapter 5 is dedicated to such topographical influence on PEEM imaging, based on simulations performed with SIMION software [131].

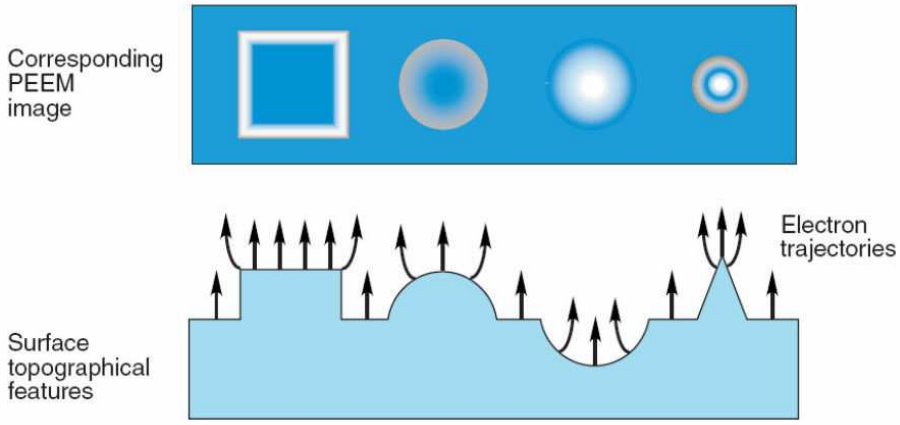

Figure 1.18: *Topographic contrast in PEEM imaging due to local electrostatic fields [132].*

Thus, topography can be responsible for contrast variations due to the presence of local electrostatic microfields [130]. Lateral field strength increases with the step height of the structure and influences the photoelectron trajectories, creating a topographic image contrast, as presented in figure 1.18.

The surface relief is also partially responsible for contrast variations in imaging which limit the lateral resolution: geometrical structures present step edges which create shadow zones in the images depending on the illumination angle of the sample. We mention this point since it was a necessary requirement when realizing a new batch of localized epitaxial silicon doped patterns for this thesis. Our aim was to minimize the step height between the different doped zones. Rempfer *et al.* [133] have gone further in this way, reporting the effects of positive and negative surface relief in PEEM imaging.
In their review, Schneider and Schönhense [95] describes other contrast mechanisms, such as Smoluchowski contrast or interference effects but in our case, these effects were not the most important.

Electric contrast Electric contrast is the last important factor deteriorating the resolution, but not represented in figure 1.17. Electrons are sensitive to the presence of potential microfields at the sample surface. Such fields distort the normally strong acceleration field between the extractor lens and the sample surface, deviating the electron trajectories, hence changing the image intensity. They appear at the junction when considering two zones with different work function, but they can appear artificially when applying external bias on the sample surface [134, 135]. PEEM can be used to visualize and measure the distribution of electric field and potential on the surface either in the case of beam restriction by a contrast aperture, or without restriction of the photoelectron beam [136]. This point will be discussed in chapter 5 where simulations and experiments performed during this thesis will be compared.

1.4.3.2 XPEEM imaging at threshold

Many authors, have contributed to the understanding of the contrast in PEEM images at threshold. We have reviewed in table 1.3 all the studies carried out up to now in order to highlight the peculiarities of our study.

First Author	Reference	Excitation	Sample	Filtering	Passivation
Hovorka	[137]	Synchrotron	p subs. 10^{15} n: 10^{15} to 10^{19}	High pass	Yes
Hovorka	[138]	UV Hg	p and n subs. 10^{15} n and p: 10^{16} to 10^{19}	High pass	No
Ballarotto	[108]	FEL UV 4.2 eV - 5.2 eV	n subs. 10^{14} p: 10^{17} to 10^{20}	No	No
Ballarotto	[103]	UV Hg	n subs. 10^{14} p: 10^{18} to 10^{20}	No	No
Phaneuf	[94]	Synchrotron 496.4 eV	n subs. 1.6×10^{14} p: 10^{18}	SPEM	No
Frank	[139]	UV Hg	n subs. 5×10^{14} p: 10^{19}	High pass	No
Frank	[121]	UV Hg 4.9 eV	p subs. 10^{15} n: 10^{19}	High pass	No
Giesen	[135]	UV Hg 5.15 eV	n subs. 1.6×10^{14} p: 10^{18}	No	Yes
Giesen	[110]	UV Hg 4.96 eV	n subs. 10^{14} p: 10^{18}	No	No

Table 1.3: *State of the art of contrast imaging studies with PEEM on silicon pn junctions.*

We note that most of the photon sources used in these studies are near-threshold excitations. These latter present two drawbacks: firstly, they can have a possible influence on the contrast observed, allowing photoelectrons to be excited in the direct transition type. Secondly, core- and valence- levels are not accessible, to fully characterize the band alignments. Regarding the instrumentation used to understand the doping contrast in the literature, the instrument used in this work, the NanoESCA, has several advantages which will be detailed in chapter 2:

- a full band-pass energy filter, which can be used with high energy resolutions, and allows a complete spectroscopic analysis of the sample to be studied,
- high excitation energies, either using a laboratory X-ray source or synchrotron radiation, far from the nominal silicon photothreshold, which is not the case when considering near-threshold excitation sources. The tunability of the synchrotron to vary the photon energy is particularly well adapted for our studies to probe different sampling depths,
- the combination of a good energy and lateral resolutions, thanks to the double hemispherical analyser compensated for aberrations, which reduces the instrument aberrations to those of the immersion lens,
- the possibility to perform spectromicroscopy, i.e. the ability to obtain laterally resolved XPS spectroscopy from different doped areas in order to quantify photoyield difference.

More sophisticated analyses with energy filtering have begun to appear, demonstrating contrast inversion as a function of the electron kinetic energy [138]. According to Giesen *et al.* [135], the contrast in PEEM imaging for various surface states gives qualitative information about the position of the surface states within the gap which renders this technique well adapted for pn junction characterization.

1.5 Surface Photovoltage investigation: impact on 2D dopant techniques

One has to be careful when studying silicon doped pn junctions since a photovoltaic effect can influence the observations. It can be intentionally studied, to determine the carrier diffusion length and can be used as a contactless technique to characterize semiconductors surface states [140]. It is also capable of providing informations on a variety of other quantities such as surface charge, surface dipole, surface and bulk recombination rates, distribution and properties of surface states and bulk states.
It occurs whenever light induced charge carriers, under the shape of electron-hole pairs, are separated within a depletion zone, electrons being moved in the conduction band and holes in the valence band.
Two very good reviews on this factor theory and history were performed by Kronik and Shapira [141], and by Schroder [142]. Two other reviews discuss SPV experimental set-up and present applications for surface and interface characterization [142, 143].

1.5.1 Carrier generation and recombination

Electron-hole pairs are generated by two main factors: the thermal excitation and the optical one. In this thesis, we will not consider the case where electrons thermally excited across the gap produce electron-hole pairs at high enough temperatures.
An excitation source can also create excess carriers by illuminating the surface of a semiconductor. If the incoming photons have an energy $h\nu$ higher than the semiconductor gap E_g, they excite electrons from the valence band across the gap into the conduction band, hence generating an electron-hole pair. This second factor, combined with the space charge region created by the surface states, is responsible of the surface photovoltage. Note that a surface photovoltage can also be observed when the surface is illuminated with photon energies smaller than the band gap, due to photostimulated population and depopulation of localised trap states within the gap. More complex scenarii are also possible such as transfer between several states into the band gap but are not detailed in this section.

1.5.2 Surface Photovoltage

As mentioned previously, in the absence of radiation, the equilibrium carrier concentration of semiconductors is established by a dynamic balance between thermal and optical generation of electron-hole pairs on the one side, and annihilation of these same pairs on the other side.
Under illumination, incident light leads to a non equilibrium where excess charge carriers

are generated via band-to-band transitions and release captured carriers via trap-to-band ones. The electric field present in the depletion zone causes majority carriers to be carried out into the bulk whereas the minority ones are trapped near the surface. They compensate the space charge hence, change the surface potential and produce a change of the band bending compared to equilibrium value. This shift is called the *surface photovoltage* (SPV) and is presented in figure 1.19. It occurs only if carrier generation is followed by a net charge redistribution. It depends on photon flux, recombination rate, temperature and band bending. For a constant temperature, the SPV increases exponentially with the fundamental gap width. There is also an important dependence of the SPV magnitude on photon intensity at room temperature. Even at low temperatures, SPV effects in photoemission are still observed [144].

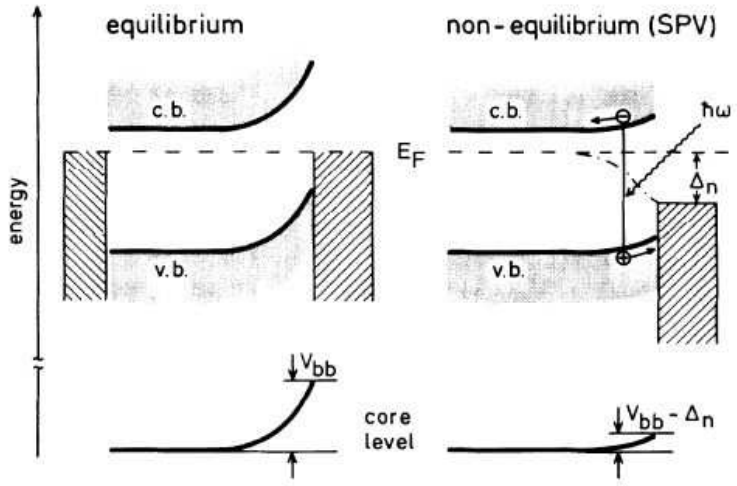

Figure 1.19: *Schematic drawing of the surface photovoltage influence Δn on the band bending V_{bb}, considering a band bending upwards [144].*

Since electron-hole pairs are created, their number being equal, SPV has a more important impact on the concentration of minority carriers than on the majority ones. Hence, this injection of minority carriers into the near surface produces indeed a reduction of the band bending and tends to flatten the energy bands at the sample surface, whatever the type of the semiconductor:

- if it is n-doped, the band bending at the surface is upwards and the SPV goes downwards,
- if it is p-doped, the band bending at the surface is downwards and the SPV goes upwards.

We will see in the next chapter that XPS technique alone or combined with an XPEEM, requires a bright excitation source, which can influence the band bending at the sample surface. With synchrotron radiation, the high intensity of the beam induces a strong SPV which has an influence on the band back bending, as developed now.
Hecht [145] has modeled the SPV by equating the current of minority carrier produced by X-ray excitation to a current of majority carriers flowing through the depletion layer,

given only the position of the Fermi level at the surface. If the surface is the dominant site for recombination, the photocurrent density of minority carriers arriving at the surface J_{pc} is proportional to the photon flux illuminating the sample. In the theory of the thermionic emission, the photocurrent density of majority carriers through the depletion region is:

$$J_{th} = J_0 e^{\frac{-V_d}{E_0}} \left[1 - e^{\frac{-qV}{kT}}\right] \ , \tag{1.9}$$

where the sensitivity of the surface potential to illumination is set by J_0 which is exponentially dependent on the Schottky barrier height V_n:

$$\mathrm{J}_0 = A^* T^2 e^{\frac{-qV_n}{kT}} \ , \tag{1.10}$$

E_0 depends on the dominant current flow mechanisms, k is the Boltzmann constant, and T the temperature. Thus, in the stationary state, SPV can be evaluated from the balance of the surface current densities for minority and majority carriers. Setting $J_{pc} = J_{th}$, and considering low temperatures $V \geq \frac{kT}{q}$, we can focus on contributions from thermionic emission over the barrier and field emission through it:

$$V_d = E_0 ln\left(\frac{J_0}{J_{pc}}\right) \ , \tag{1.11}$$

where

$$\left(\frac{J_0}{J_{pc}}\right) = \frac{1}{J_{PCO}} A^{**} T^2 exp\left[\frac{V_n}{E_0} - \frac{qV_n}{kT}\right] \left(\frac{q}{\alpha kT}\right) \sqrt{\frac{\pi E_{00} q N_d}{2\epsilon_s}} \left[cosh(\frac{qE_{00}}{kT})\right]^{-1} \ , \tag{1.12}$$

with

$$\mathrm{E}_0 = E_{00} coth\left(\frac{qE_{00}}{kT}\right) \ , \tag{1.13}$$

and

$$\mathrm{E}_{00} = 18.5 \times 10^{-15} \sqrt{\frac{N_d}{m_r \epsilon_r}} \ . \tag{1.14}$$

This last factor is 0.0259 eV, in the case considered.

1.6 Conclusion

In this chapter, we first highlighted the need, driven by the ever increasing specifications of the International Technology Roadmap for Semiconductors, for multiscale 2D characterization of doping in advanced semiconductor devices, the scale of which extends

from the nanometer- (22 nm nodes and beyond for CMOS transistors) to the micron-range (HFET devices for power applications, micro-/nano-systems). Such a spread of the characteristic scales to be addressed requires the use of complementary characterization techniques, with, for each of them, a comprehensive understanding of the contrast mechanisms involved for a quantitative analysis of images of doped semiconductors. Prototypical devices for such an understanding are pn junctions.

We have introduced the fundamental physical concepts around silicon pn junctions, recalling the characteristic electrical quantities relevant for the experimental and theoretical work performed in this thesis (depletion width, built-in potential and resulting electric field across the junction).

Then, a review of the state-of-the-art in existing techniques performing 2D characterization of doping was made. Five different methods were considered: scanning ion probe techniques (Tof-SIMS), near-field probes (KFM, SCM, SSRM), conventional electron microscopies (SEM, holographic TEM), atom-probe methods (APT) and photoemission-based techniques (SPEM, PEEM). This has highlighted their complementarities in terms of sample preparation, lateral resolution, quantitative capabilities, accessible doping concentrations and sensitivity, depth sensitivity. Among electron microscopies, the peculiarities of PEEM-based methods were recognized for their intrinsic surface sensitivity and specific contrast mechanisms like the work function contrast. However, we showed that, although many studies in the field were already reported over the last decade, such contrast mechanisms were not fully exploited due a lack of energy filtering and the use of excitation sources limited to the low-energy UV range. The importance of the control of the surface properties (residual oxide layer, carbon contamination) was also underlined. Therefore, we conclude that in-situ spectroscopic control of the surfaces imaged is necessary for a better understanding of the contrast obtained.

These considerations underline the specificity of the work presented in this manuscript, with the combined use of spectroscopic, energy-filtered PEEM and high energy photon excitation in the X-ray range, enabling imaging with true secondary electrons and a simultaneous spectroscopic control of the surfaces imaged. The latter is fundamental since, in energy-filtered XPEEM, spectroscopic imaging is performed and therefore the image contrast of pn junctions is highly dependent upon the relative position of the electronic energy levels. We have reviewed the effect of surface photovoltage which may affect the relative energy level positions, and hence, the resulting image contrast in energy-filtered XPEEM.

Chapter 2

Energy-Filtered XPEEM

Contents

Benefits of the energy filtering, when considering electron microscopy have been introduced. X-ray Photoelectron Emission Microscopy (X-PEEM) can make a significant contribution to the emerging surface analysis techniques thanks to its principle characteristics: non destructive, elemental, chemical and electronic state sensitivity, lateral and energy resolution and depth sensitivity. We will now focus on it and to go deeper in the understanding of this technique.

This chapter is dedicated to the explanation of the two surface analysis techniques which have a key role in the development of spectromicroscopy: X-ray Photoelectron Spectroscopy (XPS) and X-ray PhotoElectron Emission Microscopy (XPEEM). We will then present a new generation of PEEMs with energy filtering. To finish, we show the state-of-the-art laboratory results on improved lateral resolution obtained with this instrument.

2.1 Principles

2.1.1 Photoelectron Spectroscopy

2.1.1.1 Background

Photoelectron Spectroscopy was first developed by Kai Seigbahn and his research group at the university of Uppsala in Sweden. He published his first results study on XPS in 1957 and was rewarded in 1981 for his research with the Nobel Prize.
First known under the acronym of ESCA for *Electron Spectroscopy for Chemical Analysis*, the use of an X-ray source to extract the photoelectrons from the sample gives it the name of XPS for *X-ray Photoelectron Spectroscopy*. It is a powerful analytical method in applied and fundamental surface science whose use has steadily increased over the last decades [146]. The possibility of spatially resolving elemental and chemical states with a good sensitivity has also attracted considerable interest [147]. Firstly, we will describe the principle of this technique, giving theoretical aspects about threshold and core-level analysis. We will finish this section by presenting in more detail the instrumentation.

2.1.1.2 Theoretical background

XPS reveals the chemical elements present at the surface of a sample and informs about the chemical bounds nature existing between them. It is based on Einstein's explanation of photoelectric effect discovered, in 1887 by Hertz [148]. The interaction of a photon of sufficient energy $h\nu$ with a solid results in the emission of an electron from its surface. The photon radiation, is capable to induce electrons not only from the outer shells, but also from core-levels of elements. If this energy is sufficient, the electron leaves from its atomic orbital and is extracted from the surface with a kinetic energy E_k.

The process can be described by the Einstein equation:

$$h\nu = E_B + E_k \ , \tag{2.1}$$

where E_B is the binding energy of the electron. Thus, measuring the kinetic energy E_k and knowing the energy of the photon source $h\nu$, E_B is easily determined.

Irradiating a sample can be done with photon sources of different energy, depending on the type of electrons studied:

- It can be either photons emitted in ultraviolet (UV), with low energy, which only probe the outermost electrons broadened in the valence band. This first kind of spectroscopy is called UPS for *Ultraviolet Photoelectron Spectroscopy*. It uses photon sources such as He I or He II respectively at 21.2 eV and 40.8 eV, or Hg, at 4.9 eV.

- It can also be an X-ray source which, thanks to its higher photon energy, can also probe the core-level atoms. This second kind of spectroscopy is called XPS, as already presented. Two X-ray sources in common use are based on the Kα radiation from Al (1486.7 eV) or Mg (1253.6 eV).

To summarize, XPS analyzes the kinetic energy distribution of electrons emitted by the photoelectric effect when the sample surface is irradiated by a photon source. It provides qualitative and quantitative informations on all the elements in presence (except H and He), giving some of their chemical properties. To be more precise, we can graphically represent the energy distribution of the electrons in the figure 2.1 and detail it with the following features:

- A large peak at low kinetic energy is due to the secondary electrons.
- The center of the spectrum is composed of peaks corresponding to the atomic orbital from which the photoelectrons are ejected. They are called *core-level photoelectrons* and come from localized levels. These latter are sensitive to the chemical environment of the atom. As we will see in subsection 2.1.1.4, the chemical nature of the neighboring atoms of the emitter can be determined.
- *Valence electrons* come from delocalized levels which determine the electronic structure of the material, giving its nature: conductor, semiconductor or isolant.

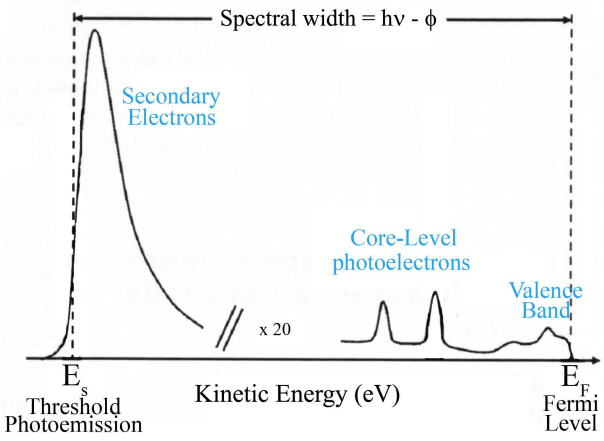

Figure 2.1: *Schematic of a full photoemission spectrum [149].*

The measured intensity depends on the instrument transmission, the elemental concentration, the *atomic photoionization cross-section* σ of the considered atomic level, and the depth probed. This depends on the *inelastic mean free path* λ.

Photoionization cross-section σ The atomic photoionization cross-section σ represents the probability of an incident photon to ionize an orbital for a given element. It depends on the atomic number of the atom, the core-level considered, and the photon energy. Values are typically taken from the calculations of Scofield [150] or Yeh and Lindau [151] and can be represented graphically, as in figure 2.2, for the silicon core-levels $2s$, $2p$, $3s$ and $3p$ with an AlKα excitation.

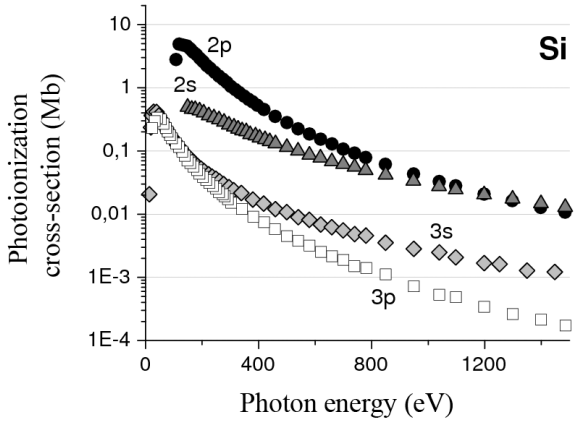

Figure 2.2: *Silicon case. For a given photon energy, σ of a core-level increases as the binding energy increases [151]. The cross-section unit is given in Mb: 1 Mb = 10^{-18} cm^2.*

Inelastic mean free path λ XPS is a surface characterization technique which gives informations only in the near surface because the emitted photoelectrons are likely to lose energy due to inelastic collisions before they escape from the surface. The important factor here is the mean free path. It is defined by the International Organization for Standardization ISO 18115:2001 as *the average distance that an electron with a given energy travels between successive inelastic collisions.* It strongly depends on the kinetic energy of the electrons and varies with materials. It can be obtained theoretical or with certain types of experiments. The physical parameter of interest is the electron attenuation length, defined as the thickness of material through which electrons may pass with a probability e^{-1} that they survive without inelastic scattering. It is obtained experimentally from overlayer-film experiments and with use of a model in which the effects of the elastic electron scattering are ignored.

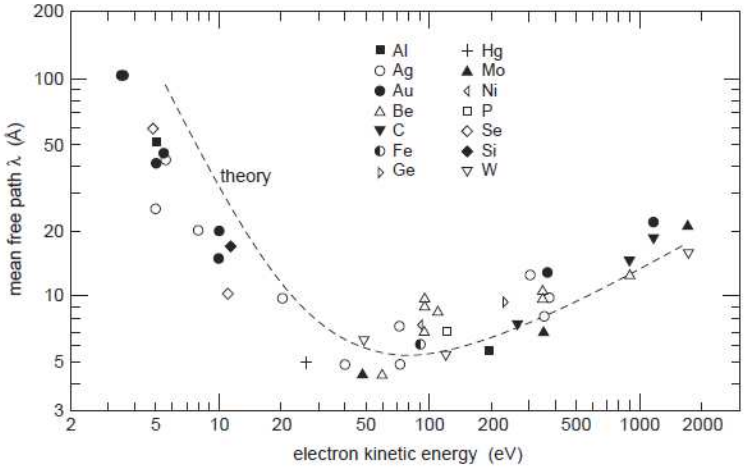

Figure 2.3: *Universal curve of the inelastic mean free path λ for electrons in solids for various materials in symbols [152]. The dashed line describes the experimental data fit [153].*

Figure 2.3 shows the experimental values of mean free path for different materials: λ

depends on the density, the nature of the matrix, and also on the photoelectron kinetic energy. As can be seen on the curve, the mean free paths are very high at low energies, fall to 0.4-0.8 nm for energies in the range 30-100 eV and then rise again as the energy increases. This makes XPS a unique surface-sensitive technique for chemical analysis.

Powell *et al.* [154] summarize procedures to accurately determine this fundamental material parameter among others. Tanuma *et al.* [155] report calculations of electron mean free path in a group of 15 inorganic compounds, including SiO_2. In their paper [156], Gergely *et al.* present past and present research on this topic, giving a comparison between calculation and experiment.

Escape depth The contribution of an overlayer of thickness z with a detection angle with respect to the surface normal θ is given by:

$$I = I_\infty \left(1 - \exp \frac{-z}{\lambda \sin\theta}\right) \ , \tag{2.2}$$

where I_∞ is the XPS signal obtained for an infinitely thick layer, and $\lambda \sin\theta$ is called *escape depth*. It is determined as the distance normal to the surface at which the probability of an electron escaping without significant energy loss due to inelastic processes drops to $1/e$.

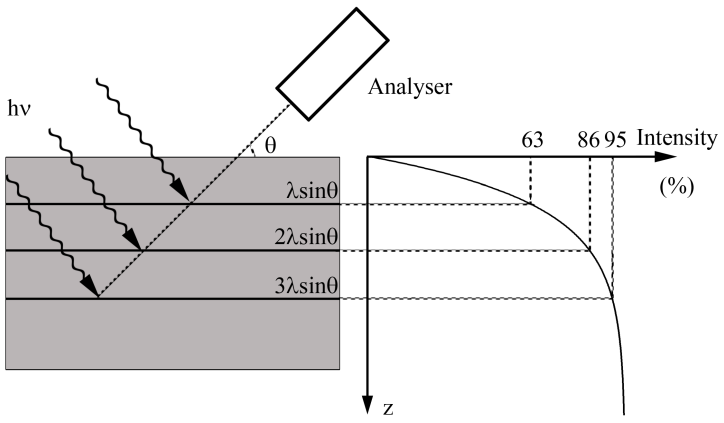

Figure 2.4: *Relative contributions of the signal intensity of different layers of thickness* $\lambda \sin\theta$ *[157, 158].*

The *information depth* d is the average distance normal to the surface from which a specified percentage of the detected electrons originates. The overlayer films of thickness $\lambda \sin\theta$, $2\lambda \sin\theta$ contribute respectively to 63 % and 86 % of the XPS total signal. When the percentage of detected photoelectrons is 95 %, d is called *sampling depth* and is estimated to be:

$$d \approx 3\lambda \sin\theta \ , \tag{2.3}$$

Using Al or Mg X-rays, the probe depth is generally a few nanometers.
In their papers [159, 160], Jablonski and Powell summarize the relevant theory to define practical expressions of the inelastic mean free path, the sampling depth and the effective attenuation length in materials.

2.1.1.3 Binding energy calibration

In XPS, the sample is in electrical contact with the spectrometer. This puts the Fermi level E_F of both the sample and spectrometer at the same energy at thermodynamic equilibrium. The difference in energy between the Fermi and the vacuum levels corresponds to the minimum energy required to eject an electron from the highest occupied level into vacuum. It is called work function. Hence, we introduce the spectrometer work function Φ_{sp} and the sample work function Φ_s [161].

Halas *et al.* calculate work function of elements and express it in terms of Fermi energy and bulk properties [162–164]. See also theoretical and experimental work by Henke *et al.* [165] or by Takeuchi *et al.* [166].

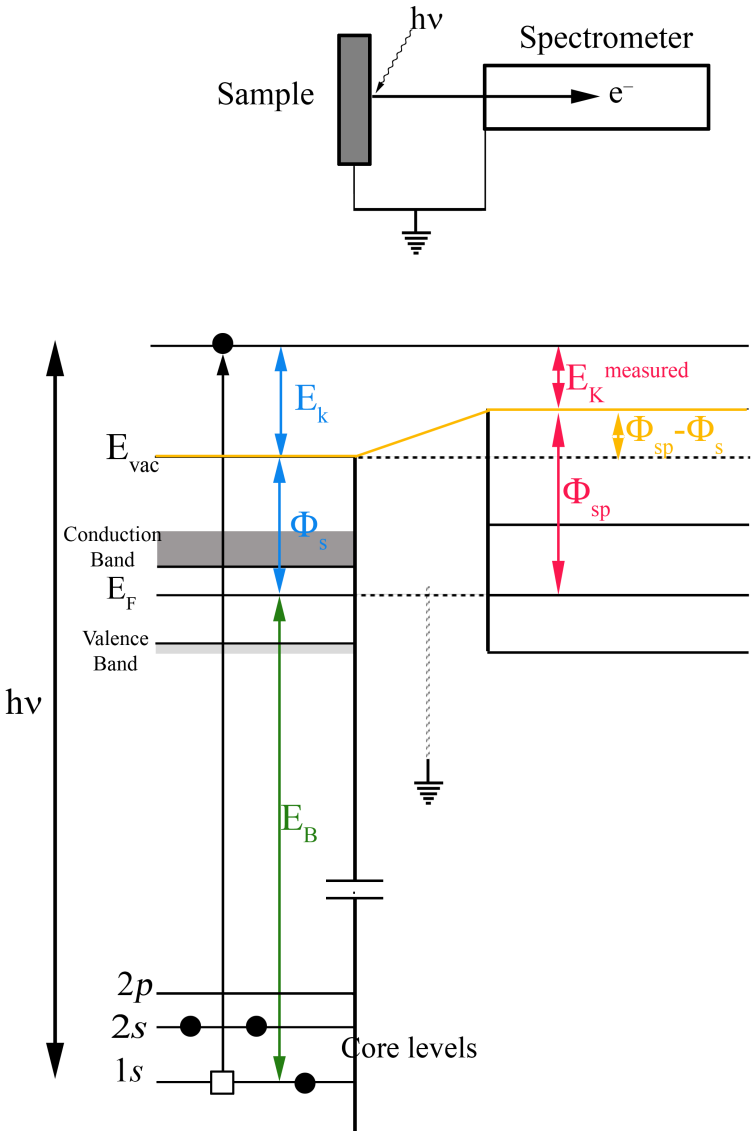

Figure 2.5: *Energy level diagram for a sample grounded to the spectrometer.*

Referring to figure 2.5, we can define the photoelectron binding energy E_B^f measured by the spectrometer and referenced to their common Fermi level as:

$$E_B^f = h\nu - E_k - \Phi_s \ , \tag{2.4}$$

where E_k is the photoelectron kinetic energy with respect to the sample vacuum level. But the spectrometer measures kinetic energies $E_{kmeasured}$, stated:

$$E_{kmeasured} = E_k - (\Phi_{sp} - \Phi_s) \ . \tag{2.5}$$

Thus, the binding energy measurement is independent of the sample work function Φ_s, but dependent on the spectrometer work function Φ_{sp} and can be expressed as:

$$E_B^f = h\nu - E_{kmeasured} - \Phi_{sp} \ . \tag{2.6}$$

The local work function is related to the photoemission threshold. In a similar manner, information about electronic states close to the Fermi level can be deduced from the valence band photoelectrons and chemical information from the core-level ones. Keeping in mind figure 2.1, considering the case $(\Phi_{sp} - \Phi_s)$ negative [118] we can add some precisions:

- The spectrum low energy cut off is at $E_k = \Phi_s$. Below this value, electrons have a kinetic energy smaller than the sample work function.
- The high energy cut off is at $E_k = h\nu - \Phi_s$ when the electrons are ejected from the Fermi level whose binding energy is defined to be 0 eV.

2.1.1.4 Core-level analysis

Variations in terms of binding energy for core levels arise from different effects, which can be divided into two groups, namely *initial state* and *final state*. The initial state before photoemission is determined by the chemical environment of the atom of interest. The latter is due to the intervention of the photoelectrons with all the other electrons in the solid. We will detail now these two processes.

Core-level chemical shifts One of the most important features of XPS is that the core-level positions depend on the valence state of the atoms: changes in the local charge and potential of an atom cause shifts in the core-level binding energy and are called chemical shifts. By studying them, one can obtain information on the valence state of an atom.

The basic physics underlying the change in binding energy is as follows. The energy of an electron in a tightly bound core state is determined by both the attractive potential of the nuclei and the repulsive core Coulomb interaction with all the other electrons. We can use a simple model to relate the binding energy to the effective charge:

$$E_B = {E_B}^0 + ke + qV \ , \tag{2.7}$$

where E_B is the binding energy of the considered core-level in the atom, ${E_B}^0$ is a reference energy, k is a constant, e is the valence charge on the atom and V is the potential at the atom due to point charges on surrounding atoms.

A change in the chemical environment gives rise to a spatial rearrangement of the valence charges, leading to a different potential created by the nuclear and electronic

charges on all other atoms in the compound. Thus, the shift in binding energy ΔE_B of a core-level measured for an atom in two different compounds A and B with valence charges respectively e^A and e^B, is given by:

$$\Delta E_B = K_c \left(e^A - e^B\right) + q\Delta V \ . \tag{2.8}$$

The first term is called *real chemical shift*. It reflects the initial state effects on the chemical environment of the atom A, i.e. before photoemission. It describes the difference in the electron-electron interaction between core orbital c and the valence charge, the coupling constant K_c being the two-electron integral between core and valence electrons. A change in the atom charge of $K_c \left(e^A - e^B\right)$ forces thus all core-levels of the atom to shift their binding energy by the same value. This phenomena includes in the case of semiconductor samples, a possible shift of the Fermi level position in the gap, depending on the nature and the temperature of the dopants, and also on their concentration.

For two atoms A and B with the same valence band filling but an electronegativity $EN_A < EN_B$, B tends to attract electrons from the valence band of atom A. The charge transfer of an electron from A to B gives rise to a contraction of both core hole and core-levels of the atom A, as shown in figure 2.6. Thus, an increase in positive charge is therefore accompanied by an increase in binding energy, this is why atoms of higher positive oxidation state exhibit a higher binding energy.

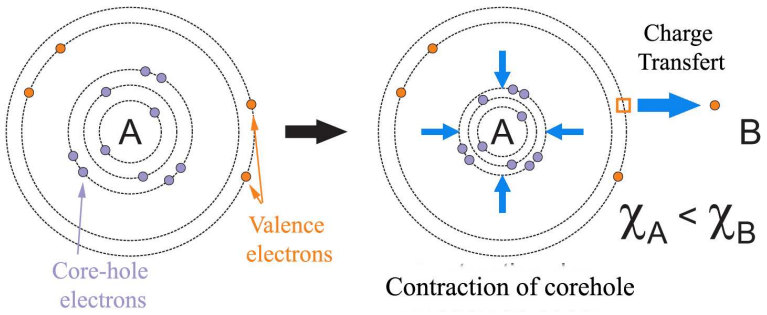

Figure 2.6: *Representation of the initial state effect on the binding energy on a core-level. The more the atoms surrounding atom A are electronegative, the higher the binding energy of core-level electrons of atom A.*

The second term $q\Delta V$ represents the influence of the final state. When an electron escapes from its core-level, as seen in figure 2.7, the valence orbitals contract, screening the positive charge created. The core-hole of the final state has a polarizing effect on surrounding electrons and corresponds to *relaxation*. This contraction of the valence levels corresponds to a decrease of the final energy $q\Delta V$ which, by convention, is positive. In their paper for XPS analysis [167], Pauly and Tougaard have focused on two effects: the core hole left behind in an XPS process which causes intrinsic excitations on the one hand, and excitations due to the photoelectron on its way to the surface region on the other.

Shape of photoemission peaks Photoemission peaks are not simply delta functions and broadening occurs due to different effects which have to be considered. The shape

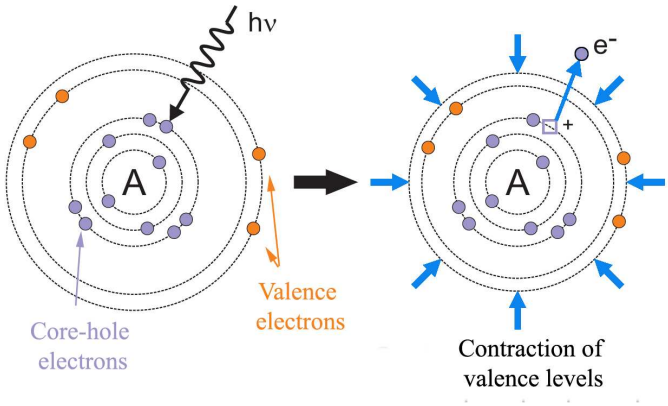

Figure 2.7: *Representation of the final state effect on the binding energy of a core-level: core-level binding energies increase with the atom oxidation state.*

of a peak should be determined separately for every chemical compound. Practically in most cases (except high-resolution measurements) the symmetric peak shape can be well-described by the Gauss-Lorentz (Voigt) profile for semiconductors and insulators and the asymmetric peak is described by the Doniach-Sunjic profile for metals. Resolving peaks due to different chemical states depends on their energy separation and the experimental resolution.
The ejected photoelectron leaves behind a positive core hole which decays when another electron relaxes to fill it according to an associated lifetime. This effect causes Lorentzian broadening of the photoemission peak. The term ΔE_n is determined by a lorentzian function and corresponds to the lifetime of the core-hole state after the photoelectron emission. From the Heisenberg's uncertainty principle, we obtain the inherent line width of a core level:

$$\Delta E_n = \frac{h}{\tau} \ , \tag{2.9}$$

where h is the Planck's constant, and τ the core-hole lifetime. The deeper the orbital, the shorter the lifetime of the core level remaining after photoemission and the broader the peak width.

The XPS analyzer broadening ΔE_a is described by a Gaussian profile. X-ray sources, either laboratory or synchrotron, present also a Gaussian spectral shape ΔE_s because of the instrumental broadening introduced by a monochromator.

The observed photoelectron peak through the instrument has a width ΔE defined as the full-width-at-half-maximum of the peak after background subtraction. The several contributions can be approximated by the overall energy resolution of the instrument:

$$\Delta E = \sqrt{(\Delta E_n)^2 + (\Delta E_s)^2 + (\Delta E_a)^2} \ , \tag{2.10}$$

where ΔE_n is the natural linewidth of the core level, ΔE_s is the photon band width and ΔE_a is the analyser resolution. The determination of this last factor ΔE_a will be explained in equation 2.13.

Shape of photoemission background All photoemission spectra contain background due to inelastically scattered electrons from the processes. Scattered emitted electrons

which have lost energy due to inelastic interactions, but still have enough energy to escape from the surface, contribute to the background signal in an XPS spectra. To estimate the real peak shape from an experimental spectrum, the background has to be subtracted. Different models of background shape can be used: a simple linear-type background can be chosen for fast spectral analysis, whereas for more accurate line shape analysis, more sophisticated background are to be preferred.
Shirley suggested a background shape on the assumptions of a constant energy spectrum of scattered photoelectrons and a constant scattering probability in the peak region [168]. This Shirley background is a smoothed step function which is a good approximation to fit the background intensity.
Other backgrounds used for subtraction from photoemission spectra include a linear function, and a Tougaard background (a more complex smooth step background used to account for inelastic processes).

For all core level photoemission spectra in this thesis, a Shirley background has been removed. To go further in understanding the different methods and procedures for background subtraction on spectra for monochromatic Al X-ray, see for example Powell [169].

2.1.1.5 Instrumental aspect

A high vacuum environment is necessary to enable the emitted photoelectrons to be analysed without collisions with residual gas molecules. Moreover, the surface composition of the sample should not change during the experiment: it is important to avoid surface contamination. XPS experiments are performed in UHV, at pressures less than 5.10^{-10} mbar. The equipment is also fitted with mu-metal shielding to prevent magnetic field penetration into the analyser and the analysis space.

Electrostatic analyser The analyser is an electrostatic hemispherical deflector analyser, also called Hemispherical Single Analyser (HSA). It is composed of two concentric hemispheres, biased negatively with respect to V_0 which is the median equipotential surface between the hemispheres, and respectively in absolute value, higher for the inner sphere and lower for the outer. This analyser disperses electrons according to their kinetic energy and focuses them from the entrance plane to the exit one. Variable slits are located at both the entrance and the exit of the analyser, controlled by a rotary feedthrough. Though it is not schematically represented in figure 2.8, it is important to mention the presence of an input electrostatic lens at the entrance of the hemisphere. This latter collects the photoexcited electrons and focuses them onto the entrance slit w_1 of the hemisphere, adjusting their kinetic energy to match the pass energy of the analyser. This lens defines also the analysis area and the angular acceptance 2α of photoelectrons passing through the hemispherical analyser.

The two hemispheres have radii respectively R_1 and R_2. The mean radius is R_0. The entrance and exit slits are both centered on R_0 as represented schematically in figure 2.8 a). A potential is applied on each hemisphere, respectively V_1 and V_2 producing an inverse squared $1/R^2$ electrical field between the two hemispheres is produced, bending the photoelectrons trajectories. Its equipotentials are green lines simulated in figure 2.8

b).

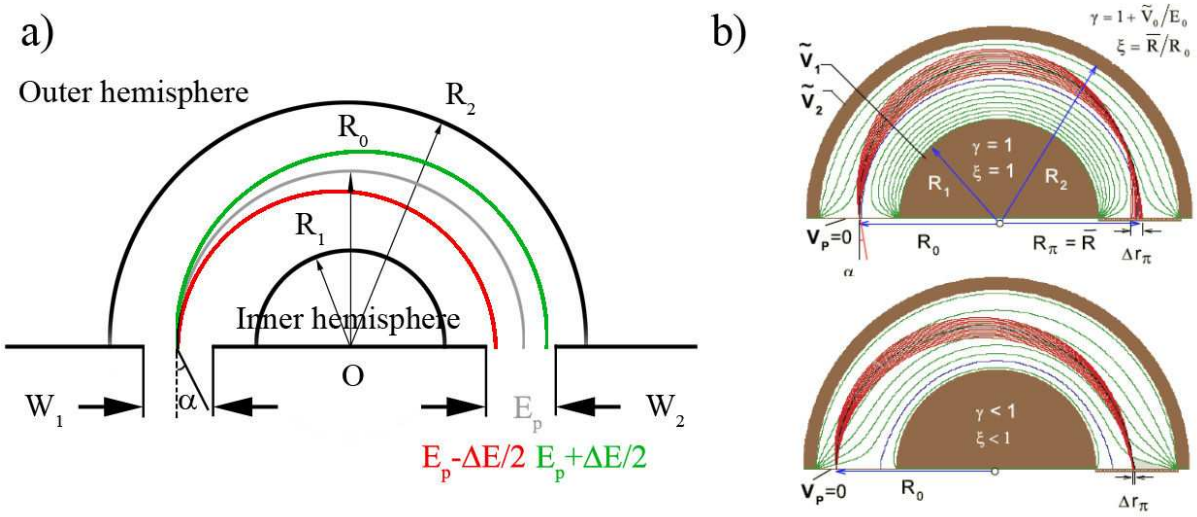

Figure 2.8: *a) Representation of an HSA. b) Simulation of electron trajectories [170]. The blue line is the equipotential for 0 V.*

The geometry of the analyser and the potential applied on each hemisphere define the analyser energy, also called *Pass Energy*, E_p, as:

$$E_p = \frac{q\,(V_2 - V_1)}{\left(\frac{R_2}{R_1} - \frac{R_1}{R_2}\right)}\ , \tag{2.11}$$

where q is the electric charge.
This value corresponds to the energy an electron should have when entering into the analyser to exit from it with a trajectory of mean radius R_0. Electrons whose kinetic energy is less than $E_p - \frac{\Delta E}{2}$ strike the inner sphere. Those whose energy is higher than $E_p + \frac{\Delta E}{2}$ are stopped by the outer sphere. A retarding voltage R is applied at the entrance of the analyser to select the kinetic energy.

There are two modes of analysis: the photoelectrons kinetic energy can be scanned either by varying directly the pass energy, while holding the retarding ratio constant, or by varying the retarding ratio, while holding the analyser pass energy constant.
In the first mode, electrons entering the analyser are retarded by the entrance lens by a constant proportion of their kinetic energy, so that the ratio of electron kinetic energy E_k to analyser pass energy E_p is kept constant. This ratio k is called *retarding ratio*:

$$k = \frac{E_k}{E_p}\ , \tag{2.12}$$

During a spectrum acquisition, the pass energy of the analyser is continuously varied to maintain k constant. Since sensitivity and resolution are proportional to the pass energy, they also vary. The lack of a fixed resolution is a limitation of this mode called *Constant Retard Ratio* (CRR).

Most of XPS instruments are run in the second mode known as *Constant Analyser Energy* (CAE) scan mode. In this mode of operation, the analyser pass energy is held constant, and the retarding voltage is changed thus scanning the kinetic energy of detected electrons. The resolution obtained in CAE is constant throughout the whole kinetic energy range.
For more details on an analyser transmission equipped with an universal lens enabling both kinds of analysis, see the paper written by Ruffieux *et al.* [171].

Energy resolution The analyser energy resolution ΔE_a depends on the pass energy E_p, the mean radius R_0, the angle of electrons entering the analyser at the entrance slit α with respect the the optical axis of the analyser (see figure 2.8), and the width of the entrance and exit slits, respectively w_1 and w_2. It can be expressed as:

$$\Delta E_a = E_p \left(\frac{(w_1 + w_2)}{2R_0} + \alpha^2 \right) . \tag{2.13}$$

Figure 2.8 shows that decreasing the slit widths reduces the half angle of acceptance α, which improves the energy resolution. However, high resolution, obtained by choosing small slits, reduces count-rate. It is important to find a good compromise between resolution and good signal-to-noise ratio.

The detector The detector is a channel electron multiplier (Channeltron) placed in the analyser exit plane. It amplifies the current of a single photoelectron by a factor about 10^6. This small current pulse is passed through a vacuum feedthrough and then brought directly to the preamplifier. The signal is first filtered to reduce noise. Then, it is converted into an optical signal, and transfered via an optical fiber in order to maintain low noise to a receiver unit. This last system converts the optical signal into an electronic pulse which is counted by a pulse counter.

The recorded spectra are sets of data containing the intensity corresponding to the total counts versus the electron kinetic energy referred to the sample Fermi level ($E-E_F$). The intensity is most of the time given in counts per seconds. The energy scale can be expressed either in terms of measured kinetic energy or, if the position of the Fermi level is known, in terms of binding energy.

2.1.1.6 Depth profiling by Angle-Resolved XPS (ARXPS)

We define the angle θ as the angle between the sample surface and the analyser direction. If the sample is rotated by θ, maintaining the photon source and the detector in fixed position, the effective sampling depth decreases by a factor $\sin\theta$, as seen in equation 2.3. The electrons emitted have to travel through more material at higher angles, so that only those originating from the vicinity of the surface tend to escape with no energy loss, as presented in figure 2.9. The relative intensities of surface and subsurface XPS peaks change when the photoemission angle varies.
We have chosen to detail this method since the system of ARXPS is available on the Multiprobe XPS instrument (MXPS). We used it to study the efficiency of a passivation protocol on our samples. This point will be detailed in chapter 3 section 3.3. Current status and future prospects for ARXPS are described by Herr [172].

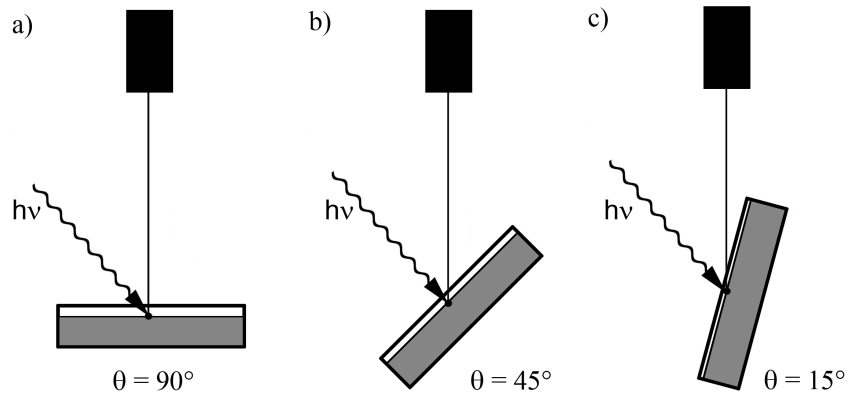

Figure 2.9: *Angular-Resolved XPS: a) θ=90°, the depth probed is maximal. Since θ decreases in b) and c), the sampling depth decreases.*

2.1.2 PhotoEmission Electron Microscopy (PEEM)

This section is dedicated to the PEEM instrumentation. This includes the electronic optical column and the detector. It is completed by the presentation of X-ray photon sources, especially those used in laboratory and in synchrotron environment during this thesis.

2.1.2.1 Background

PhotoElectron Emission Microscopy (PEEM) dates back to the 30s [173, 174] when electron lenses were being developed. The first commercially available PEEM based on a cathode lens system was built in the 60s, but its applications were restricted due to the limitations in terms of vacuum quality [175].

PEEM systems with high lateral resolution have now been available for 15 years using low-energy UV sources. Full field imaging combining XPS and PEEM has existed since the 1980s [176, 177] giving information about the chemical composition of the surface. However, due to the lack of high-transmission on the one hand, and the scarcity of bright X-ray sources on the other hand, it was difficult to perform core-level imaging with good resolution [178]. Nowadays, a new PEEM conception allows better imaging of core-levels either with synchrotron radiation or in the laboratory, and will be described in sections 2.2.3 and 2.2.4.

2.1.2.2 Electron optics: the PEEM column

PEEM column PEEM without energy filtering is the simplest case encountered. There are two basic conceptions of PEEM imaging:

- The sample is near ground potential and the extractor anode, part of the first lens in the immersion objective, is at high positive voltage, as illustrated in figure 2.10 a). The PEEM column consists of electrostatic elements: the immersion objective lens composed of an electrostatic octupole stigmator, an adjustable contrast aperture

situated in the back focal plane of this objective lens, and two projective lenses which are necessary to project the intermediate image onto the screen.

- The sample is held at a high negative potential and an electric field is created between it and a grounded anode. The whole column is biased to negative voltage to focus the photoelectrons on the image plane. The lenses are, in this case, magnetic. Most of PEEMs installed in synchrotron beamline are of this kind.

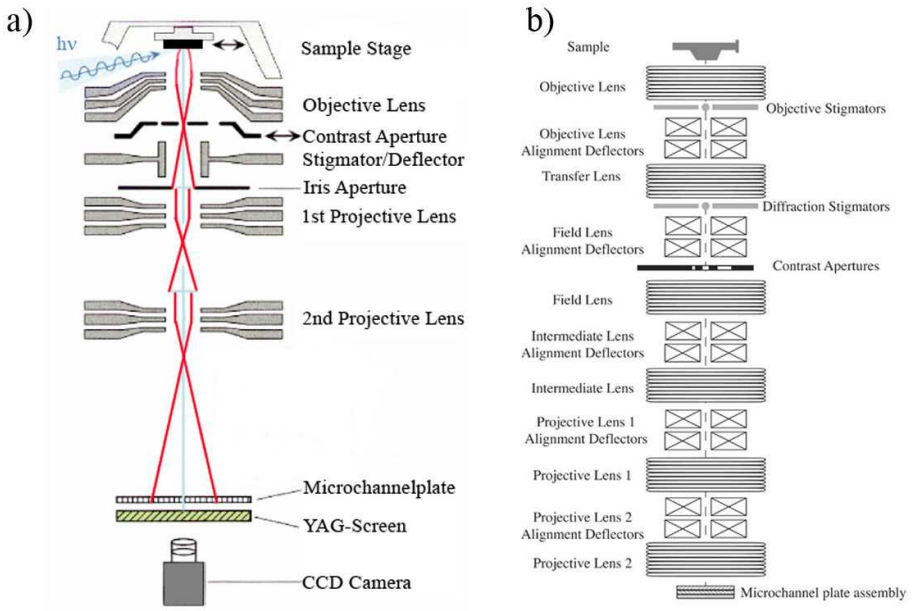

Figure 2.10: *a) Schematic layout of a PEEM column [91] where the sample is at ground potential. b) Schematic layout of a PEEM column [179] where the sample is held at high negative voltage. This Spectromicroscope for PHotoelectron Imaging of Nanostructures with X-rays (SPHINX) X-PEEM, is installed at the University of Wisconsin Synchrotron Radiation Center.*

In general, small fields of view improve imaging conditions. The photoelectron trajectories are very closed to the optical axis corresponding to approximately Gaussian optics.

PEEM transmission The combination of an immersion lens and a contrast aperture has a pronounced low-pass filter behavior. In figure 2.11 a) and b), the secondary electrons yield sees its distribution in energy decrease after passing through the optics. The width of the low-pass filter depends on the contrast aperture diameter placed in the focal plane, as presented by Anders *et al.* [180]. Figure 2.11 c) represents the energy distribution of electrons transmitted through a PEEM column using apertures of different diameters: the smaller the aperture, the smaller the energy width and the lower the intensity of the secondary electron spectrum.

2.1.2.3 The detector

The detector consists of three elements: microchannel plates (MCPs), a fluorescent screen and a CCD. The aim is to convert the electronic signal collected by the column in an

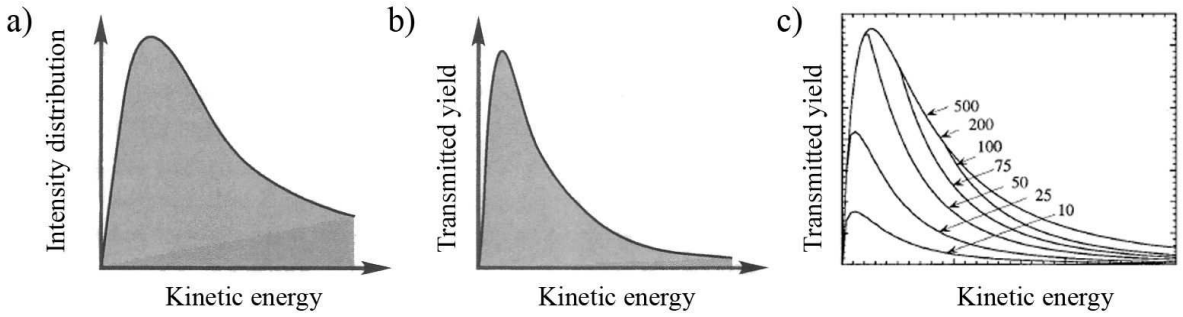

Figure 2.11: *SE spectrum before a) and after b) passing through a PEEM column [91, 95]. c) Energy distribution of electrons transmitted through a PEEM, using apertures of different diameters (in μm) [180].*

optical one, which can be recorded by a camera.
This implies firstly to emphasize the collected signal: incident electrons are multiplied thanks to an avalanche multiplication system when passing through the MCP [181] which are compact electron multipliers with high gain. Then, these electrons are accelerated onto a fluorescent screen. The screen can be made of YAG crystal or phosphor, and emits a photon when an electron hits it. A cooled CCD equipped with a lens collects these photons. The optical image resulting on the fluorescent screen corresponds to the electronic image of the surface obtained by the PEEM. Details about such system are well presented by Moldovan *et al.* [182].

2.2 Energy-Filtered XPEEM

Over the last two decades, PEEM imaging has seen an important breakthrough thanks to the development and the implementation of several energy filters on PEEM columns. This section is organised as follows: after some state-of-the-art of actual trends in energy-filtered PEEM, we will present some general features concerning the instrument used during this thesis: the NanoESCA. Then, we will detail its overall performances before finishing with some details concerning its operation with laboratory sources and in a synchrotron environment.

2.2.1 Present trends in energy-filtered PEEM

PEEM combined with the energy filtering of the photoelectrons allows spectroscopic imaging. Alternative approaches of energy-filtered PEEMs and their main characteristics are now briefly presented. The aim of this overview is not to realize an exhaustive list of energy filtered PEEMs existing, but almost to situate our NanoESCA instrument among the PEEMs family. In their review on photoelectron microscopy, Günther *et al.* [91] have described the different alternative approaches of energy-filtered PEEM systems more in detail.

Wien Filter A Wien filter consists of orthogonal electric and magnetic fields, respectively $\vec{E}$ and $\vec{B}$, perpendicular to the photoelectron trajectory. Only the photoelectrons satisfying the condition $\vec{E}=\vec{v} \times \vec{B}$, travel undeflected through the Wien filter [183]. By choosing kinetic energies characteristic of the elements thanks to a slit placed after the Wien filter, the image reflects their distribution, as presented in figure 2.12 a). However, one drawback is the low sensitivity, since the acceptance angle is small. A solution simulated with the charge simulation method by Niimi is to correct it with a multipole arrangement [184, 185].
A detailed view of an XPEEM system using a Wien filter-type electron energy analyzer is presented in figure 2.12 b). Tsutsumi *et al.* have developed this kind of energy-filtered PEEM, which has the advantage to carry out an easy alignment of the electron optical axis. They also discuss about future applications to organic devices [186, 187].

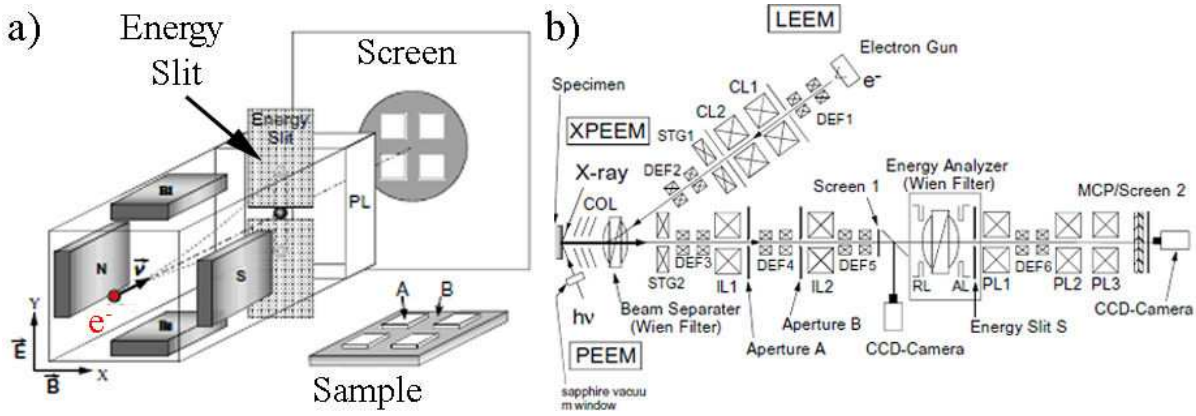

Figure 2.12: *a) Wien-filter scheme [188] and b) energy-filtered PEEM equipped with a retarding Wien-filter [183].*

Omega Filter The Omega filter system is implemented on the *Spectro-Microscope with Aberration correction for many Relevant Techniques* SMART instrument, available on BESSY II facility. It consists of four sector magnets arranged like the greek capital letter omega. It is also combined with multipole magnet correctors, as can be seen in figure 2.13. The configuration discriminates the photoelectrons and the secondary electrons. A slit in the dispersion plane of the Omega filter allows to define an energy window. The pass energy is kept constant in order to avoid magnet realignments. Basic principles of the Omega system, and the various modes of operation and the optical design of the SMART instrument are presented by Fink *et al.* [189].

Time of Flight (TOF) This mode is similar to spectroscopic TOF experiments, but implemented in a PEEM. It requires a linear microscope column and a pulsed photon source which can be either a laser or a synchrotron source.
When emitted after a single impulse of photon, photoelectrons are dispersed in time according to their velocity. The rear part of the PEEM column is elongated with a drift tube at reduced potential, where electrons are retarded to the desired drift energy allowing the detection of the dispersion. To analyze the energy distribution of photoelectrons in

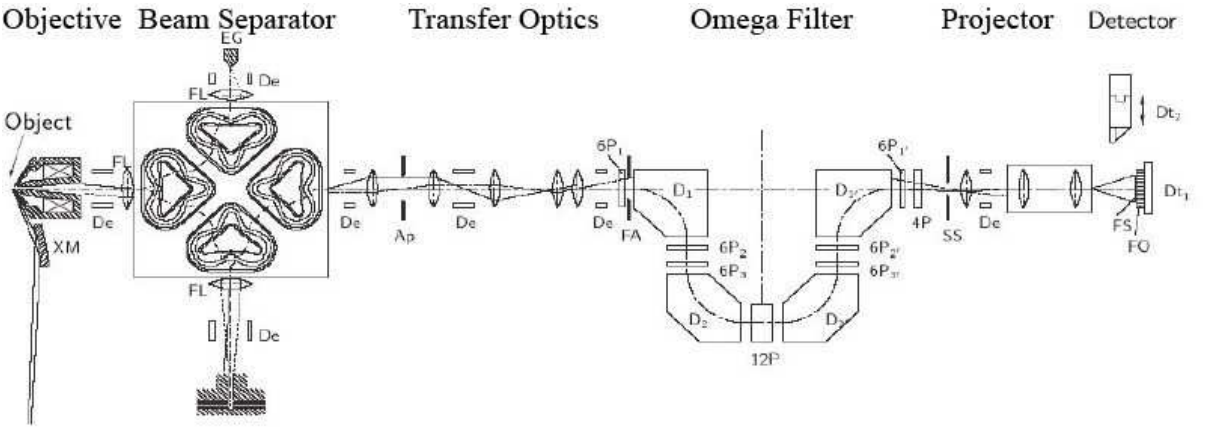

Figure 2.13: *SMART instrument schematic layer including an Omega filter [190].*

PEEM, the time of flight for electrons passing this section is measured, referenced to the time structure of the pulsed photon source. Figure 2.14 presents a schematic view of this setup. One characteristic of ToF PEEM is to reduce the chromatic aberrations of the microscope due to the energy distribution of the secondary electrons.

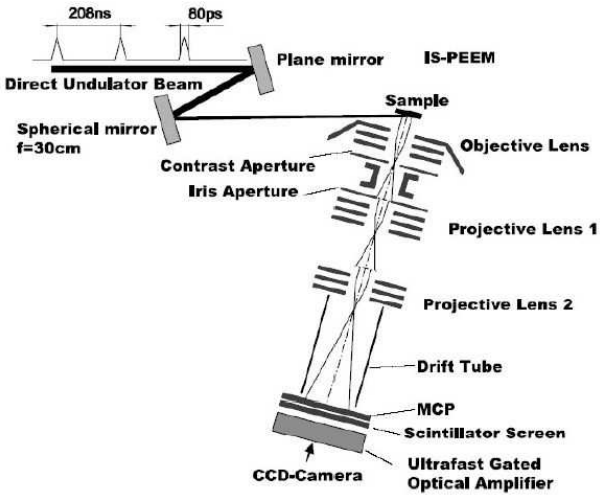

Figure 2.14: *Schematic view of a Time of Flight PEEM called IS-PEEM [191].*

Two ways of fast image detection can be encountered at the back of the instrument: either a fast gated intensified CCD camera as presented in figure 2.14, or a special counting electronics in combination with a delay line detector. This latter collects all electrons arriving at different times in a 3D (x,y,t) data histogram: both the two dimensions positions (x,y) and the time marker of the excitation are acquired simultaneously. Compared to a CCD camera with an ultrafast gated optical intensifier, it has a superior time resolution in the sub-nanosecond range since it detects any single counting event. Its principle is well explained by Oelsner *et al.* [192]. The main limits of the delay line detectors are determined by the detector system, but nowadays, time resolution down to about 100 ns is possible [193].

Good work presenting the developments in time and energy resolved PEEM over the

past few years was also realized by Oelsner *et al.*. Characteristic parameters for both pulsed excitation sources suitable for ToF PEEM and time-resolving detection units are tested and presented by Schönhense *et al.* in tables 1 and 2 of reference [194]. With such systems, studies of magnetization dynamics can be done at sub-picosecond time resolution [195].

Retarding Field Filter The retarding field analyzer can be designed either with a retarding field lens system or with a combination of two retarding lenses L_1 and L_2 plus double grids G_1 and G_2 [196] as visible in figure 2.15. The lens elements form the pre-retardation optics: voltages are set to decelerate photoelectrons and to achieve normal incidence of their trajectories on the grids. These grids are connected together and form an homogeneous electric field. The behavior of such system is a high-pass one, allowing only photoelectrons having an energy higher than G_2 voltage to pass through.

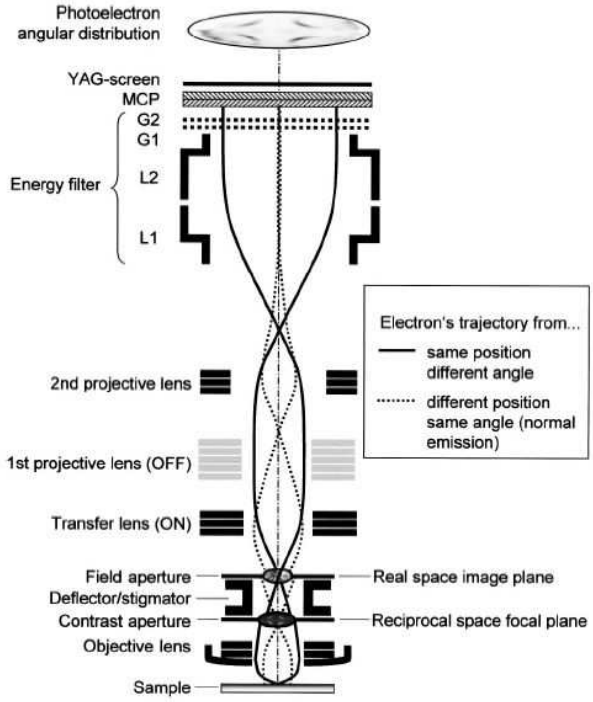

Figure 2.15: *Schematic view of the lenses optics of a PEEM, including a retarding field filter in front of the MCP [197].*

Hemispherical Deflector Analyzer This filter presented in figure 2.16 is the electrostatic analyser used in XPS spectroscopy, as detailed in section 2.1.1.5, which acts as a band-pass filter [198]: only photoelectrons having an energy in the pass energy range can travel through the electrodes forming the analyzer at constant radius, and can be imaged thanks to a 2D detector positioned at the screen plane.

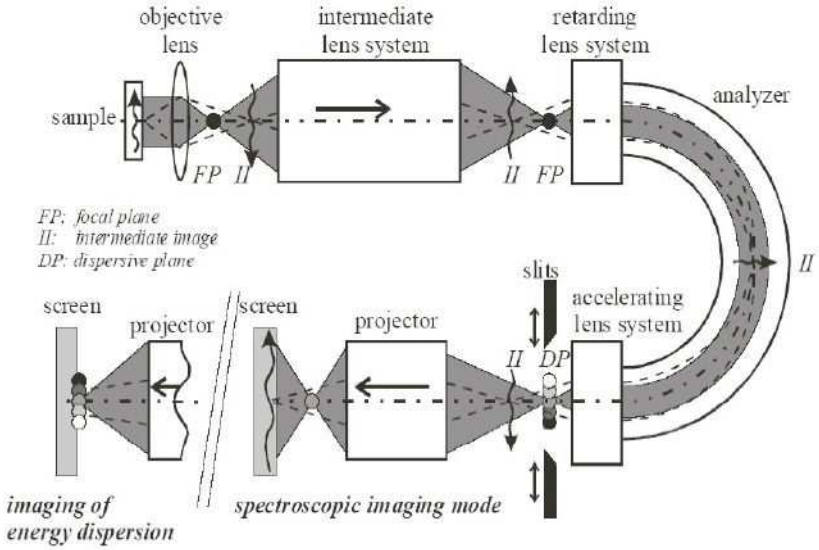

Figure 2.16: *Hemispherical Deflection Analyzer [199].*

Double Hemispherical Analyzer Last but not least, among XPEEM instruments fitted with high transmission band-pass energy-filters [200], one has to consider those equiped with a double hemispherical analyser. It is based on a tandem arrangement of two hemispherical energy analysers used as an imaging energy filter. A good review on such a system was realized by the manufacturer Omicron [201]. The main spherical aberration (α^2-term) of the analyser is corrected by the antisymmetry of the tandem configuration which leads it to be a state-of-the-art energy filtered spectromicroscope. The advantages of such configuration over a simple hemispherical analyser are:

- its lateral resolution independent of the pass energy, and the total resolution is only limited by the aberrations of the PEEM lenses,
- high transmission imaging is available at low pass energies with good lateral and energy resolution, since the second hemisphere compensates the aberrations of the first one,
- real core-level and valence band imaging can be performed since this configuration provides band pass filtering of photoelectron kinetic energies.

It is possible to use it with a bright laboratory X-ray source [202] as described in subsection 2.2.3 and with synchrotron radiation. Photoelectrons from several range of kinetic energies can be imaged, bringing lots of information about the surface properties, as depicted in figure 2.17. The blue rectangles represent the energy windows available with such instrument. This figure is the same as figure 2.1 completed with properties deduced from each kind of energies. A wide series of studies led with this instrument can be given in example: single silicon nanowires [203], doped patterned surfaces [101], work function of single copper grain [127], magnetic domains imaging [204–206], or pre-solar meteorites [207, 208].

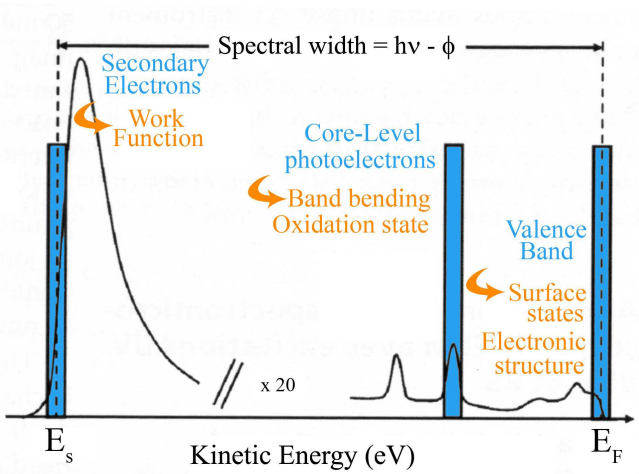

Figure 2.17: *Range of kinetic energies observable in energy-filtered PEEM imaging and informations deduced [149].*

2.2.2 The NanoESCA

2.2.2.1 Introduction

The NanoESCA represents a new concept for spectroscopic imaging. The design combines a fully electrostatic PEEM column and a double hemispherical analyser as energy filter. Figure 2.18 shows a side-view of the instrument indicating the different optical paths corresponding to three different operation modes:

- Direct non energy filtered PEEM imaging: 1
- Selected area spectroscopy: 2
- Energy filtered PEEM imaging : 3

The description of the instrument presented in figure 2.18 can be detailed as follows:

- The PEEM column is composed firstly by the immersion objective lens, which consists of a sample near ground potential and an extractor anode that can be kept up to 15 kV. The electrons are focused onto the entrance slit of the energy analyser. The lens is used in CAE scan mode, hence retards the electrons relative to the energy at which they leave the sample surface. It also provides variable magnification and angular acceptance to select the sample analysis area. A variable iris aperture in the PEEM allows to select areas down to 1 μm diameter for microspectroscopy. The projective lenses are either used to project the first intermediate image onto the screen for the mode 1, or to adapt the electron energies to the pass energy of the analyser for modes 2 and 3. The electrons being decelerated towards the column and not towards the analyser, this has the advantage to maintain high transmission.
- Two hemispherical energy analysers of 125 mm mean radius, with double focusing geometry thanks to a transfer lens in between,

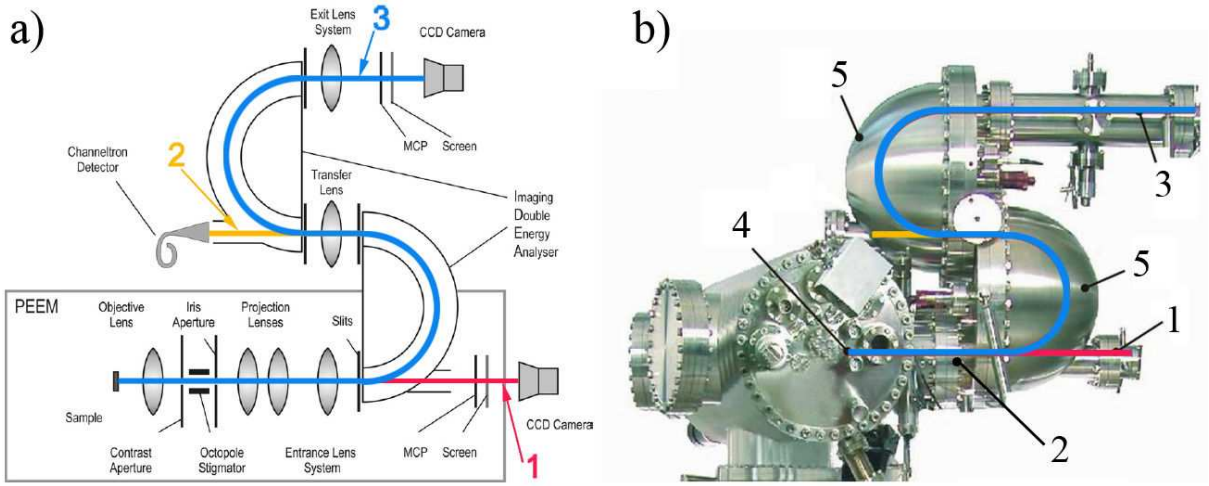

Figure 2.18: *a) Schematic representation of the different operation modes of the NanoESCA [209]. b) Photography of the instrument: 1 and 3: MCP, 2: PEEM column, 4: X-ray source detailed further on subsection 2.21 and 5: IDEA [201].*

- A set of slits at the entrance and exit of the energy analyser defines the resolution of the analyser,
- A detector consisting of a Channeltron electron multiplier mounted focusing the exit slit of the second hemisphere,
- Two imaging units, based on an MCP, a fluorescent screen and a CCD for the two modes 1 and 3.

For the mode 2, the second hemisphere deflection field is switched off: the electrons are focused by the transfer lens into a Channeltron detector allowing microspectroscopy in the field of view.

We will focus now on the double hemispherical analyser implemented as energy-filter [210], also known as *Imaging Double hemispherical Energy Analyser* (IDEA).

2.2.2.2 Characteristic of the NanoESCA: the IDEA system

The principle is based on Kepler's law of planetary motion on ellipses: the electron trajectories after a complete revolution coincide, independently of start energy or angle, as seen in figure 2.19 a). The second half of the elliptical orbits compensates the aberrations of the first half, generating an achromatic image without geometrical aberrations. Their action is illustrated in figure 2.19. This underlines the importance of the second analyser which corrects for the α^2 term due to the angle of acceptance, responsible of the blurring energy-filtered images at low-pass energies, as seen in figure 2.19 b).

In defining the NanoESCA performances, it is as important to consider both the energy and lateral resolution and their influence on transmission.

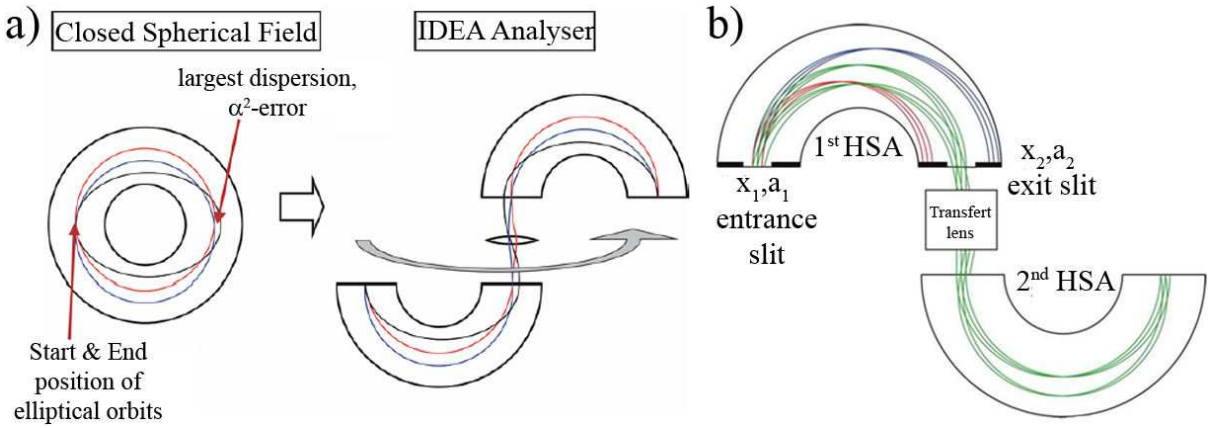

Figure 2.19: *a) Absence of geometrical aberrations in a closed spherical sphere [201]. b) α^2 aberrations introduced while passing through the first hemisphere are compensated by the trajectories in the second [209].*

2.2.2.3 Energy resolution

The energy resolution of the IDEA analyser is the same as determined in formula 2.13 [201] for a HSA:

$$\Delta E_a = E_p \left(\frac{(w_1 + w_2)}{2R_0} + \alpha^2 \right) \ . \tag{2.14}$$

It depends on the electron pass energy E_p, the slit widths w and the acceptance angle of the lens system α with respect to the optical axis of the analyser. To obtain a good energy resolution, providing the α^2-term is negligible, one has just to increase the transmission of the NanoESCA.

The transmission T is given by the equation [209]:

$$T \propto \frac{\Delta E}{\sqrt{E_p}} \alpha 2R \ , \tag{2.15}$$

where α is the constant aperture angle at the analyser's entrance slit, as already defined. Decreasing the pass energy, or taking small slit widths, is an advantage to acquire images with good spatial and energy resolutions, but it is necessary to keep in mind that the photon flux of the excitation source is intense enough to observe a good signal-to-noise ratio. A typical value of E_p is 100 eV but it is possible to go down to 50 eV.

2.2.2.4 Lateral resolution

The IDEA system itself does not limit the lateral resolution since the second of its two hemispherical analysers always compensates the dispersion of the first one. Hence, contrary to a HSA, the lateral resolution of the NanoESCA is independent of the pass energy and depends only on the aberrations of both the extracting field and the optics before and behind the IDEA, but especially those of the cathode objective lens [211].

According to Escher *et al.* [209], the total resolution d_{tot} can be approximated by the resolution disc diameter:

$$d_{tot} = 2\sqrt{d_{r_c}^2 + d_{r_s}^2 + d_{r_d}^2} \ , \tag{2.16}$$

where $d_{r_c}^2$, $d_{r_s}^2$ and $d_{r_d}^2$ are respectively the chromatic, the spherical and the diffraction contributions to the disc radius. These parameters can be expressed as:

$$dr_c = \left[l\frac{E_0}{U_{ext}} + C_c \left(\frac{E_0}{U_{ext}} \right)^{3/2} \right] \frac{\Delta E}{E_0} \alpha_0 \ , \tag{2.17}$$

$$dr_s = \frac{1}{4} \left[l\frac{E_0}{U_{ext}} + C_c \left(\frac{E_0}{U_{ext}} \right)^{3/2} \right] \alpha_0^3 \ , \tag{2.18}$$

$$dr_d = \frac{0.73}{\sqrt{E_0} sin\left(\alpha_0\right)} \ , \tag{2.19}$$

where l is the field length, U_{ext} the potential of the extractor anode, E_0 the starting kinetic energy of an electron which leaves the sample surface with a starting angle α_0, and C_s and C_c respectively the spherical and chromatic aberration coefficients. The definition of these aberrations and their influence on image formation and resolution obtained are well explained by Rempfer *et al.* [212, 213].

The lateral resolution of the NanoESCA objective lens for electrons with 100 eV kinetic energy has been calculated and is presented in figure 2.20 for three different values of the extractor potential. The resolution decreases when decreasing the contrast aperture diameter and increasing the extractor potential. It is easy to understand why small apertures improve the spatial resolution of the instrument: these latter filter indeed photoelectrons, conserving only the closest to the optical axis, and those with small entrance angles, allowing to approach Gauss conditions. However, small contrast aperture does not correct aberrations due to the PEEM column, they only limit them. The minimum of lateral resolution is limited by the three dashed lines corresponding to the aberrations intrinsic to the system. Two values obtained from real experiments (red stars) with 12 kV extractor voltage were also added.

Astigmatism is another factor which has an influence on lateral resolution. It has also to be taken into account, even if it does not appear in figure 2.20. It comes from a problem of symmetry around the optical axis due to a misalignment between the sample and the optical column, or due to a misalignment between the different lenses of the PEEM column. The octupole stigmator implemented on the PEEM column can compensate this astigmatism. A patent was registered during this thesis on an astigmatism correction method for secondary electron imaging but above all for core-level imaging. This will be detailed in subsection 2.4.3.

Another strong feature of this instrument is that it can be operated using both laboratory X-ray or UV sources and synchrotron beamline. Thus, we can use UV (Hg or D_2 radiation) and VUV (He I and He II) sources, but also monochromatic AlKα radiation using a laboratory Focused X-ray Source (FXS). We will detail the two X-ray sources used on the instrument: the FXS, and synchrotron radiation.

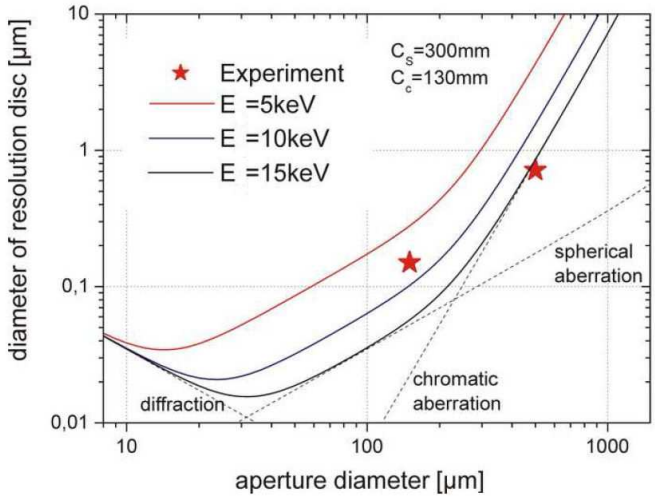

Figure 2.20: *Lateral resolution of the NanoESCA objective lens for an extractor potential U_{ext}=E of 5 kV, 10 kV and 15 kV [201].*

2.2.3 The laboratory Focused X-ray Source (FXS)

The laboratory X-ray source used in the NanoESCA is a unique high flux X-ray source, providing a bright focused monochromatic beam on the sample surface whose size can be adapted to provide the most uniform illumination conditions. It is more intense than conventional AlKα source since it uses a focused electron beam scanned upon an aluminum anode for X-rays generation. Moreover, thanks to the high cooling efficiency of this anode, this latter tolerates higher heat brought by the small electron beam, and thus, delivers a higher photon flux density.
An ellipsoidal quartz crystal monochromatizes the X-ray beam and focuses it onto the sample.

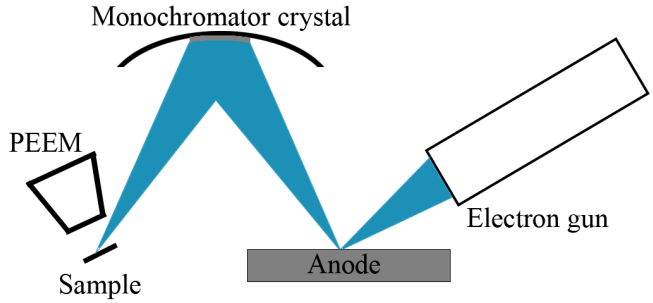

Figure 2.21: *Focused X-ray Source scheme.*

2.2.3.1 The electron gun theory

The electron gun filament is a LaB_6 source. Appropriate voltages give an intense finely focused electron beam which is scanned across the X-ray anode, stimulating the emission of X-rays from the anode. The movement of the electron beam across the anode is

reflected by the X-ray beam across the sample. The electron beam size determines the X-ray beam one.

2.2.3.2 The monochromator

The monochromator is based on a 200 mm Rowland circle where a quartz (100) crystal is bent on an ellipsoidal substrate whose center is tangent to the Rowland circle in order to generate micro focused X-ray beam.

The X-ray energy dispersion eliminates the K$\alpha_{3,4}$, K$\alpha_{5,6}$ and Kβ X-ray lines and also the Al bremsstrahlung radiation background. It also narrows the AlKα_1 line, allowing core-level and valence band spectra to be acquired with both high energy resolution and good signal-to-noise ratio. The narrower X-ray line width, the higher analyser energy resolution, as seen in equation 2.10.

The ellipsoidal monochromator operated according to Bragg's law for X-ray diffraction. A single wavelength of Kα X-ray from a conventional aluminum anode is reflected from (100) quartz crystal surface at a specific angle of reflection θ:

$$n\lambda = 2d\sin\theta \ , \tag{2.20}$$

where n is the integer determined by the order chosen, d is the spacing between the planes in the atomic lattice and λ the wavelength considered. In the specific case of AlKα_1, the values of these factors are: d = 0.4255 nm, λ = 0.834 nm, $\theta = 11.5°$.

Typically the X-ray source monochromator delivers Al Kα_1 radiation with the following features:

- 1486.7 eV of photon energy,
- 0.26 eV of photon bandwidth (ΔE_s),
- A photon flux of 10^{12} photons.s^{-1}.mm^{-2},
- The X-ray beam is incident at the sample surface at an angle of 66° with respect to the surface normal,
- The X-ray spot size on the sample surface can be adjusted between 30 μm and 200 μm,
- A 30 μm X-ray spot size corresponds to a power load on the Al-coated anode of 4.3 W.

2.2.4 Synchrotron sources

Synchrotron radiation was first observed from accelerators dedicated to particle collision experiments in nuclear physics. One observed that the charged particles lost kinetic energy under the form of electromagnetic radiation when they were orbiting in the synchrotron. For the collision experiments, the energy loss was an undesired effect but one discovered the advantages of such radiation. In the 1970s, storage rings dedicated for this purpose were started to be built.

The principle is as follows: charges submitted to an acceleration, moving in a closed curved path under the influence of magnetic fields, radiate some electromagnetic radiation. Their kinetic energy being highly relativistic, due to this acceleration, and combined with a deviation of their trajectory, they emit light in a continuous spectrum whose intensity maximum is proportional to the radius of curvature and inversely proportional to the cube of the electron energy. Moreover, the emitted radiation is concentrated in a very narrow cone tangential to the electron orbits whenever a magnetic devices force the particles to change their trajectory. We will come back on this point later.

A synchrotron radiation source is composed of three accelerators: a linear accelerator the LINAC, and a circular one, the booster. The last one is the storage ring itself, where the circulating particles are kept at the operating energy. These different parts of most of third generation synchrotron installations are now detailed. The parameters values are given for the SOLEIL machine in Saint-Aubin (France). Figure 2.22 displays a schematic of the synchrotron facility.

The LINAC A *LINear ACcelerator* (LINAC) is used as a pre-injector which accelerates charged particles. It is composed of adjacent metal cylinders at opposite electrical potential, called *drift tubes*. The metal acting as equipotential surface, particles travel at a constant velocity. The LINAC runs in two main operation modes: the multibunch mode is the standard user operation mode in which the storage ring is filled with 416 bunches of electrons for a total current of 500 mA. The temporal structure mode corresponds to the use of 8 bunches separated by 140 ns, and its lifetime is 18 hours.

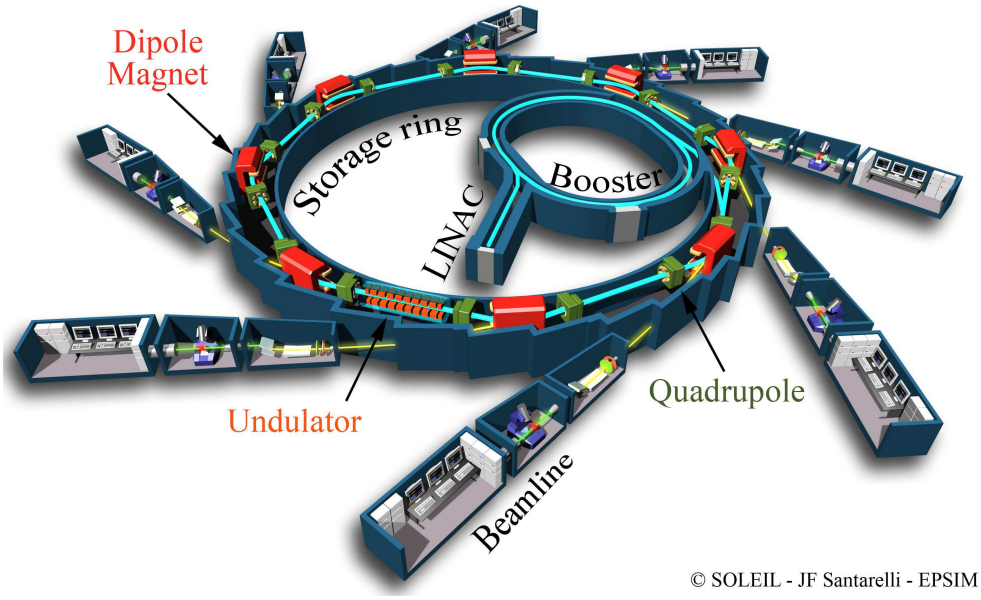

Figure 2.22: *Synchrotron SOLEIL principle. Courtesy of SOLEIL [214].*

The electrons extracted from the LINAC have an energy of 100 MeV and must be accelerated to higher energies. This is the aim of the injector called *booster*, a circular accelerator of 157 meters diameter, in which the electron beam circulates several times

before being injected into the storage ring. For each revolution, electrons pass through two radio frequency cavities in which electromagnetic fields oscillate. They are increased until the beam operating energy is reached, i.e. at 2.75 GeV.

The storage ring The storage ring allows the current of electrons to circulate along a closed trajectory of 354 meters perimeter under vacuum, around 1.10^{-9} mbar. The energy lost by the radiating electrons is restored by radio frequency cavities which are regularly positioned around the ring. The third generation synchrotron light sources can produce light with high spectral flux and brilliance in a wide range of energies thanks to magnetic devices inserted into straight sections of the storage ring which induce deviations of the trajectories of the relativistic electrons. *Wigglers* are more effective insertion devices than simple bending magnets since they correspond to an association of several magnets with alternating field directions.
Most modern machines preferentially use *undulators* instead of wigglers since they are the most powerful generators of synchrotron radiation. They generate a thin beam of coherent light. The emitted radiation intensity is proportional to the square of the number of magnets. Its polarization can be linear, elliptical or circular, depending on the magnetic geometry used.

The synchrotron radiation can be of different ranges of energies: the low energies are covered by radiation coming from bending magnets and undulators, whereas the high energy range is covered by radiation coming from wigglers. Synchrotron radiation has a broad continuous spectral range. In the case of insertion devices, intensity is concentrated in harmonics typical of the undulator or wiggler setting.

The beamline Each beamline has its own insertion device to optimize the X-ray beam characteristics for its specific experiments. After the beam of light is generated in the storage ring, it travels towards the experiments through several elements which are necessary for beam conditioning:

- *Windows* are thin sheets of metal, which transmit almost all of the beam, but protect the storage ring vacuum from contamination.
- A *monochromator* filters out a single desired wavelength of radiation with a narrow bandwidth. For radiation in the UV region of the spectrum, a reflection grating monochromator is used. The incident beam is focused onto the grating by a first mirror. The grating Bragg diffracts the beam, distributing the different wavelengths over a cone of radiation. By use of a suitable slit, the desired wavelength can be chosen and the resulting monochromatic beam is focused onto the exit of the monochromator by a second optical system.

Advantages for photoelectron spectroscopy The advantages of synchrotron third generation sources can be summarized in three points:

- Tunability: The continuum spectrum synchrotron radiation covers from the far infra-red to X-rays. It is possible to probe the sample, obtaining hence spectroscopic informations either from the surface or the volume bulk without changing

the detection angle by exploiting the kinetic energy dependence of the inelastic mean free path 2.1.1.2. Here, the energy distribution spectrum is recorded at a fixed value of emission angle for several photon energies. Band structure, electronic surface states or the density of states can be determined. Moreover, choosing the wavelength of the synchrotron beam allows optimization of photoionization cross-section which helps in having better chemical sensitivity than in laboratory.

- Variable polarization of synchrotron light: it is possible to select linear or circular one with the appropriate undulator. Synchrotron light is horizontally polarized in the deflection plane of the storage ring. When moving up or down, polarization becomes circular, which can be of interest in magnetic dichroism studies.

- High brilliance: thanks to the small divergence of the beam and the use of insertion devices, the brilliance available with synchrotron light is six orders of magnitude bigger than that of laboratory sources between 10^{14} and 10^{20} photons.s^{-1}.mm^{-2}.mrad^{-2}.

The use of synchrotron radiation also helps in increasing the overall energy resolution of the system (source+IDEA), since its own resolution is given by the relation:

$$\Delta E_s = \frac{h\nu}{RP} \ . \tag{2.21}$$

where $h\nu$ is the energy of the synchrotron beam and RP is the resolving power of the optics used in the beamline to bring the X-ray beam to the instrument.

During this thesis, two synchrotron campaigns were performed on the Time resolved Experiments on Materials with PhOtoelectron spectroscopy (TEMPO) beamline at SOLEIL (Saint-Aubin). TEMPO is a soft X-ray beamline designed for time dependent studies of electronic and magnetic properties. Its resolving power is 5000. The energy range available is from 50 eV to 1500 eV.
We usually worked with a linear horizontal polarization since it offers the best signal intensity. For each beam energy used to carry out the experiments, the NanoESCA pass energy was not set constant. This is due to the photoionization cross-section σ which decreases for high excitation energies. Increasing the pass-energy for high photon energies can help in compensating the decrease of σ to maintain a high sensitivity.

Some very good reviews have been published on the physical principles and the experimental realization of the PEEM using synchrotron radiation for chemical [215] [92] or magnetic imaging [91]. Concerning this topic, Schneider and Schönhense [95] have reviewed PEEM imaging of magnetic systems and resume very well electron-optical considerations. Störh and Anders [132] provides many examples to illustrate the various applications of the XPEEM technique in technological areas (TiSi interconnexions, thin-films polymer blends, antiferromagnetic exchange bias materials, etc.). Finally, chemical imaging of surfaces and interfaces by XPEEM is discussed by Locatelli and Bauer [92].

2.3 Information available from Energy-Filtered PEEM imaging

2.3.1 Data format

The images are recorded by a 12-bit cooled CCD camera which produces images with different binning, the binning 1 corresponding to (1024×768) pixels. Images are stored in a 16-bit fit format for data preprocessing, 'fit' standing for Flexible Image Transport standard.

The data are recorded either as single images or as image stacks. In the latter case, a predefined range of photoelectron kinetic energies is scanned by changing the voltage applied to the sample, according to a chosen energy step size. This implies an automatic refocusing of the immersion lens. Hence, a 3D image stack is obtained. Each image corresponds to the intensity distribution I, as a function of the position within the field of view. Each step represents the kinetic energy E with respect to the sample Fermi level, within a determined range: I(x,y,E), as represented in figure 2.23 a).

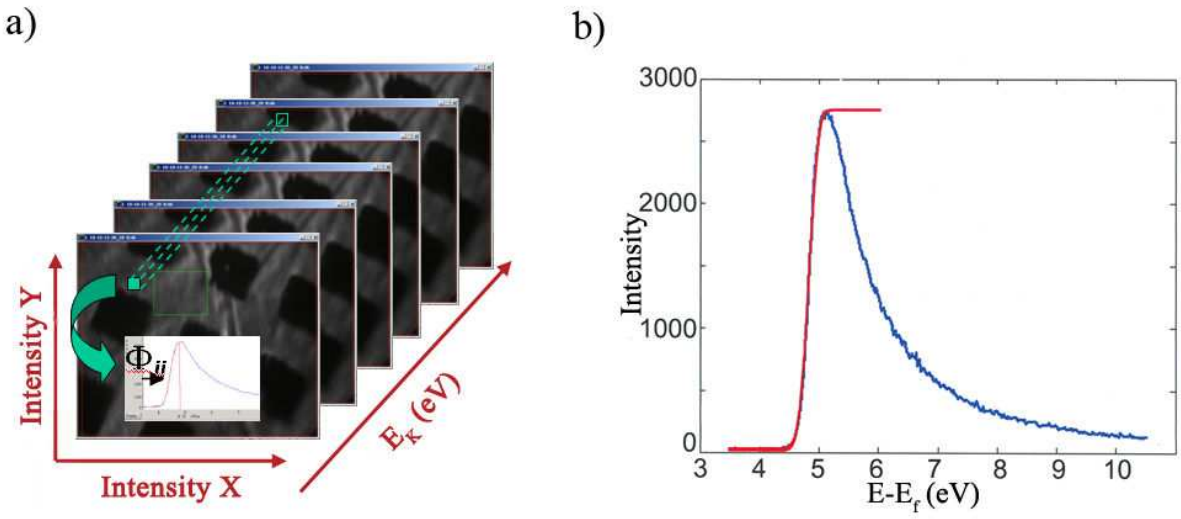

Figure 2.23: *a) Image stack representation in 3D: I(x,y,E). b) Local extraction of the spectrum for the area presented in green in a), and threshold fit corresponding in red.*

Thus, the photoelectron spectra and the intensity maps can be extracted from the data 'cube' in the range of interest: secondary electrons, core-levels or valence band. XPEEM spectromicroscopy thus provides full spectral information at every pixel of an image, and spectra can then be extracted from chosen areas within the field of view, as seen in figure 2.23 b). Thus a complete chemical mapping of the imaged surface area is possible.

In the next subsections, we will explain how it is possible to extract local work function from the threshold image series or to realize spectroscopic core-level imaging. To finish, we will describe the preprocessing steps required to extract the maximum information from the acquired images.

2.3.2 Work function mapping

In PEEM, the absolute work function is deduced from the SE emission threshold, since the energy scale is measured with respect to the sample Fermi level [216]. The local work function can be extracted either using the whole secondary electron energy distribution with Henke's model, or just considering the rising edge at threshold. In our experiments and MATLAB developments, the second option was used.
For example, the photoelectron spectrum of the area of interest represented by the green square in figure 2.23 a) was extracted. It was then fitted in red, as presented in figure 2.23 b).

The work function Φ of this specific area can be deduced by fitting the threshold with a Heaviside function convoluted with a Gaussian [127], which corresponds to the complementary error function:

$$I\left(E-E_F\right)=\frac{I_{max}}{2}.\mathrm{erfc}\left[\frac{\Phi-\left(E-E_F\right)}{\sigma\sqrt{2}}\right]+I_{off}\ , \tag{2.22}$$

where σ is the standard deviation of the gaussian due to the energy broadening of the analyser at the pass energy used, I_{max} measures the step magnitude, I_{off} represents a constant offset and $(E-E_F)$ is the photoelectron kinetic energy above the Fermi level. The fit use a function that solves nonlinear curve fitting problems in the least squares sense. That is, given input data, and the observed output data, it performs weighted least squares fit applied to the equation with which we want to fit our data.
Two further steps are necessary:

- Considering ideal conductors, one has firstly to include a shift in energy of the work function of 98 meV due to the Schottky effect caused by the strong accelerating field E applied by the extractor lens on the sample [163]. Considering a charge in vacuum, at a distance x from the sample surface, E induces an opposite charge on this latter, at a distance $-x$ from its surface. This image potential gives thus rise to an attractive force which corresponds to the potential energy of an electron at this distance x from the sample. The Schottky barrier lowering at a metal surface is estimated to be:

$$\Delta E_{schottky}=-q\sqrt{\left(\frac{qE}{4\pi\epsilon_0}\right)}\ , \tag{2.23}$$

  where q denotes the electric charge, and ϵ_0 the vacuum dielectric constant. For others materials, such as semiconductors, this value is only an upper limit.

- Secondly, the filtered images obtained by the NanoESCA have to be corrected for an intrinsic energy dispersion over the image ΔE. In a given field of view, as a function of position along the vertical plane, non-isochromaticity occurs, as outlined by Zagonel *et al.* [217]: each filtered image does not correspond to photoelectrons having a kinetic energy E, but $(E+\Delta E)$, where ΔE is calculated to be:

$$\Delta E=E_p\left(\frac{M_1 y_0}{f}\right)^2\ , \tag{2.24}$$

where M_1 is the first lateral magnification of the microscope in the image plane in front of the analyser, and y_0 is the distance between the line of the image considered and the line where the minimum in dispersion occurs in the field of view. f is the focal length of the extractor voltage, which is 29 mm in our NanoESCA instrument [201].

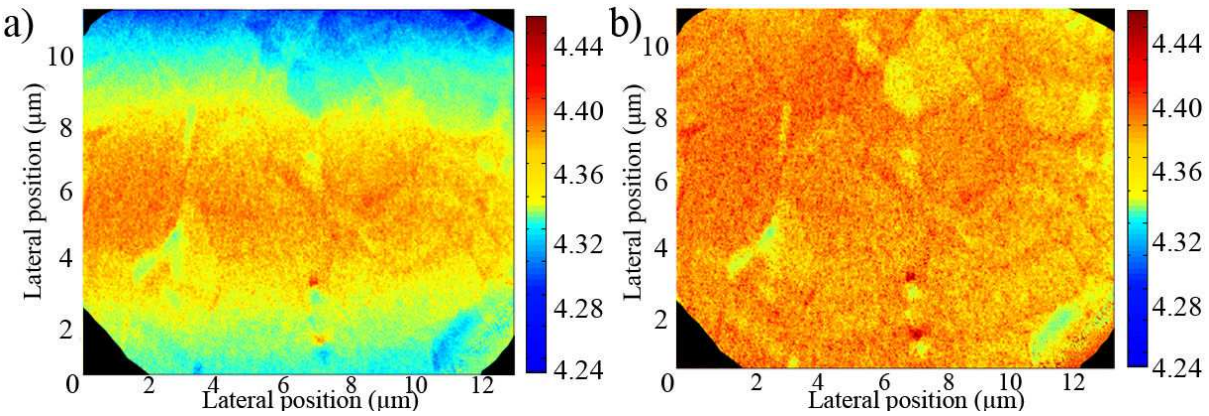

Figure 2.24: *Work Function mapping of copper surface: a) from image series non corrected for the dispersion in energy and b) from image series corrected for the dispersion in energy. Field of view: 15 µm.*

To correct this energy spread inside the energy-filtered images, a MATLAB routine was developed. The extraction and fit of the local spectrum are then performed for each pixel of the image in order to determine the local work function. Thus, we are able to map the work function within the field of view chosen to realize the image series [218]. This correction efficiency is clearly seen in figure 2.24: in a) the work function values extracted from both top and bottom regions are lowered due to the non isochromaticity of the image stack, giving wrong information about the surface. After correction, as presented in b), it is possible to compare any area of the field of view without error. This process will be of prime importance in our studies on doped silicon patterns at threshold to highlight work function trends.

2.3.3 Core-Level imaging

CCD noises and pre-process steps CCD sensors directly produce images with a good sensitivity in digital format, suitable for immediate computer processing. A good compilation of the principles of a CCD has been realized by the Class of Physics of the Royal Swedish Academy of Science [219]. Since we consider electronic image sensors, noise is present and deteriorates the images. It is necessary to ensure that the signal-to-noise ratio is sufficient to allow capture of accurate image information.

The three sources of noise in a CCD imaging system are dark noise, read noise and photon noise, all of them must be considered when preprocessing image stacks. See chapter 7 of the book written by James Janesick [220] for a detailed overview of these factors. In a few words, we can define each noise and give the protocol to remove them:

- During the exposure, a parasitic thermal signal consisting in an accumulation of electrons generated at the level of each pixel is created. This signal is called *dark signal* since it can be observed even when the sensor is in total darkness. The principal consequence of the dark current is a noise added on the image, proportional to the square root of the thermal signal. To remove this noise, it is necessary to acquire several images in darkness with an exposure time equal to the one used to acquire the image series to be processed. Then, one has to average them, hence obtaining an image of this dark signal. The correction of this noise on the image series is made by a simple subtraction.

- There is also nearly constant offset signal added to the image, independent of the integration time. It changes the true intensity levels, rendering for example a black object into gray level on the image. This *offset* is induced by the CCD output amplifier and video electronics features. It can easily be determined by averaging several images acquired with a minimum integration time in darkness. This noise is eliminated by subtracting the offset image from the images to be processed.

- The CCD pixels do not all have the same sensitivity to the light. Hence, if the detector is illuminated with an uniform source, the resulting image will not be necessarily uniform. This non-uniformity to light corresponds to local fluctuations of the pixels gain. This effect can be corrected by dividing the acquired images by the image of an uniform field. The resulting image is called the *flat-field*.

Core-level imaging Since core-level images can have a lower SNR than SE imaging, it is usually necessary to acquire several series in the same range of kinetic energies. Thus, the addition of images with the same energy improves the SNR. For all the core-level images obtained, specially for the lateral resolution measurement presented on subsection 2.4.4, we defined a protocol during this thesis to process the images in order to extract the maximum of information from this energy filtered image series: due to the non constant offset of the CCD used, we just have to remove the dark noise from our single images by a simple subtraction, and then dividing them by the non uniform flat field taken out of focus. Hence, after correcting these preprocessed images for photoemission background measured on either side of the peak considered, we are able to obtain true XPS imaging coming from a core-level such as those presented in figures 2.25 and 2.26 corresponding respectively to the Ge $2p_{3/2}$ and the Si $2p$ transitions.

This is the strength of the energy-filtered technique: contrast in core-level imaging brings chemical informations about the surface. Figure 2.26 presents an example of silicon doped patterns imaged at the Si $2p$ transition with a synchrotron source at 160 eV. Extracting photoemission spectra from different zones of a full core-level image series allows determination of the local variations in XPS spectra.

In this figure, the difference in spectra shape clearly appears as a function of the doping type: though the oxide component corresponding to the peak towards high binding energies is similar, the Si^0 peak shifted 4 eV towards lower binding energies is different between the p-doped zone represented in red and the n-doped zone represented in green. A contrast in the image series presented below the spectra is visible on the two doped zones, specially at lower binding energies, in the vicinity of the Si^0 peak. This reveals

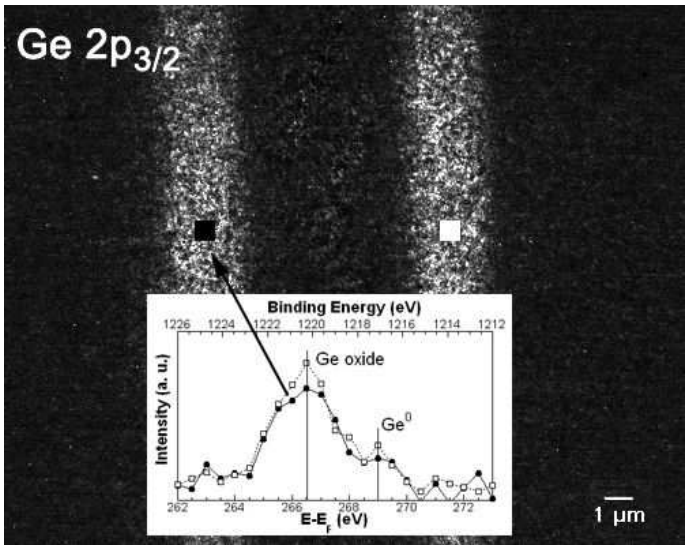

Figure 2.25: *XPEEM image obtained over the peak of the Ge $2p_{3/2}$ peak after standard Shirley background subtraction [221].*

doping dependent variations of the native oxide thickness: the signal substrate is more attenuated over the P zone than over the N^+ zone, which suggests that the native oxide is more important on low p-doped region.

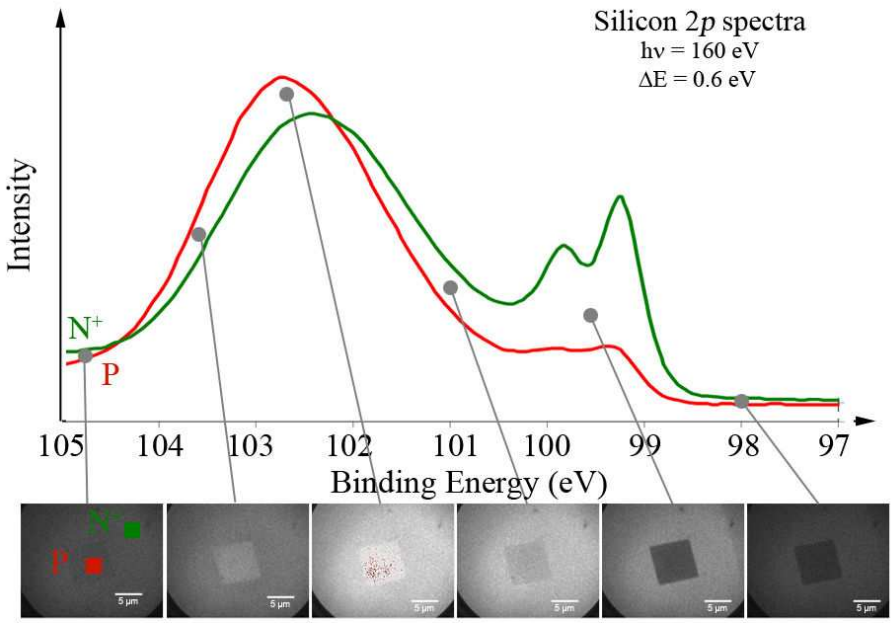

Figure 2.26: *Contrast on Si 2p core level imaging of highly n-doped patterns on p-doped substrate. The oxide thickness is function of the doping.*

We can go further in the estimation of the native oxide thickness depending on the doping type and concentration. A study performed by de la Peña *et al.* on the core-level image stacks acquired by Barrett [101] shows that the depth distribution of the silicon sub-oxide as a function of the doping can be extracted pixel per pixel [222].

It is thus possible to map each oxidation state within the field of view, as can be seen in figure 2.27. We can also extract the oxide and sub-oxides thicknesses for each pixel of the whole image stack. In such case, thanks to the full capabilities of the spectromicroscopy, it is possible to probe the silicon structure at the SiO_2/Si interface, specially their distribution over pn junctions. The Si 2*p* spectra is extracted pixel per pixel, fitted iteratively with a five components model which will be detailed in chapter 3. This analysis helps in deducing the variations in the thickness of the different oxide layers on micron scale silicon doped patterns.

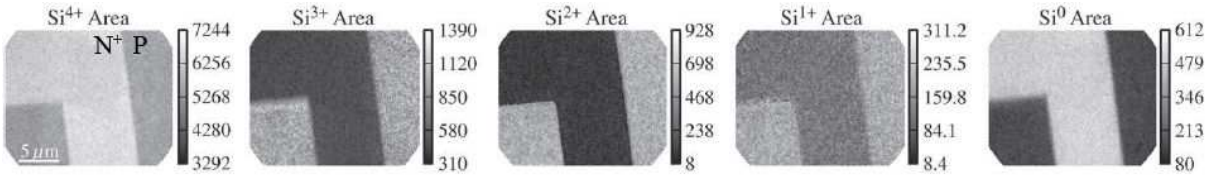

Figure 2.27: *Silicon sub-oxide peak area maps obtained from best fits to the Si 2p spectra generated from the highly n-doped zone on p-doped silicon bulk [222].*

2.4 Improvement of state-of-the-art spatial resolution with core-level laboratory XPEEM

2.4.1 Introduction

The aims of this experiment were to:

- Improve a measurement protocol dedicated to core-level imaging in laboratory. It includes to take into account and remove numerical noises due to the CCD, to increase counting statistics, as seen in section 2.3.3.
- Improve the best lateral resolution measurements obtained in laboratory with an energy-filtered PEEM.

Factors which have to be taken into account to improve the best lateral resolution are numerous: they concern not only the instrument itself, but also the sample to be studied. We have already mentioned the physical and electrical topographies which play an important role for imaging with high resolution: the less the topography, the better the resolution. Moreover, the use of X-ray sources delivering high photon flux induces image blurring: Locatelli *et al.* have reported a degradation of more than 50 nm on both core-level and secondary electron images acquired with an energy-filtered PEEM, for a photon flux of 2.10^{13} photons.s^{-1} [223].
The lateral resolution is also limited by the aberrations of the objective lens, which, contrary to the IDEA system, are not compensated.
The predominant aberrations depend on the photon energy range used for excitation:

- For UV-PEEM, the most important aberrations are the chromatic and spherical ones of the accelerating field between the extractor lens and the sample.

- For X-PEEM, one has also to take into account the chromatic and spherical aberrations of the focusing lenses.

These aberrations have been detailed in subsection 2.2.2.4. Different approaches exist to reduce them in electron microscopes. We can quote as examples: electron mirrors, Wien filters, or multipoles [224] but also electrostatic correctors [225]. Schönhense [226] summarizes the available ways for aberration correction and gives at the same time another approach, based on the use of time structure of pulsed excitation radiation.
With the NanoESCA, obtaining a ultimate lateral resolution implies:

- A well adapted and dedicated sample, with low electric and geometric topographies,
- Increase the extractor voltage up to 15 kV,
- Reduce the contrast aperture diameter to 30 μm if the signal-to-noise ratio allows,
- Optimize the astigmatism correction,
- Minimize and account for the image background intensity which can decrease the image contrast for core level acquisition, thus hiding the smallest objects and limiting the measured resolution [212],
- Improve the counting statistics thanks to high MCP voltages, and accumulate several image series.

Before optimizing these parameters, it is important to understand the definition of lateral resolution, and to review the measurements already obtained with energy-filtered PEEM.

2.4.2 Lateral resolution measurement

There are different methods to measure lateral resolution [227]:

- The straight edge method, suitable for instruments where the lateral resolution is expected to be larger than 1 μm,
- The grid method, suitable if the lateral resolution is expected to be less than 1 μm but more than 20 nm,
- The gold-island method, suitable for instruments where the lateral resolution is expected to be less than 50 nm.

Following ISO standards 18115:2001 and 18516:2006, the resolution can be defined as the distance over which the signal has changed from 12 % to 88 % of its maximum value. With this definition, the signal can be modeled as the convolution of an ideal step function with a gaussian function $exp(-x^2/2\sigma^2)$ representative of the NanoESCA transfert function [102]. The lateral resolution is taken to be the gaussian function FWHM, which is 2.35 σ. Another possibility to test lateral resolution is to use new type of certified reference material for length calibration, such as the BAM-L200 composed of epitaxially grown layers of $Al_xGa_{1-x}As$ and $In_xGa_{1-x}As$ [228, 229]. It provides a pattern with square-wave gratings and isolated strips.

Table 2.1 summarizes the different lateral resolution measurements as a function of the photon energy, obtained with the NanoESCA. We have already presented the lateral resolution obtained with the FXS source in laboratory. Note that core-level Ga $3d$ measurements using the synchrotron radiation at 400 eV were performed on the BAM-L200 sample, as were the secondary electrons with a laboratory UV source.

Wavelength range	Photon source considered	Lateral Resolution	Reference
UV	Hg = 4.6 eV	35-40 nm	[127]
X	AlKα_1 = 1486.7 eV	650 nm	[230]
SR	400 eV	150 nm	[201]

Table 2.1: *Lateral resolution measurements with the NanoESCA depending on the photon source considered.*

Even with synchrotron radiation, there are still a very limited number of published studies reporting on the use of XPEEM for true core-level imaging using band-pass energy filters [101,222,231,232]. This indicates the difficulty of core-level imaging at high lateral and energy resolutions. Hence, we improve high lateral resolution on core-level images on the NanoESCA with the laboratory X-ray source by defining a protocol presented below.

2.4.3 Improving the lateral resolution

Lateral resolution measurements have been performed on a sample made of cross-sectioned epitaxial Si/SiGe layers.
A method for correcting astigmatism of an electron emission spectromicroscope has been developed and a patent has been registered [233]. It applies to samples which do not have on their surface symmetrical patterns to help astigmatism correction. This was the case for the Si/SiGe layers, as can be seen in the top image of figure 2.28 a) and b).

The first step consists in making a reference pattern in the vicinity of the area of interest, as can be seen in figure 2.28 with, for example, FIB. The instrument must be itself corrected for astigmatism defects so as not induce distortions in the reference structure. The shape, size and almost nature of material of this pattern are determined depending on several parameters whose some are listed:

- The shape must be symmetrical, either round or square. The topography of the deposited pattern must be as flat as possible, less than 20 nm if possible, to avoid possible distortions of the images. A SSRM study has been necessary to determine the best parameters in terms of depth and diameter for milling and depositing, as presented in figure 2.28 c).

- The material choice for the reference structure must enable firstly contrast at threshold. Moreover, for core-level imaging, one of its constituent elements must have a high photoionization cross-section at the excitation energy of interest. An estimation can be given greater than or equal to around 0.1 Mbarn. If possible the core-level photoelectrons imaged should have a binding energy not too far from the core-level of the pattern of interest. This, in order to correct astigmatism in the same energy range.

- Depending on the lateral resolution expected, which depends itself on the XPEEM configuration, the reference structure size and shape are chosen: the distance between the different portions of the reference structure and their width may be greater than or equal to around two times, or between around 1.5 times and 2.5 times, the best spatial resolution of the spectromicroscope during an observation of the structure of interest.

- The reference structure on the sample must be deposited near the structure of interest. However, the distance must be greater than 100 μm from the structure, to avoid any deterioration or contamination of it when depositing the material.

In our case, tungsten patterns have been chosen since their work function is different from the silicon bulk one: 4.55 eV against 4.85 eV. Figure 2.28 a) shows the contrast in PEEM imaging of such reference structure on silicon bulk at threshold. Moreover, its core-level W $4f$ has a high photoionisation cross section at 1486.7 eV ($\sigma_{W_{4f}}$=0.15 Mbarn), though the binding energy is low, around 33.6 eV, which degrades the NanoESCA transmission.

The second step consists in correcting the astigmatism aberration at threshold, using the SE signal. We first optimize instrumental settings such as focus voltage, deflection, and then improve the instrument astigmatism correction thanks to the reference patterns dropped on the sample surface. Since a variation in diameter of the field of view appears when changing the photoelectrons kinetic energy, it is important to calibrate the pattern size at threshold.

The last step is dedicated to correct the astigmatism aberration on the reference pattern at core-level, using the correction determined for the nearby reference pattern, before imaging the pattern of interest.

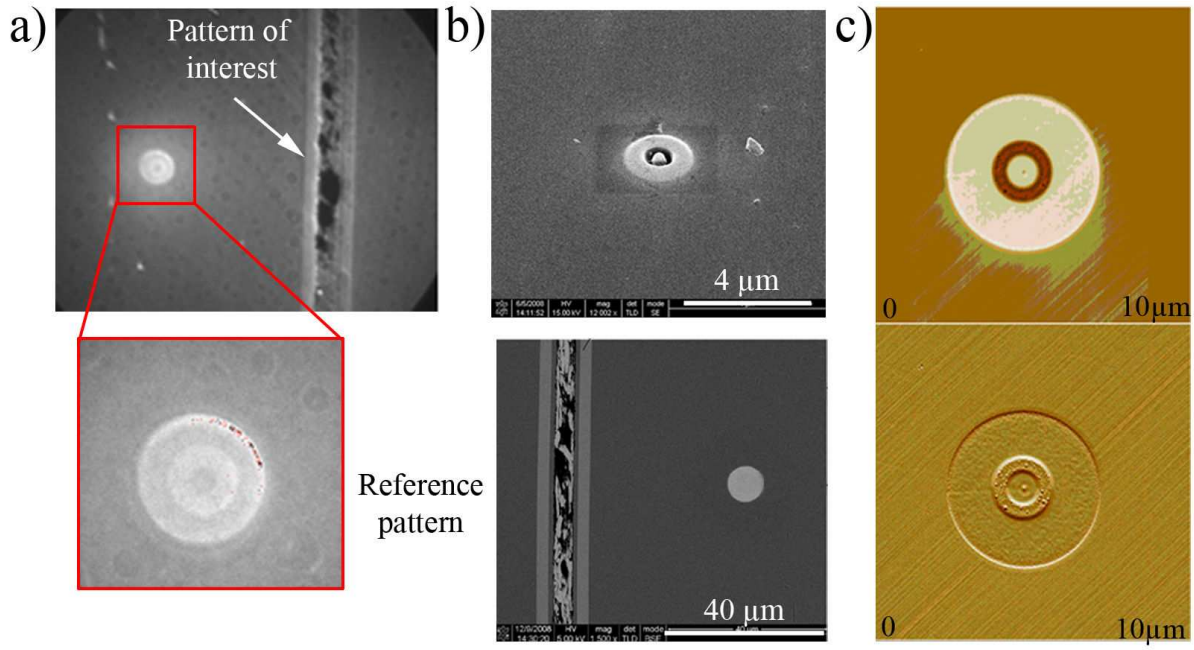

Figure 2.28: *W pattern realized by FIB and observed by: a) Energy-Filtered PEEM, b) SEM, c) AFM.*

For both threshold and core-level imaging, the astigmatism correction is realized by changing the focus and observing the deformation of the imaged pattern. An alternative for astigmatism correction is presented for electron microscopes in the patent [234].

2.4.4 Results achieved with an AlKα laboratory X-ray source

To improve lateral resolution, it is necessary to select core-levels with a low kinetic energy, thus to increase the transmission. This is why our choice was to image Ge $2p_{3/2}$ core-level of cross-sectioned epitaxial Si/SiGe layers.

The first step is to acquire images at threshold. After calibration of the field of view, we can determine the size of the structure which will help in the quantitative of core-level imaging. The results on lateral and energy resolutions on cross-sectioned epitaxial Si/SiGe layers are presented at threshold in figure 2.29 a). This cross-section was imaged with a photoelectron energy of 266.4 eV referred to the Fermi level of the sample, which corresponds to the Ge $2p_{3/2}$ transition [221] in figure 2.29 b). In this experiment, the PEEM objective lens was set to 15 keV, and images were acquired with a double hemispherical analyser pass energy of 125 eV, and the entrance slits width of 1 mm.
Despite an elemental contrast of only 50 %, XPS imaging performed by this mean had an edge lateral resolution of (477 ± 110) nm and an energy resolution of 0.56 eV. This result is the best ever obtained in XPS imaging [91, 235]. It constitutes an improvement of nearly one order of magnitude with respect to existing laboratory data.

The experimental result obtained has the same order of magnitude expected theoretically from the contrast aperture diameter expressed in nanometers i.e., 500 nm [236].

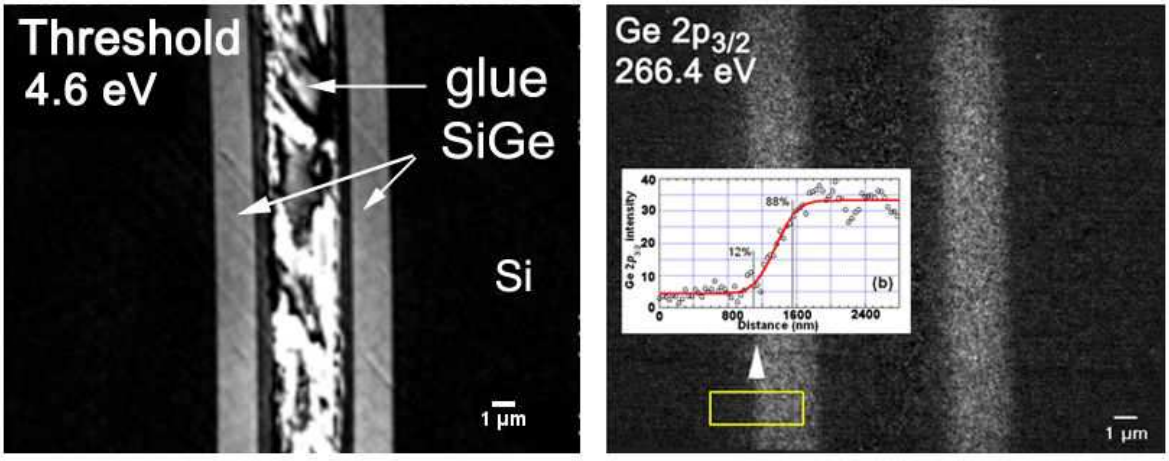

Figure 2.29: *a) Cross-sectioned epitaxial Si/SiGe layers imaged at threshold [221]. b) Single energy of the SiGe layers at 266.4 eV corrected from photoemission background. Inset: intensity profile extracted from the region marked on the image. The fit of the experimental profile is performed with a complementary error function and is displayed in red [221].*

2.5 Conclusion

Spectromicroscopy is a unique tool for spatially and energy resolved electron spectroscopy on the micron scale. Full-field imaging spectromicroscopy is a non destructive technique which enables spectroscopic measurements with high lateral and energy resolution. Energy-filtering provides information on the local chemical and electrical properties of the surface, using secondary, core-level or valence band electrons.

The NanoESCA is a state-of-the-art of energy-filtered XPEEM instrument. Its main characteristics are its double hemispherical analyser as energy filter, whose geometrical and chromatic aberrations are compensated by the system configuration. Moreover, its relatively high transmission factor over a wide range of photoelectron energies makes its particularly suitable for XPS imaging. Its complementary operating modes in synchrotron and laboratory environment make it particularly interesting to observe samples in both sources environments. Thanks to a patented protocol, we are able to correct the instrument for astigmatism aberrations. This has led to an improvement of the lateral resolution on core-level images obtained with a high intensity optimized Al K_α X-ray source, reaching a state-of-the-art measurement in laboratory environment down to (477 ± 110) nm with an energy resolution of 0.56 eV.

The full spectromicroscopic potential of the NanoESCA makes it an ideal instrument for studying the physics governing the contrast in PEEM images of silicon pn junctions. The results are presented in the following chapters.

Chapter 3

Patterned doped silicon samples by localized epitaxy

Contents

At the origin of our work is a previous study using energy-filtered PEEM which was led on n-doped patterns on a p-doped bulk, and p-doped ones on a n-doped bulk, both covered with a native oxide. Quantitative band alignments were extracted from the different zones of these samples [101].
We deepen this study, using the same kind of samples, but bringing also some improvements in terms of pattern technological choices and surface cleaning. Our objective was to use dedicated silicon samples which allow better understanding of their flat band electronic structure by exploiting the full capabilities of the energy-filtered PEEM.

The first section introduces the basis of photoemission in silicon for the understanding of our interpretations in chapter 4. The second part deals with the sample definition and preparation. Obtaining flat band conditions requires removing the native oxide from the

sample surface. The last section reviews the passivation study performed on silicon doped samples.

3.1 Framework for XPEEM studies: photoemission in silicon

In energy-filtered XPEEM, spectroscopic XPS imaging is performed. The image contrast of patterned semiconducting surface governed by the relative XPS intensity at a given photoelectron energy is highly dependent on the relative position of the electron energy levels. In order to understand the experimental results presented in chapters 3 and 4, we recall the characteristic features of photoemission from silicon surfaces.

3.1.1 Flat band conditions and band bending

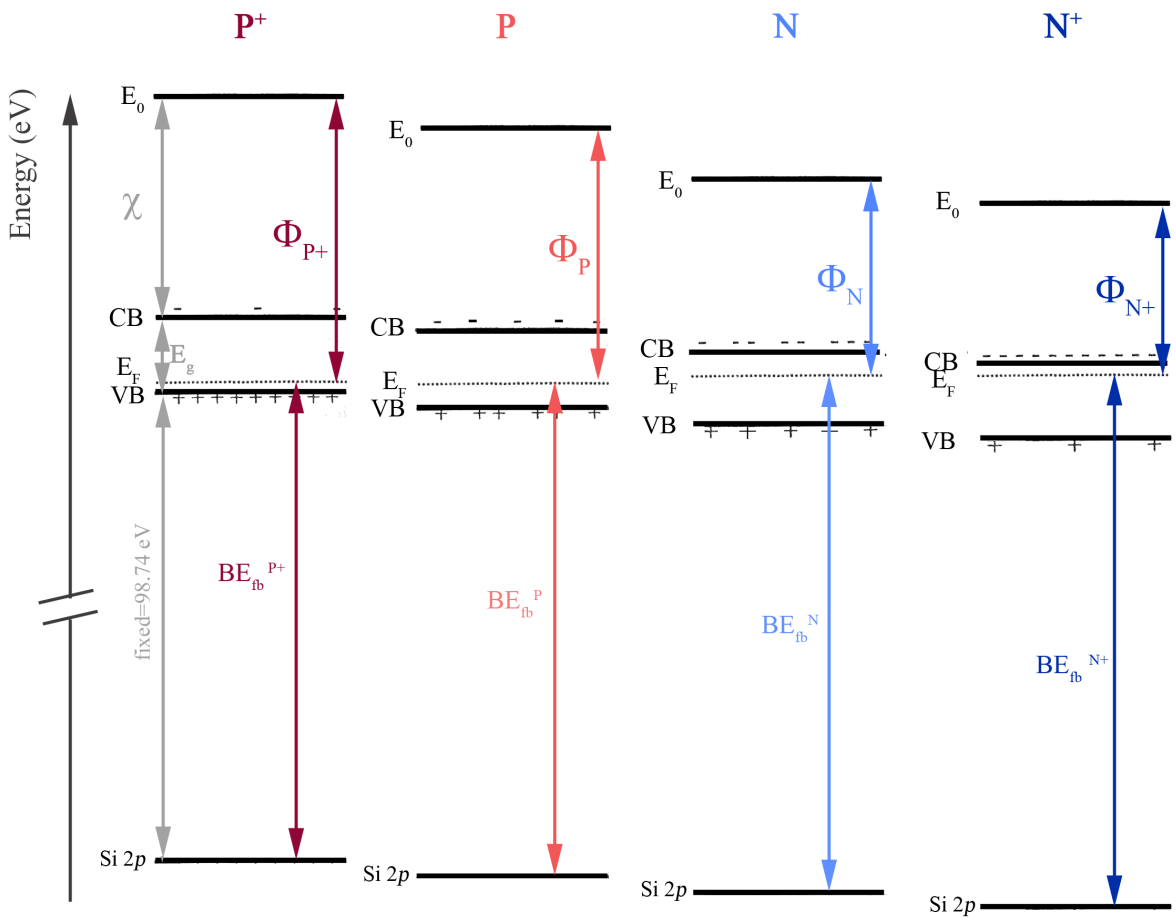

Figure 3.1: *Schematic representation of band structure for different doping types.*

Flat band conditions The general electronic band diagram at the silicon surface is given in figure 3.1 a): the conduction band (CB) and the valence band (VB) are separated

by an energy corresponding to the silicon bandgap E_g equal to 1.12 eV at 300 K. The energy between the conduction band and the vacuum level E_0 is the electronic affinity χ which is 4.05 eV for silicon.
The Fermi level E_F for a doped silicon sample is defined regarding the intrinsic Fermi level E_{Fi} of the matrix (not represented in figure 3.1), and the carrier density N_d concerning the electrons and N_a concerning the holes:

$$E_F^{doping} = E_{Fi} + kTln\left(\frac{N_d}{n_i}\right) \text{ , for the n doped zone} \tag{3.1}$$

$$E_F^{doping} = E_{Fi} - kTln\left(\frac{N_a}{n_i}\right) \text{ , for the p doped zone.} \tag{3.2}$$

where k is the Boltzman's constant, n_i is the intrinsic carrier concentration for silicon (1.4×10^{10} atoms.cm^{-3})and T is the temperature.
The core-level binding energy BE_{mes} corresponding to Si $2p$ transition is thus given by the energy between the Fermi level and the core-level, as presented in figure 3.1. The energy difference between the valence band maximum (VBM) and the core-level Si $2p$ is fixed at 98.74 eV. This situation is described as flat band conditions, the effect of the surface state on the band line-up has not been considered.

Band bending Charges in surface or interface states cause an electrostatic potential that bends the bands near the surface, as schematically represented in figure 3.2 in case of patterned silicon surface. A number of surface of interface states in the gap to about 1/1000 of a monolayer is sufficient to induce band bending [237].

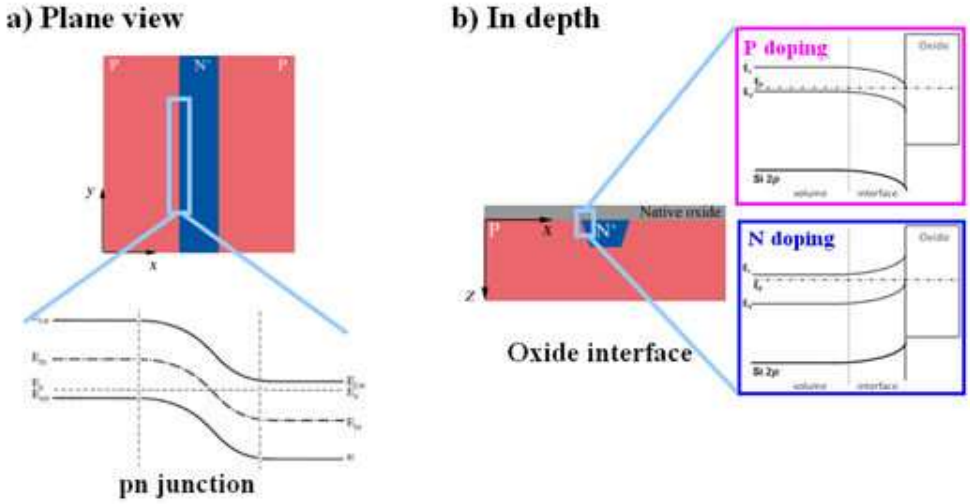

Figure 3.2: *Band bending and band lineup represented schematically on the two views: a) plane view (x,y) and b) in depth (z).*

Studying the electronic structure of doped silicon patterns consists in determining the band alignments as a function of the position within the pn junction. However local variations in depth of band bending have also to be taken into account: they are called *band lineup*. This implies to consider the problem of band bending in 3D: when observing

the band bending at the interface of a pn junction, as illustrated by figure 3.2, below the surface oxide in the plane (x,y), it is necessary to include this band bending variation at the oxide/semiconductor interface in the plane (z).

Figure 3.3 takes into account the band bending direction and strength at the silicon surface due to localized surface or interface states, which depends on the doping type and level:

- This band bending is upwards for N- type doping, and downwards for P-type.
- The magnitude of the band bending depends on the doping concentration: the higher the doping, the stronger the band bending, and the smaller the depletion width.

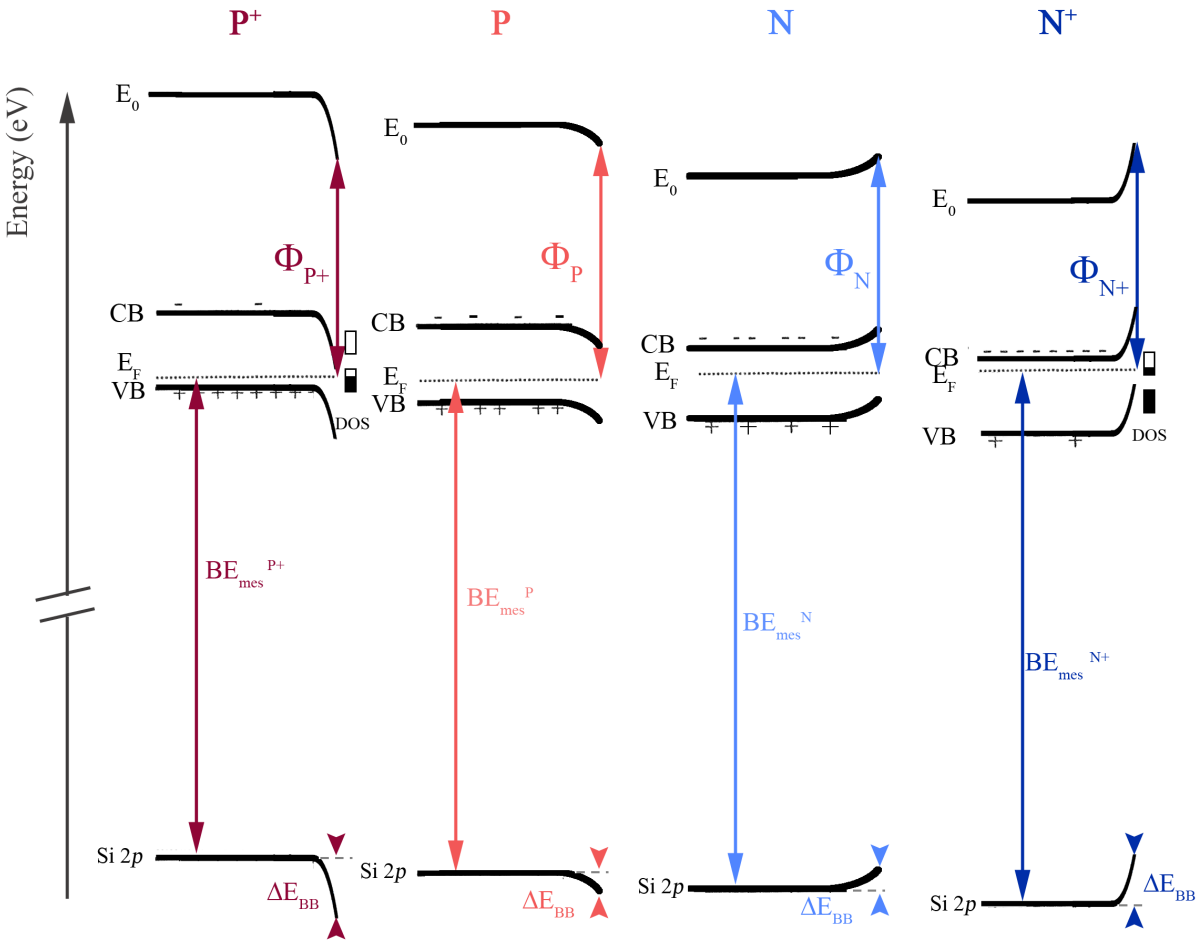

Figure 3.3: *Schematic representation of band structure for different silicon doping types with band bending. For the two extreme cases P^+ and N^+, the surface Density of States (DOS) is schematically represented.*

Referring to the electronic band structure for silicon mentioned in figures 3.1 and 3.3 we will now present more in detail what happens in terms of work function and core-level binding energy variations for ideal flat band case and experimental case.

3.1.2 Work function and core-level studies

Work function Theoretically, the work function ϕ_{Si} can be calculated thanks to the following equation:

$$\phi_{Si} = \chi_{Si} + E_F^{doping} \ , \tag{3.3}$$

where χ_{Si} represents the silicon electron affinity (4.05 V), E_F^{doping} is the Fermi level position depending on the doping level and type, as defined in equations 3.2 and 3.1 for respectively p-doped and n-doped silicon, with respect to the conduction band.

Figure 3.1 helps in understanding the influence of doping type on work function measurements, for different silicon doped samples in theoretical flat band conditions. We observe a shift in the values which depends on the doping type and level, since it depends on the Fermi level position within the gap. The expected ranking for the work-function values in flat band conditions is as follows:

$$\Phi_{P^+} \geq \Phi_P \geq \Phi_N \geq \Phi_{N^+} \tag{3.4}$$

Considering band bending of the electronic levels on the sample surface as presented in figure 3.3, the work function measurement is modified. Since it depends on the band bending magnitude, work function shifts due to differences in terms of doping concentration and type can be strongly attenuated, even inverted, with respect to theoretical flat band case.

And thus, the ranking of the work-function values mentioned in 3.7, can be modified in presence of band bending at the silicon surface:

$$\Phi_{P^+} \leq \Phi_P \tag{3.5}$$

and

$$\Phi_{N^+} \geq \Phi_N \tag{3.6}$$

To conclude, the exact ranking of the work-function will depend on both the doping level and the degree of band bending.

Core-level binding energies In flat band conditions, the Si $2p$ core-level energy is measured relative to the Fermi level, and thus, is shifted with the sample doping type and concentration in the following rank:

$$BE_{fb}^{P^+} \leq BE_{fb}^{P} \leq BE_{fb}^{N} \leq BE_{fb}^{N^+} \tag{3.7}$$

It depends on two terms: the fixed reference energy between the valence band maximum and the Si $2p$ core-level (equal to 98.74 eV) and the quantity (E_F-E_{VBM}) known from bulk doping and inducing the Fermi level movement since it depends on the doping level and type.

When considering band bending due to interface states ΔE_{BB}, and measuring the binding energy of a core-level photoelectron BE_{mes}, its value can be inferred from a relation linking this binding energy BE_{mes} with several factors:

$$\Delta E_{BB} = BE_{mes} - \Delta E_F^{doping} - \Delta E_{SPV} \ , \tag{3.8}$$

where ΔE_F^{doping} is the binding energy of the Fermi level depending on the doping type and level considered (see equations 3.2 and 3.1), and ΔE_{SPV} is the binding energy shift due to the surface photovoltage introduced in chapter 1.

3.1.3 Objective

Several studies and interpretations of contrast over pn junctions [120, 121, 135, 138, 238] at threshold or at Si $2p$ core-level have already been carried out to characterize silicon doped areas in terms of band alignments and band bending as a function of the underlying doping level and type. Our objective is to use the full spectromicroscopic capabilities of our XPEEM to study the correlations between contrast obtained in core-level PEEM imaging and localised Si $2p$ and valence band microspectra. The interpretation of work function variations but, above all, of core-level shifts at silicon doped surfaces will help in such a reasoning.

3.2 Sample fabrication and characterization

3.2.1 Requirements

3.2.1.1 Technological choices

Planar pn junctions can be fabricated either by implantation or by epitaxy. For XPEEM studies, it is desirable to image well defined planar junctions with the highest possible in-depth doping uniformity (this latter being ideally bigger than the probing depth) and the lowest surface roughness. Although implantation is the conventional way to perform doping, it has intrinsic drawbacks:

- The high temperatures, around 1000°C, required for the activation of dopants induce diffusion of both boron and phosphorus across the junction. This broadens the originally sharp junction. A low thermal budget surface preparation is preferable to avoid significant redistribution of the dopants.

- Ion implantation introduces defects, such as vacancy impurities or clusters, as well as generation and migration of electrically active defects over thousands of angstroms or microns, farther than the projected range of the implanted ions [239]. Studies at ultra low energy ion implantation suggest that it is possible to achieve phosphorus doping of silicon without annealing, but this remains a special case [240].

Contrary to implantation, localized epitaxy does not require significant annealing to activate the dopants. This process is successfully used in the growth of high mobility strained SiGe channels of sub-32 nm MOSFETs requiring a high control of doping. Figure 3.4 shows such results a TEM images of such a device with a 23 % Ge content, by electron holography. The sharp edges between source/drain zones and substrate indicated by the arrows illustrate the high quality of the process, controlled at the decananometric level. The dark-field electron hologram of figure 3.4 c) is an additional evidence of the perfect control of this process.
For all these reasons, we have chosen to focus on silicon patterns fabricated by localized epitaxy. The samples were prepared in the LETI clean rooms at MINATEC.

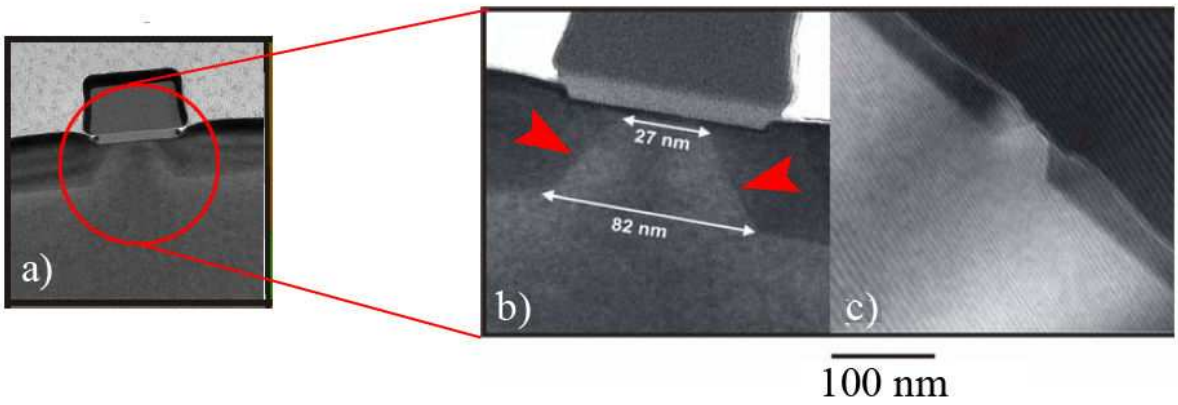

Figure 3.4: *a) High-resolution TEM image of 23 % SiGe CMOS device. b) high resolution bright field image and c) dark hologram of the region of interest [241].*

3.2.1.2 Sample structure and doping choices

We have optimised the choice of both p and n doping concentrations. The objective is to obtain a set of planar homo-junctions (same doping type on both side) and hetero-junction (different doping type) samples with different doping concentrations affecting the depletion width and the electrical field across the junction. Therefore, the requirements are the following:

- To have both bulk p and n doped silicon. For an easier fabrication, they will be slightly doped and named as substrate P and N.
- For the patterns, it is interesting to have strong doping concentrations in order to obtain asymmetric depletion zones on either side of the junctions. These will be in the following named as pattern zones P^+ and N^+.

These considerations lead to four major combinations to realize various pn junctions: P^+/P, N^+/P, N^+/N, P^+/N. They correspond to the schematic presentation in figure 3.5.

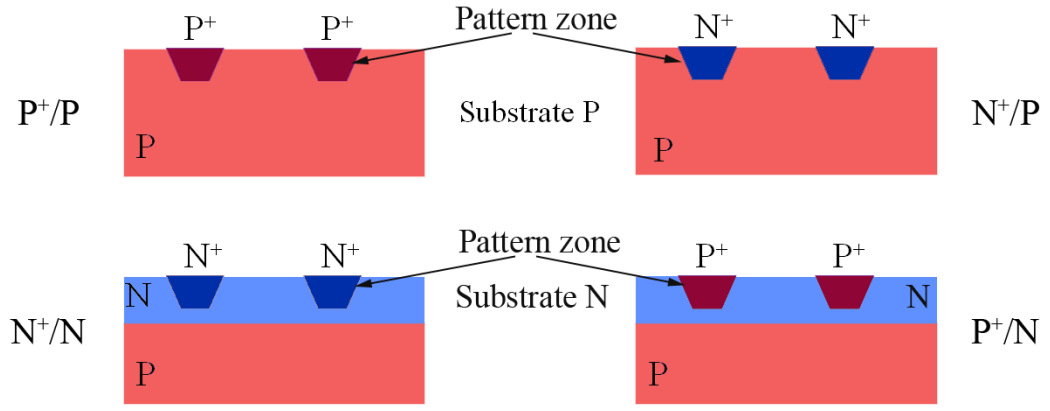

Figure 3.5: *Panel of the different samples realized in this set: P^+/P, N^+/P, N^+/N, P^+/N.*

The second question is the quantitative dopant levels, which have to be chosen with regard to two points:

- The doping levels should be compatible with typical technological requirements.
- In order to quantify the influence of lateral electric fields across pn junctions on PEEM imaging, different field strengths across pn junctions are necessary, of the same order of magnitude as the extractor field, which is 6.6 kV.mm^{-1}.

Several combinations of doping level were tested thanks to a MATLAB program developed in this purpose and calculating several factors based on equations of section 1.2.1. This enabled to evaluate the built-in voltage in the depletion zone, the depletion zone width and the maximal intensity of the electric field across these junctions. Taking into account the localized epitaxy capabilities in terms of dopant concentration, the values chosen for each sample set, either full wafer or patterned samples, and the expected values in terms of factors of interest are presented in table 3.1.

Doping/bulk	Concentration (atoms.cm^{-3})	V_{bi} (V)	Total depletion width (μm)	Electric field maximum intensity (kV.mm^{-1})
P^+/P	$2\times10^{19}/10^{15}$	0.851	1.05	-1.62
N^+/P	$4\times10^{19}/10^{15}$	0.869	1.06	-1.63
N^+/N	$4\times10^{19}/10^{17}$	0.988	0.114	-1.74
P^+/N	$2\times10^{19}/10^{17}$	0.970	0.113	-17.21

Table 3.1: *Built-in voltage, depletion width and maximal electric field across the junction for theoretical doping concentrations of the selected samples of interest: P^+/P, N^+/P, N^+/N, and P^+/N.*

Finally, we wish to analyse contrast in relation with surface properties in quasi flat-band conditions. This underline the necessity of studying samples after a well controlled passivation. Such a point will be detailed in section 3.3 but requires preliminary tests to check this passivation efficiency. For this reason, silicon doped full-sheet wafers have been prepared for each of the four doping types.

3.2.1.3 Fabrication process

The mask The mask for the nanoscaled planar pn junction fabrication (total chip size is (21×21) mm^2) is composed of 46 zones, whose size is (3×3) mm^2. Each zone is dedicated for a certain analysis, and is identified by a number located on their top right. A special zone of (3×6) mm^2 dedicated to SEM observations is one of interest for this work.

The mask is in positive lithography: a line implies the presence of chromium, thus a presence of resin on the wafer. In the SEM zone, two types of structures are present: lines and dots. We concentrate on the lines, which are themselves divided into two groups, the difference being the basis structure, repeated several times, for several line widths:

- a) The line widths L are: 70, 80, 120, 140, 160 and 200 nm. The spacings S are proportional to them: S=L, S=1.5L, S=2L.

- b) The line widths L are: 0.25, 0.5, 1, 2, 5, 10, 20, 40, 80 and 100 μm. The spacings vary between 10, 20 and 40 μm.

Each group of lines was identified by figures and shapes with identical doping levels. They are schematically represented in figure 3.6.

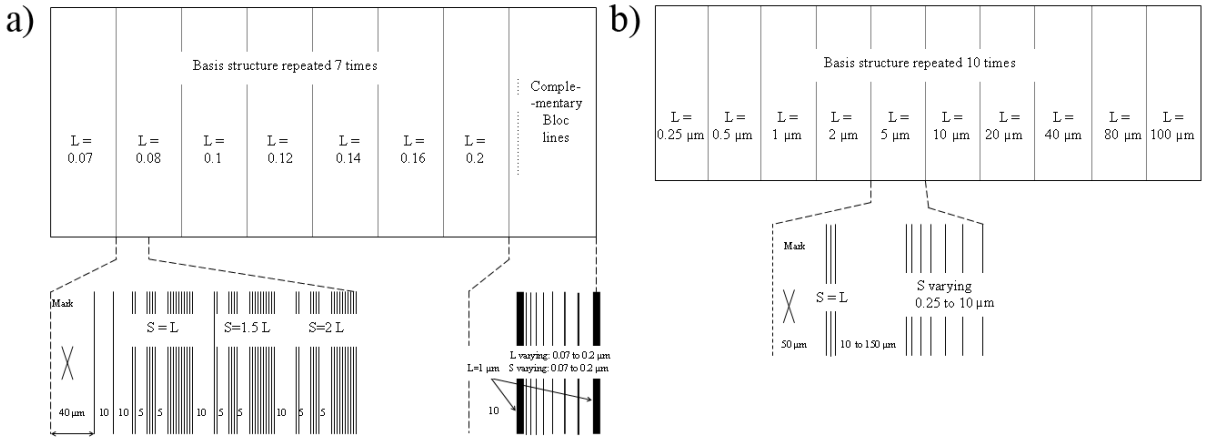

Figure 3.6: *Schematic representation of the patterns a) and b) in the region SEM of interest.*

Sample fabrication The bulk chosen is Si(100) slightly p-doped on 200 mm wafers, with a resistivity of 5-10 Ω.cm. This process is realized inside the 200 nm Epi Centura, Reduced Pressure-Chemical Vapor Deposition (RP-CVD) [242, 243]. For samples where the bulk needed is n-doped, a first epitaxy of 150 nm thick n-type silicon is deposited on the p-type full-sheet wafers.
The organization of the different zones at the wafer surface follow a chess like organisation: only every second chip is observable, the other being etched and then recovered by a thermal oxide, as can be seen in SEM in figure 3.7. This figure shows line structures in cross sections observed under two different angles. The line width equals the spacing width (300 nm).

The fabrication process consists of six main steps summarized here, but visible in detail in figure 3.11:

- The active area is patterned by a Deep-UV photolithography and cleaned by an HF-last wet cleaning at 950°C, in an automated bench that gets rid of native oxide.

- The bulk is then partially etched over 100 nm at 750°C using gaseous HCl in high partial pressure of 180 Torr. This selective etching is realized in the Si active areas and leads to the formation of faceted cavities, clearly visible on SEM, as shown in figure 3.8. Since this etching is isotropic, even silicon under the thermal oxide is laterally etched. This trimming was chosen to reduce the patterns size by 20 nm from each side. Thus, the nominal line dimensions given above need to be corrected.

  The recess cleans the cavities, however some surface defects can remain in the bottom of the cavities, either between patterns, or in the open zone, i.e. the large zone without patterns over distances greater than 500 μm. These latter were observed in

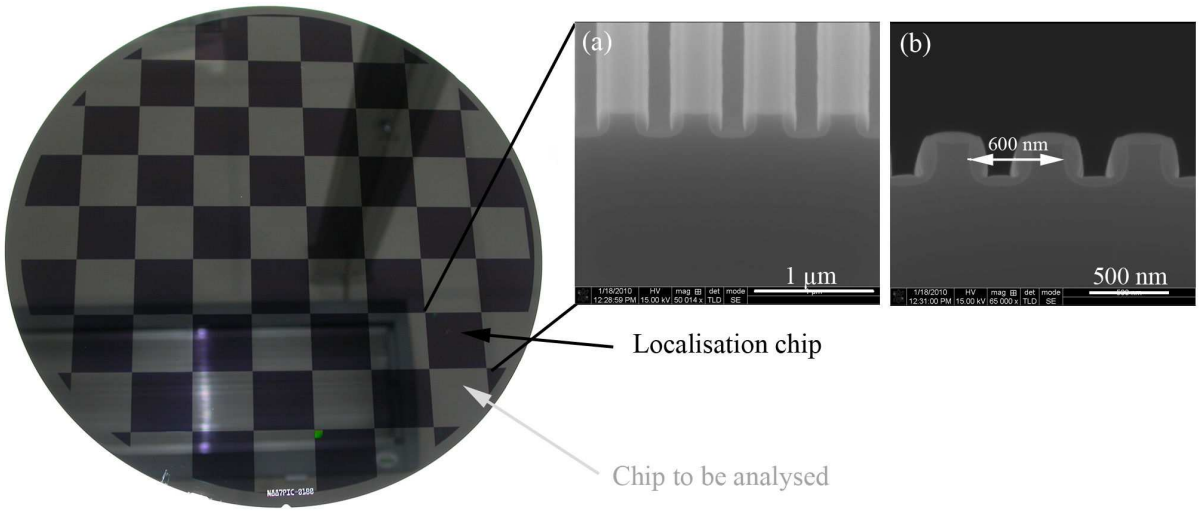

Figure 3.7: *Optical image of a wafer. Onset: SEM images of one cross-sectioned silicon chip used for localisation: one clearly sees the oxide coverage in light gray on a) 45° view, and b) normal observation. S=L=300 nm.*

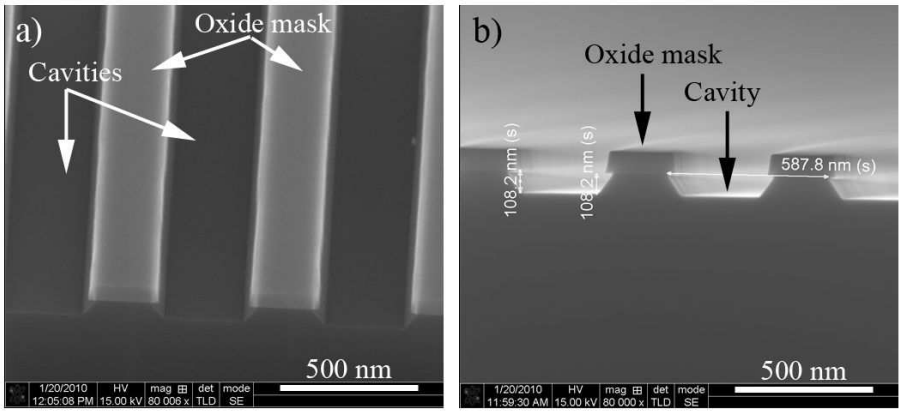

Figure 3.8: *SEM images of cross-sectioned silicon chip after HCl recess: view at a) 45° and b) normal observation.*

SEM shown in figure 3.9 a) and could be organic residuals which have settled after etching. AFM measurement in b 1) gives a roughness of 60 nm at the bottom of the large areas, and the work function contrast obtained in b 2) by KFM confirms that its chemical nature is different from the substrate one. Hence, we have to consider the silicon growth in the cavities could locally cover such defects.

- After patterning, a selective epitaxial growth of around 100 nm of boron-doped and phosphorous-doped silicon is done at 950°C and 20 Torr, in the cavities. Pure dichlorocylane SiH_2Cl_2 is chosen as Si gas precursor. Diborane B_2H_6 is used for p-doped zones, and phosphine PH_3 for n-doped ones. These two gases are diluted in H_2 at 950°C. By varying the mixing, it is possible to obtain a large range of dopant concentrations, as presented by Gonzatti *et al.* [243] who have done four points probe measurements on B and P activated ion concentrations.

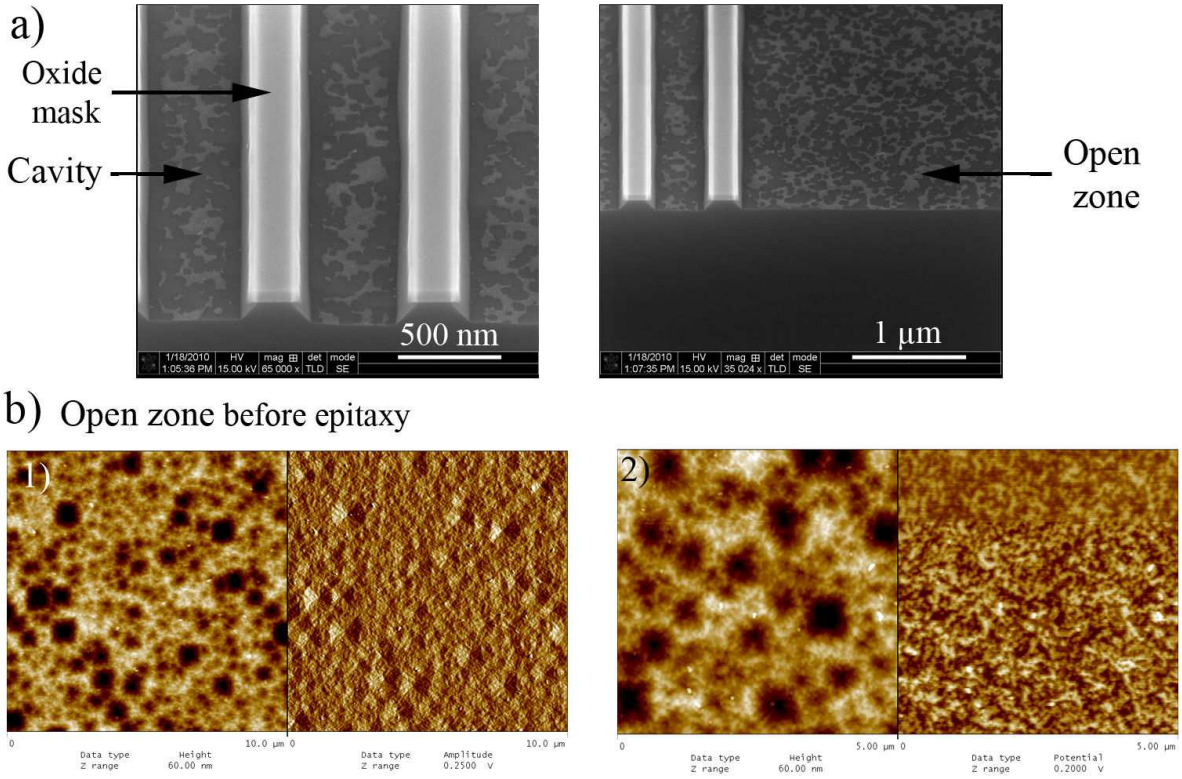

Figure 3.9: *a) SEM images of cross-sectioned silicon chip after HCl recess at 45°. b) AFM images of open zone: 1) amplitude and phase. 2) corresponds to the potential observed in KFM.*

The resulting structure SEM cross-section structure is presented in figure 3.10: the localized epitaxy top is at the same level as the bulk, if the bright lines corresponding to unremoved oxide on the sidewalls from the sample surface are neglected.

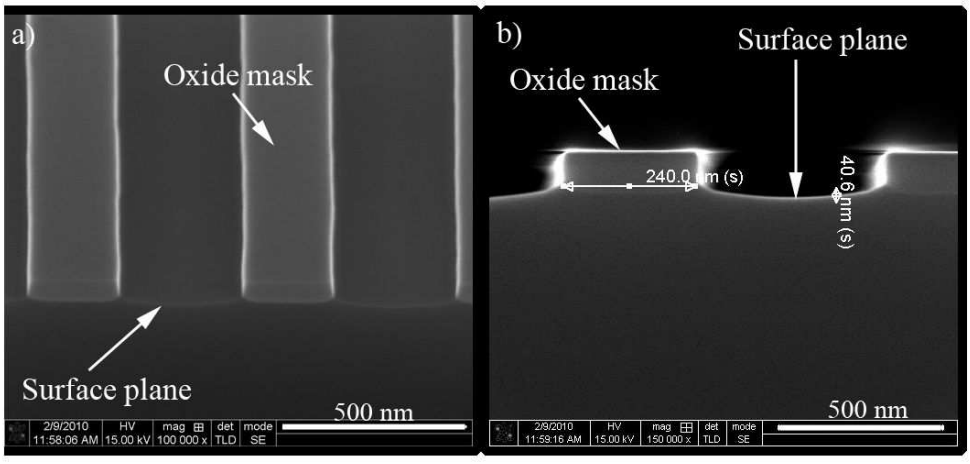

Figure 3.10: *SEM images of cross-sectioned silicon chip after localized boron epitaxy at a) 45° and b) normal observation.*

As mentioned previously, figure 3.11 shows the different steps of the patterned samples fabrication. For the samples with N substrate, a first step is added at the beginning of

this process, consisting in an epitaxially growth of a 150 nm thick N layer over the P wafer.

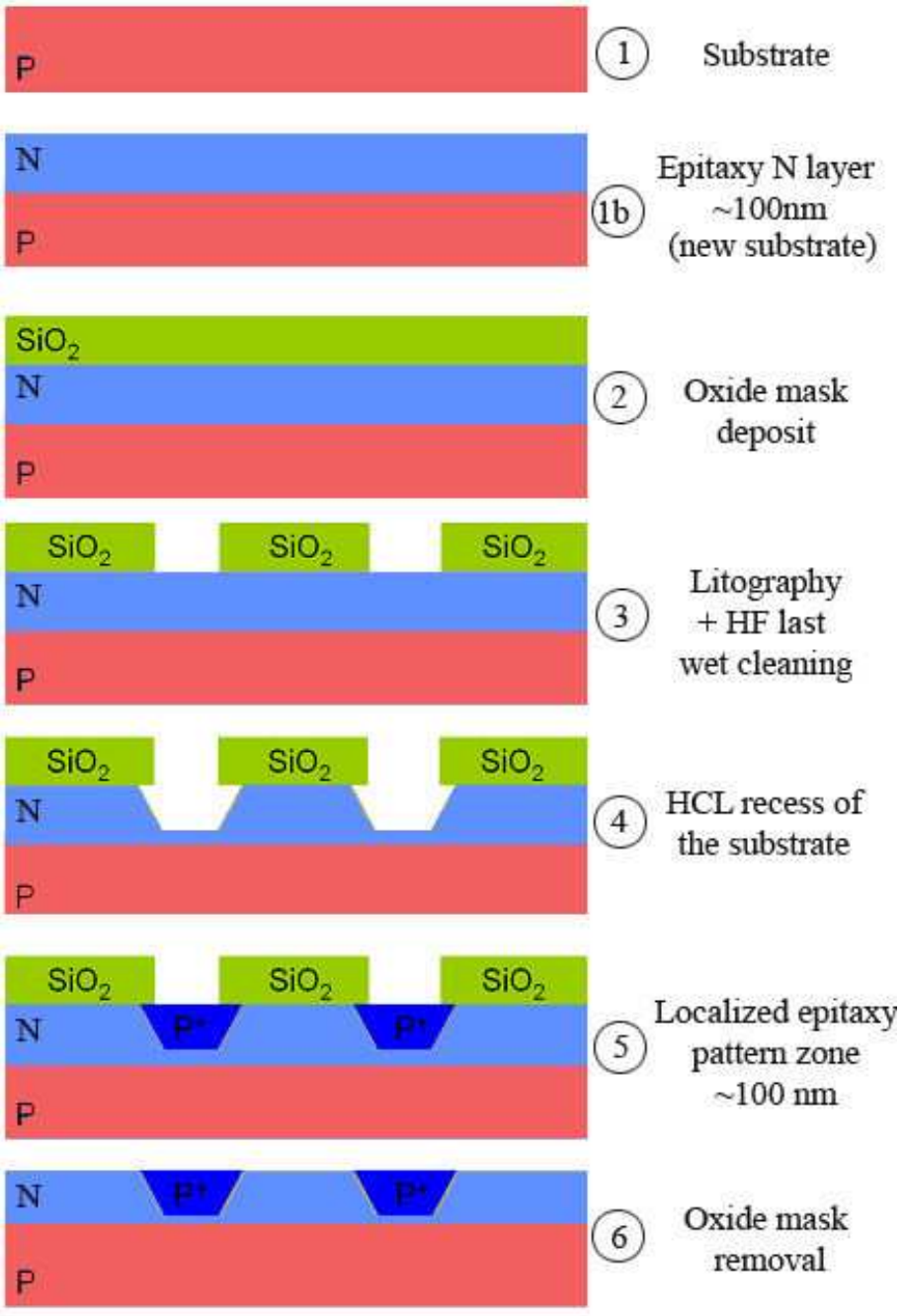

Figure 3.11: *Schematic protocol of the sample fabrication, for samples with N substrate, the step 1b) has to be added in the protocol.*

3.2.2 Characterization

The pn junctions of interest in this thesis are not only simple lines, but also more complex patterns, such as numbers, located next to lines to give their theoretical width, as described. We focused on two numbers: 'zero' and 'eight' because they are numerous on the sample surface and contain both open and closed highly doped areas.

SCM, SSRM, SEM and optical microscopy were performed on the same junctions analyzed by XPEEM with synchrotron radiation. For SIMS and infra-red spectroscopy FTIR, however, the patterns were taken from the same wafers, from chips in the vicinity of the one observed by the other techniques. Hence, the section concerning the effective doping concentration measurements deals with the four sample combinations, the two others, focused on topography, roughness and lateral measurements concern only the junctions: P^+/P, N^+/P and P^+/N observed by XPEEM using synchrotron radiation.

3.2.2.1 Characterization of doping

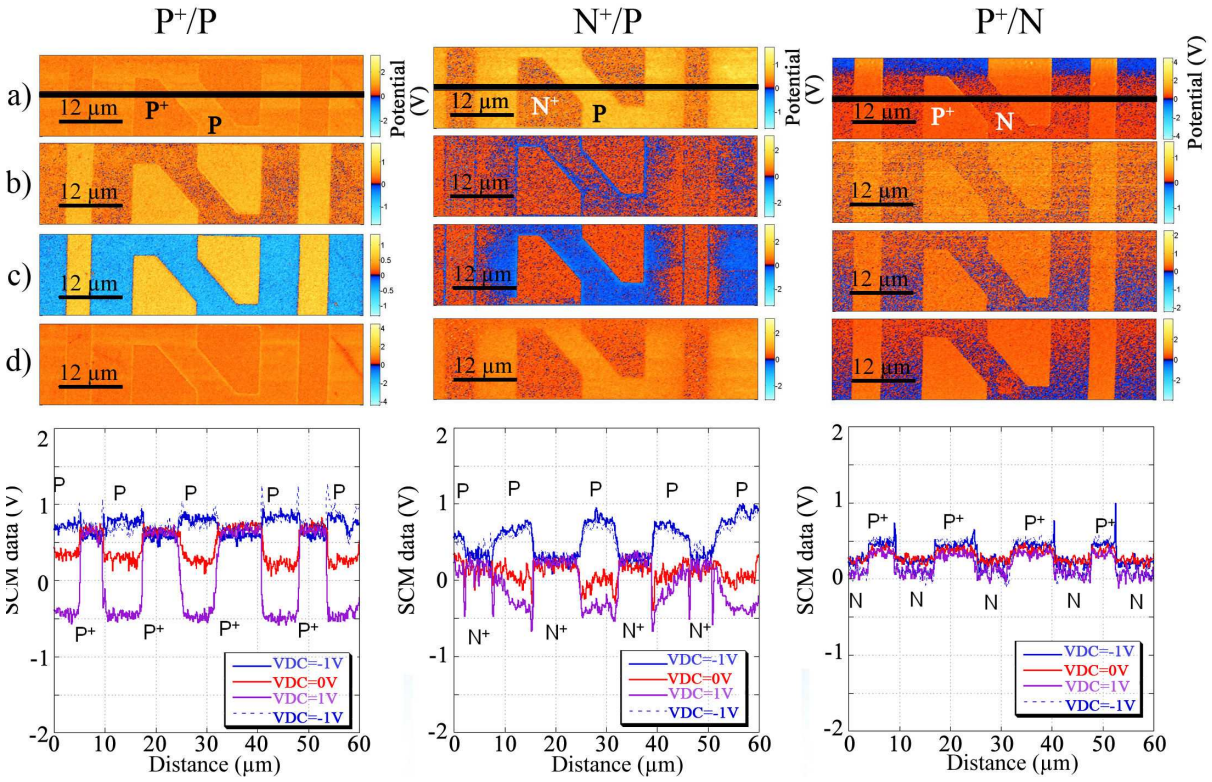

Figure 3.12: *SCM measurements on P^+/P, N^+/P and P^+/N samples. The scans are presented for several V_{dc} values: a) -1 V, b) 0 V, c) +1 V, d) is the return to -1 V. The profiles below are extracted from the zone presented in a).*

Nature of doping at the sample surface AFM in SCM mode can be used to distinguish the carrier type of the patterns. For pn junction imaging, the technique is utilized at constant voltage mode and the alternating current V_{ac} bias voltage applied to the sample is maintained at 1 V. For different values of V_{dc}: -1 V, 0 V, +1 V, the

change in capacitance is recorded as a function of doping and carrier concentration under the tip, at a scan rate of 0.1 Hz. After the V_{dc} sweeping, another scan is done for -1 V to check the reproducibility of the measurements and the absence of charging effects.

Both samples and tip spent one night under dry nitrogen purge before analysis. The results are presented in figure 3.12. For each of them, a section is taken by averaging eleven lines within the thick black line shown in panels a) of figure 3.12.

The results are in good agreement with the localization of the dopants on the samples. The zero corresponds to the bulk.
The measurements are reproducible after V_{dc} sweeping, for P^+/P and N^+/P: this means there is no memory effect of the voltage on the P^+ and N^+ doped areas. For P^+/N, the reproducibility is acceptable, but the SCM signal is lower compared to the data obtained for the two previous samples, evidence that V_{dc} has a small effect on both the P^+ and N doped areas.

Effective doping concentrations in depth uniformity The effective doping concentration was measured on as-prepared silicon doped patterns (i.e. with a native oxidation layer) with a SIMS Cameca IMS-5f instrument. The zone chosen to perform this analysis is not the SEM zone presented previously, but a zone where the doped patterns are series of line of 500 μm wide.
To improve resolution, a 1 keV O_2^+ (Cs^+) primary beam for boron (phosphorus) profiling were used. The primary beam is incident at 45°. Since an oxidized surface improves the silicon ion yield, the observations are performed at a pressure of 3×10^{-6} mbar. The raster area is 200 μm. The spectrometer measured the emission of positive secondary ions clusters from silicon surface. Sputter rate has been determined from depth information of a profiling reference sample to be 0.018 $nm.s^{-1}$. Boron concentration was determined from the Relative Sensitivity Factor relative to ^{28}Si signal at 9.8×10^{22} $atoms.cm^{-3}$. For the phosphorus profiling, a 1 keV Cs^+ primary beam was used.

Figure 3.13 shows the profiles obtained for P^+, N and N^+. The P profile is not represented in figure 3.13, since the doping values were below the instrument detection limit. However, a mean estimation of the surface doping concentration was still possible using the wafer datasheet (electrical specifications of the manufacturer).
For both P^+ and N^+ doping conditions, SIMS measurements show the same order of magnitude as the nominal doping concentrations.

The analysis shows also a non uniform in-depth doping concentrations, specially important for N-doping with a variation of about two decades. This non uniformity is typically the sampling depth in photoemission and XPEEM. Moreover, the major observation is a variation in dopant concentration near the surface that is as yet not fully understood. This non uniformity over the first nanometer can have the following origins:

- a measurement artifact affecting partially the near-surface profile due to an effect of ion-induced roughness.
- residual doping atoms on the Si substrate after epitaxy, perhaps incorporated in

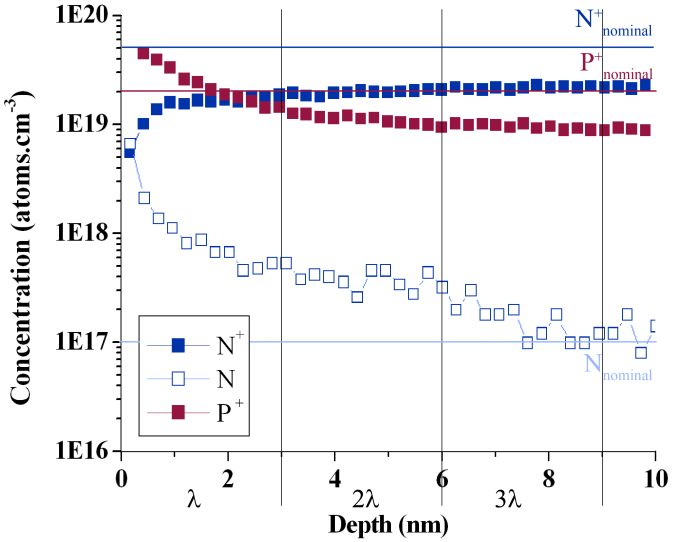

Figure 3.13: *Phosphorus and boron concentration depth profiles in the silicon samples.*

the native oxide, or due to segregation. However, in the case of boron, the additional atoms can be considered electrically inactive under the shape of clusters in interstitial sites [243].

- a shadowing effect of the incident beam produced by the initial sample roughness.

In table 3.2 we compare the required, nominal doping concentrations, with different doping concentrations relevant to photoemission measurements with XPS or XPEEM, as deduced from the SIMS profiles of figure 3.13:

- First we can consider a doping concentration of interest in XPS, corresponding to an average concentration over the Si $2p$ photoelectron escape depth concerning 65% of the collected signal. For a collection angle of 90°, this depth is determined by the inelastic mean free path which is 2.96 nm in the case of Si $2p$ in silicon oxide [155].

- The second relevant doping concentration D_{eff} is integrated over the whole sampling depth 3λ (see figure 2.4) taking into account the relative contributions to the photoemission signal of three first layers of thickness equal to the escape depth. We can express this effective doping concentration as:

$$D_{eff} = 0.63 \times D_1 + 0.23 \times D_2 + 0.09 \times D_3 \ , \tag{3.9}$$

where D_1 is the doping concentration averaged over the first layer (3 nm depth), D_2 the one integrated over the second layer (3 nm to 6 nm depth), and D_3 the one integrated over the third layer (6 nm to 9 nm depth).

From table 3.2, we see that D_{eff} is similar to the doping concentration at 3 nm for both P^+ and N^+ doping. Therefore, for both patterns, it is reasonable to approximate D_{eff} by the doping at 3 nm. We give thus in table 3.3 a modification of table 3.1 taking into account the experimental doping concentrations at 3 nm for all sample combinations.

Doping	Doping type	Nominal doping concentration (atoms.cm^{-3})	Doping concentration at 3 nm (atoms.cm^{-3})	Integrated doping concentration (atoms.cm^{-3})
P^+	Boron	2×10^{19}	1×10^{19}	1.3×10^{19}
P	Boron	1×10^{15}	4.0×10^{15}	-
N	Phosphorus	1×10^{17}	5.4×10^{17}	6×10^{17}
N^+	Phosphorus	4×10^{19}	1.8×10^{19}	1×10^{19}

Table 3.2: *Nominal doping concentration and experimental one for each kind of doping type in patterned samples at 3 nm depth and integrated over 3 nm, deducted from figure 3.13.*

Doping/bulk	Concentration (atoms.cm^{-3})	V_{bi} (V)	Total depletion width (μm)	Electric field maximum intensity (kV.mm^{-1})
P^+/P	$1\times10^{19}/4\times10^{15}$	0.869	0.533	-3.26
N^+/P	$1.8\times10^{19}/4\times10^{15}$	0.884	0.540	-3.29
P^+/N	$1\times10^{19}/5.4\times10^{17}$	0.996	0.050	-41.70

Table 3.3: *Built-in voltage, depletion width and maximal electric field across the junction for experimental doping concentrations.*

3.2.2.2 Topography

Even if the process of localised epitaxy is well controlled, the surfaces are not atomically flat. Some SEM images taken on P^+/P sample cross-section and plane view, show on both large patterns and straight lines that topography is clearly visible on the sample, especially in the vicinity of the pn junctions by contrast variations in a) or simply by the step difference between two zones in b).

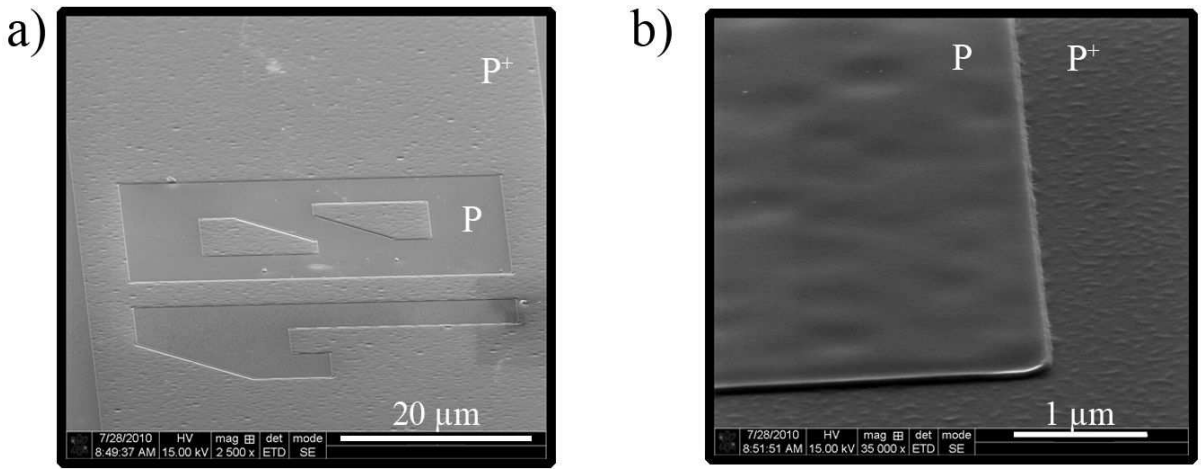

Figure 3.14: *a)In-plane SEM imaging of a sample surface, and b) zoom on the junction between the two doped zones P^+/P. The images seem distorted because the observation angle is 45°.*

Topographic measurements were performed in KFM-tapping mode using a Digital Instrument Nanoscope IIIa Dimension 3100 AFM. Figure 3.15 concerns a larger patterns,

the 'zero'. To evaluate the topography, the step size values are quantified in table 3.4. This information is of interest because XPEEM imaging is sensitive to microlocal fields created by the sample roughness [129].

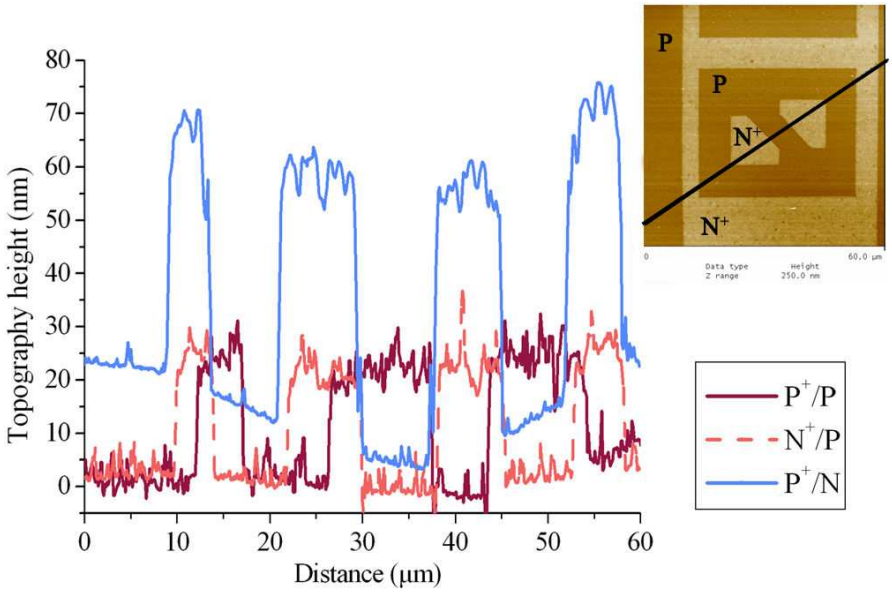

Figure 3.15: *AFM in tapping mode: topographic measurements of P^+/P, N^+/P and P^+/N samples on large pattern. The profiles are taken along the thin black line in the images.*

Sample	Topography (nm)
P^+/P	20
N^+/P	20
P^+/N	75

Table 3.4: *Maximum topography measured by AFM on the patterns junction.*

3.2.2.3 Patterns size

Due to the recess step in the process of fabrication samples, it is not possible to trust the line widths given by the lithography mask. To have an independent estimation of the pattern sizes, lateral measurements were carried out on each kind of sample by optical microscopy.
An optical micrograph overview of the SEM zone is shown in figure 3.16 a): one clearly distinguishes the lines and the dots, localized by respectively, a six and a seven in the top right corner. The measurements obtained on such patterns are presented in figure 3.16 b) in dark field optical microscopy to enhance the contrast between the two zones by highlighting the topography present at the interface bulk/doped zone. They are similar for each kind of sample, the doping concentration has no influence on the imaging.

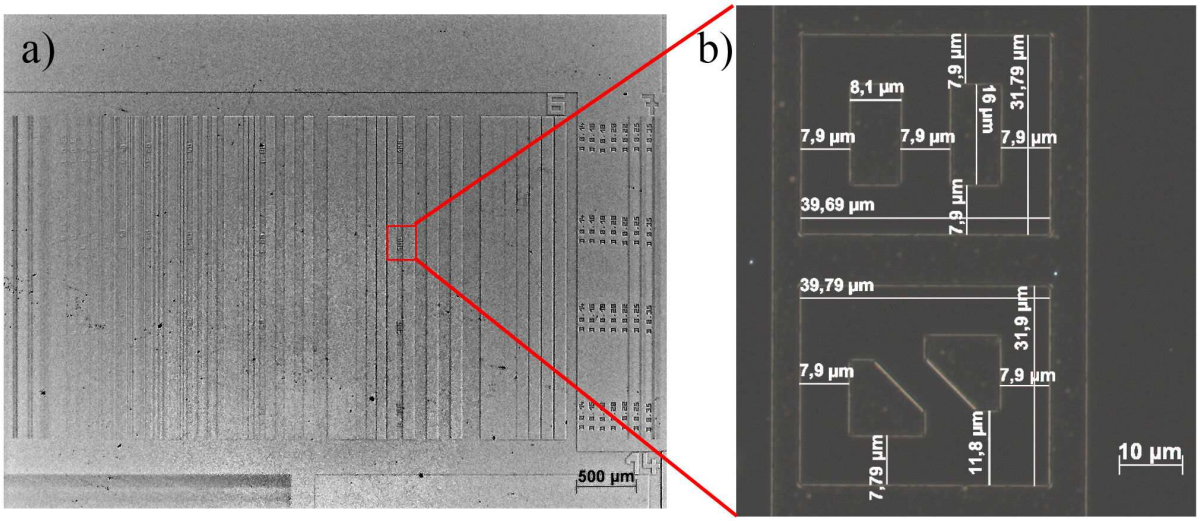

Figure 3.16: *a) Overview of the SEM zone by Zeiss optical microscope. b) Optical image of a pattern of interest, here on P^+/P sample.*

3.2.2.4 Summary

Customized samples have been prepared by rigorous clean room methods. Complementary techniques have been used to fully characterize them, quantifying dopant concentration and surface topography:

- SIMS profiles show an heterogeneous profile for N-type doping whereas those for the other doping are better, especially on the analyse depth XPS and XPEEM are interested in, i.e. the three first nanometers. We compared the concentration difference in measuring at 3 nm below the surface with the integrated signal taking into account the relative contributions to the photoemission signal of three first layers of thickness equal to the escape depth. Since the difference remains faint, we consider for the following of the study the data at 3 nm.
- AFM measurements give a non negligible topography for all the samples, up to 75 nm which can have an impact on PEEM imaging, as will be discussed in chapter 5.

We now focus on the passivation protocol to reach surface flat band conditions for XPEEM analysis.

3.3 Sample passivation

3.3.1 Objective

In the case of unpassivated silicon surfaces, the native oxide introduces a high density of electronic interface states which causes pinning of the Fermi level and band bending, modifying the measured silicon binding energies. In some cases, this can yield to inversion of the expected values of the core-level binding energies of p and n doped silicon. For the planar pn junctions imaged by energy-filtered XPEEM, a potential consequence is

contrast inversion in both core-level and secondary electron imaging. Consequently, for data interpretations from band bending, it is necessary to perform the analysis in near flat-band conditions. This is usually realized by deoxidation of the silicon surface, followed by a passivation process which saturates the silicon dangling bonds.
In the following, we present the methodology followed to attempt to reach a control of the silicon surface state. This was performed firstly on dedicated full wafer silicon samples before focusing on the doped patterns of interest.

3.3.2 Literature review on silicon passivation

The chemical etching of silicon to obtain oxide-free surfaces has been studied for years. Since 1970, the silicon passivation by HydroFluoric acid (HF), yielding chemically clean stable surfaces has become a key step to improve industrial processes [244]. Hydrophobic surfaces were explained to be due to Si-F bonds since their the relative strength is superior to the Si-H one, respectively 6 eV against 3.6 eV [245]. In the middle of the 1980s, this idea has evolved thanks to the breakthroughs in characterization, especially infrared spectroscopy. Ubara *et al.* [246] considered that the Si-F bonds are unstable in HF solutions due to a strong polarization of the Si back-bonds: this facilitates attack by HF molecules and results in a release of SiF_4 molecules in solution whereas the surface becomes H-terminated.

Yablonovitch *et al.* [247] showed using multiple-internal-reflection infrared spectroscopy (MIR), that the surface appears to be covered by covalent Si-H bonds, leaving virtually no surface dangling bonds.
The chemisorption system of hydrogen bonded to atomically clean silicon was firstly explained by Trucks *et al.* [248] who tested the argument that H atoms should saturate dangling orbitals at the surface of silicon to form Si-H covalent bonds. Thanks to ab-initio molecular-orbital theory, they unraveled the mechanisms of HF etching. A schematic of the mechanisms leading to hydrogen-passivated silicon surfaces is reproduced in figure 3.17. Part a) corresponds to the initial surface upon oxide removal by HF where a -F termination of the silicon dangling bonds can be found. The ionic nature of the Si-F bond polarizes the silicon back-bond as follows:

$$\equiv Si^{-} - Si^{+}\mathrm{F} \ , \tag{3.10}$$

The polarization enables the insertion of HF into the silicon back bond, as can be seen in figure 3.17 b). This leads to an hydrogenation of a silicon atom from the second layer of the sample surface. Repeating the same process twice leads to a removal of the silicon atoms of the first layer as SiF_4, in c) and d).

This global mechanism can be then expressed by:

$$\equiv Si^{-} - Si^{+}\mathrm{F_3} + \mathrm{HF} \longrightarrow \equiv \mathrm{SiH} + \mathrm{SiF_4} \ , \tag{3.11}$$

An attack of SiH bonds by HF is possible but the activation barrier is significantly higher than the previous reaction for Si-Si bond cleavage:

$$\equiv \mathrm{SiH} + \mathrm{HF} \longrightarrow \quad \equiv \mathrm{SiF} + \mathrm{H_2} \ , \tag{3.12}$$

Hence, fluorine is indeed a minority species on the surface, and HF treatment results in an inert hydrogen-terminated surface, which is stable against native oxidation for several

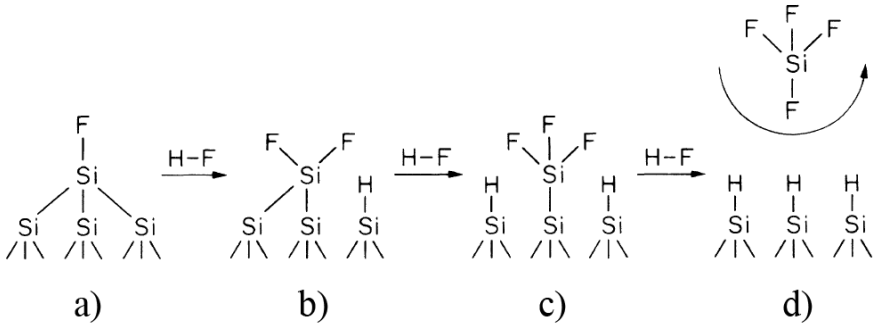

Figure 3.17: *Schematic representation of the mechanisms of H-passivation [248].*

hours. Huang *et al.* [249] found that hydrogen termination of the dangling bonds on silicon (100) is an effective way to reduce surface gap states on n- or p- doped zones. Using XPS on several silicon samples after an HF-etching with different concentrations, they concluded that HF cleaning passivates the surfaces electrically. Above all, it is possible to reach near-flat band conditions with a band bending less than 0.1 eV under some conditions.

MIR spectroscopy has been used by Chabal *et al.* [250] to identify the chemical nature of chemically oxidized silicon surfaces. They showed that aqueous HF solutions of various concentrations induce microscopic roughness on both Si(111) and Si(100). It has been found that the pH of the HF solutions alters the roughness and the associated -H terminations at the surface of the cleaned samples. Higashi *et al.* [251] studied this effect by measuring the SiH stretch vibration with infrared absorption spectroscopy: the surfaces are the smoothest for an pH etchant ranging between 3 and 8. The lower the etchant pH, the rougher the sample surface.
Hence, whereas etching in aqueous HF produces atomically rough surfaces, the same treatment in ammonium fluoride NH_4F results in atomically flat ones with well ordered terraces which extend thousands of angstroms [252]. Thus, NH_4F is a better etchant than HF, but it is not perfect: the dissolved oxygen contained in a 40% NH_4F solution can be responsible for etch-pits growth, observed by Wade *et al.* [253] by ex-situ STM.

The cleaning procedures can differ from groups to groups [254, 255]. However, it is possible to find a reliable method of surface preparation. This was proposed firstly by Higashi *et al.* [251]. The recipe consists of three steps [256]:

- Degreasing of the sample surface.
- Etching/oxidization cycles of the surface.
- The final step, is the final etching using HF buffered with NH_4F at 40 %. A quick dip in de-ionized water for a few seconds is then necessary to remove traces of fluorine at the surface.

This process leads to a surface state distribution which can be significantly reduced, down to $1.2\times10^{10}\text{cm}^{-2}.\text{eV}^{-1}$, obtained on atomically flat H-terminated silicon [257, 258]. Studies on wet chemical etching procedures are in progress to control the stability of

passivation or the topography of the etched surface [259]. Nowadays, improvements are still possible and the passivated surface can be stable against oxidation for at least three hours in atmosphere [260].

3.3.3 The three-steps passivation protocol

In practice, performing the cleaning itself is not an easy task. We have tested variations in the etching product, the bath duration, and characterized the results by XPS on full-sheet doped silicon samples defined in section 3.2.1.2.

3.3.3.1 Protocol

- Degreasing is done with pure thrichlorethylene of VLSI quality for 30 minutes. The sample is rinced in pure acetone, and then, in ultrapure deionized water with 18 MΩ.cm resistivity and an organic contamination lower than 20 ppb.

- First etching is done for 30 minutes, using Buffered Oxide Etchants. BOE are blends of 49% HF and 40% NH_4F in various predetermined ratios NH_4F:HF. Here, the solution ratio was 7:1.

- The sample is then rinsed in deionized water before being dipped into a piranha solution at 135°C for 20 minutes. The role of this solution is to chemically reoxidize the sample surface. Piranha is a solution of H_2O_2 and H_2SO_4 in ratio 1/3-2/3. They are of VLSI quality and concentration: 96% for H_2SO_4 and 30% for H_2O_2, respectively.

- The sample is rinsed again before being etched a second time in the BOE bath, again for 30 minutes.

- This protocol ends with a rinsing in ultrapure water which allows to check the hydrophobic nature of the surface, and dried under N_2.

Dedicated Teflon tweezers and baskets were used for all the steps of this cleaning.

3.3.3.2 First validations of the protocol

XPS survey Survey spectra acquired on a full sheet silicon doped sample surface are presented before and after passivation in figure 3.18. These general spectra are representative of the whole surface since they have been acquired for several locations on the sample to validate the process homogeneity.

- Before passivation, in a), the peaks visible are Si $2p$ and Si $2s$, at 100 eV and 150 eV binding energy respectively. The O $1s$ is clearly observable at 530 eV, and a carbon C $1s$ peak appears at 285 eV, these two peaks are the signature of the native oxide and surface contamination.

- After passivation in b), the spectrum presents only residual traces of carbon or oxygen, validating the general passivation efficiency.

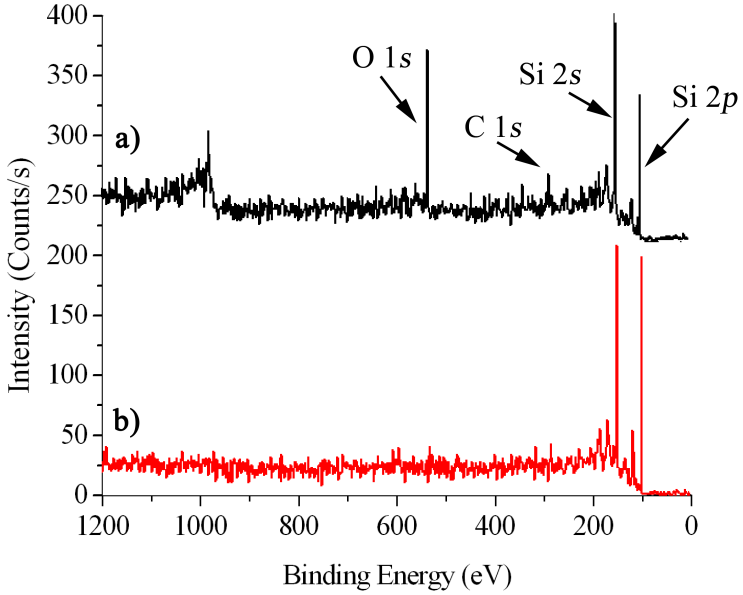

Figure 3.18: *XPS survey scan of silicon doped surface a) before and b) after the passivation using the protocol detailed previously. Photon energy: 1486.7 eV. FoV: 127 μm.*

Fourier Transform InfraRed Spectroscopy analysis Infrared spectroscopy provides an improved surface sensitivity. It is particularly suitable for investigating the atomic bonding configuration of hydrogen on the surface and studies to characterize Si-H layers are still in progress [261, 262]. Figures 3.19 a) and b) present the FTIR spectra collected in Attenuated Total Reflectance (ATR) mode, over a large range of energies, expressed in wavenumber. It can be seen that the samples with high dopant concentration, represented in b), N^+ and P^+, have an important absorption peak which hides the Si-H vibrational modes of interest around 2100 cm^{-1}. The intensity of the tail of the absorption peaks has to be removed to estimate the Si-H absorption mode.

In the literature [263, 264], no vibrational mode related to $SiHO_2$ and $SiHO_3$, respectively around 2200 cm^{-1} and 2250 cm^{-1} is observable, for a) and b) which confirms the passivation efficiency performed on all silicon sample, indepdtly of their doping. Figure 3.19 c) shows the spectral region 2000-2300 cm^{-1}, characteristic of the Si-H stretching modes at 2084 cm^{-1}. The infrared absorption spectra of the samples presents as the dominant absorption band the Si-H stretching mode. The presence of small contributions from either SiH_2 or SiH_3 modes [265] can be related to the surface topography. The ratio differs from one sample to another, which can be interpreted in terms of different roughness depending on the doping concentration.

To conclude, FTIR confirms that Si-H is the dominant bonding at the sample surface after passivation.

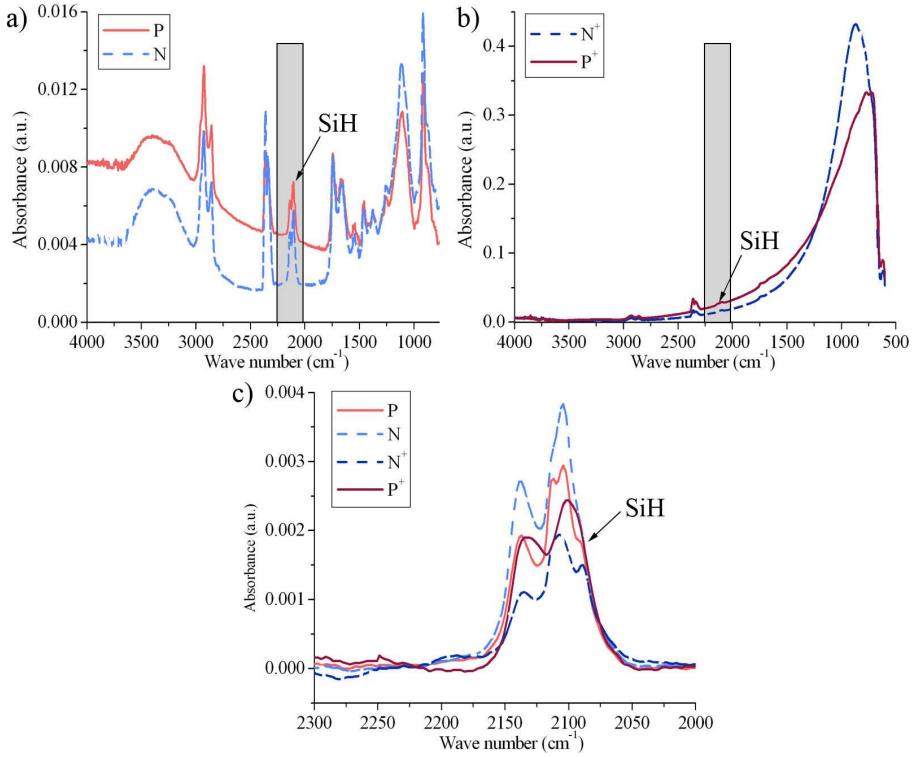

Figure 3.19: *FTIR spectra in ATR mode, for different silicon doped samples: P, N, N^+, P^+ in a) and b) large wave number range, and c) in the Si-H vibrational mode around 2100 cm^{-1}.*

3.3.4 XPS analysis of the passivation process

3.3.4.1 Samples and conditions

The ARXPS analysis was performed on full wafer doped silicon samples prepared by epitaxy similarly to the patterned samples presented in section 3.2.1.1. The doping values of these samples given in table 3.5 are measured by SIMS at 3 nm below the surface. They are the same order of magnitude than the patterned samples ones recalled in the last column.

Doping Type	Doping concentration at 3 nm Full wafer samples (atoms.cm^{-3})	Doping concentration at 3 nm Patterned samples (atoms.cm^{-3})
P^+	2.4×10^{19}	1×10^{19}
P	4.0×10^{15}	4.0×10^{15}
N	3.4×10^{17}	5.4×10^{17}
N^+	1.6×10^{19}	1.8×10^{19}

Table 3.5: *Experimental doping concentration at 3 nm depth for full wafer samples for each kind of doping type and comparison with doping concentration of patterned samples deducted from figure 3.13.*

The analysis was performed on a multi-probe XPS system (Omicron Nanotechnology), see chapter 2 subsection 2.1.1.6. A monochromatized AlKα radiation (photon energy of 1486.7 eV) with an EA125 electron analyser (radius 125 mm) were used. The analyser

pass energy was 50 eV, and the entrance slits 2 mm, yielding an overall energy resolution of 0.70 eV.
The analyser was operated in medium magnification mode, hence collecting the emitted photoelectrons with a maximum acceptance angle of ±4°.

The Si 2*p* core-level spectra were collected at two collection angles 90° and 15°, yielding respectively sampling depth of 8.88 nm and 2.30 nm. This latter angle of 15° was chosen since it enables the maximum surface sensitivity necessary for probing ultrathin overlayers.

3.3.4.2 Surfaces before passivation

Figure 3.20 presents the Si 2*p* core-level XPS spectra of the different samples at these two collection angles.

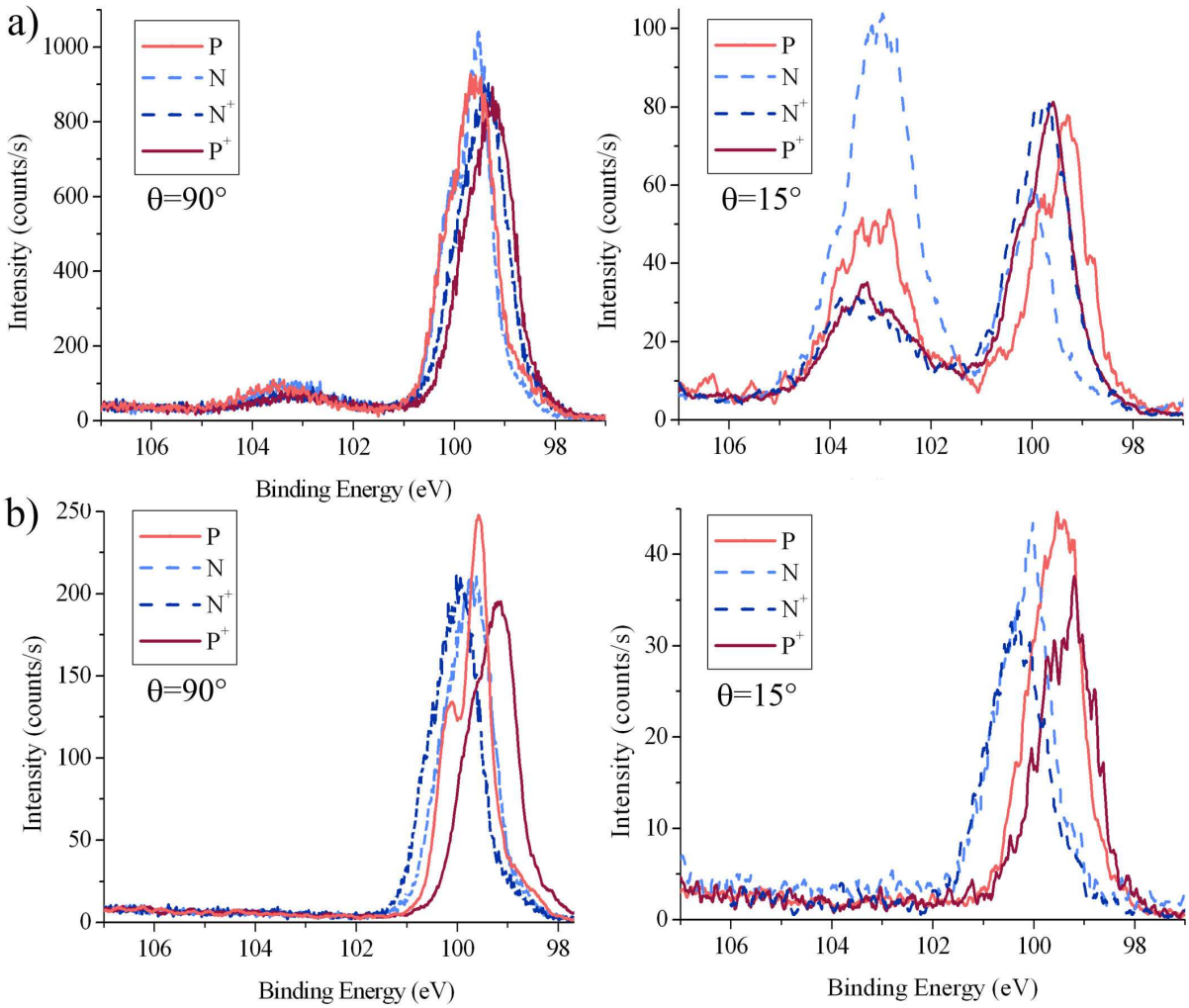

Figure 3.20: *Si 2p XPS spectra for different silicon doped samples a) before passivation and b) after passivation. Colour code chosen: blue = n-doping, pink = p-doping. The spectra are exceptionally presented by lines, and not by unjoined symbols since they corresponds to smooth data in order to remove noise.*

Comparing spectra at both angles before and after passivation in figure 3.20 respectively a) and b), one clearly sees the disappearance of the SiO_2 peak around 103 eV, indicative of a successful oxide removal from the surface.

Before passivation, the difference in sampling depth at the two angles is clearly seen: the SiO_2 peak intensity is the same order of magnitude at 15° as the component due to unoxidized Si in the range 98-100 eV, whereas it is much weaker on spectra acquired at 90°. This can be understood in terms of sampling depth differences:

- At 90°, the sampling depth is important (d=8.8 nm), the analysis is less sensitive to the native oxide if this latter is thin.
- At 15°, the sampling depth is lower (d=2.3 nm), which results in an enhancement of the oxidized silicon signal on the spectra.

The thickness of the native oxide was measured for each full wafer samples using spectra collected at 90°, following the procedures described in the recent literature [266–269]. The values were found to range between 1.15 nm and 1.8 nm with an uncertainty corresponding to the uncertainty of the inelastic mean free path taken at 20%. They have to be compared with the thickness results obtained on patterned samples, which were found to be ranging between 0.66 nm to 0.86 nm.

After passivation, no oxide component is visible on the spectra, even at 15° where the sensitivity to the surface is enhanced.

3.3.4.3 Surfaces after passivation: laboratory XPS study on full wafer samples

Results and fits Figure 3.21 presents the angle resolved Si 2p spectra for passivated P^+ and N^+ surfaces after fitting. The cases of P and N doping are not detailed since the spectrum shape was similar, however, the quantitative results of the fits are presented in table 3.6.

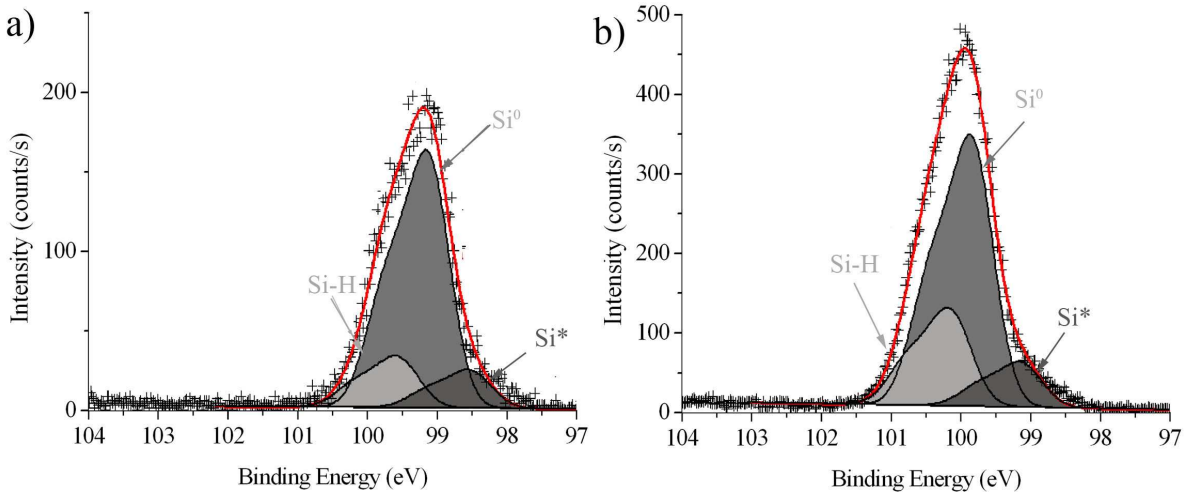

Figure 3.21: *Si 2p spectra for a) P^+ and b) N^+ doped zone at a collection angle of 90°.*

For the fitting, a Shirley background is subtracted, and a gaussian-lorentzian line-shape is used, with a spin-orbit splitting of the Si $2p$ doublet of 0.603 eV. In a first approximation, we considered a fixed full width at half maximum for the Si^0 and Si-H components taken at 0.70 eV, close to the overall energy resolution.

- The line shape for this Si-H peak and the Si^0 are set at 100% gaussian. These values are kept constant, whatever the dopant type, the dopant concentration, and the collection angle.
- The binding energies vary from a sample to another, but, for a given sample, they do not change significantly with the take-off angle.

The fittings reveal three components. Besides the main Si^0 peak, we must include two additional components: a first one related to Si-H bonds and a second one named Si^*. The presence of Si-H is in agreement with the FTIR measurements presented in paragraph 3.3.3.2. The chemical shift of the Si-H peak relative to Si^0 is +0.44 eV, in agreement with literature [270].

To achieve high quality fit for the spectra, a small contribution appearing to the low binding energies, Si^* set to Si^0 -0.70 eV is added, with a peak line shape set at 100% gaussian.

Table 3.6 shows the relative intensities of the Si^0, Si^* and Si-H components.

Peak	P^+		P		N		N^+	
	15°	90°	15°	90°	15°	90°	15°	90°
Si^*	8.45	10.05	38.31	16.65	3.45	9.88	2.29	9.13
Si^0	39.07	76.2	23.86	76.99	49.89	73.56	62.97	86.31
Si-H	52.49	13.75	37.83	6.36	46.66	16.56	34.74	4.56

Table 3.6: *Relative contributions of each peak relative to the total Si 2p peak intensity in P, P^+, N and N^+ cases at 90° and 15°.*

The Si-H component From this table, it is possible to extract some common trends:

- The Si-H peak contribution is higher for a collecting angle of 15° than at 90°, confirming the localisation of this bonding at the surface.
- Conversely, the Si^0 peak contribution is higher for a collecting angle of 90° than at 15°. It is however worth noting that the Si^0 variations between 90° and 15° are variable from sample to sample.
- For P type doping, the concentration of Si^* decreases with decreasing sampling depth, as observed by Ying *et al.* [271, 272]. The trend is similar for N doping but no comparison with literature was found.

At grazing incidence, the analysis technique is more sensitive to the top most layers of the surface, highlighting the presence of Si-H bounds. When probing deeper, the photoelectrons emitted from the bulk silicon are greater and the technique is less sensitive

to the passivated layer at the surface.

The XPS experiments have been repeated, in order to test the passivation after exposure to two weeks ultra-high vacuum. The resulting spectra were identical than the first ones, with a quasi-complete absence of native oxide and contamination on the sample surface.

The Si* component The additional Si* component is mentioned in several studies which are summarized in table 3.7. The chemical shift of this component relative to Si^0 is found to be -0.70 eV, in agreement with ΔS_1 of table 3.7.
In the literature, we find several detailed studies of silicon passivation presenting the decomposition of the Si $2p$ core-level spectra. Whatever the surface reconstruction type, some spectral components appear at low binding energies. Most of the studies cited in table 3.7 were performed with synchrotron radiation. In general, three additional peaks, labeled S_1, S_2 and S_3 were observed close to Si^0 peak: S_1, S_2 are shifted to lower binding energies whereas S_3 is shifted to slightly higher binding energies. Therefore, our Si* component corresponds to S_1 component whereas S_2 and S_3 can not be separated from the Si^0 peak, due to the low energy resolution of the experiment.

Main Author	Reference	ΔS_2	ΔS_1	ΔS_3	Reconstruction
Landemark	[273]	-0.23	-0.5	+0.22	Si(001)-4×2
Kakiuchi	[274]	-0.23	-0.5	+0.23	Si(100)-2×1
Himpsel	[275]	-	-0.5	-	Si(100)-2×1 and 7×7
Karlsson	[276]	-0.264	-	+0.19	Si(111)-1×1
Karlsson	[277]	-	-0.7,-0.8	+0.3,+0.4	Si(111)-7×7
Chao	[278]	-0.21	-0.5	+0.21	Si(100)-2×1
Cerofolini	[279]	-0.27	-	+0.28	Si(100)-2×1
Ying	[271, 272]	-	-0.4		Si(100)-2×1 and poly-Si
Mizokawa	[280]	-	-0.4	-	Si(100)-2×1 and poly-Si
Yamashita	[281]	-0.21	-0.48	+0.24	Si(100)c(4×2)
Enta	[282]	-	-0.5	+0.2	Si(100)
Jolly	[283]	-0.21	-0.44	+0.19	Si(100)-2×1 and 7×7
Gomoynova	[284]	-0.2	-0.7	+0.24,+0.28	Si(100)2×1 and Si(111)7×7

Table 3.7: *Binding energy shifts measured in eV, referenced to bulk silicon for different passivated silicon surfaces.*

We review the physical interpretations of both S_1, S_2 and S_3 components:

- In case of Si(100)-2×1, the S_1 and S_2 peaks are attributed to the dimers. For a clean silicon surface reconstructed in this way, the atoms of the topmost layers form symmetric or asymmetric dimers [273]. For symmetric model, the shifted S_2 component is due to one monolayer corresponding to covalent dimer atoms [285, 286], as presented in figure 3.22 b).

- For an asymmetric dimer S_1 is attributed to the up-dimer atom whereas and a

second component situated 0.06 eV above the Si^0 component is assigned to the lower atom [278] as shown in figure 3.22 c).

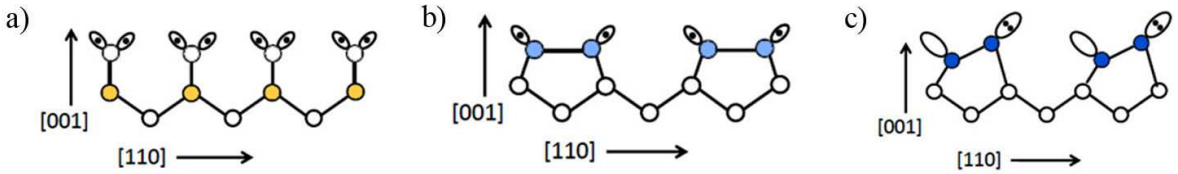

Figure 3.22: *Sections through a) the Si second layer, b) the Si (2×1) symmetric dimer surface and b) the (2×1) asymmetric dimer surface. The dimer bond is in the plane of the paper, the dimer rows running perpendicularly out of the plane of the paper.*

- The S_3 component is attributed to the Si second-layer atoms [274] and the subsurface atoms [281], as shown in figure 3.22 a).
- Gomoynova *et al.* [284] consider this S_1 peak as dangling bonds of the rest atoms, as does Himpsel *et al.* and Grupp *et al.* [275, 287] for 7×7 silicon (111) reconstructed.
- Another group of studies led by Ying *et al.* [271, 272] and Mizokawa *et al.* [280] on heavily P-doped Si(100) and P-doped poly Si observed S_1 at -0.4 eV with respect to Si^0. They ascribe it to silicon atoms adjoining vacancies, voids or interstitial silicon or phosphorus.
- Landemark, Kakiuchi and Chao [273, 274, 278] suggested that the peak S_2 around -0.2 eV can be assigned to the silicon third layer, but may also include contributions from surface defects, as presented by Yamashita [288] and Karlsson [276].
- Jolly *et al.* consider the two components S_2 and S_3 as interfacial components close to the interface between the native oxide and the surface, due to a possible effect of oxygen second neighbors on the Si $2p$ binding energies [283].

In our case, no LEED data is available, consequently, we can not draw a firm conclusion on the surface reconstruction. However, we refer to recent STM study on epitaxial silicon samples prepared with the same protocol as ours which showed a (2×1) reconstruction [242]. We will almost remember that Si^* can be a possible fingerprint of residual dangling bonds at the passivated surface.

Binding energy values The binding energies deduced from the spectra fits are given in table 3.8. In figure 3.23, we compare the experimental values with values predicted from the SIMS derived doping concentrations in flat band conditions:

- The Si^0 binding energy values $BE_{th.3nm}$ predicted for flat band conditions, and derived from SIMS doping measurements at 3 nm.
- The Si^0 binding energy values measured BE_{exp}, referenced relative to the Fermi level which depends on the doping type and concentration, as seen in equations 3.1 and 3.2.

	Si^0_{P+}	Si^0_P	Si^0_N	Si^0_{N+}
BE_{exp} (eV)	99.12±0.35	99.58±0.35	99.58±0.35	99.73±0.35
$BE_{th.3nm}$ (eV)	98.77	98.97	99.76	99.85
$BE_{th.3nm}$ -BE_{exp}	-0.35	-0.61	+0.18	+0.12
Si* proportion (%)	11.7	17.8	11.8	9.5

Table 3.8: *Binding energies BE_{exp} for bulk silicon Si^0 for different doping types extracted from XPS spectra deconvolution.*

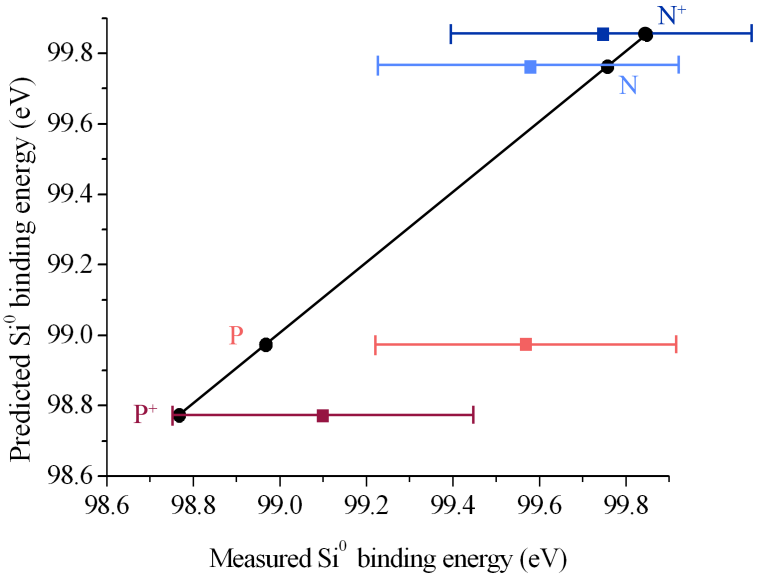

Figure 3.23: *Si^0 binding energy measurements for different doping types, and comparison with predicted values from doping in flat band conditions.*

The binding energy values measured for both N and N^+ doping are in good agreement with those expected from flat band conditions whereas for P samples, the difference between experimental and theoretical values is higher. Its is especially important for P type doping where the difference reaches 0.62 eV. This can be related to the strong Si* contribution in the Si 2*p* spectra with respect to the low Si-H one, which can be responsible to a stronger band bending, and thus, to a stronger shift, as presented in last line of table 3.8 where the ratio $\frac{Si^*}{Si^0+Si^*}$ is given for all doping.

In case of P doping, the ratio is really important and thus, can be related to a stronger shift in terms of binding energy. However, though the ratio for P^+ is better than for N doping, the measured binding energy is more shifted. We can give an explanation given by Schlaf *et al.* which have shown that a residual band bending due to the fluorine coverage can remain on silicon doped patterns, depending on the doping density and HF concentration used for etching [289] since an extremely small number of surface states is required to pin the Fermi level.

Focusing on the shifts in terms of Si^0 binding energy values measured relatively to flat band conditions, a trend appears: the measured values are higher than theoretical ones in case of P doping whereas they are lower for N doping. We observe the band bending

direction due to residual interface states within the silicon bandgap depending on the doping type: the bands for a P doping are bent downwards (i.e. an increase in terms of binding energy) whereas a N doping presents a band bending upwards, and thus, a decrease in the measured binding energy.

3.3.4.4 Case of passivated patterned samples: micro-XPS with XPEEM

The passivation study was performed on full wafer silicon samples with the MXPS. We compare now its efficiency on passivated patterned ones by core-level microspectra acquired with the NanoESCA by microspectroscopy. The pass energy was 100 eV and the entrance slit width was 1 mm, giving the same overall energy resolution as the MXPS experiment, i.e. 0.48 eV.
Figure 3.24 presents Si 2*p* core-level spectra acquired for a collecting angle of 90°, on highly doped silicon P^+ and N^+.

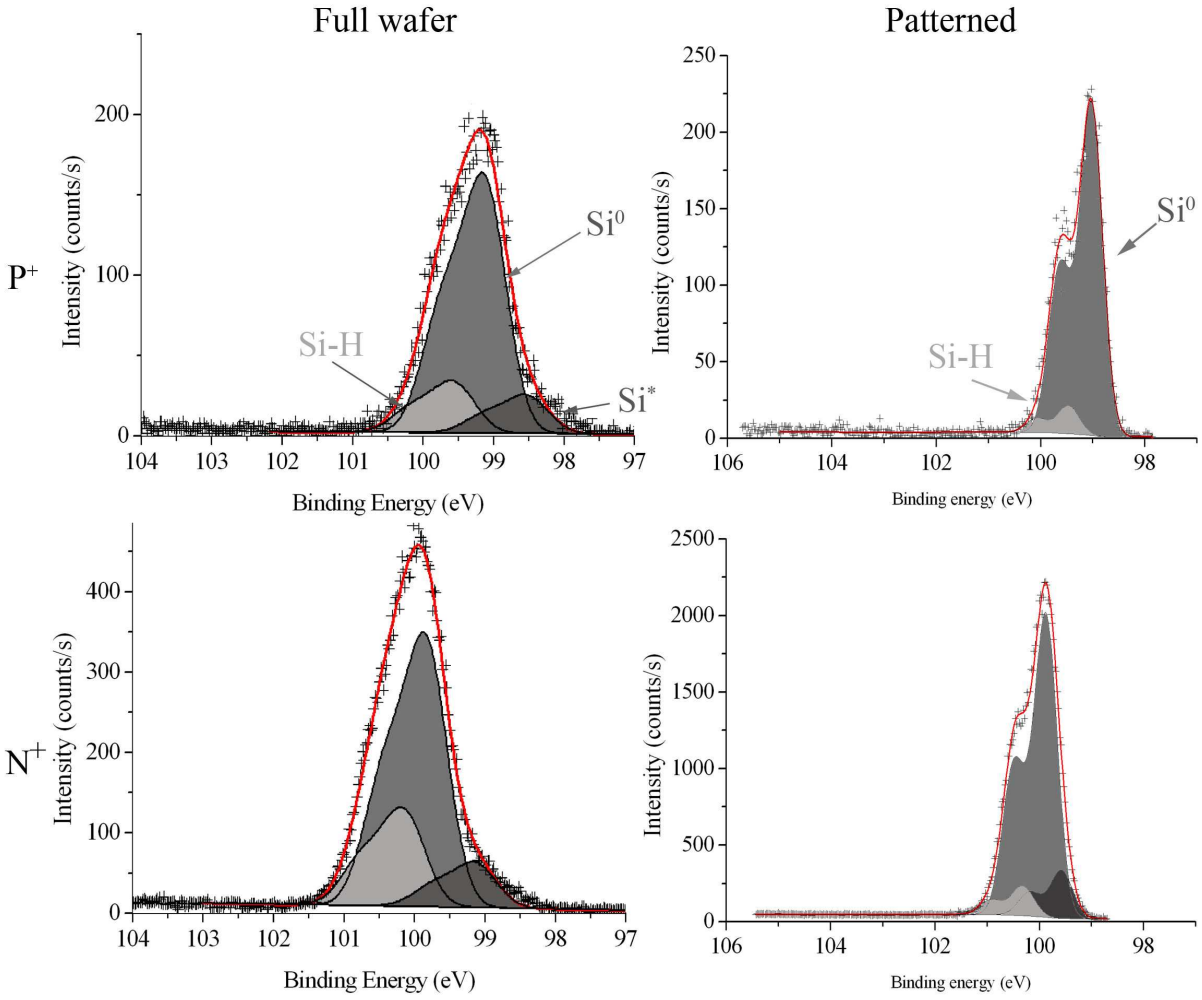

Figure 3.24: *Si 2p core-level microspectra of P^+ and N^+ acquired on full wafer and patterned samples.*

The spectra are similar and can be compared, even for lightly doped zones which are not presented here. The contribution of the different components Si^0, Si^* and Si-H varies between full wafer samples and patterned ones: especially, the Si^* component seems

to be lower proportions when observed with the NanoESCA. As mentioned in section 3.3.4.2, the native oxide being thinner on patterned samples than on full wafer samples we expected the passivation to be at least as efficient on both kind of samples, which is the case. This validates our protocol for the study of passivated patterned samples observed with the energy filtered XPEEM.

3.3.4.5 Synchrotron experiments: reproducibility of the passivation

We have also observed the Si 2*p* core-level spectra for samples passivated in synchrotron, just before imaging in the SOLEIL premises, in a dedicated chemistry laboratory. The photon energy tunability of synchrotron helps in probing a sampling depth lower than the one probed at 1486.7 eV (8.8 nm). At 128.9 eV and 700.3 eV, *d* corresponds respectively to 2.3 nm and 4.8 nm.

We present in figure 3.25 microspectra extracted from core-level image series acquired with the NanoESCA, for the two doped zones P^+ and N^+. The experimental conditions are presented in table 4.14. We do not detail here the fitting spectra choices chosen, these will be discussed in chapter 4 section 4.2.2.

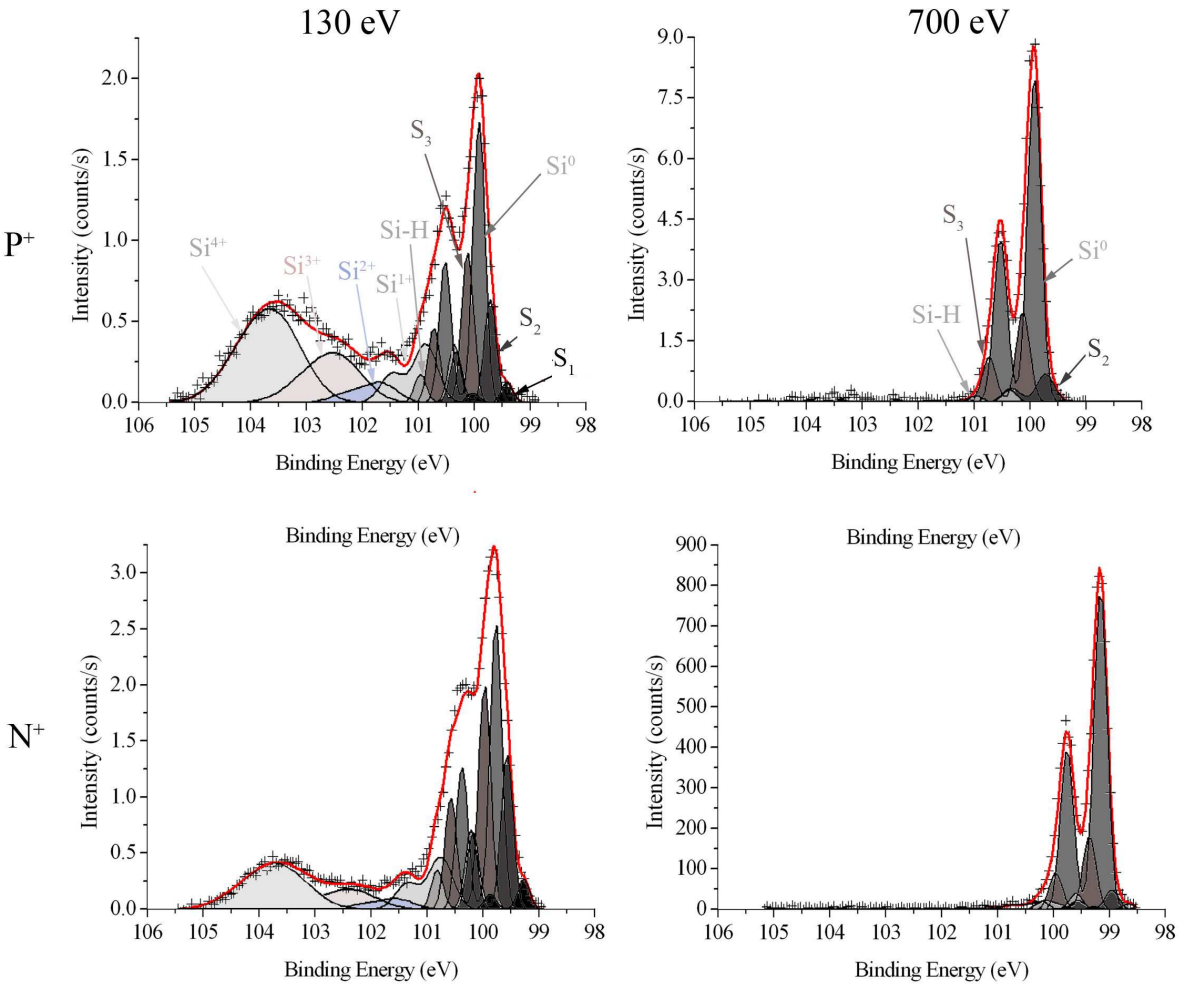

Figure 3.25: *Si 2p core-level microspectra of P^+ and N^+ doping zones acquired at 128.9 eV and 700.3 eV.*

Contrary to core-level laboratory spectra acquired also on passivated samples, we observe oxide and suboxide components at binding energies higher than Si^0 peak which indicates the presence of a residual native oxide. The more important the photon energy, the less the presence of suboxide components, which confirms that this oxide is thick. Though the passivation protocol was kept constant, the passivation performed at SOLEIL chemistry laboratory was less efficient for these samples than for those observed in laboratory. We have to deal with a non reproducibility of the protocol though it is well controlled.

3.4 Summary and conclusions

In this chapter, we have first presented the design, the fabrication process and the extensive characterizations performed on the patterned doped silicon surfaces which will be imaged with XPEEM and studied in the next chapters.

The choices for the sample design were driven by the necessity to realize various doping combinations yielding different electrical characteristics of the resulting planar pn junctions, possibly affecting the XPEEM images. We chose localized epitaxy as the growth method for its low thermal budget and the in situ doping process providing potentially homogeneous in-depth doping concentration profiles. These choices resulted in three sample configurations:

- Two samples with different doping combinations (N^+ and P^+ patterns on P substrate) yielding similar junction depletion with (550 nm) and a maximum electric field across of 3.3 $kV.mm^{-1}$.
- One sample consisting of P^+ patterns on N substrate with a much smaller depletion width (50 nm) resulting in a more than ten times larger electric field across the junction (41.7 $kV.mm^{-1}$).

The samples, processed in the LETI clean rooms in six technological steps, were then characterized extensively from the surface topography and more particularly the doping in depth uniformity point of view. At the junction, a residual step in the 20-75 nm was found. The doping concentration, measured by SIMS as a function of depth over 10 nm, on as-grown samples (i.e, before passivation) was found to be not perfectly uniform: variations of half a decade for the patterns (N^+ and P^+ doping) and two decades for N doping (P doping concentration could not be reliably determined for sensitivity reasons) were measured. The doping concentration at 3 nm depth, beyond which doping variations were found to be negligible (1/10 decade), and corresponding to the Si $2p$ photoelectron escape depth, was chosen as reference data for further quantitative determinations of the residual band bending from photoemission data.

In a second step, we have aimed at producing deoxidized and passivated silicon surfaces in order to be as close as possible to flat band conditions. Following literature, a three-step surface passivation protocol was performed and extensively characterized on full wafer samples (N^+, P^+, N and P doping), with the same doping concentration as the patterned ones, using FTIR and especially XPS.

First-order validations of the efficiency and uniformity of this ex situ surface preparation protocol showed effective deoxidation (ARXPS in surface sensitive conditions) and passivation of the obtained surfaces (Si-H bonds by FTIR). The obtained surfaces were then more extensively studied from accurate fits of the high-resolution (0.7 eV) Si $2p$ core-level spectra, including Si-H bonding states.
A pronounced shouldering to lower binding energy was found on all samples. This resulting Si* bonding state component was tentatively assigned to the so-called S_1 states of silicon atoms reported in the literature of mainly (but not exclusively) reconstructed Si(100) surfaces studied by high-resolution photoelectron spectroscopy. This literature study suggested also the existence of two other components S_2 and S_3 which are of interest for the XPS analysis performed with synchrotron radiation, as presented in chapter 4. The true origins of such a component, however, is still matter of debate and various interpretations are suggested, including dimer surface states and dangling bonds. Therefore, we cannot conclude on the perfect efficiency of our surface preparation protocol for the passivation of the surface electronic states. We were able to qualitatively relate this to a pronounced band bending found for both P^+ and P dopings. Conversely, N doped surfaces have been observed in nearly flat band conditions, consistent with a much higher proportion of Si-H bonds and/or a much lower proportion of Si* states. However, we found it difficult to make quantitative correlations between the magnitude of the band bending and the amount of defective/passivated silicon states.

Finally, we presented complementary XPS analyses on the patterned samples after passivation performed in different environments, before laboratory XPS at LETI and before synchrotron radiation experiments at SOLEIL. The results highlight that, in the most surface sensitive conditions (130 eV photon energy excitation, equivalent to a 0.3 nm photoelectron escape depth), residual oxide coverage remains. However, this oxide coverage is not detectable under slightly increased bulk sensitive conditions (700 eV excitation), indicative of sub-ML coverage. Therefore, we conclude that the passivation process is not reproducible between laboratory and synchrotron environments. This shows that for both sets of sample (laboratory and synchrotron), a systematic study including careful spectroscopic analyses at the microscopic level must be performed for a proper interpretation of the images, as will be done in chapter 4.

Chapter 4

Energy-filtered XPEEM of passivated patterned silicon samples

Contents

This chapter is dedicated to the results of the energy-filtered XPEEM experiments performed on three patterned doped silicon samples after passivation, the fabrication and characterization of which were presented in chapter 3. We present a full spectro-microscopic analysis using all the characteristic electrons accessible with the instrument: secondary electrons, core-level electrons and valence band electrons.

In the following of this manuscript, we will distinguish two sets of samples and experiments performed after passivation:

- patterned silicon samples imaged with laboratory source including an X-ray source (1486.7 eV excitation energy) and a VUV source (21.2 eV excitation energy).
- patterned silicon samples studied with synchrotron radiation at two photon energies: 128.9 eV and 700.3 eV.

4.1 Secondary electrons: work function mapping

In this section, we compare first the work-function mapping of silicon patterned samples acquired in laboratory after passivation. Then, we focus on synchrotron experiments, performed at the TEMPO beamline of the SOLEIL synchrotron for two excitations energies.

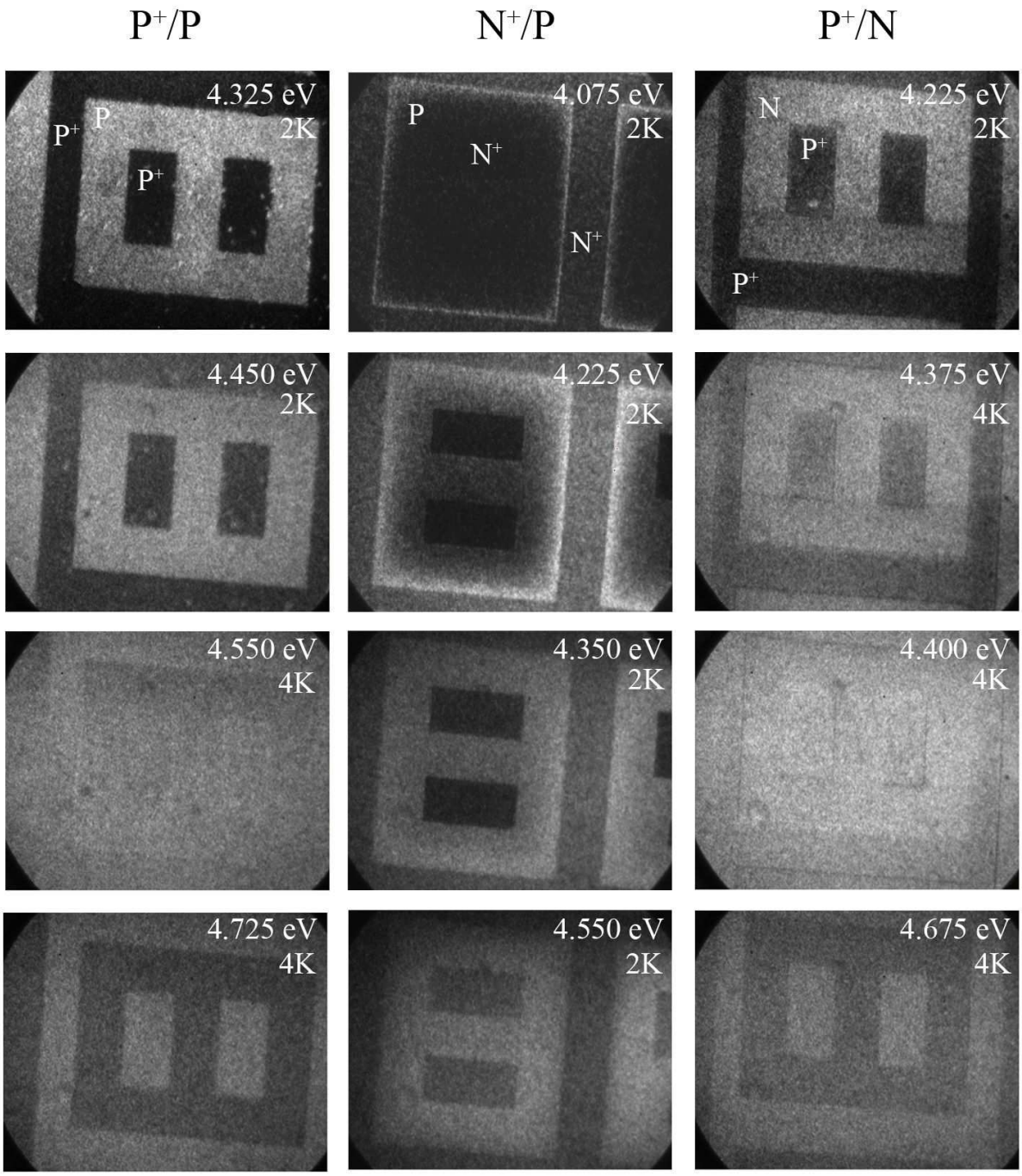

Figure 4.1: *Image series taken at threshold (excitation: 1486.7 eV) for different energy (E-E_F) given in the top right corner of each image. The field of view is 62 µm. The intensity scale is given by the maximal value in the image 2048 a.u. or 4096 a.u.*

4.1.1 Experimental conditions and work function analysis protocol

The acquisition conditions at threshold are summarized for both laboratory and synchrotron analysis in table 4.1.

Parameters	Laboratory	Synchrotron	
	1486.7 eV	700.3 eV	128.9 eV
Extractor voltage	12 kV	12 kV	12 kV
Contrast aperture	70 μm	70 μm	70 μm
Field of view	62 μm	62 μm	62 μm
Entrance slit width	1 mm	0.5 mm	0.5 mm
Pass energy at threshold	50 eV	50 eV	50 eV
Acquisition time	120 s	1 s	5 s
MCP voltage	900 V	900 V	900 V
Overall energy resolution	0.33 eV	0.1 eV	0.1 eV

Table 4.1: *General acquisition condition in laboratory and synchrotron environment for threshold studies.*

A typical example of image series at threshold corrected for dispersion in energy, and noise and obtained on the samples is given in figure 4.1. Because here we perform energy-filtered imaging, we do not observe the contrast obtained in non filtered PEEM or SEM with P zones being usually brighter than N zones.

We also show the threshold spectra collected for different areas of interest represented in coloured squares with a threshold shifted as a function of the local work function in figure 4.2 a). We are able to extract from this threshold the local work function value.

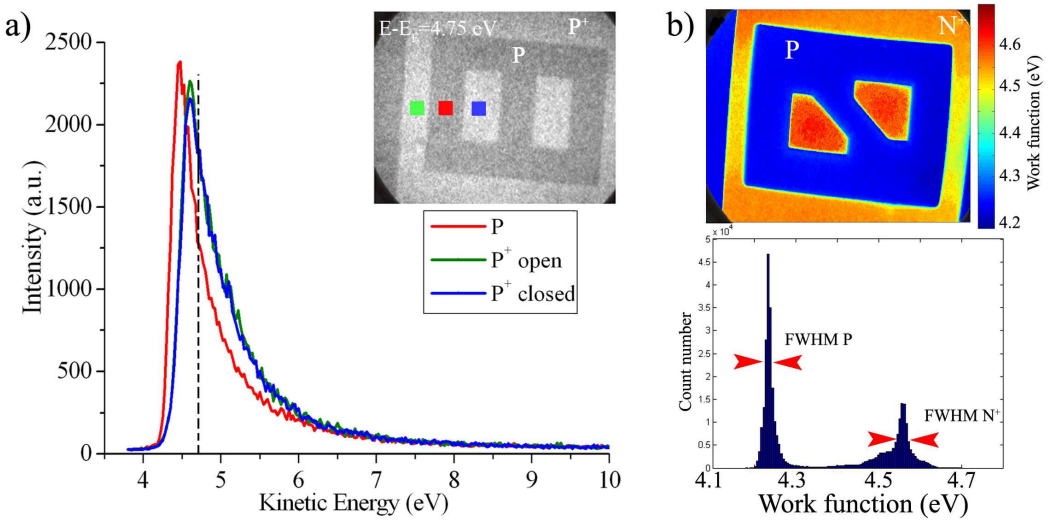

Figure 4.2: *a) Image XPEEM of P^+/P sample taken at threshold and spectra extracted from several area of interest. b) Work function mapping of N^+/P sample and histogram deduced. (FoV:62 μm)*

The work function mapping is performed in a similar way, but pixel per pixel, using

the protocol detailed in chapter 2 section 2.3.2. The coloured images presented through this section are maps giving the local work function obtained from the pixel per pixel error function fit at threshold for all samples, as can be seen in figure 4.2 b). Histograms of work function values are extracted, in order to determine accurately the average work function and the experimental uncertainty of each doped zone, determined by the FWHM of the peaks.

4.1.2 Work function mapping with laboratory excitation

4.1.2.1 Results

The work function mapping of the passivated samples is presented in figure 4.3.

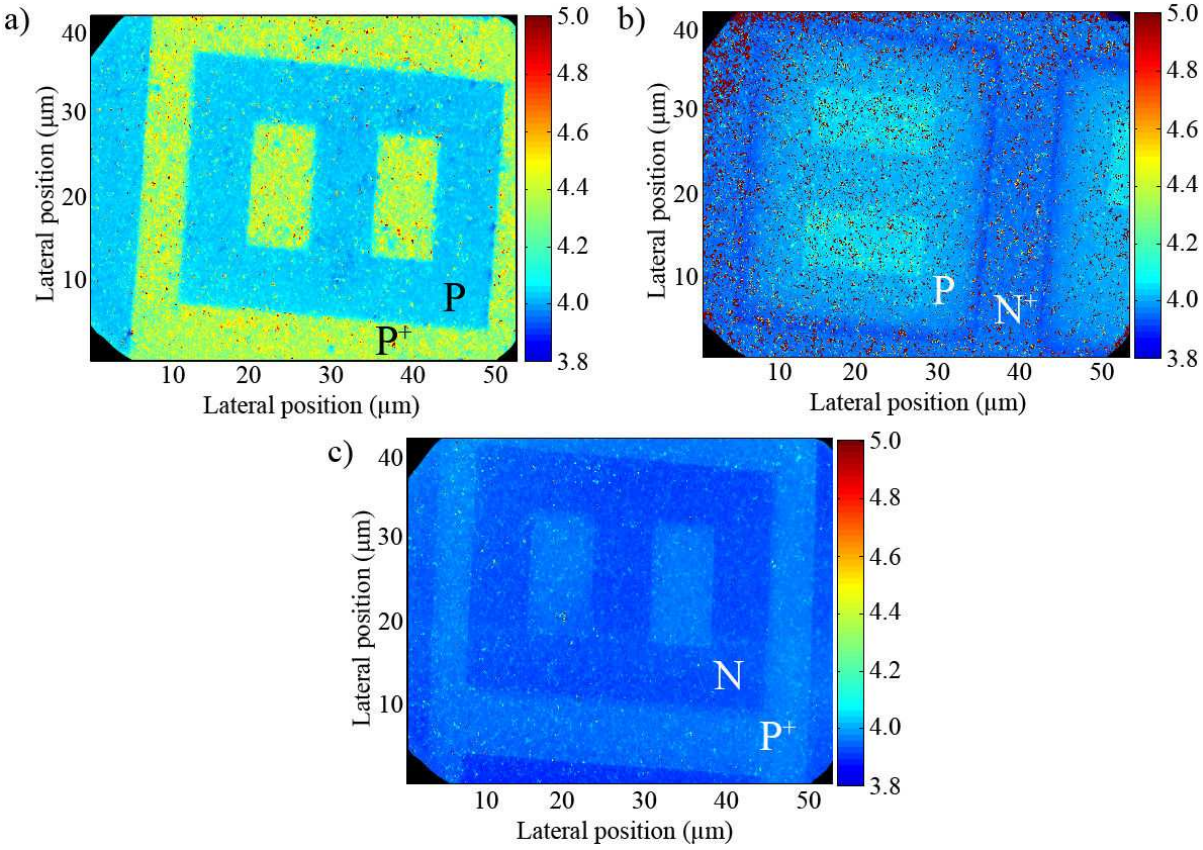

Figure 4.3: *Work function mapping (excitation: 1486.7 eV) after passivation: a) P^+/P, b) N^+/P, and c) P^+/N. The field of view is 62 µm.*

We have checked that the uncertainty was not greater than 0.03 eV. For each particular area of interest, we note a narrow distribution of the work function, the results being that the map reproduces the original shape of the patterns, as seen from the images.

Secondly, we notice noise on the maps. This is supposed to be due to the fitting method used in the MATLAB program to minimize the error between experimental and fitting values.

Lastly, focusing on the N^+/P sample, we observe a different work function value depending on whether the N^+ area of interest is a closed area (i.e. surrounded by P doping) or in an open zone. This behavior is not observed for the other samples. In chapter 5, we will interpret this specific phenomenon.

The values deduced from this mapping are presented in table 4.2.

Sample	P^+	P	N	N^+
P^+/P	4.30±0.02	4.17±0.02	-	-
N^+/P	-	4.15±0.03	-	4.00±0.03 and 4.08±0.03
P^+/N	4.16±0.02	-	4.11±0.02	-
WF	5.14	4.93	4.16	4.07

Table 4.2: *Work function values in eV measured from mapping after passivation.*

Based on equation 3.3, the last line of table 4.2 presents the theoretical work function values expected in flat band conditions for the different samples.

4.1.2.2 Interpretations

We start by comparing the experimental work function values obtained with the theoretical ones in flat band conditions, shown in table 4.4. Firstly, we observe a reasonably good coherence of the work function values for a similar doping in a different sample, except maybe for the N doping case, and, to a less extent, for the P^+ case.

Secondly, we comment on the work function values with respect to the theoretical ones. We observe an excellent agreement for N doping. However, the values obtained for the two P dopings are far from those expected. In case of P^+ doping, the value derived from mapping is 1 eV lower than the theoretical one, a difference corresponding to the silicon band gap. For P doping, the difference is also very high: 0.76 eV. We interpret these differences as be due to band bending arising from a non complete surface passivation. The influence of band bending on the measured work function is illustrated in figure 3.3: for P doping, strong band bending results in a strongly decreased work function, with respect to flat band conditions. For N doping, the variation is opposite.

We can relate tentatively the differences observed between theoretical and experimental values with a sample-dependent quantity of electronic surface states. A specific evidence of these surface states due to residual dangling bonds was shown in the XPS study of chapter 3. The high resolution Si $2p$ core-level spectra were shown to contain a spectral component, Si^*, which is assigned in the literature to various defects and arrangements in silicon atoms of the outermost surface layers. These defects are likely to induce electronic states within the gap which, in turn, produce band bending. This assumption is verified in table 4.3 which shows a qualitative correlation between the work function differences and the relative intensity of Si^* states related to the Si^0 states. Particularly, the table shows that for both N doping which exhibit a small work function difference with theory, the relative number of Si^* states is minimum. Conversely, for both P doping, we have a much higher Si^* proportion in relation with an higher work function difference.

Doping	P^+	P	N	N^+
Si^* proportion (%)	13.0	17.8	11.8	9.5
WF_{fb}-$WF_{exp.}$	0.98	0.76	0.05	0.03

Table 4.3: *Si^* proportion related to the Si^0 states and work function difference between experimental $WF_{exp.}$ and theoretical flat band case WF_{fb} for each doping type.*

This interpretation is based on the examination of core-level spectra for full wafer samples. In figure 3.24, we show that the shape of the Si^* component, corresponding mostly of the S_1 contribution, differs when considering patterned samples, more particularly for P^+ doping, we do not observe an important Si^* contribution. However, due to the low energy resolution of the analysis, we cannot exclude, on the pattern samples, the presence of structural defects (identified on synchrotron experiments by the S_2 and S_3 components [271, 272]) giving rise to a non negligible density of surface states.

We now compare for a same sample the work function shift $\Delta\Phi$ between a patterned zone and a substrate zone. We define the experimental work function shift, $\Delta\Phi$ as:

$$\Delta\Phi = \Delta\Phi_{pattern} - \Delta\Phi_{substrate}. \tag{4.1}$$

Similarly, we consider the same theoretical quantity $\Delta\Phi_{fb}$ in case of flat band conditions, based on the doping values measured by SIMS at 3 nm depth, already considered for the XPS study in chapter 3.

Sample	$\Delta\Phi_{fb}$	$\Delta\Phi$
P^+/P	0.21	0.13
N^+/P	0.86	0.07
P^+/N	0.98	0.05

Table 4.4: *Work function difference in eV between two doped zones within each sample, in theoretical flat band case (fb) and experimental case.*

Considering experimental measurements, all samples exhibit a difference between the two doped zones, but lower than expected in flat band conditions. For homojunctions, the difference between the theoretical and experimental shifts is only about 50% whereas it is much lower for the two heterojunctions. This has to be related to a cancellation effect due to the inverse variations of the band bending in P doped and N doped zones.

From the image contrast point of view, the work function relates the photoemission threshold of each doping type without taking into account the photoemission yield and thus, gives an estimation of the Fermi level position within the band gap. Thanks to work function maps, it is possible to localize easily zones with different doping.

These remarks indicate that though the passivation of the samples P^+/P, N^+/P, and P^+/N tends to remove both contamination and native oxide, as seen previously, it does not imply necessarily that flat band conditions are obtained. These first observations led on laboratory have allowed to make a first set of results. We complete this study of work function mapping by varying the photon energy thanks to synchrotron experiments on similar samples.

4.1.3 Work function mapping with synchrotron radiation

4.1.3.1 Acquisition conditions

The two nominal photon energies 130 eV and 700 eV were used with synchrotron radiation. The photon energy was calibrated by measuring the Fermi edge of the valence band of a clean silver sample. Figure 4.4 presents the two XPS spectra acquired for a) 700 eV and b) 130 eV. It is easy to determine the true energies: 700.3 eV and 128.9 eV.

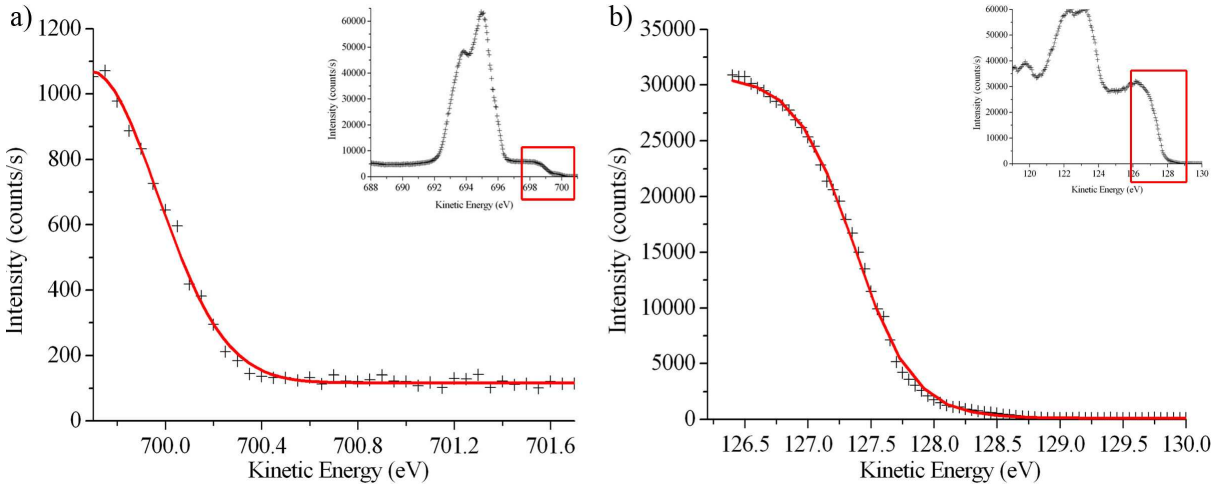

Figure 4.4: *Photon energy calibration on clean Ag sample for nominal photon energies a) 700 eV and b) 130 eV.*

For estimating the overall energy resolution, we take into account the spectral width of the photon source of the TEMPO beamline: this latter is calculated using the relation 2.21. We find respectively 0.14 eV at 700.3 eV and 62 meV at 128.9 eV.
Including the photon energy at 1486.7 eV, the sampling depth probed are summarized in table 4.5.

Photons energy (eV)	Sampling depth d (nm)
128.9	2.3
700.3	4.8
1486.7	8.8

Table 4.5: *Sampling depths depending on the photon excitation energy chosen.*

4.1.3.2 Results

For these experiments, passivation was performed just before imaging in the SOLEIL premises, in a dedicated chemistry laboratory. Despite a similar passivation protocol as for the laboratory experiments was used, the equipment at our disposal was not exactly the same.

For imaging, we have chosen the 'zero' shaped patterns, since these are present in large quantity at the sample surface, thus enabling to keep fresh areas for an increase

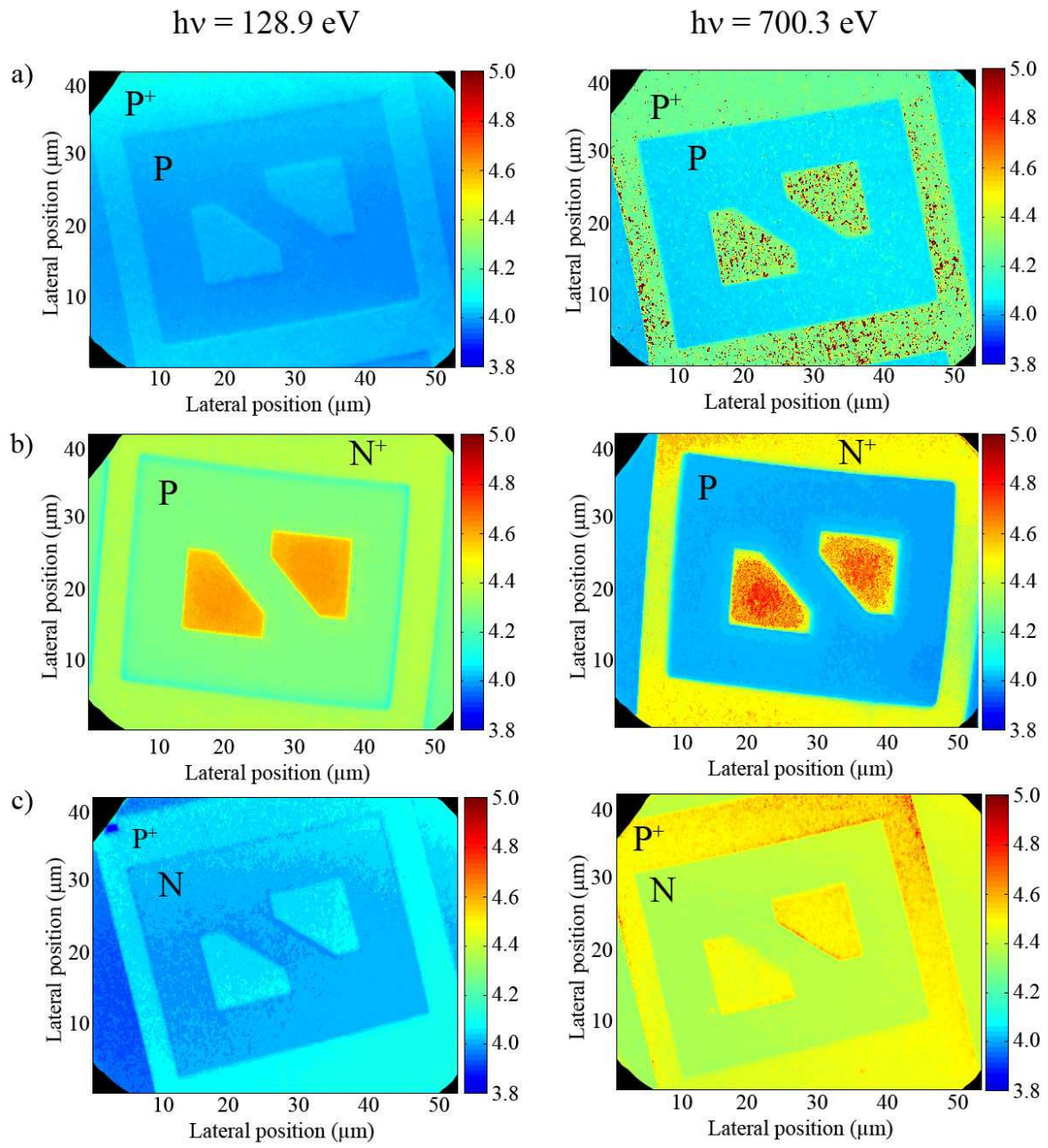

Figure 4.5: *XPEEM images at threshold for two photon energies 128.9 eV and 700.3 eV: a) P^+/P, b) N^+/P, and c) P^+/N. The field of view is 62 µm.*

reliability of the analysis. It is indeed notorious that surfaces exposed to synchrotron radiation can alter quickly with time [290].

Figure 4.5 presents the work function maps generated from image series acquired at two different excitation energies. The colour scale is the same as for figure 4.3.

4.1.3.3 Comments

Here again, the maps shows a clear work function contrast between the different doped zones, and reproduces the original shape of the patterns, whatever the photon energy. We can make similar comments as for the laboratory case: particularly the triple contrast is observed only for the N^+/P sample. However, the maps clearly show that the extracted work functions are different than the laboratory case. For the particular N^+/P case, this even leads to inverted work function shifts $\Delta\Phi$ between N^+ and P zones, the P work function being lower than the N^+ ones. This is observed for both photon energies. The values are presented in tables 4.6 and 4.7.

Sample	P^+		P	
	128.9	700.3	128.9	700.3
P^+/P	4.10±0.02	4.46±0.03	4.05±0.02	4.17±0.03
N^+/P	-	-	4.38±0.01	4.25±0.02
P^+/N	4.19±0.02	4.55±0.05	-	-
Flat band	5.14		4.93	

Table 4.6: *Work function values in eV measured from mapping after passivation for two photon energies 128.9 eV and 700.3 eV.*

Sample	N		N^+	
	128.9	700.3	128.9	700.3
P^+/P	-	-	-	-
N^+/P	-	-	4.44±0.01	4.56±0.03
P^+/N	4.16±0.01	4.42±0.02	-	-
Flat band	4.16		4.07	

Table 4.7: *Work function values in eV measured from mapping after passivation for two photon energies 128.9 eV and 700.3 eV.*

First, at a given photon energy we observe consistent values for the two zones having the same doping level. This is particularly true for P^+ doping where the work function shifts between P^+/P and P^+/N are less than 0.1 eV for a given photon energy. For P doping, the difference is more important at 128.9 eV where it reaches 0.33 eV. No comparison is possible for N dopings since we have only one measurement at our disposal.

The work function measurements, though consistent with each other, are far from those expected from flat band case. We are thus in presence of residual band bending. Depending on the doping type, we expect regarding figure 3.3:

- For a given N doping, the work function decreases with the photon energy.
- For a given P doping, the work function increases with the photon energy.

This is verified for P dopings, except for P substrate of N^+/P sample, but we have already underlined the inversion in the work function mapping between the two doped zones. For

N dopings, the expected behavior is not observed, the work function increasing with the photon energy increase.

Similarly to the previous section, we define the work function shifts $\Delta\Phi_{700.3}$ and $\Delta\Phi_{128.9}$ between a pattern zone and a substrate zone and compare them in table 4.8 with $\Delta\Phi_{fb}$ for the flat band conditions case.

Sample	$\Delta\Phi_{fb}$	$\Delta\Phi_{700.3}$	$\Delta\Phi_{128.9}$
P^+/P	0.21	0.29	0.05
N^+/P	0.86	0.31	0.06
P^+/N	0.98	0.13	0.03

Table 4.8: *Work function difference in eV between two doped zones within each sample, in theoretical case (th), and after passivation for photon sources of 1486.7 eV, 700.3 eV and 128.9 eV.*

We see that $\Delta\Phi_{700.3}$ is systematically much closer to $\Delta\Phi_{fb}$ than at 128.9 eV or in laboratory conditions (see table 4.4). This is an agreement with the assumption of the influence of SPV effect. Reported in chapter 1 (see section 1.5.2), it tends to flatten the bent bands at a semiconductor surface upon high intensity photon illumination. At the TEMPO beamline, the photon flux delivered by the undulator at 700.3 eV photon energy is higher by half a decade than the flux delivered by the undulator at 128.9 eV, which is consistent with a more important shift in work function between the two doped zones at the highest photon energy, assuming an influence of the SPV effect.

4.1.4 Summary

Work function mapping enables first to check the uniformity and the efficiency of the sample passivation. It is necessary to passivate the surface, but flat band conditions are not reached and residual surface states induce band bending. We have shown that for laboratory results, we find no inversion in terms of work-function value, whatever the sample considered, whereas an inversion has been observed at both 128.9 eV and 700.3 eV for N^+/P sample in synchrotron environment. Hence, work-function mapping is a good tool to estimate the cleaning efficiency, but one has to be careful for interpretations not to forget the influence of residual band bending which can invert work function measurements depending on the doping type and level.
Depending on the photon energy, we have seen that:

- For N doping, the work function value decreases with the photon energy.
- For P doping, the work function value increases with the photon energy.

The difference in work function between two doped zones reached better agreement with expected values in flat band conditions when the photon flux is important, i.e., when the SPV adds its contribution to unbend the bands.

4.2 Si 2*p* core-level microspectra and imaging

It is interesting now to show the NanoESCA capabilities in terms of pn junctions imaging with high lateral and energy resolution. All images were acquired in similar acquisition conditions. This section is dedicated to the analysis of core-level PEEM imaging and high resolution XPS spectra acquired on the Si 2*p* peak after passivation in laboratory and with synchrotron radiation obtained over these passivated doped samples.

4.2.1 Laboratory study

4.2.1.1 Si 2*p* XPEEM spectromicroscopy

Experimental conditions All images were acquired with similar acquisition conditions for all samples, summarized in table 4.9.

Parameters in laboratory	
Extractor voltage	12 kV
Contrast aperture	500 μm
Field of view	62 μm
Entrance slit width	1 mm
Pass energy	50 eV
Acquisition time	600 s
MCP voltage	950 V
Overall energy resolution	0.33 eV

Table 4.9: *General acquisition condition in laboratory for core-level study.*

We have chosen to privilegiate energy resolution which means a lower counting statistics. For this reasons, the imaging of the patterns used for work function mapping was difficult. In order improve the signal-to-noise ratio of P^+/P and P^+/N samples, the acquisition in laboratory was performed on a sample zone where one half of the field of view is covered by each doping type. However, for the sample with the highest Si^0 intensity (N^+/P sample), images were still recorded on the same patterned zone as the one used for secondary electron study.

Image series were recorded from 101.5 eV down to 98 eV with energy steps of 0.05 eV. Due to the low counting statistics, the energy filtered images are not presented. Instead, we present images representing the integrated silicon intensity, after Shirley background subtraction, generated using the Multipak software.

Results Figure 4.6 shows the contrast obtained on the Si 2*p* integrated images. In order to present all core-level images in the same conditions, we present the integrated intensity of Si^0 peak, in the energy range 98 eV to 101.5 eV. This signal corresponds to the true spatial distribution of the XPS silicon intensity on passivated silicon doped patterns.

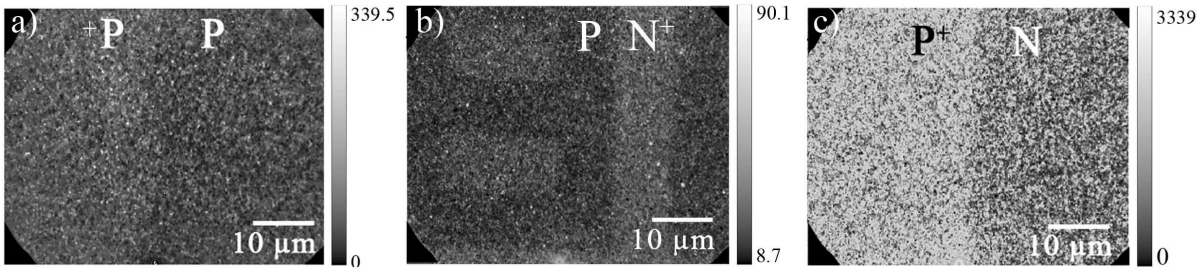

Figure 4.6: *Energy-filtered XPEEM images at the Si^0 core-level at 1486.7 eV photon energy (energy range: 98 eV to 101.5 eV).*

Comments We have checked in section 3.24 that no residual oxide was present on the sample surface. Therefore, the contrast obtained can not be explained in terms of different attenuations of the bulk substrate signal by a surface oxide. We still observe a contrast even if the surface is deoxidized. This difference in intensity between the two doped zones is unexpected since we assume that the silicon density is the same for all samples whatever the doping type and level.

The collected intensity from an area of interest I_{Si} can be written as:

$$I_{Si} \propto \Phi n_{Si} \sigma_{Si} \lambda_{Si} T_{Si} \ , \tag{4.2}$$

where Φ is the incident photon flux per second, n_{Si} is the atomic density, σ_{Si} the photoionisation silicon cross section at 1486.7 eV, λ_{Si} is the inelastic mean free path and T_{Si} the transmission on the double analyser for the Si $2p$ electrons.

Following this relation, we expect a similar intensity whatever the doping. Therefore the contrast observed in the integrated images cannot be explained in terms of intensity differences arising from bulk photoemission. In case of homojunction P^+/P, contrast is fainter than heterojunction but it is still observable: high doped pattern zones are brighter than substrate zone for all samples. We will see that similar contrasts in integrated core-level images are found with synchrotron radiation. In the following, with a detailed examination of the core-level microspectra we will tentatively explain the origin of this latter.

4.2.1.2 Si $2p$ microspectroscopy

Experimental conditions Spectra were recorded in microspectroscopy mode, due to the low signal-to-noise ratio of the spectra generated from the image series used in the previous section for the integrated core-level images. To increase this signal-to-noise ratio, spectra were acquired on field of view of 127 μm diameter in zones of homogeneous doping. The pass energy was 100 eV and the entrance slits width 1 mm, giving an overall energy resolution of 0.48 eV.

Results The different spectra are compared for each kind of patterned sample in figure 4.7. In this figure, we concentrate on the Si^0 component (binding energies range: 98 eV to 101.5 eV), the whole spectrum showing no oxide component being presented in figure

3.24. We observe Si 2*p* spectra for the two doped zones, with close binding energies, for a given sample. The shift in binding energy is the greatest on N^+/P sample whereas it is the smallest for P^+/N sample.

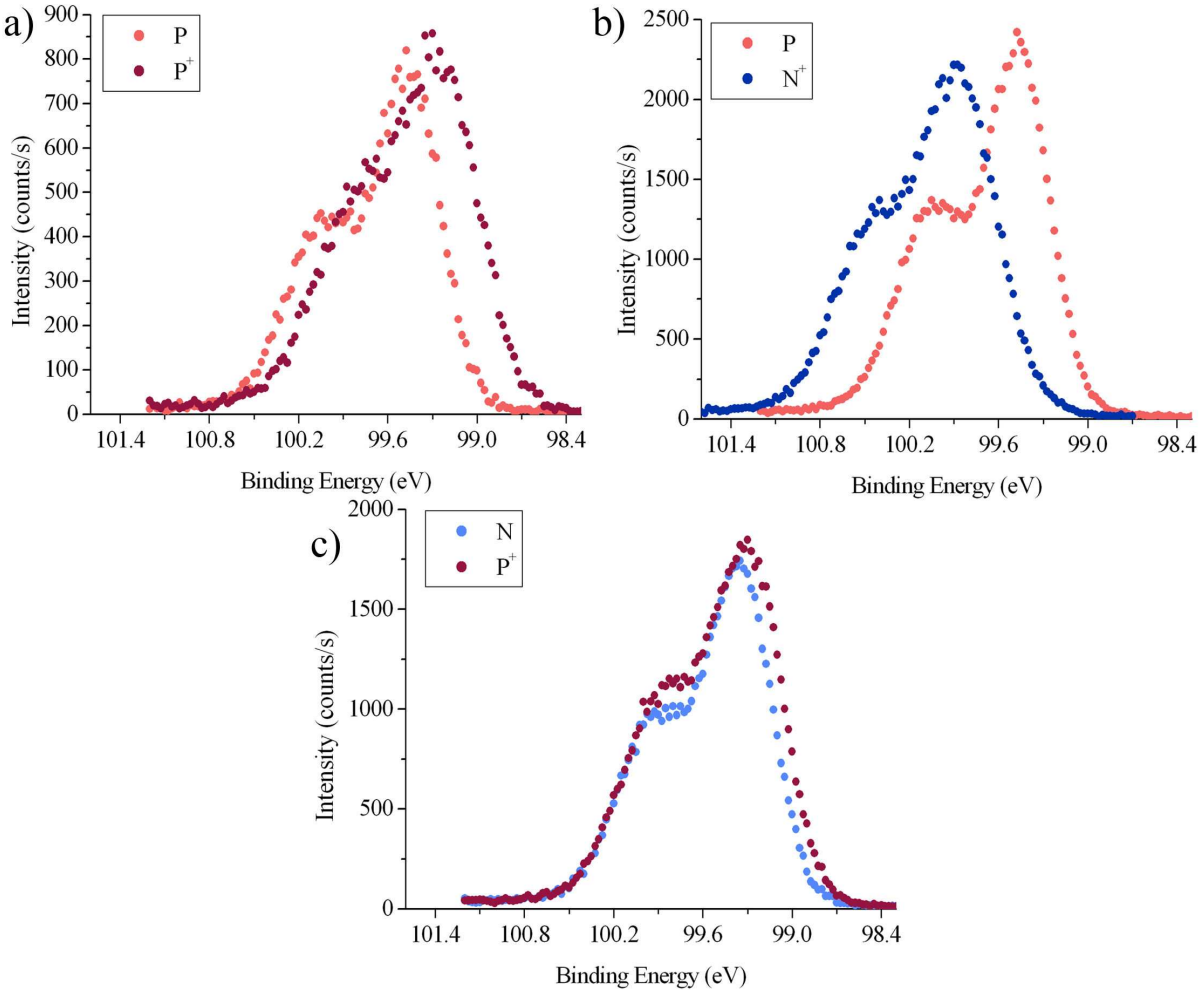

Figure 4.7: *Si 2p core-level microspectra for each kind of sample: a) P^+/P, b) N^+/P, and c) P^+/N. The photon excitation energy is 1486.7 eV.*

We note that the shape of the Si 2*p* spectra differs from one doping to an other. Moreover, for a given sample, we observe that the brightest zone in the integrated Si^0 images (see image 4.6) corresponds to the one who has the largest Si 2*p*, i.e., the highest integral intensity.

Applying the deconvolution protocol already established in chapter 3, we compare the different Si^0 values for the different doped zones after passivation. The Si^0 binding energies are presented in table 4.10 and the fitting of the spectra are shown in figure 4.8. For a given doped area, the core-level spectra were found to be the same from one sample to another, therefore, only one spectrum will be presented per doping condition. However, table 4.10 is complete: it summarizes the measured and calculated values for all doping type and level. Regarding the theoretical values, the binding energy for nearly intrinsic silicon being well-known and taken to be 99.35 eV.

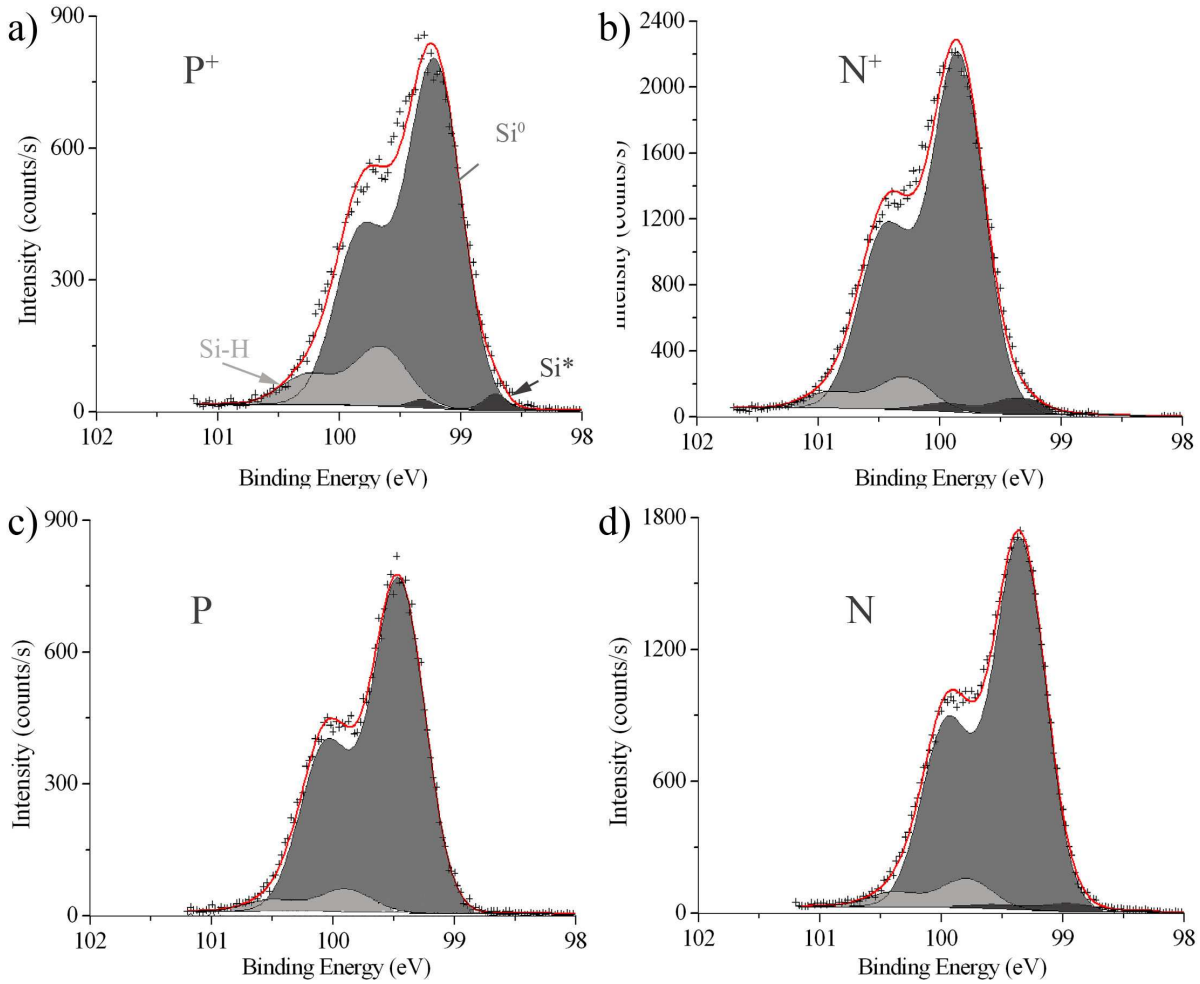

Figure 4.8: *Si 2p core-level deconvolution: a) P^+, b) N^+, c) P and d) N. The photon excitation energy is 1486.7 eV.*

Sample	P^+	P	N	N^+
P^+/P	99.21±0.26	99.46±0.25	-	-
N^+/P	-	99.47±0.25	-	99.85±0.26
P^+/N	99.30±0.25	-	99.35±0.25	-
Flat Band conditions	98.82	99.03	99.80	99.89

Table 4.10: *Si^0 binding energy in eV measured from XPS spectra. Theoretical values are also given for the doping level considered.*

Comments ***Binding energy analysis*** In table 4.10 we first observe an excellent reproducibility of the binding energy values for each doping between two different samples lower than 0.1 eV. We focus now on the difference of the measured binding energies with respect to the expected values given by flat band conditions (still estimated from the measured SIMS doping values at 3 nm depth). We observe that:

- For N^+ doping, a good agreement is found, and for N doping, the measured binding energy is 0.45 eV lower than the expected value.

- For P^+ and P doping, the binding energy is higher than the theoretical value by 0.44 eV for P doping and up to 0.48 eV for P^+ doping.

Hence, for N^+ doping, we can conclude that we are in nearly flat band conditions, whereas we observe consistent band bending for N, P and P^+ doping: i.e., lower binding energies for N doping, and higher binding energies for P doping. This last result on patterned samples is consistent with what we found from the work function mapping in the previous section (see table 4.3):

- The N and N^+ doping areas were found to have work function very close to the expected work function for flat band conditions.

- Conversely, for P doping, the work function difference of 0.76 eV was found, which is comparable to the difference in the binding energies observed in the core-level spectra. Therefore, a reasonable consistency is observed between the core-level results and the work function results derived from spectromicroscopy data.

Particularly, we observe a really small difference in terms of binding energy between the two doped zones for P^+/N sample. This results has to be related to the probing depth in these acquisition conditions: for a collecting angle of 90°, we have to deal with d=8.8 nm.
The depletion width of the band bending can be estimated thanks to the Debye Length L_D, which is a characteristic length: it is about $8L_D$ for silicon. Table 4.11 gives the widths that can be expected for the band bending at room temperature, i.e. 300 K.

Doping/bulk	Concentration (atoms.cm^{-3})	Debye Length (nm)	Depletion width (nm)
P^+	1×10^{19}	1.3	10.4
P	4×10^{15}	64.8	518.4
N	5.4×10^{17}	5.6	44.8
N^+	2×10^{19}	0.9	7.4

Table 4.11: *Debye Length and depletion width calculated for theoretical doping levels and types.*

The higher the doping, the stronger the band bending, and the smaller the depletion width. This will affect the binding energy measurements, if after passivation, there remains a residual density of surface states on the sample surface. Taking into account the band bending direction opposite for opposite doping type we can expect a reduction of the difference in terms of binding energies for different doping type and level.

Fitting of the XPS microspectra Referring to core-level spectra acquired on full wafer samples, we observe the non reproducibility of the passivation process since the proportions in terms of relative intensities of Si^0, Si-H and Si^* measured in table 4.12 are far from those obtained in table 3.6. In figure 4.8, we observe a small contribution of the Si^* component, even nil for P doping.

Particularly, the table 4.13 shows the Si * contribution relative to Si ^{0} one for each doping type, comparing with the difference in core-level binding energy between the

Sample considered	P^+/P		N^+/P		P^+/N	
Doping type	P^+	P	N^+	P	P^+	N
Si^*	11.43	-	3.72	-	3.52	2.14
Si^0	75.59	93.44	88.22	95.18	86.65	90.68
Si-H	12.98	6.56	8.04	4.82	98.3	7.18

Table 4.12: *Relative contributions of each peak relative to the total Si 2p peak intensity in P, P^+, N and N^+ doping type for the three samples of interest at 90°.*

Sample considered	P^+/P		N^+/P		P^+/N	
Doping type	P^+	P	N^+	P	P^+	N
Si^* proportion (%)	13	1	3.9	-	3.9	2.3
BE_{fb}-$BE_{exp.}$	-0.40	-0.43	+0.04	-0.44	-0.44	+0.45

Table 4.13: *Si^* proportion related to the Si^0 states and binding difference between experimental $BE_{exp.}$ and theoretical flat band case BE_{fb} for each doping type of each sample.*

measurement and the theoretical value expected from doping concentrations given by SIMS at 3 nm.

There is no systematically relation between the magnitude of the binding energy shifts and the Si * contribution: though the contribution of Si * is faint, we observe important shifts of the binding energy values with respect to expected values. This is to relate to the residual band bending whose depletion zone is probed in our acquisition conditions, but may also due to variations in the effective doping level. The passivation process might have removed the surface layers from the sample surface which had higher doping, explaining the shift with the theoretical value expected from doping concentrations given by SIMS at 3 nm. We have also to assume that the shift can be increased by a band bending induced by fluorine coverage [289].

4.2.2 Synchrotron radiation study

4.2.2.1 Si 2*p* spectromicroscopy: images

In this section, we focus on the same samples as the patterned ones imaged with secondary electrons for work function mapping (see subsection 4.1.3), taking advantage of the high photon flux of synchrotron radiation enabling a much higher counting statistics than in laboratory conditions.

Experimental conditions The acquisition conditions on the silicon doped patterns are summarized for both photon energies in table 4.14.

The image series over the Si 2*p* core-level were recorded from 105 eV down to 98 eV with an energy step of 0.05 eV.

Results In figure 4.9, we focus on the integrated intensity images acquired on the Si^0 peak, in the energy range 97 eV to 101.5 eV, and corrected from photoemission background. Figure 4.10 presents selected energy Si 2*p* images at two photon energies

Parameters	Synchrotron	
	700.3 eV	128.9 eV
Extractor voltage	12 kV	12 kV
Contrast aperture	70 μm	70 μm
Field of view	62 μm	62 μm
Entrance slit width	1 mm	1 mm
Pass energy	50 eV	50 eV
Acquisition time	120 s	60 s
MCP voltage	930 V	930 V
Overall energy resolution	0.244 eV	0.202 eV

Table 4.14: *General acquisition conditions in synchrotron environment.*

for two patterned samples. We consider the case of N^+/P and P^+/N sample to show a complete set of results.

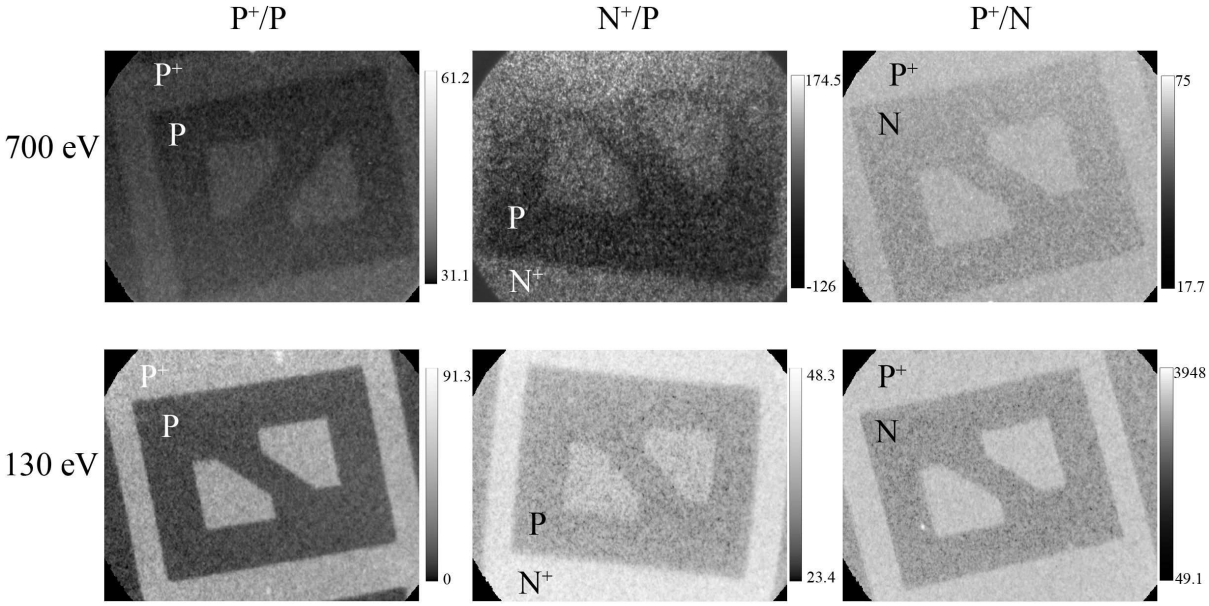

Figure 4.9: *Energy-filtered XPEEM images of the integrated Si^0 intensity for different excitation energies for P^+/P, N^+/P and P^+/N samples (energy range: 97 eV to 101.5 eV). At 700 eV, the higher Si 2p kinetic energy yields to a smaller field of view.*

Comments

- In figure 4.10, contrast variations between patterned and substrate zone appear for different kinetic energy. Contrast reversal appears on all doping types but for some energies, it disappears when the photoemission yield is the same for both dopings.
- In figure 4.9, we see that the intensity difference remains the same whatever the photon energy for both P^+/P and N^+/P samples. This has to be related to the relative shift and shape of the microspectra presented in the next section. However, for the particular case of N^+/P, the intensity difference changes. Moreover at

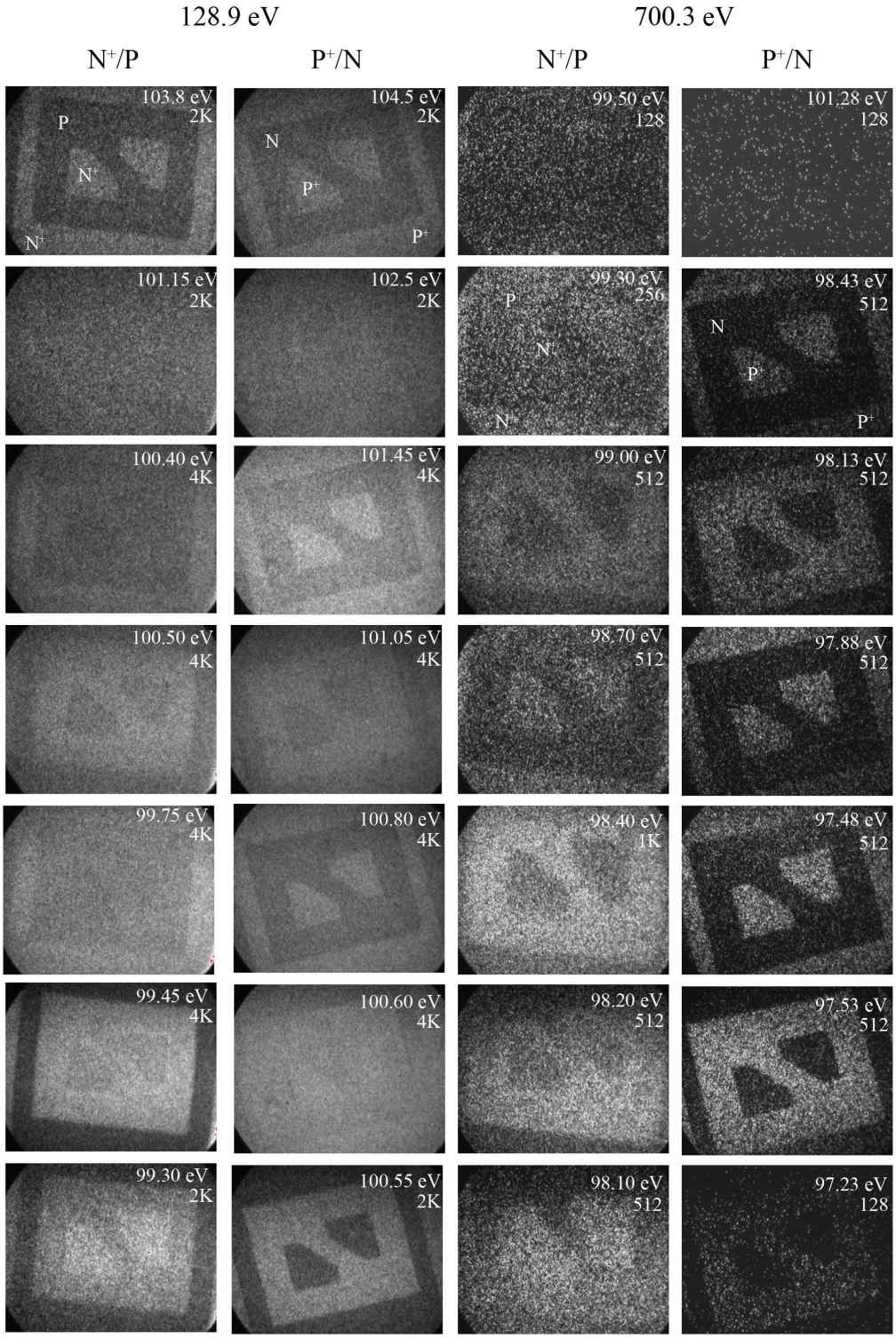

Figure 4.10: *Images of N^+/P and P^+/N samples taken from image series on the Si 2p core level for two photon energies a) 700.3 eV and b) 128.9 eV.)*

128.9 eV a triple contrast is observed, with the N^+ doped closed zones being darker than the open ones. As already mentioned in section 4.1, the N^+/P sample exhibits

this peculiar behavior of triple contrast in the work function maps. It is therefore reasonable to think that the inversion in the intensity differences at 700.3 eV and 128.9 eV is related to the triple contrast phenomenon. This will be discussed in more details in chapter 5.

- We can compare the core-level integrated images on Si^0 peak in both laboratory and synchrotron environment: we observe the same behavior, the highly doped pattern zone being brighter than the substrate one, whatever the photon energy. As for the laboratory case, we will explain the contrast in the integrated images by a difference in the width of the Si^0 peak, seen on the spectra presented in the next section.

4.2.2.2 Si 2*p* spectromicroscopy: spectra

Experimental conditions The acquisition conditions are as follows:

- Image series through the Si 2*p* core-level are acquired in 0.05 eV steps.
- Spectra were extracted from these image series after correcting for residual energy dispersion. The areas of interest were squares of 20 pixels per side, which corresponds to an area of (3.3×3.3) μm^2.

Three zones have been chosen: a substrate zone, an open pattern zone, and a closed pattern zone.

Results In figure 4.11 we present the Si 2*p* core-level microspectra for the three samples of interest at two photon energies. We note that the spectra at 128.9 eV show up oxide and suboxide components whose magnitude depends on the considered zone. The intensity of the oxide and suboxide components relative to the Si^0 one is weak. Considering a mean free path at 128.9 eV of 0.3 nm, the oxide thickness is less than one monolayer. Moreover, the residual oxide is non uniform on the sample surface, even within a zone of a tenth of microns: the surface chemistry appears thus to be very dependent of the area considered.

Comments A first remark about the microspectra acquired on P^+/N at a photon energy of 700.3 eV can be done: the binding energies seem to be shifted towards low values, down to 98 eV which are really far from the energies measured at 128.9 eV.

In the following, we will discuss about different comments that can be done on the spectra presented in figure 4.11, regarding: the peak shape, the intensity of the Si^0 components, the detailed spectra fitting, the binding energy shifts, the relation between some spectral components and the contrast obtained on images integrated over the whole Si2*p* peak.

Peak shape

- There is a residual oxide peak found for the most sensitive surface conditions at 128.9 eV. Therefore the passivation performed just before the synchrotron experiments at SOLEIL in the chemistry laboratory, did not remove completely the surface oxide. We note that the shape of the oxide part varies with the sample: for P^+/N, an important signal of suboxides is observed, this signal being much less

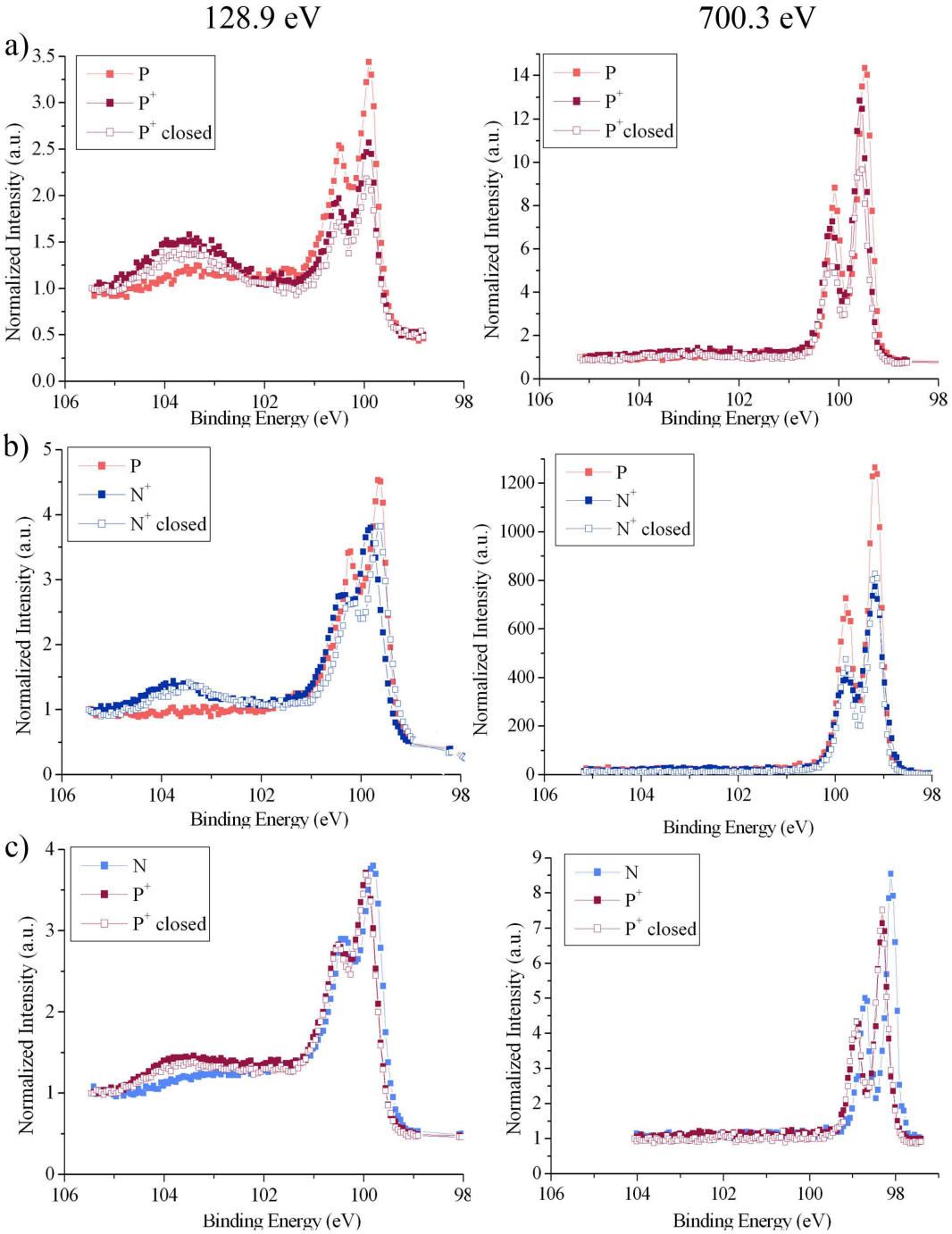

Figure 4.11: *Si 2p core-level microspectra for each kind of sample: a) P^+/P, b) N^+/P, and c) P^+/N. The photon energy is 128.9 eV on the left column and 700.3 eV on the right.*

important for both P^+/P and N^+/P samples. Moreover, we observe a non uniform deoxidation since the residual oxide peak is found systematically smaller for the substrate zone than for the pattern regions.

- Regarding the width of the Si^0 component, we find systematically a broader peak at 128.9 eV than at 700.3 eV. This is related to the differences in sampling depth

with the surface components Si-H, S_1, S_2, S_3 (see table 3.7 in passivation literature section of chapter 3) being more pronounced, relative to the Si^0 peak, at 128.9 eV than at 700.3 eV.

- The substrate peaks are always better resolved in energy than the epitaxial doped zone, whatever the photon energy. This can be related to the proportion of S_3 component in Si*, in the Si $2p$ core-level.

Si^0 intensity Despite the areas selected for the extraction of the Si $2p$ microspectra have exactly the same area, we observe a difference in the intensity of the Si^0 peak with respect to background at both energies:

- At 700.3 eV, we note that the Si $2p$ spectra intensity of the substrate zone is systematically higher than the intensity of the patterned zones. We can relate this difference to the intensity differences observed in the integrated images presented in figure 4.9: despite the higher intensity of the Si^0 component in the substrate, the brightest zone in the integrated images is always the highly doped pattern zone presenting at first glance a lower intensity of the Si^0 component.

- At 128.9 eV photon energy, the differences in the Si^0 intensity cannot be directly related to the integrated images intensity differences due to the oxide signal which changes depending on whether substrate or pattern zone are considered. However, the brightest zone in the integrated images is always the highly doped pattern zone.

Spectra fitting Referring to table 3.7 we have chosen to include the S_3, S_2 and S_1 surface components though their energy shift relative to the Si^0 peak is at the limit of our instrument capabilities in terms of energy resolution.

The Si $2p$ peak at 700.3 eV is rather simple: it shows the bulk silicon Si^0, the bonds Si-H and the S_2 and S_3 components. The spectra at 128.9 eV is more complex. Applying the basic five component deconvolution, simulating the Si^0, silicon sub-oxides and Si^{4+} components and adding the peaks S_3, S_2 and Si-H is not enough. A component S_1, shifted by -0.4 eV relative to the bulk Si peak is necessary. The origin of these three components has already been mentioned. These latter are due to defects or to different layer beneath the top most silicon layers: either symmetric or asymmetric dimers, dangling bonds of the rest atoms, silicon adjoining vacancies, voids or interstitial silicon, or the silicon second and third layers (see 3.3.4.3).
The parameters for each components are given in table 4.15 for the two photon energies. In the following figure 4.12, we present the fitting of the core-level microspectra for each doping type, since, for a same doping type, the spectra are similar.

We present the binding energy measurements without correction for the SPV since we do not know how this latter acts with a non-complete passivated surface. Moreover, due to the different oxidation degrees from a sample to another, we were not able to estimate the variation in terms of SPV values depending on the oxide thickness.

Tables 4.16 and 4.17 show the concentration ratio of each component of interest around the Si^0 peak, i.e. without considering the oxide components. We present separately the S_3 component shifted towards 0.2 eV relative to the Si^0 peak, and add the contributions of S_2 and S_1 (named Si*) shifted towards negative values with respect to Si^0.

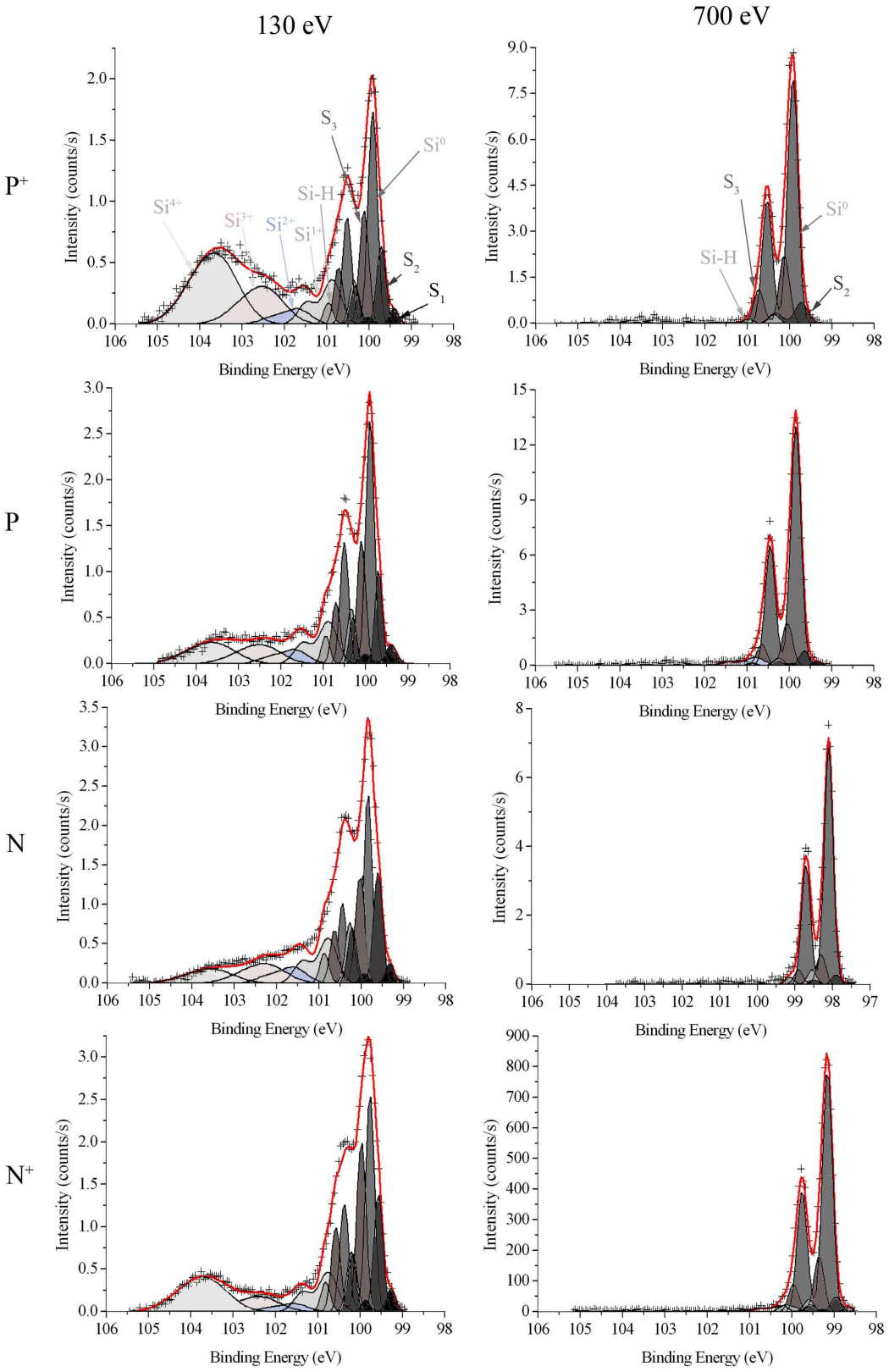

Figure 4.12: *Fitting of spectra acquired for two photon energies.*

Peak	128.9 eV		700.3 eV	
	Energy position	FWHM	Energy position	FWHM
S_1	-0.4	0.25	-0.4	0.28
S_2	-0.2	0.25	-0.2	0.28
S_3	+0.2	0.25	+0.2	0.28
Si^0	0	0.25	0	0.28
Si^1	+0.95	0.5	+0.95	0.5
Si^2	+1.7	0.7	+1.7	0.7
Si^3	+2.34	1.0	+2.34	1.1
Si^3	+3.6	1.13	+3.6	1.15

Table 4.15: *Fitting parameters taken for the different Si 2p components. The energy position is given relative to the Si^0 component. The spin-orbit splitting is fixed at 0.603 eV and the peak shape is chosen 100% gaussian.*

Sample considered	P^+/P		N^+/P		P^+/N	
Doping type	P^+	P	N^+	P	P^+	N
Si^*	20.39	20.0	23.91	52.16	13.97	24.63
S_3	**24.34**	23.33	**28.99**	13.27	**28.68**	20.15
Si^0	46.05	46.19	36.96	24.69	37.87	43.66
Si-H	9.22	7.48	10.14	9.88	19.48	11.56
Si^0 $BE_{exp.}$	99.92	99.90	99.77	99.80	99.89	99.82
Si^0 $BE_{fb.}$	98.82	99.03	99.89	99.03	98.82	99.80
Si^0 $BE_{fb.}$-$BE_{exp.}$	-1.1	-0.87	+0.12	-0.77	+1.07	-0.02

Table 4.16: *Si^*=Si_1+S_2, S_3 and Si-H proportions (%) related to the Si^0 states and experimental binding energy $BE_{exp.}$ for Si^0 at 128.9 eV.*

Sample considered	P^+/P		N^+/P		P^+/N	
Doping type	P^+	P	N^+	P	P^+	N
Si^*	9.34	6.17	16.26	42.09	9.822	3.17
Si_3	**14.07**	13.92	**31.22**	10.31	**12.50**	10.29
Si^0	73.48	78.18	48.56	44.91	74.70	81.27
Si-H	3.11	1.74	3.96	2.69	2.98	5.27
Si^0 $BE_{exp.}$	99.93	99.85	99.14	99.22	98.32	98.11
Si^0 $BE_{fb.}$	98.82	99.03	99.89	99.03	98.82	99.80
Si^0 $BE_{fb.}$-$BE_{exp.}$	-0.82	-0.52	+0.75	-0.19	+0.50	+1.69

Table 4.17: *Si^*=Si_1+S_2, S_3 and Si-H proportions (%) related to the Si^0 states and experimental binding energy $BE_{exp.}$ for Si^0 at 700 eV.*

Binding energies We first note less band bending $BE_{fb.}$-$BE_{exp.}$ at 700.3 eV than at 128.9 eV, which is expected from figure 3.3 when probing deeper the surface, the band bending tends to decrease.

We observe for all samples an inversion in terms of binding energies:

- Figure 4.12 presents well the inversion: when analysing the figure from top to

bottom, i.e. from highly P doping to highly N doping, we observe a shift of the spectra towards low binding energies, whereas we expect the opposite behavior.

- The P^+ binding energy is higher than P and N and the N^+ is lower than P.
- For P^+/P sample, the Si^0 binding energy of P^+ is greater than the P one. This shows, with respect to figure 3.3, that the band bending at the P^+/oxide interface has shifted the Si levels sufficiently so that the 2 p core-level in the P^+ region has a higher band bending than in the P region, i.e., the relative difference is smaller than the expected flat band difference (0.08 eV at 700.3 eV and 0.02 eV and 128.9 eV for experimental values ($BE_{fb.}$-$BE_{exp.}$) against -0.21 eV in flat band case). This also implies that the $2p$ binding energy measured is that of the bent bands, consistent with the XPS probing depth with respect to the expected depletion width. However, such inversion was not observed in work function mapping for these two energies.
- The same remark can be done for P^+/N sample, where the Si^0 binding energy of P^+ is greater than the N one. This inversion has not been observed in work function mapping. This can also be explained by a stronger band bending for the highly P^+ doped zone than for the lightly N zone, which creates an inversion in terms of binding energy on the interface oxide/sample.
- For N^+/P sample, we have found trends for the two photon energies in good agreement with work function mapping: the inversion type is present, the P binding energy being higher than the N^+ one.

Moreover, we observe that the binding energy of P doping decreases with increasing the photon energy, except for P^+ doping in P^+/P sample where it remains nearly constant. This behavior is the one expected when probing the residual band bending for P doping, as seen in figure 3.3. Conversely, for N dopings, we expect the opposite behavior, the Si^0 binding energy increasing with the photon energy increase. We have already observed this unexpected behavior in work function mapping (see 4.1.3).

Image contrast To finish, we note a correlation between fit and integrated images. In tables 4.16 and 4.17, we have highlighted the most important contribution within the Si $2p$ spectra, for the two doped zones of each sample. Thus, the brightest zone in the integrated Si^0 core-level image is the one where the proportion of S_3 is the most important. The different contributions below the Si^0 peak, i.e. S_1 and S_2 are summarized in the component Si^*. Laboratory spectra have shown that the relative intensity of Si^* component, determine the brightest zone in the core-level image: the higher its contribution in a doped zone, the brightest this zone. This remark is also verified on integrated images taken on Si $2p$ peak in laboratory: the brightest zone is the one where the Si^* component is more important. However, it concerns in this case the S_1 component whereas the S_3 peak is integrated in the Si^0 peak.
With synchrotron radiation, we have found the same behavior, not considering Si^*, but the S_3 component, observed 0.2 eV above the Si^0 peak. It is assumed to be interfacial components due to a possible effect of oxygen second neighbor on the Si 2p binding energy. The higher the relative intensity of the S_3 component with respect to the Si $2p$ peak, the brighter the zone, whatever the relative intensity of the Si^* component.

Jolly *et al.* consider that S_2 and S_3 can also be related to silicon close to the interface between the native oxide and the surface, negatively charged with respect to the bulk. We assume thus, that the most important contribution between S_2 and S_3 on the one side, and S_1 on the other depends on the sample surface state. As a result, if the passivation is not complete, for a given oxidation state, one contribution will be stronger, enhancing the contrast in core-level imaging.

4.2.3 Summary

Thanks to the spatially resolved core-level measurement, we have shown that residual band bending is dependent on the doped zone considered. It is important to understand the influence of passivation on the sample surface at the spectroscopic level. XPS microspectroscopy and spectromicroscopy performed respectively in laboratory and synchrotron environment have outlined the difficulty to obtain similar surface states. As a result, and depending on the sampling depth, different oxidation states are observed on the sample surface, varying from a sample to another. Hence, we do not observe electronic states in flat band conditions, but we have to deal with a residual band bending. In laboratory, we observe Si $2p$ binding energy shifts in good agreement with the expected band bending direction depending on the doping type and level. Moreover, these results are in good agreement with those obtained using secondary electrons.
We expect using synchrotron radiation, that the variation of photon energy probes this band bending, i.e.:

- For P doping, the binding energy measured decreases with the photon energy increase.

- For N doping, the binding energy measured increases with the photon energy increase.

We can assume thanks to the core-level measurements that there is a residual band bending that can be probed when varying the photon excitation energy. However, though this is verified for P dopings, we observe an unexpected behavior for N doping, already observed using secondary electron with synchrotron radiation.

Regarding the contrast on integrated Si^0 images, for all samples, we have seen that the highly doped zone was always the brightest. Thanks to the detailed fitting of the microspectra, we have shown that the contrast in the integrated Si^0 images is due to subtle changes in the outermost surface layers.

4.3 Valence band microspectroscopy

From the previous results, we have seen that depending on the surface considered, residual band bending was more or less pronounced. In this section we bring additional experimental evidence from the analysis of the VBM by VUV and synchrotron experiments.

4.3.1 Laboratory He I excitation

4.3.1.1 Experimental conditions

Valence band microspectra have been acquired near the top of the valence band up to the Fermi level in laboratory, using the HeI excitation source at 21.2 eV. The experimental conditions are:

- The pass energy of the double hemispherical analyser is 50 eV,
- The slits width is 1 mm.
- The spectra are the result of 20 scans over the binding energy range from 13 eV to -1 eV, with a step of 0.025 eV.

This analysis performed in laboratory with the HeI source is carried on the same passivated samples as those used for core-level and threshold spectromicroscopy (see sections 4.1.2 and 4.2.1.2).

4.3.1.2 Results

The spectra were corrected from the HeI β at 23.09 eV, and HeI γ at 23.74 eV contributions emitted from the Helium source, respectively 1.8% and 0.5% of the HeI α intensity at 21.2 eV otherwise, in some cases, negative values of the Fermi energy can be found.
In figure 4.13, a small but significant contribution from the Si $3p$ orbitals, situated around 3 eV below the Fermi level which comes from the underlying substrate. We can extract from these spectra the upper edges of the Si $3p$ orbitals. These Valence Band Maximum (VBM) are determined by taking intersection between the best straight line fitting the Si $3p$ leading edge and the base line. A first determination of the valence band onsets is presented in table 4.18 for each kind of sample.

Sample	P^+/P		N^+/P		P^+/N	
Doping type	P^+	P	N^+	P	P^+	N
Si $3p$	0.44	0.61	0.76	0.37	0.45	0.52
Si $3p_{fb}$	0.03	0.23	1.11	0.23	0.03	1.02
Si $3p_{fb}$-Si $3p_{exp.}$	-0.41	-0.38	0.35	-0.14	-0.42	0.50
Core-level Si^0_{fb}-$Si^0_{exp.}$	-0.40	-0.43	0.04	-0.44	-0.48	0.45

Table 4.18: *Valence Band Maximum extracted on P^+/P, N^+/P and P^+/N after passivation at 21.2 eV.*

4.3.1.3 Comments

We compare in the same table 4.18 the experimental Si $3p$ onsets, to those expect in flat band conditions, Si $3p_{fb}$ defined as:

$$Si3p_{fb} = \frac{E_{gSi}}{2} - \Delta E_{Fdoping}, \tag{4.3}$$

where E_{gSi} is the silicon band gap.

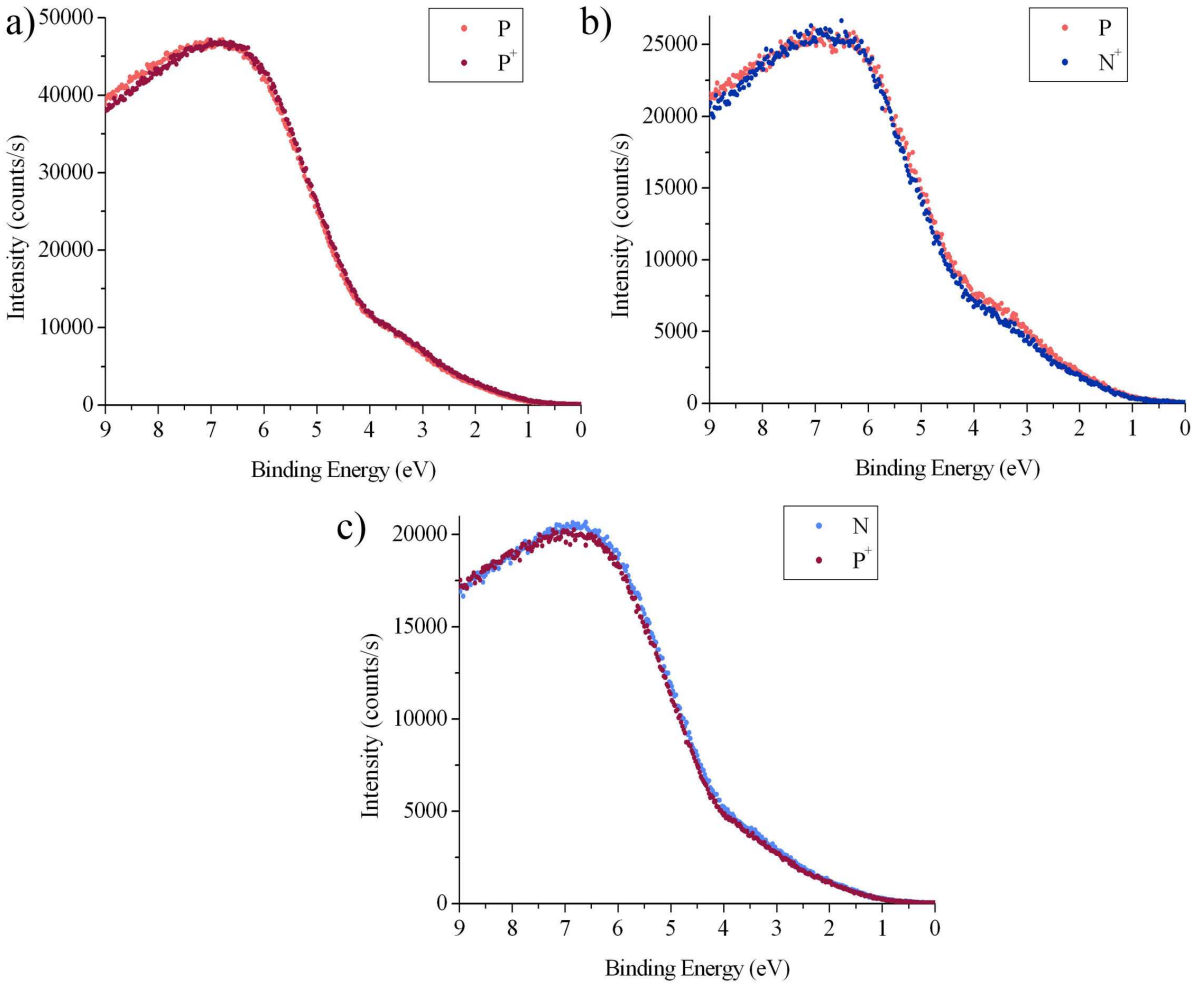

Figure 4.13: *Top of valence band spectra acquired for the four samples types, before and after passivation in laboratory, using an He I lamp: a) P^+/P, b) N^+/P, and c) P^+/N.*

The VBM measured are far from the expected values in flat band conditions, but are in good agreement for a given doping type. The trend of the VBM variation with doping type is in good agreement with what expected: for a given sample, the VBM of P doping is lower than the one of N doping. Moreover, for a P doping, the higher the doping, the lower the VBM, and for a N doping the higher the doping, the higher the VBM.

Observing the difference between experimental VBM and theoretical one Si $3p_{fb}$-Si $3p_{exp.}$, we measure shifts in good agreement with the difference found at core-level for each sample between experimental Si^0 binding energy and theoretical one (see table 4.10). Those shifts are recalled in last line of table 4.18. The band bending measured for each doping type and level is in good agreement with the one probed at core-level.

4.3.2 Synchrotron excitation

4.3.2.1 Experimental conditions

This analysis is carried on the same passivated samples as those observed at core-level and threshold with the synchrotron source at 128.9 eV and 700.3 eV. The spectra are acquired from 5 eV to -2 eV by step of 0.025 eV.

4.3.2.2 Results

Valence band spectra recorded in synchrotron environment on passivated samples are presented in figure 4.14. The Si $3p$ valence band onset is determined by the sample protocol as previous section i.e. extrapolating the upper edge of the peak to zero.

4.3.2.3 Spectra analysis

The Si $3p$ orbitals are clearly visible at 128.9 eV, however, their contributions can vary from a doping type to another:

- On the P^+/P, their intensity is slightly more important in the P substrate zone, than in the highly p-doped zone. This is to put in relation with the Si $2p$ core-level spectra acquired at the same photon energy in figure 4.11. The residual oxide present on the sample surface at this energy is more important on the P^+ zone than on the P one: it is obvious that the thicker, the better hiding the Si $3p$ density of states.

- The same remark can be done on the N^+/P sample, the residual native oxide being more important on the highly N^+ zone, the contribution of the Si $3p$ orbital is smaller, compared to the P bulk one.

- The 3 p intensities of the two doped zones in sample P^+/N, are similar, suggesting a more homogeneous passivation.

- At 700.3 eV, the valence band spectra acquired on P^+/N sample present, as for Si $2p$ spectra shift towards low binding energies, giving a negative VBM. It seems that at this photon energy, for this sample, the results are not correct and cannot be taken into account.

In terms of VMB, tables 4.19 and 4.20 summarizes the values interpolated from the spectra for the two photon energies.

Firstly, we focus on a given doping and a given photon energy, without considering the P^+/N sample at 700 eV due to its important shift not understood. We observe that the VBM measured are in good agreement, with a difference less than 0.2 eV.

Secondly, we observe at 128.9 eV an inversion in terms of VBM for a given sample, either P^+/P or P^+/N: the VBM of the P^+ doping should be less than the one of the P and N dopings, which is not observed. However, for N^+/P sample, the VBM measured of the N^+ doping is more than the one of the P doping, as expected. At 700.3 eV, the good trend is observed for all samples.

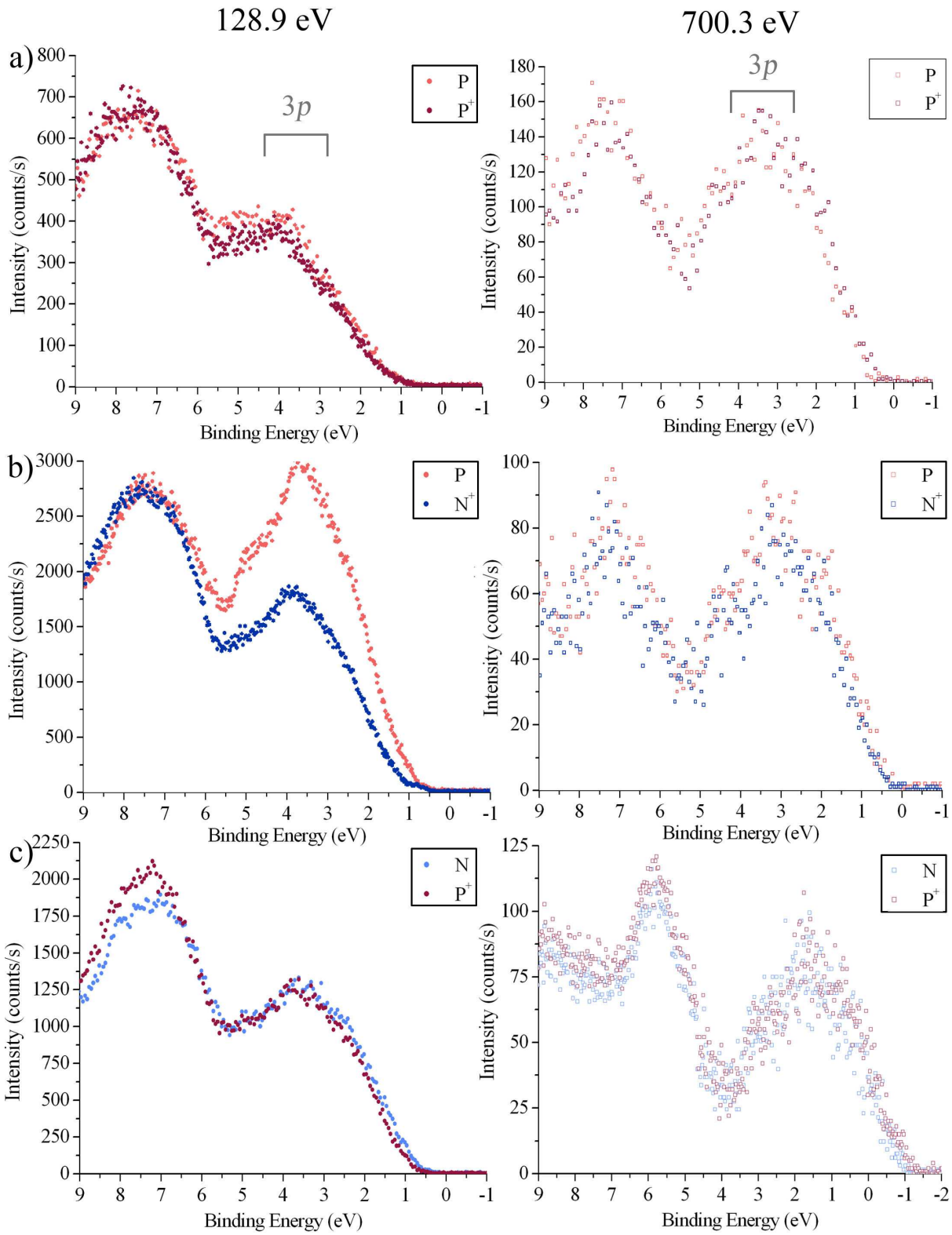

Figure 4.14: *Top of valence band spectra acquired for the three sample types after passivation for two photon energies 128.9 eV and 700.3 eV, for: a) P^+/P, b) N^+/P and c) P^+/N.*

Sample considered	P^+/P		N^+/P		P^+/N	
Doping type	P^+	P	N^+	P	P^+	N
Si $3p_{exp.}$	0.75	0.71	0.90	0.62	0.65	0.45
Si $3p_{fb}$	0.03	0.23	1.11	0.23	0.03	1.02
Si $3p_{fb}$-Si $3p_{exp.}$	-0.72	-0.48	+0.21	-0.39	-0.62	+ 0.57
$BE_{fb.}$-$BE_{exp.}$	-1.1	-0.87	+0.12	-0.77	+1.07	-0.79

Table 4.19: *Valence Band Maximum extracted after passivation at 128.9 eV on P^+/P, N^+/P and P^+/N.*

Sample considered	P^+/P		N^+/P		P^+/N	
Doping type	P^+	P	N^+	P	P^+	N
Si $3p_{exp.}$	0.28	0.55	0.35	0.20	-0.7	-1.2
Si $3p_{fb}$	0.03	0.23	1.11	0.23	0.03	1.02
Si $3p_{fb}$-Si $3p_{exp.}$	-0.25	-0.32	+0.76	+0.03	+0.73	+2.22
$BE_{fb.}$-$BE_{exp.}$	-0.82	-0.52	+0.75	-0.19	+0.50	+0.92

Table 4.20: *Valence Band Maximum extracted after passivation at 700.3 eV on P^+/P, N^+/P and P^+/N.*

What clearly appears also, is that the difference between experimental valence band onsets and theoretical ones are important whatever the samples. We expect a VBM shift between two doped zones within a sample to be in the same range of values than core-level shifts measured in section 4.2.2, and recalled in last line of tables 4.19 and 4.20, but we observe larger shifts. Moreover, some shifts present even a sign inversion, specially P^+/N sample at 700.3 eV and N^+/P sample at 128.9 eV.

We also note, that we probe the band bending when varying the photon energy: the VBM of P dopings decreases with the photon energy increase. However, we do not observe an increase of the VBM for N dopings when increasing the photon energy, but a decrease of the VBM, like a P doping zone.

4.3.3 Summary

The determination of experimental band offsets is an other way to probe the band bending at the oxide/semiconductor interface. We have found measurements in good agreement for core-level and VMB shifts from data obtained in laboratory. However, we have found unexpected variations in terms of VBM determination with synchrotron radiation. We expected the trend:

- For N dopings, the VBM increases with the photon energy increase.
- For P dopings, the VBM decreases with the photon energy increase.

However, we find a similar behavior for N doping as those mentioned at secondary electron and Si $2p$ core-level levels, i.e. that N dopings behave like a P doping.

4.4 Conclusion

In this chapter, we performed three kind of energy-filtered XPEEM analyses on our micron-sized, passivated, patterned silicon surfaces : (i) spectromicroscopy at threshold with secondary electrons, (ii) high-resolution Si $2p$ core-level and valence band microspectroscopy and (iii) high-resolution Si $2p$ core-level spectromicroscopy. In each case, both laboratory and soft X-ray synchrotron excitations were used for refining the surface sensitivity and increasing the lateral and energy resolutions.

Spectromicroscopy with secondary electrons enabled us to generate work function maps of the doped silicon patterns by a pixel-to-pixel fitting of the photoemission threshold. From a qualitative point of view, these maps first exhibit a narrow distribution of the work function and reproduced the expected shape of the doped patterns, thereby pointing on the uniformity of the doping at the microscopic level. Second, they highlight systematically, independent of the excitation energy, a sample-dependent work function contrast behaviour from the close doped zones : for both P^+/P and P^+/N samples, both close and opened zones had the same work function ; however, in the particular case of the N^+/P sample, the work function of the close zone is higher than in the opened zone, yielding a 'triple contrast' in the image. Therefore, we show that the work function contrast can be, depending on the doping combinations, highly dependent on the geometry of the observed doped patterns. This triple contrast will be interpreted in chapter 5.

From a quantitative point of view, we observed sample-dependent differences of the measured work function with respect to the expected value determined from the doping level measured by SIMS at 3 nm depth (see chapter 3) and for flat band conditions. With laboratory excitation, the differences are minimal for N doping, but are in the 0.8-1 eV range for both P and P^+ doping. Therefore, for the patterned zones with high N and P doping, we observe that flat band conditions are not reached. This influences in an important way the resulting pattern/substrate contrast in both work function and energy-filtered threshold images. With synchrotron radiation, the difference with the flat band value follows a similar trend, however it is reduced in case of significant higher source flux (700.3 eV) compared to lower ones (128.9 eV). This is interpreted in terms of surface photovoltage with a resulting decrease of the magnitude of the band bending.

Regarding Si $2p$ core-level analyses, we followed a combined spectromicroscopic, microspectroscopic and imaging approach focusing on the contrast obtained in images of the integrated Si^0 intensity ('integrated Si^0 images'). For both laboratory and synchrotron excitations, the highest energy resolution (respectively 330 and 200-244 meV) ever considered for imaging silicon patterned structures were used.

First, similarly to the work function images, the triple contrast on the N^+/P sample is observed again in the integrated Si^0 images.

Second, whatever the excitation energy, we find an unexpected pattern/substrate contrast in the integrated Si^0 images which cannot be explained by a different attenuation of the photoemitted intensity due a surface oxide, since the micro- Si $2p$ spectra reveal no

or very little oxide ($<$ 1 ML) in the ultimate surface-sensitive conditions (hν=128.9 eV). Instead, a more or less defective and hydrogen-passivated outermost surface layer, inducing a variable overall width of the Si 2p core-level, is found responsible for the observed contrast.

The H-passivated features in the Si 2p micro-spectra, along with the defective states already introduced in chapter 3 on the full-wafer samples (Si^* as possible dimer states reported by various works in the literature), are clearly evidenced thanks to the very high energy resolution of the analysis at the microscopic level. The evidence of these defective silicon surface states in a proportion depending on both the sample and the pattern/substrate zone, (between 13% and nearly 50% the Si^0 intensity) brings support to our previous assumption of measured local work functions influenced by a more or less pronouced band bending.

Such a band bending is further consistently evidenced from the measured Si 2p binding energies in core-level spectromicroscopic and valence band micro-spectroscopic data. However, it remains difficult to make a systematic quantitative correlation to relate the magnitude of the band bending and the overall quantity of defect states. Nevertheless, we have shown that the contrast in Si 2p core-level integrated images of carefully deoxized surfaces contain information related to differences in the outermost surface silicon layer.

Chapter 5

Discussion of the energy-filtered XPEEM imaging of pn junctions

Contents

Energy-filtered XPEEM technique is used in this thesis to characterize pn junctions through the experiments carried out on silicon doped samples, by acquiring image series in spectromicroscopy mode. However, though we use image series at different kinetic energies to extract electrical and chemical informations, we have not yet considered the contrast in secondary electron itself. Hence, we focus now on a brief study of contrast at threshold with the energy filtered PEEM, regarding the doping type and level of our silicon doped samples. Chapter 5 starts by presenting the results of this study and highlights a peculiar behavior that has been observed on one of our sample of interest: the N^+/P case.

Previous chapters have also shown the full field imaging capabilities to extract information of prime interest with good lateral and energy resolutions. However, it is necessary to take into account the presence of a lateral electric field across pn junctions. Hence, we focus on their influence on PEEM imaging: SIMION simulations of pn junctions observed by PEEM are described. The main results are presented and compared with experiments.

5.1 Contrast of threshold XPEEM images

5.1.1 Definition of the contrast

Results presented in this section are related to other chapters of the manuscript. We focus on the influence of passivation and of photon excitation energy on doping induced contrast at threshold imaging.

We have analysed the intensities extracted from areas in image series taken at threshold using a laboratory X-ray source at 1486.7 eV (see 2.2.3) and corrected for non isochromaticity. These images were those used for performing work-function mapping in chapter 3.

The area of interest are chosen to be squares of 15 pixels side, which corresponds to a surface of 1.08 μm^2. Three areas are compared, as can be seen in figure 5.1:

- intensity coming from the substrate (red),
- intensity coming from the doped zone (green),
- intensity coming from the doped zone enclosed within the substrate pattern (blue).

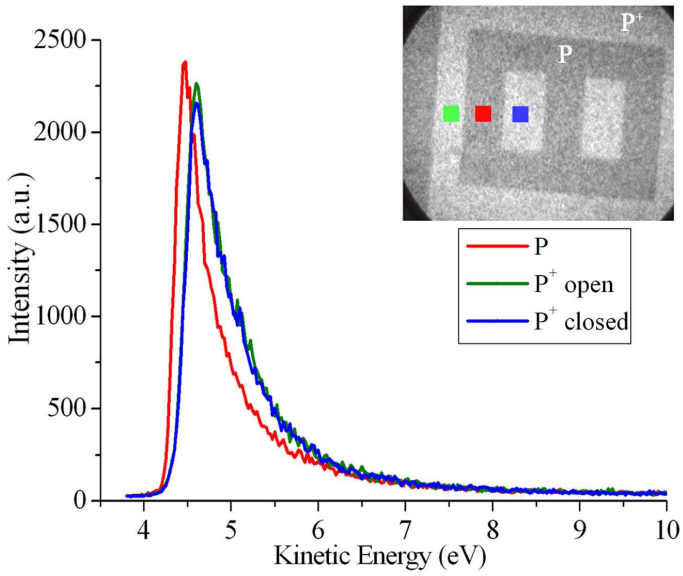

Figure 5.1: *Image XPEEM of P^+/P sample taken at threshold. The photon energy is 700.3 eV.*

Since we consider image series at threshold corrected for dispersion in energy, and noise, equation 1.8 can be simplified, and gives:

$$C = \frac{I_{dep} - I_{sub}}{I_{dep} + I_{sub}} \ . \tag{5.1}$$

This parameter will be used to quantify the contrast evolution with doping type and level through this section, regarding several studies that have been performed during this thesis.

5.1.2 Factors influencing the contrast

5.1.2.1 Influence of passivation on doping induced contrast

Conditions SE contrast is observed at threshold for all kind of samples: the energy filtered images acquired as a function of kinetic energy show variations in intensity between the different doped zones. We have firstly decided to examine the experimental secondary electron distribution of silicon doped zones depending on the sample surface state, providing the acquisition conditions remain as constant as possible for all the experiments.

For details regarding the acquisition conditions (see table 4.1), the slit width at the entrance of the analyzer is 1 mm, and the pass energy of the analyser 50 eV, which give an overall energy resolution (photon+analyser) of 0.33 eV. Image series at threshold were acquired as a function of photoelectron kinetic energy with a 0.025 eV energy step with an acquisition time is 120 seconds per image.

Results Thus, we compare the SE yield when the surface was covered with a native oxide, and after passivation. As can be seen in figure 5.2, taking the case of P^+/P sample:

- Low energy secondary electrons give rise to a positive doping contrast, which means that P substrate is brighter than P^+ doped zone.
- For kinetic energies in the range of 4.5 eV to 7 eV, SE give rise to a contrast inversion, P^+ becoming brighter than P-type. This inversion is visible on filtered images, as can be seen in figure 5.2 comparing those arbitrary chosen taken at 4.375 eV and 5.225 eV.
- The contrast extracted from image series is higher after passivation and appears slightly shifted towards higher kinetic energies.
- The contrast decreases with kinetic energy.

The results for the two other samples N^+/P and P^+/N are given in figure 5.3.

We confirm that the native oxide attenuates the doping contrast. Moreover, shifts occur in the position of contrast maximum depending on the sample cleanliness. These are presented in table 5.1.

We can note that the smallest shift of the maximum contrast is the one of the homojunction P^+/P. We compare also in table 5.2 the maximum of contrast C_{max} obtained

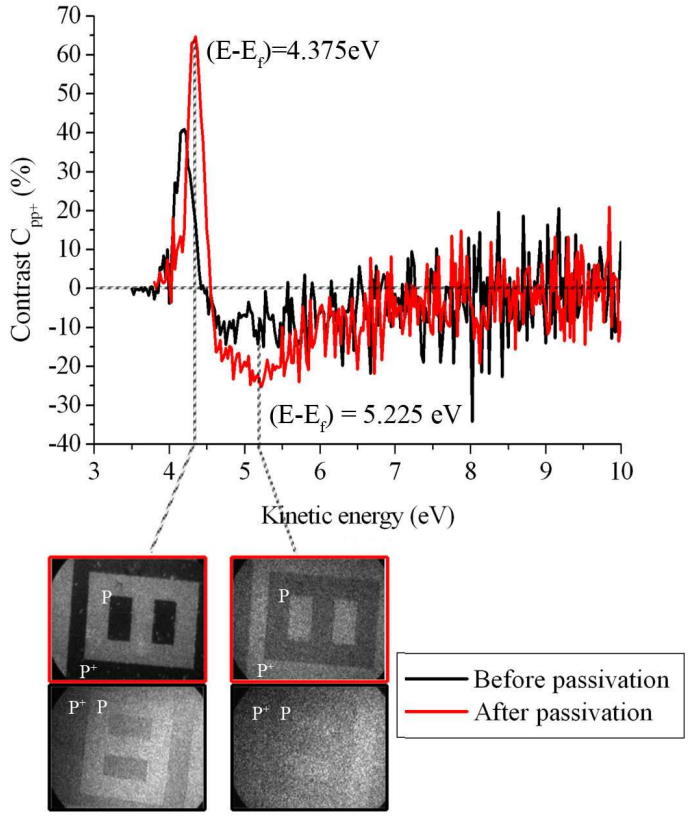

Figure 5.2: *Contrast C_{P/P^+} dependence on kinetic energy before and after passivation for P^+/P sample. The images inserted have been extracted from image series for two kinetic energies: $(E\text{-}E_f)$=4.375 eV and 5.225 eV.*

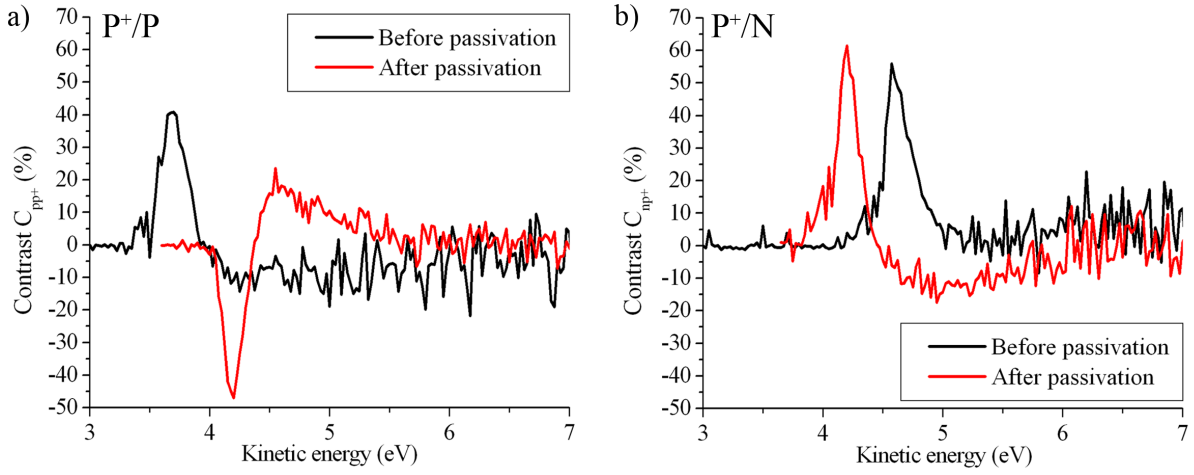

Figure 5.3: *Contrast dependence with the sample surface state and kinetic energy for a) N^+/P and b) P^+/N.*

for the sample considered, with the work function difference $\Delta\Phi$ between the two doped zones, before and after passivation. Results corresponding to work-function measurements after passivation have already been presented in table 4.4. Although the work

Sample	Maximum contrast shift (eV)
P^+/P	+0.10
N^+/P	+0.58
P^+/N	-0.38

Table 5.1: *Maximum contrast shift measured for passivated samples, with respect to kinetic energy measured on samples before passivation.*

function analysis before passivation is not shown in chapter 4, we give here the work-function measurement extracted from the image series.

	Before passivation		After passivation	
Sample	$\Delta\Phi$ (eV)	C_{max} (%)	$\Delta\Phi$ (eV)	C_{max} (%)
P^+/P	0.03	40	0.13	65
N^+/P	0.13	40	0.07	45
P^+/N	0.10	55	0.05	60

Table 5.2: *Maximum contrast C_{max} measured for samples before and after passivation, compared with the work function difference $\Delta\Phi$ between the two doped zones.*

We find higher maximum of contrast after passivation than before. Though the most important contrast is obtained for the passivated P^+/P sample where the difference in work function between the two doped zones is the highest, we find no real correlation between the shift and percentage of maximum of contrast obtained and the difference in work function between the two doped zones for a given sample.

We have then followed the study by analysing the contrast behavior on image series acquired on passivated silicon samples for three photon energies: 1486.7 eV in laboratory, and 128.9 eV and 700.3 eV with synchrotron radiation.

5.1.2.2 Influence of excitation energy on doping induced contrast

Figure 5.4 shows the contrast evolution for each kind of sample with the photon energy. What appears at first glance is the shift in kinetic energy and the differences in the intensities. The most interesting kinetic energy range where a contrast between the two doped zones can be confirmed is below 6 eV. The noise is more important above this value.

To quantify indirectly the photoyield difference between the different doped zones, we have chosen to integrate the contrast from 3 eV to 6 eV and compare them in figure 5.4 d).

We can distinguish two trends for the contrast evolution with the photon energy:

- A high contrast when the photon source is low, around 128.9 eV which decreases with the increasing energy. This is the case of sample N^+/P.

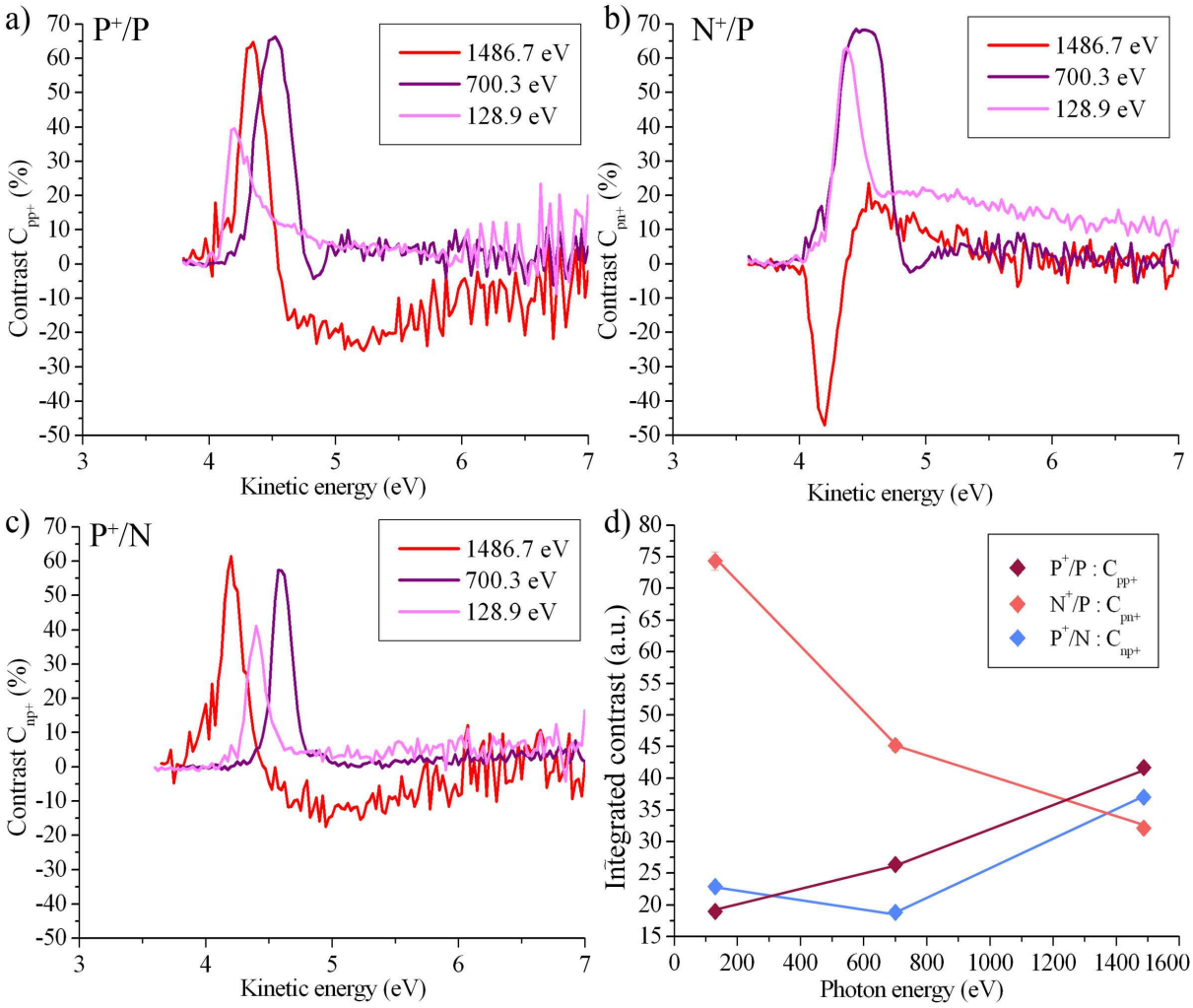

Figure 5.4: *Contrast taken at threshold for three photon energies for a) P^+/P , b) N^+/P and c) P^+/N. d) Contrast evolution of the integrated intensity between 3 eV and 6 eV, with the photon energy. The uncertainty is estimated to be ±2%.*

- A low contrast for low photon energies which increases with this latter. This is the case of samples P^+/P and P^+/N. This can be due to defects and residual oxide which can be greater for P^+ doped zone.

Finally, we have compared the photoemission yield of several doping zone depending on the excitation energy.

The set of samples we have at our disposal enables only to compare two doping types N^+ and P^+, since contrast requires a reference, we have chosen the P substrate.
In such a way, referring to the work performed by Hovorka, we use a modified contrast definition [138]:

$$C = \frac{(I_{dep} - I_{sub})}{I_{sub}} \ . \tag{5.2}$$

Figure 5.5 a) and b) present an estimation of the contrast difference between these two doped zones for three photon energies. We have chosen to compare the contrast between the heavily doped zones for the two samples where the contrast seems maximal,

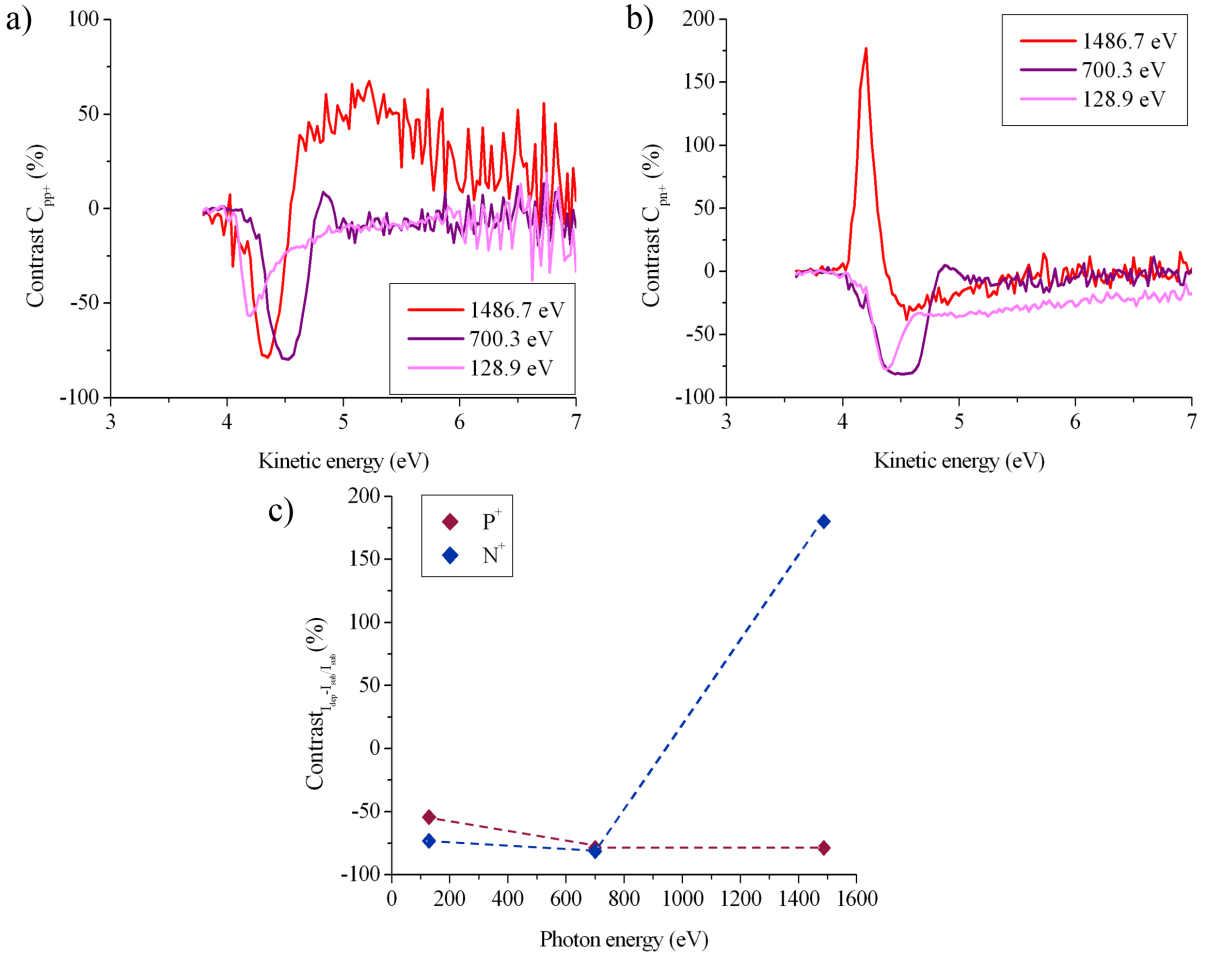

Figure 5.5: *Contrast comparison between a) P^+ and b) N^+ relatively to P bulk taken at threshold for three photon energies. c) Maximum contrast measured for several photon energies for P^+ and N^+ doping type.*

i.e., around 4.5 eV taking for reference the P substrate which should be similar in these two samples. The results are presented in figure 5.5 c). We note that:

- The contrast for P^+ seems higher for high photon energies in figure 5.5 a). The P substrate keeps being brighter than the doped layer, except in laboratory, for kinetic energies varying between 4.5 eV to 6 eV.

- We observe in figure 5.5 b) for N^+ doped zone that the N type at 1486.7 eV is brighter than P bulk for a kinetic energy range between 3.9 eV and 4.375 eV and different from other measurements acquired in synchrotron, where the substrate P is brighter than the heavily N doped zone.

We cannot deduce that one doping type is brighter than the other type, because in our case, the contrast is influenced not only by the secondary electron distribution, but also by the difference in threshold between the two doped zones, as also concluded by Hovorka *et al.* [138]. However, figure 5.5 c) leads to the conclusion that the contrast between P^+ and P is smaller than the one between N^+ and P, whatever the photon energy.

5.1.3 Summary

The present section reports the use of band pass energy-filtered imaging for the observation of dopant contrast in silicon doped samples. It was shown that dopant contrast is clearly observed in the energy-filtered images, even when the surface is covered by a native oxide.

We have presented a study of the evolution of SE contrast on image series acquired with an energy filtered PEEM, regarding different factors, such as the influence of the sample surface state. For this latter, we have shown that the contrast is enhanced between two doped zones when the surface has been passivated. Other experiments based on the excitation energy variations, and combined with the theoretical explanations of the origin of this contrast, highlight the difficulty to well appreciate the physics governing such phenomenon. The contrast is indeed influenced not only by the secondary electron distribution, but also by the difference in threshold between the two doped zones. This is true almost for electron microscopy and photoemission microscopy based techniques.

We will follow this chapter by focusing on the interpretation of the peculiar triple contrast observed firstly on PEEM imaging at threshold on N^+/P sample, as mentioned in previous chapters.

5.2 Triple contrast of XPEEM images

Among the silicon doped samples studied during this thesis, one has shown a peculiar behavior which has caught our attention: N^+/P sample. As already mentioned, we have not only to consider a classical contrast between two dopings, but also a triple contrast since the highly n-doped zones present different intensities depending on their area.
We have dedicated a special section to deepen the understanding of this phenomenon. We complete our knowledge of this structure by presenting complementary analysis techniques such as KFM, SEM, ToF-SIMS, and FIB.

5.2.1 XPEEM imaging at threshold

Figure 5.6 shows representative images from the threshold series acquired on the N^+/P sample using three different photon energies. We can see that the doping region within the 'zero' or the 'eight' pattern show a different intensity than the open regions, giving rise to a triple contrast on a sample containing only two doping levels. Moreover, on single images, a bright rim appears clearly, as presented in figure 5.6 for the SE emission at low kinetic energy. Varying the photon energy, the small n-doped zone enclosed by p-doped one does not respond in the same way as a large and open zone.

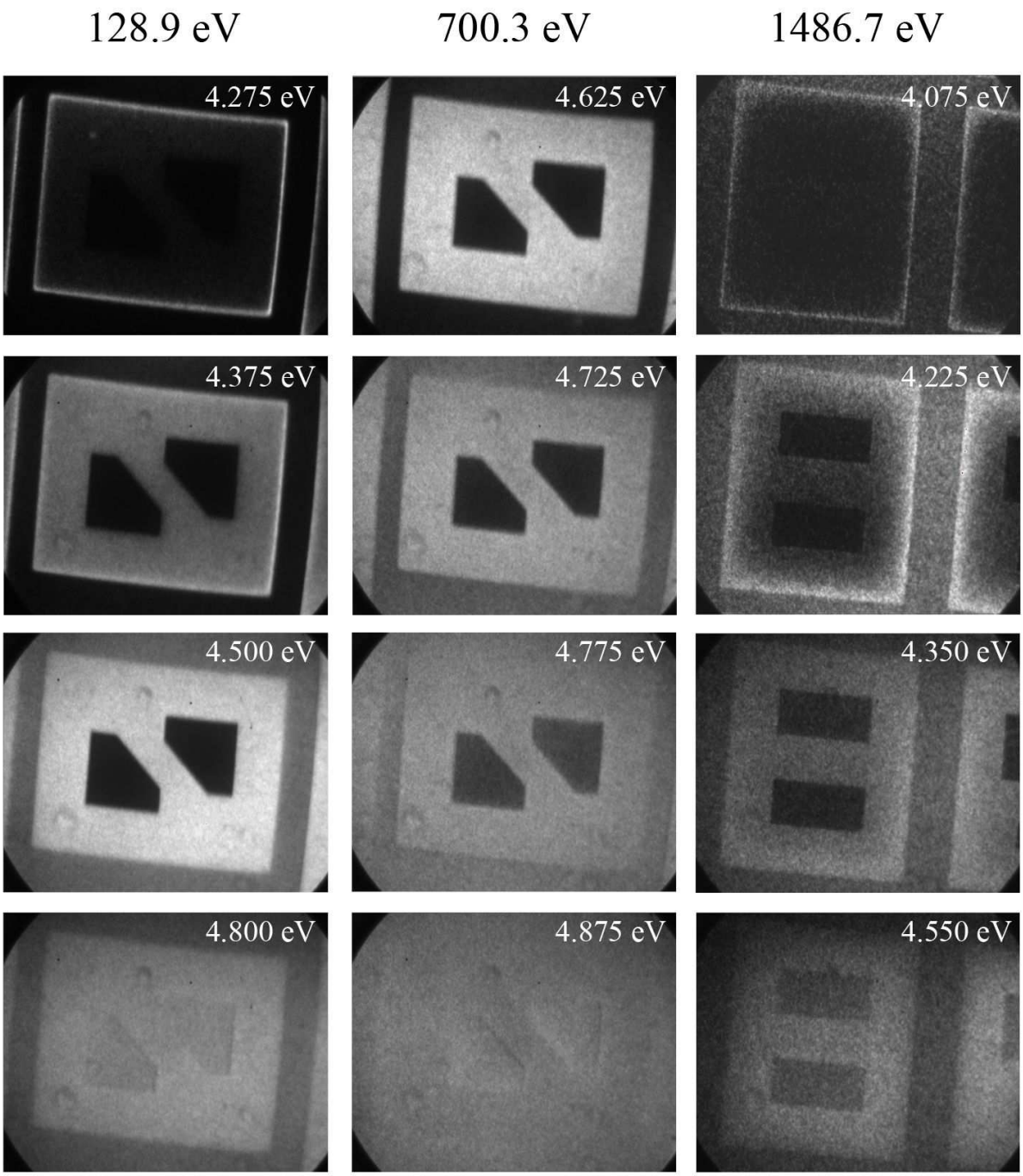

Figure 5.6: *Image XPEEM of N^+/P pattern taken at threshold for three photon energies. The energy (E-E_f) is given for each image on the top right corner. Field of view is 62 μm.*

In the literature, the only previous report of this phenomenon in PEEM is by Hovorka [137, 138].

- In 2008, Hovorka *et al.* have observed a highly silicon p-doped pattern on a n-substrate with a PEEM [138]. Without energy filtering, the closed p-doped zone has the same intensity as th open p-doped regions whereas when applying a high pass filter during the acquisition, a triple contrast appears. Figure 5.7 presents one

of their images where small p-doped zones surrounded by n-doped are brighter than large areas. They explain this phenomena by the presence of surface states which enhance the photoelectron yield. In such a case, they consider the dark rim visible in figure 5.7 b) to be due to topography.

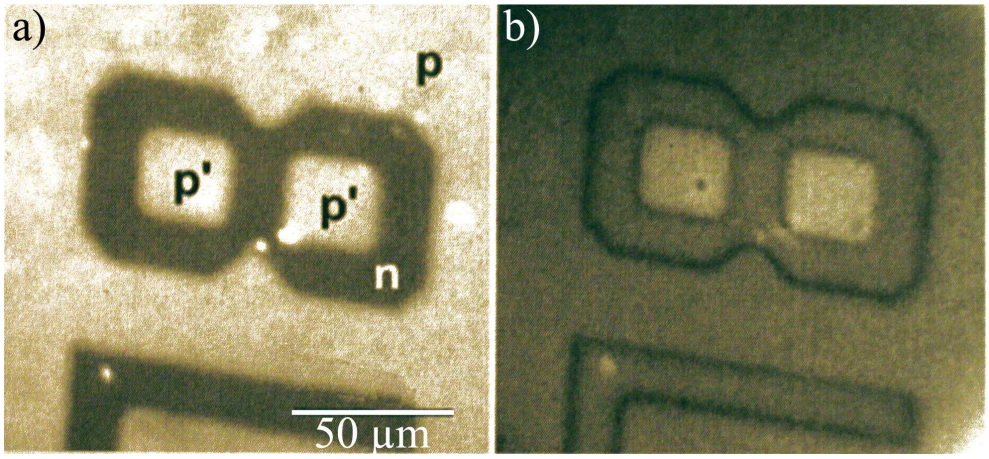

Figure 5.7: *Micrographs of p-type patterns 10^{19} cm^{-3} on a 10^{15} cm^{-3} n-type substrate [138]. a) Full photoemission signal. b) Fast electron signal.*

- In a second paper, they have presented n-type silicon doped patterns on p-type substrate images where the contrast varies with the doping concentration [137]. There is a contrast inversion as the sample voltage is varied, corresponding to a distribution of work function due to the doping level, but additionally, for some retarding voltages, a bright rim appears again on the exterior of the heavily doped patterns, (see figure 5.8), however, no explanation is given for explaining this phenomenon.

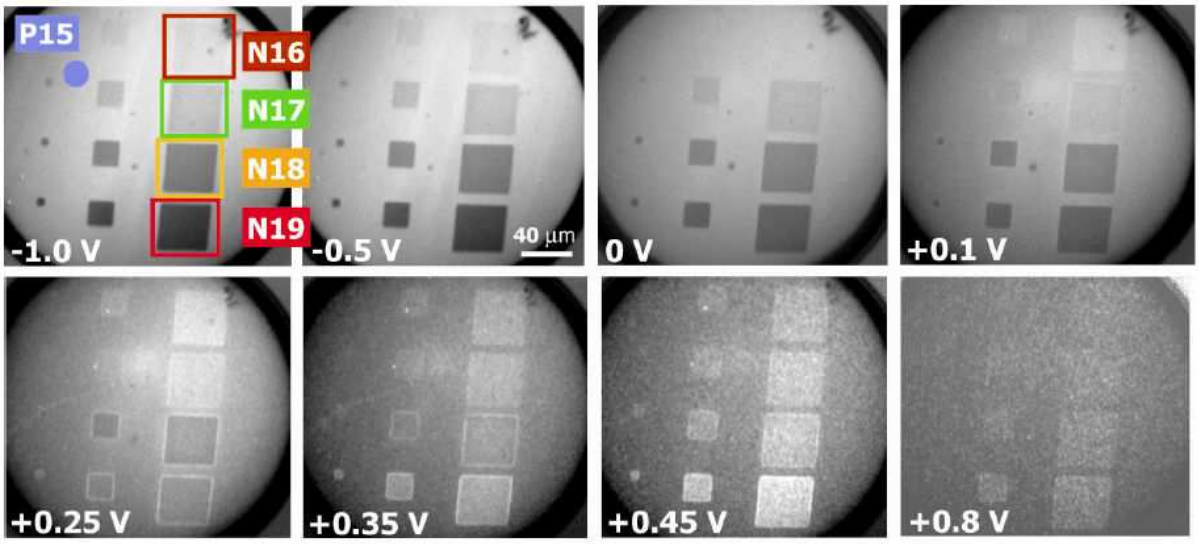

Figure 5.8: *PEEM micrographs of the chemically etched sample with differently doped n-type structures on a lightly doped p-type substrate for various retarding voltages [137]. The values given in coloured squares correspond to the doping type and concentration.*

To go further in the analysis of threshold image series, it is important not only to study the work-function mapping, but also to analyse the photoemission distribution over a wide kinetic energy range of 3 eV to 10 eV for all photon energies. This is carried out on N^+/P passivated sample for three zones of interest of 1.08 μm^2:

- Red zone corresponds to the slightly doped P substrate.
- Green zone corresponds to the highly doped N^+ open area.
- Blue zone corresponds to the highly doped N^+ closed area.

The profiles are gathered in figure 5.9.

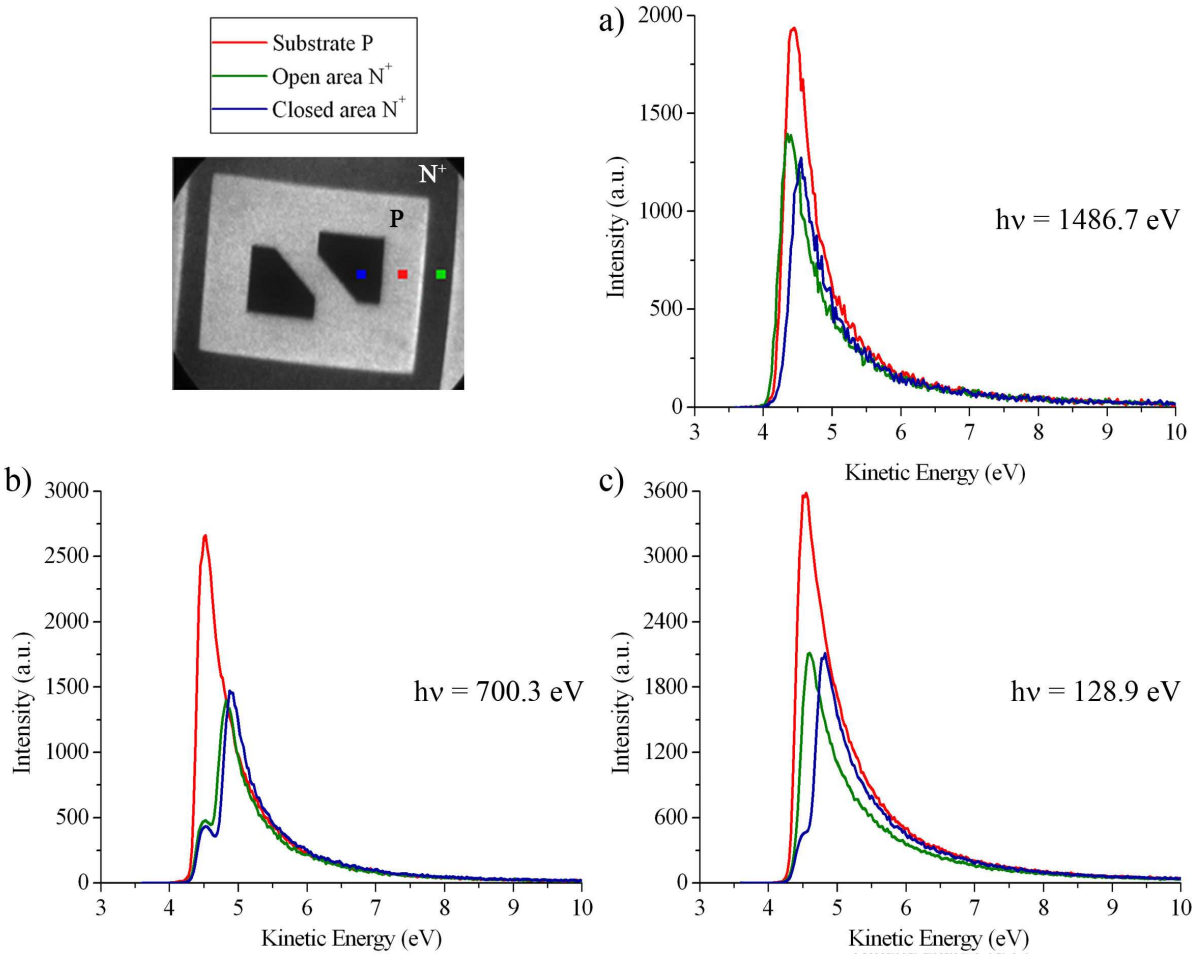

Figure 5.9: *PEEM photoemission yield extracted for three area of interest for three photon energies: a) 1486.7 eV, b) 700.3 eV and c) 128.9 eV.*

A behavior non visible at 1486.7 eV appears in synchrotron environment: a threshold shift for the highly N doped zone around ($E-E_f$=4.6 eV) is present on both open and closed areas. No such shift occurs in spectra extracted from the other samples.
The starting point to mention is that in order to perform the work-function extraction, we use the first part of the threshold, since we do not expect work function anisotropy on this sample and because the extracted values were closer to the ones found on other samples, respectively N^+/N and P^+/P for N^+ and P.

- For the open N^+ zone, this threshold shift is present only for a photon energy of 700.3 eV.
- For the closed N^+ zone, the threshold shift occurs already for a photon energy of 128.9 eV, but appears stronger at 700.3 eV.
- This shift is not an artifact since it does not occur of the spectra extracted for the P substrate.
- At a photon energy of 1486.7 eV, no threshold shift can be seen for any zone.

5.2.2 Core-level spectromicroscopy

We have acquired core-level image series on Si $2p$ peak with a photon source at 128.9 eV. After background subtraction, the resulting true core-level image taken at 103.5 eV corresponding to the SiO_2 component is presented in figure 5.10 a). A variation in intensity clearly appears between the N^+ zone enclosed and the large doped zone. The small squares represent the areas of interest of (2×2) μm^2 defined for spectral extraction. The resulting core level spectra are displayed in figure 5.10 b). They present two main peaks, one due to the native oxide, around 103.5 eV and another from the underlying bulk Si substrate at 99.5 eV. The separation of these two peaks, about 4 eV, corresponds to Si^0/Si^{4+}, and reflects the residual presence of a native oxide after passivation.

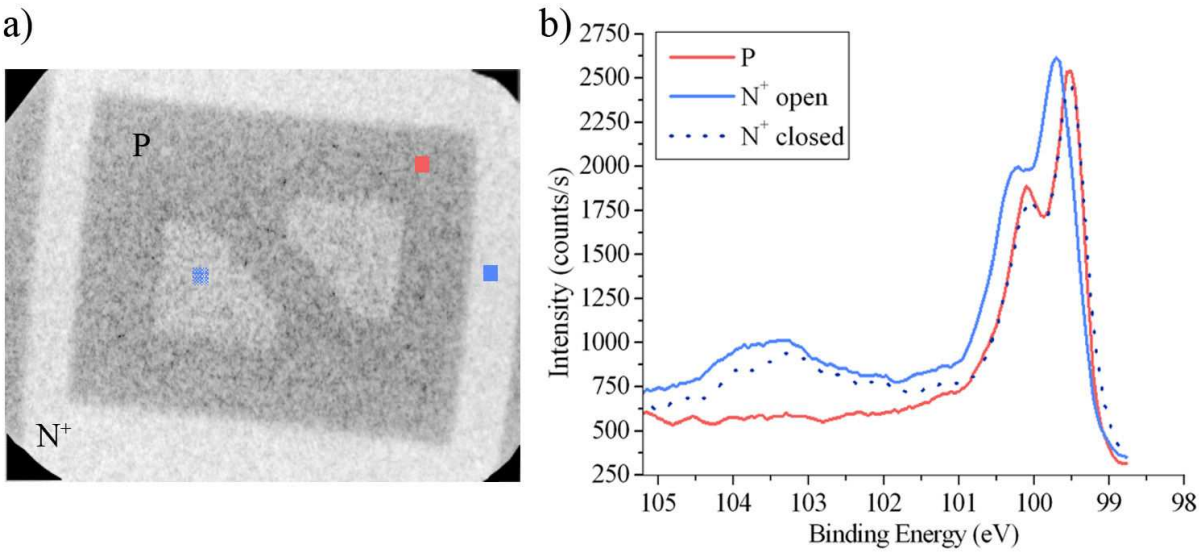

Figure 5.10: *a) True-core level Si 2p imaging of N^+/P pattern at 103.5 eV after Shirley background subtraction. Area of interest taken for extracting spectra. b) Fits for core-level Si 2p spectra obtained for different doped zones.(Photon energy: 128.9 eV)*

What appears at first glance is the presence of native oxide, preferentially on highly n-doped zone comparing to p substrate. The spectrum extracted from the enclosed N^+ doped zone presents peculiar features regarding its shape:

- Like open n-doped zone, it has a native oxide on its surface, but its bulk position is the one corresponding to the p-bulk.

- The shift measured between the Si^0 of the closed N^+ zone and the P-doped zone is 0.36 eV lower with respect to the open N^+-doped zone.

The spectra for both N^+ open, N^+ closed and P zones have been presented in figure 4.12 of chapter 4. A comparison with core-level spectra acquired in synchrotron environment from other samples is also done, where we can see that for both samples P^+/P and P^+/N, the closed doped zone presents a spectra similar than the open doped zone of the considered sample.

Spectra are decomposed by the procedure proposed previously in table 4.15 of chapter 4. Peaks position are presented in table 5.3 for excitation energies at 128.9 eV and 700.3 eV but the values are not corrected for SPV.

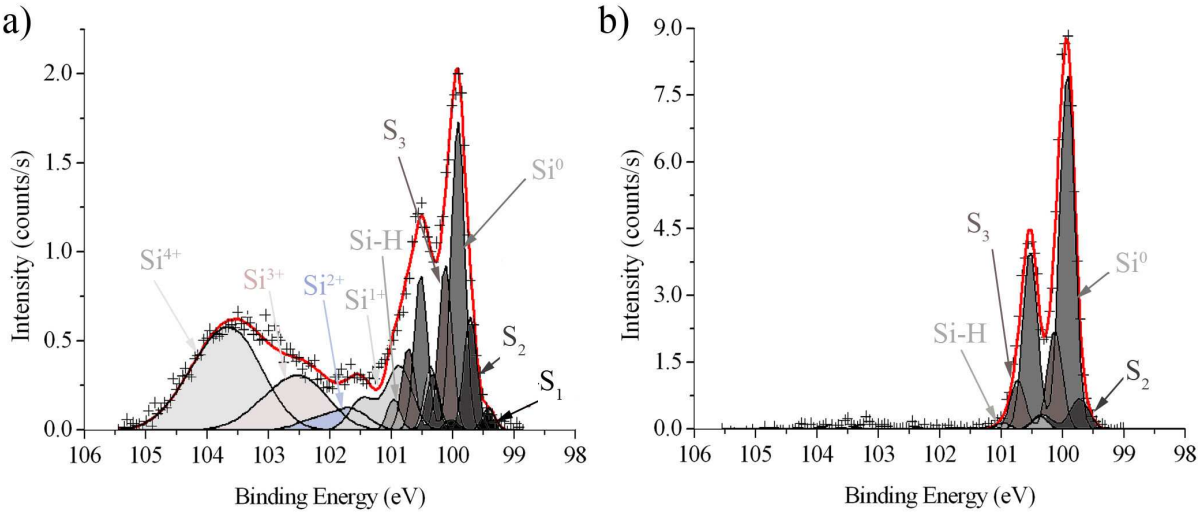

Figure 5.11: *Core-level spectra and best least square fits using standard literature parameters for Si 2p on P^+ doped zone after passivation, for a) 128.9 eV and b) 700.3 eV photon energy.*

The major drawback considering these results is that we do not have valence band image series to extract locally the valence band maximum from the small N^+ area. However, the spectra deconvolutions of the enclosed area confirms the trend, when considering the binding energy of the different Si $2p$ components:

- the peaks shape of this N closed zone spectrum are similar as those extracted from open N-doped area,
- the binding energies of the peaks corresponding to the N closed zone spectra are situated at energies closed to those obtained for the fit of the P-doped spectra at 128.9 eV. This is also the case for spectra acquired 700.3 eV, but in a less extent.
- the higher the oxidized component considered, the lower the shift between open and closed N zone.

5.2.3 Complementary analyses

Sample preparation We have emitted the hypothesis that for this sample, the epitaxy was not well processed, inducing this strange contrast. We have decided to study

Dopant type	Si^0	SiH	S_3	Si^{1+}	Si^{2+}	Si^{3+}	Si^{4+}	S_2	S_1
P at 128.90 eV	99.79	100.23	99.99	100.74	101.54	-	-	99.59	99.39
N^+ closed at 128.90 eV	99.77	100.21	99.97	100.74	101.52	102.27	103.57	99.57	99.27
N^+ open at 128.90 eV	99.64	100.08	99.84	100.59	101.54	102.27	103.44	99.43	99.20
P at 700.3 eV	99.22	99.66	99.42	100.17	-	-	-	99.11	98.72
N^+ closed at 700.3 eV	99.16	99.60	99.36	100.11	-	-	-	98.96	99.66
N^+ open at 700.3 eV	99.14	99.58	99.34	100.09	-	-	-	98.94	98.64

Table 5.3: *Energy position for N^+ open, N^+ closed and P zones Si 2p components with 128.9 eV and 700.3 eV photon energy. The uncertainty is ± 0.05 eV*

the same silicon doped patterns already observed by Barrett *et al.*, since their doping concentration for the N^+/P combination was quite similar: $1\times10^{20}/1\times10^{16}$ at.cm^{-3} [222]. For comparison with our sample, the doping is $1.8\times10^{19}/4\times10^{15}$ at.cm^{-3}. The real difference with our sample is the realisation since, in this case, it corresponds to phosphorus implantation on silicon bulk.

A preliminary study was carried out in the second year of this thesis using synchrotron radiation. Although, passivation was not efficient, and despite the native oxide still present on the surface, we were able to acquire image series at threshold.

Thus, for a photon energy of 265 eV, we have realized the work function mapping, keeping the same protocol as the one used in previous chapters. The field of view is larger, 70 μm, but the result is similar, as presented in figure 5.12:

- The work function of the N^+ closed zone is higher than the open zone one: 4.90 eV against 4.60 eV.
- A rim localized at the exterior of the pattern presents a work function of 4.45 eV.
- The open highly n-doped zone has the same work function of the p-substrate.

In figure 5.12 b) we find the work function mapping presented in chapter 3.

- The work function of the N^+ closed zone is higher than the open one: 4.73 eV against 4.5 eV, really close to the p-doped value at 4.60 eV, whereas we expect the highly doped patterns to have a smaller work function, closer to 4.45 eV.
- The bright rim has a work function of 4.45 eV.

Since we consider silicon samples with native oxide, we are not able to compare absolute work function values. We can however conclude that the work function trend of

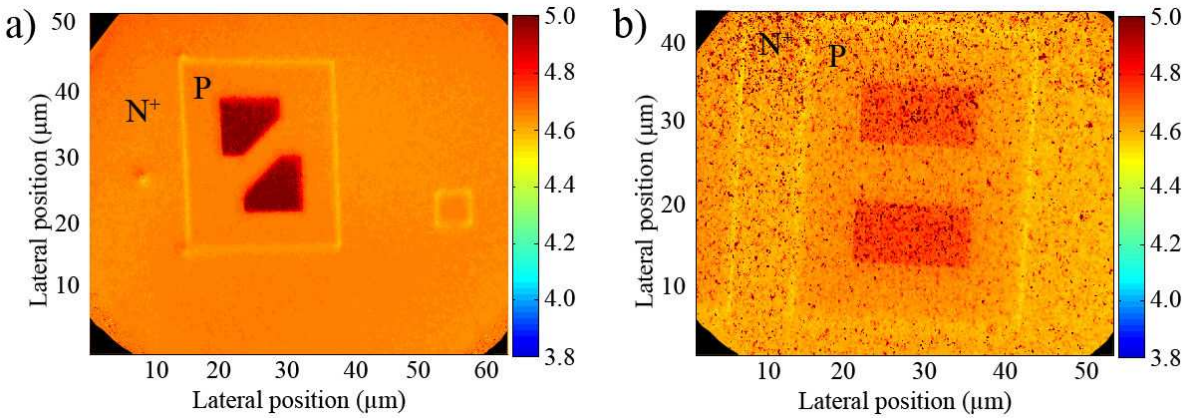

Figure 5.12: *Work function mapping on N^+/P pattern realized by: a) implantation (photon energy: 265 eV) and b) epitaxy (photon energy: 1486.7 eV).*

the two samples presenting the same silicon doped patterns, with closed doping patterns is the same, with peculiarities:

- A small difference in work function values between the p-doped substrate and the open n-doped zone. Due to the presence of an oxide on the sample surface, we are far from flat band conditions, and the band bending occurring at the interface oxide/semiconductor can be responsible.
- The closed n-doped zone presents a work function higher than the open n-doped zone, which is the opposite of what we expect.

Scanning Electron Microscopy We have decided to image the pattern with SE not filtered in energy, with a SEM.

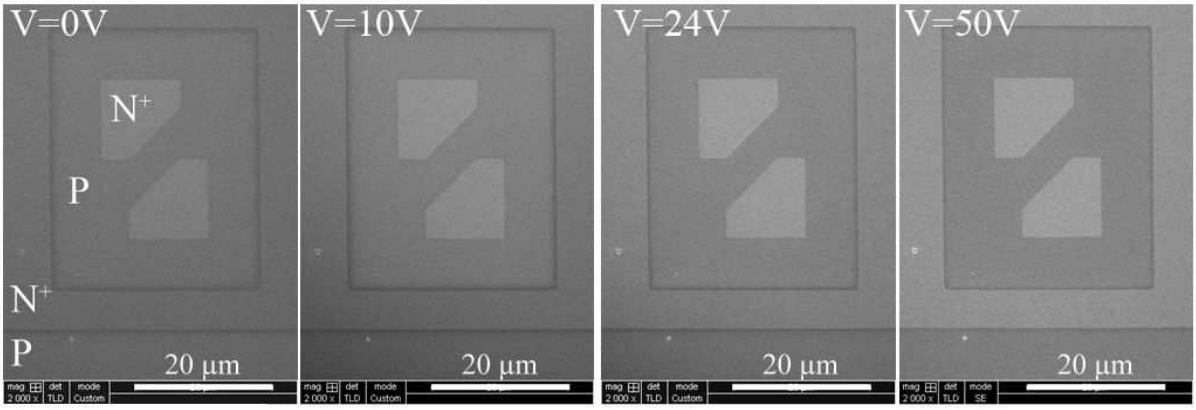

Figure 5.13: *SEM images of N^+/P pattern for several section tube voltage.*

The through-the-lens detector within the SEM column helps to eliminate backscattered electrons (BSE), as well as second generation SE produced by BSE interactions with the objective lens. Changing the input voltage of this detector highlights the influence

of BSE on triple contrast, as can be seen in figure 5.13. For a primary electron beam at 2 keV and a beam current of 0.21 nA, we have tuned the voltage between 0 V and 50 V, which is the default value. The triple contrast strongly appears at 0 V, when collecting BSE signal and the rim is also visible at the exterior of the p-doped pattern. At 50 V, the contrast difference between the open and the closed N^+ is still present but less marked.

We have also observed this triple contrast observing the secondary electrons emitted from the sample with a FIB, whose primary beam radiation was Ga^+ ions, 30 KeV energy and 28 pA current. These results imply that there is enhanced very low energy electron emission occurring in this n-doped closed region on N^+/P sample whatever the primary beam type, photonic, electronic or ionic.

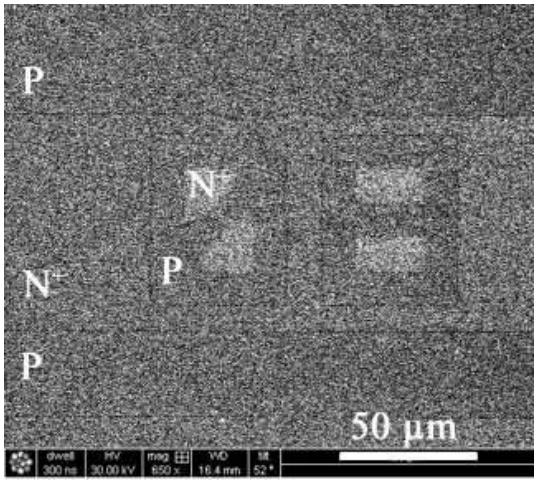

Figure 5.14: *SE image of N^+/P acquired with FIB.*

Kelvin Force Microscopy KFM has also been performed on N^+/P pattern non passivated, i.e., one has to take into account the presence of a native oxide on the sample surface. The results are presented in figure 5.15.
The coupling between topography and potential profiles seems accurate. Regarding the blue one, the localized epitaxy corresponding to the N^+ doped pattern is higher of 25 nm than the p-bulk substrate.
In such KFM configuration it is important to keep in mind that the sample work function is measured with respect to the tip one. This latter is estimated to be 5.1 eV. The potential variations measured have to be related to this value.
When plotted the red profile these potential variations from p-bulk towards n-closed doped zone can be analysed: the resistivity decreases until it reaches an inversion type within the enclosed area. As a result, the work function measurements give:

- 4.6 eV for the p-bulk.
- The open n-doped area is close to 4.7 eV.
- The closed n-doped zone has a work function which is lower by 0.14 eV with respect to the open area value, which corresponds to approximatively 4.85 eV.

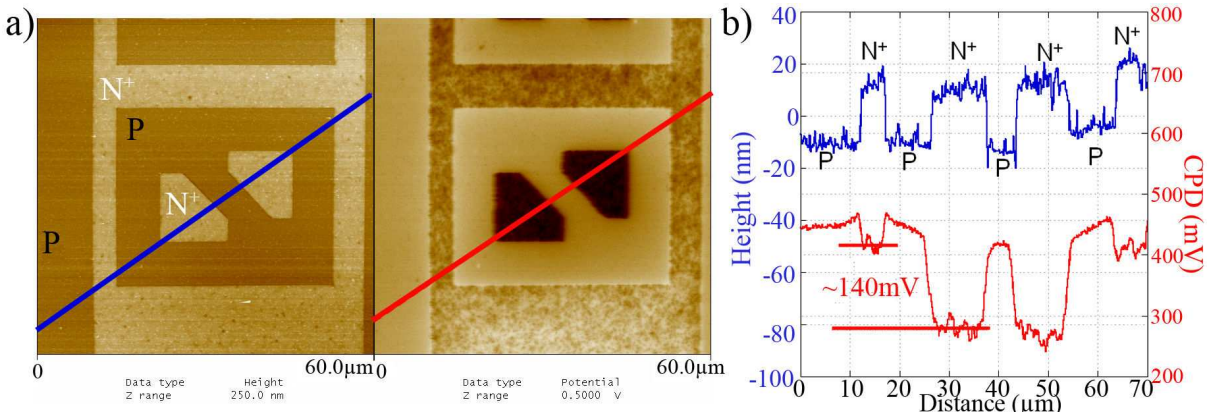

Figure 5.15: *KFM map of N^+/P pattern: a) topography and b) potential. V_{AC}= 5V.*

The work function measurements performed by KFM and PEEM at 1486.7 eV before passivation presented in table 5.4. After passivation, based on results presented in chapter 4, all work function values obtained by PEEM for different photon energies are also summarized in the same table.

Analysis	N^+_{close}	N^+_{open}	P
KFM (ox.)	4.85	4.70	4.60
PEEM at 1486.7 eV (ox.)	4.73	4.60	4.50
PEEM at 1486.7 eV (pass.)	4.08	4.00	4.15
PEEM at 700.3 eV (pass.)	4.62	4.56	4.25
PEEM at 128.9 eV (pass.)	4.65	4.44	4.38
Expected from flat band	4.16	4.16	4.93

Table 5.4: *XPEEM for different excitation energy and KFM work function measurements of passivated N^+/P pattern. Surface state is recalled in parenthesis (ox.: presence of native oxide before passivation, pass.: oxide removal by deoxidation process presented in chapter 3. The uncertainty is estimated less than 0.05 eV.*

The values obtained by both KFM technique and PEEM at 1486.7 eV before passivation are in good agreement. After passivation, for measurements performed with energy filtered PEEM, the N^+ pattern zone work function is always higher than the open area of the same doping, whatever the photon energy. All measurements are far from the theoretical values expected. We assume this shift to be due to residual band bending, as seen in chapter 3.

For Eyben *et al.*, surface states play a dominant role in SSRM measurements, depending on the dopant concentration and distribution [291]. The surface charges create variations of doping concentration at the surface shifting the junction and even creating inversion layers. But they consider inversion type on low doped areas whereas we have to consider the contrary, i.e. an inversion type over highly doped areas. Such hypothesis can not be applied to explained our observations.

Scanning Capacitance Microscopy Aware of such a strange behavior, we revisit the SCM results already presented in chapter 3 section 3.2.2.2. We quote the experimental conditions: the technique is utilized at constant voltage mode and the alternating current V_{ac} bias voltage applied to the sample is maintained at 1 V. For different values of V_{dc}: -1 V, 0 V, +1 V, the change in capacitance is recorded as a function of doping and carrier concentration under the tip, at a scan rate of 0.1 Hz. After the V_{dc} sweeping, another scan is done for -1 V to check the good reproducibility of the measurements and the absence of charging effects. Figure 5.16 is extracted from figure 3.12 and corresponds to results of N^+/P case.

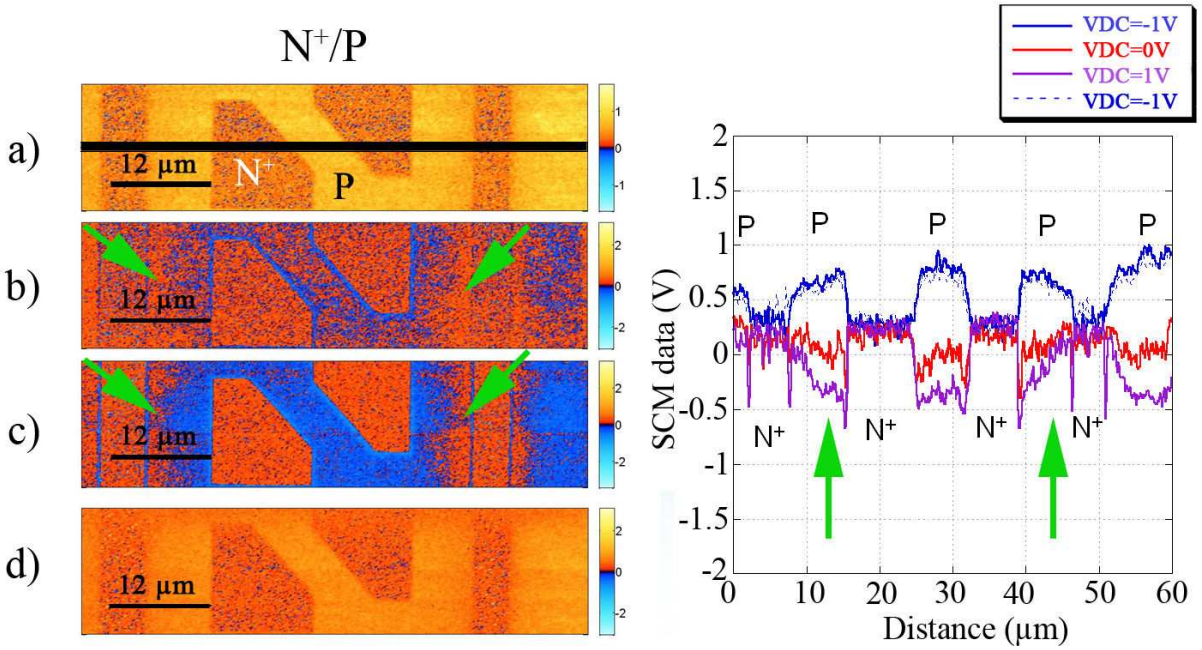

Figure 5.16: *SCM measurements on N^+/P sample. The scans are presented for several V_{dc} values: a) -1 V, b) 0 V, c) +1 V, d) is the return to -1 V. The profiles below are extracted from the zone presented in a).*

Thus, a variation in SCM signal is clearly visible at 0 V and +1 V, on the P substrate, at the position of the rim observed in PEEM at threshold.

Time of Flight Secondary Ion Mass Spectrometry ToF SIMS analysis performed on this N^+/P sample are presented in figure 5.17. The abrasion is slow for the acquisition of these images in order to keep the sample surface charged in cesium to optimize the ion yield, and also to avoid absorption of oxygen and hydrogen atoms. The abrasion speed is estimated to be 0.008 $nm.s^{-1}$. Thus, the probed depth is 5 nm $\pm$ 2.5 nm.

We are able to observe the repartition of oxygen on the surface: as already mentioned, it is preferentially situated on N^+ area, and estimated to be 1 nm thick, in good agreement with our core-level measurements. Several profiles have been extracted, specially from two different zones in N^+ area. They are visible in coloured shapes on figure 5.17 and are presented in figure 5.17 b), we choose respectively:

- Red corresponds to the N^+ closed area.
- Green corresponds to the N^+ large area.

These profiles give phosphorus concentrations, respectively for the open and closed zones: 4×10^{19} at.cm^{-3} and 1.8×10^{19} at.cm^{-3}. The uncertainty on the P^- concentration being $\pm$10-20 %, we can deduce that no variation in doping concentration between the open doped zone and the closed zone is measured. The triple contrast is therefore, not an effect of doping variation.

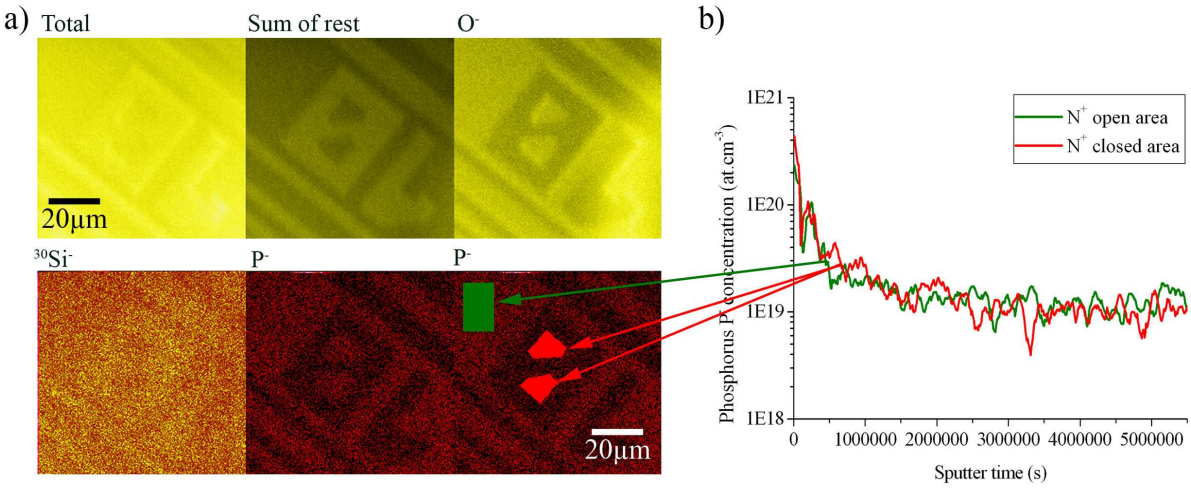

Figure 5.17: *ToF-SIMS imaging acquired on N^+/P sample: a) Localization of several species: Total, Sum of rest, O^-, $^{30}Si^-$ and P^-. b) SIMS profiles extracted from coloured shapes presented in a).*

Moreover, this measurement is in good agreement with the SIMS measurement performed in chapter 3 (see fig. 3.13) to determine the effective doping concentrations on a zone where the doped patterns are series of line of 500 μm wide: the epitaxy is homogeneous on the sample surface.

Discussion This triple contrast cannot be interpreted in terms of fully depleted zone since the thickness and the area of the N^+ doped layer are too important to allow such state with respect to typical depletion widths. We explain such contrast by a charging phenomena, based on the electrical charge transfer principle.

As already established, this peculiar contrast occurs only with the doping combination N^+/P, the other sample P^+/N whose dopant concentrations are close, presents only the expected contrast between the two doped zones.
The highly n-doped zone is surrounded by p-doped zone not only in the surface plane, but also in depth, on 100 nm. We have assumed that this surrounded zone has to be considered like a diode in 3D: the depletion zone acts like an insulator surrounding the highly doped layers which becomes a capacitor. An electrical field occurs within this space charge zone, pointing from n- to p- type. When measuring a potential thanks to the KFM tip, or measuring the kinetic energy of an electron with a spectrometer, it is important to keep a closed loop between the sample and the instrument. Charges have to pass through the

entire system. However, in our case, due to the diode created, the electric field prevents the electrons to be carried to the surface, from p- type towards n-, as schematically represented in figure 5.18. As a result, no redistribution of the charges occurs: the electrons photoemitted from the surface of the N^+ closed zone are not replaced by others coming from the substrate. A charging effect occurs, the holes concentration increasing, and the Fermi level being likely to decrease towards the valence band. This could explain the higher work function value measured on closed N^+ doped zones relative to the open one. Moreover, this effect is temporary, until it reaches equilibrium. We assume that the threshold shift observed on XPEEM in spectromicroscopy mode corresponds to the non equilibrium state of the system.

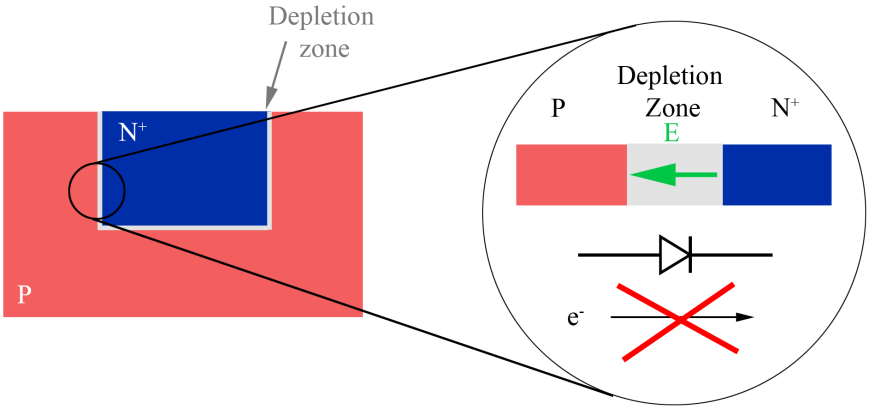

Figure 5.18: *Schematic representation of N^+/P sample as a diode.*

Such explanation can explain why this triple contrast is not visible on the reversed sample P^+/N: in this case, though the diode is in blocked mode, since the electrical field in the depletion zone is well orientated from n- zone towards p-, it allows the carriers to be transported, and thus, a good conductivity between the two zones.

This hypothesis can also brought a partial explanation on the origin of the bright rim on the exterior of the P pattern. Since the charges are not able to pass through the depletion zone, from p substrate towards highly n doped zone, they stay in the vicinity of the P zone, and since electrons are more numerous, they are more likely to be observed around this zone. However, this does not explain why this phenomena does not occur on the interface of P substrate with the smallest N^+ zones.

It is also important to focus on the N^+ large zones: triple contrast is not so strong than for closed zones however, it still occurs since the work function values measured by KFM or PEEM are inverted. A possible explanation of the fainter influence of the 3D capacitor on measurements could be to consider the size of the area of interest. At a scale of few millimeters, what we consider large N^+ doped zones in PEEM field of view are also surrounded by a P substrate zone. Hence, this zone is also a capacitor, much larger than the one corresponding to the small closed zones. As a result, though electrons emitted from the highly doped zone are not replaced in this large area, we expect a better charge redistribution on the sample surface, and thus, a lower influence of this charging effect

on secondary electron imaging.

To finish, we have realized conductive short circuits from the closed n-doped zone towards the open one to allow a better electrical contact between the two doped zones, and thus, to allow charges to be transfered. This was carried out by FIB milling over a zone of (1×10) μm over a depth of 50 nm, and studied by KFM. Results are presented in figure 5.19. The potential of the closed n-doped zone connected to the open zone is higher than the isolated n-doped zone. Though its work function value is closer to the open zone one, it is not the same. We can attribute this effect to the conductive short circuit which is not large enough to enable a perfect connection between the two zones. Moreover, the capacitor considered being the N^+ zone in 3D, the charge transfer should be also in 3D rather than in a plane. An optimization possible should be to mill deeper, towards 150 nm to create a better short circuit between the two doped zones.

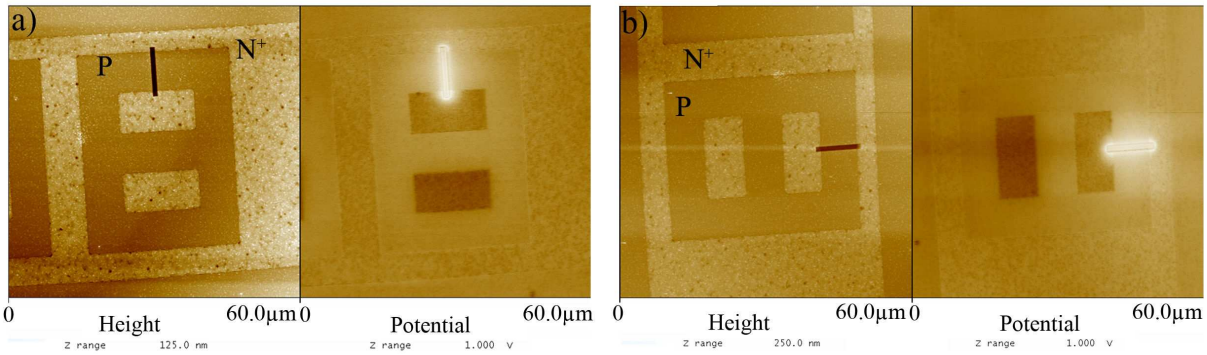

Figure 5.19: *AFM topography and potential mapping on two 'zero' patterns, whose one N^+ closed zone is connected to the large zone: a) vertical and b) horizontal analysis to check whether the variation in potential measurement is an artifact. Milled area (Ga^+/30kV/28pA, targeted depth: 50 nm, measured 40 nm. V_{AC}= 5 V.)*

5.2.4 Discussion

A peculiar triple contrast on N^+/P sample has been observed by energy-filtered PEEM, whatever the photon energy and whatever the sample fabrication (implantation or localized epitaxy). This triple contrast was also observed whatever the nature of the excitation beam, i.e. electrons by SEM and ions by FIB. Spectromicroscopy studies performed at threshold and core-level were combined with complementary analysis techniques: KFM to compare the local work function values by another method than work function mapping with PEEM, and ToF SIMS to verify that no variations in local doping concentration between the large doped zone and the closed one occur. We have assumed, regarding all these results, that a charging effect occurs in the highly N^+ doped zone, more important in the closed zone than in the open zone due to the difference in terms of area dimensions. We now focus on the influence of local electric field across pn junctions on PEEM imaging.

5.3 SIMION simulations

In this section, we present a numerical simulation of PEEM optics to calculate the PEEM imaging of a pn junction. We use the industry standard code SIMION [131] version 8.0. This software provides all the requirements necessary to simulate with high accuracy and analytically solve the mechanisms in several instrument configurations. This electrostatic and magnetic field modeling software uses a finite difference method and traces the motion of particles using a fourth-order Runge-Kutta integrator.

The organisation of this section is as follows: a first part is dedicated to the presentation of the simplified PEEM model used, and the methodology chosen for these simulations. The second part deals with simulations performed to highlight the influence of lateral electric field across pn junctions on PEEM imaging. The variations of photoelectron trajectories as a function of several factors are studied independently. Lastly we show that lateral electric field are not the only factor responsible for image variations in PEEM, and that it is important to take into account the combination of both electrical and physical topographies. This idea is developed on the basis of dark field imaging in PEEM.
We compare each simulation type with the real observations obtained with the NanoESCA. The aim is to present qualitative correlations between simulation and experiment.

5.3.1 Methodology

5.3.1.1 Modeling the PEEM column

With respect to our energy-filtered PEEM instrument, we can mention the study conducted by Zouros *et al.* [292, 293] on Hemispherical Deflector Analysers to modelize the particle orbits in such systems, and also the work performed by Sise *et al.* [294] to optimize the fringing field aberrations of HDAs. Tonner *et al.* [198] did pioneer simulations of the tolerance limits for aberrations of the various optical components of an electrostatic PEEM with a band pass energy filter. The objective lens and the PEEM acceleration field have also been modeled by Feng *et al.* [295].

For this qualitative approach of the influence of lateral electric field across a pn device on PEEM imaging, the simulations were done using a simple PEEM model, consisting of the cathode, an immersion objective lens and the screen. The immersion objective lens simulated here is modeled thanks to electrostatic lenses formed of closely spaced cylindrical electrodes. The paper of Sise *et al.* [296] is interesting to understand the requirements needed to choose the best parameter values in a three-element lens, the focal properties depending on both lens geometry and the voltage ratio between the electrodes.

For simplicity, in our model, the projective lenses have not been taken into account to magnify the final image. The different parts of the PEEM column are defined under potential arrays: the electrodes are defined as points on a grid, and in the complete workbench, points of equal potential form a connected electrode.

The PEEM column is defined so as to be similar to the NanoESCA column. It is presented in figure 5.20 a) and c): the sample is near ground potential, positioned at 1.8 mm in front of the immersion lens composed of three electrodes: the extractor which can be set up to 15 kV, the focus electrode, and the column electrode. A movable circular contrast aperture with sharp edges of 70 μm diameter, typically used for high-resolution imaging, is centered in the optical axis, in the backfocal plane of the immersion lens for bright field imaging. It can be shifted by a certain value off-axis when simulating dark-field imaging, as presented in paragraph 5.3.3. In this configuration, the PEEM magnification is assumed to be $\times 44$. This measurement was performed by measuring the simulated image size of a sample inducing no deviation of photoelectron trajectories.

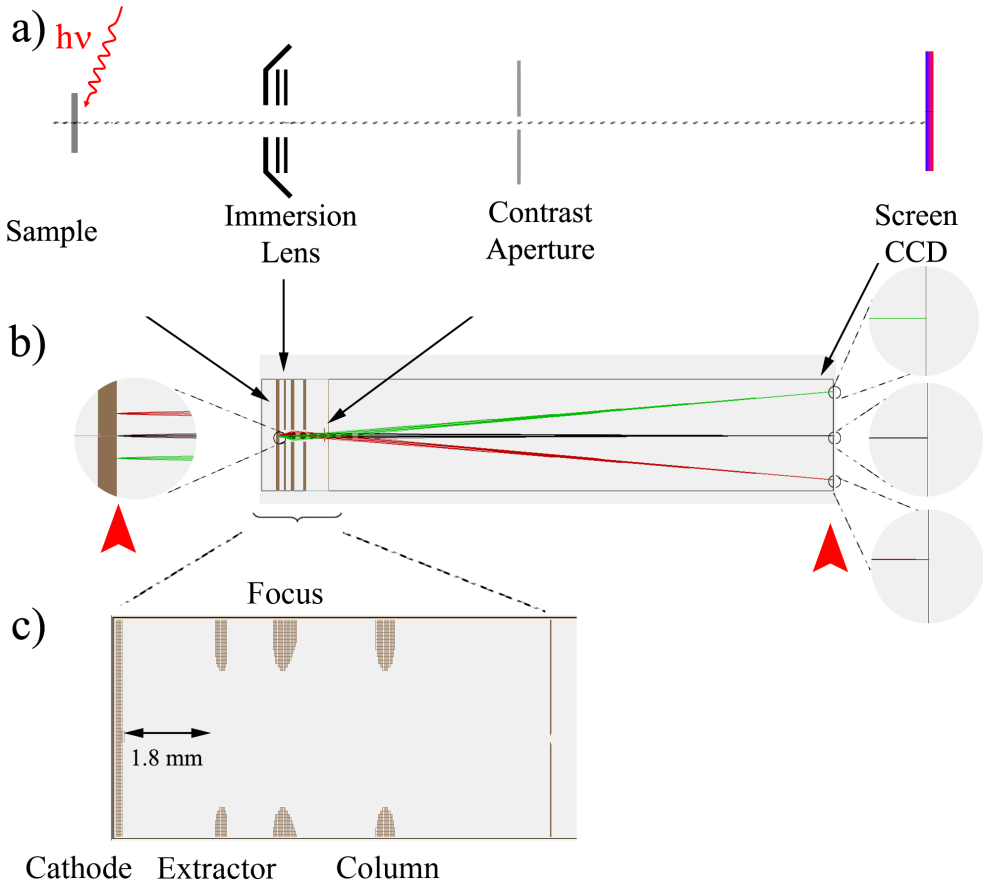

Figure 5.20: *Presentation of the simplified PEEM column: a) PEEM optical elements, b) SIMION overview, c) Zoom on the PEEM first elements simulated by SIMION.*

The electrode potentials are optimized for the best focusing: an object point on the sample surface corresponds exactly to an image point on the screen, as can be seen in figure 5.20 b). Moreover, the simulations are in good agreement with the overall NanoESCA behavior, as presented in figure 5.21. In vacuum, the emission of the photoelectrons with low kinetic energy, specially from the sample's regions near the optical axis should be transmitted through the contrast aperture of the PEEM column. For higher kinetic energies, the transmission decreases, and photoelectrons are likely to hit the contrast aperture

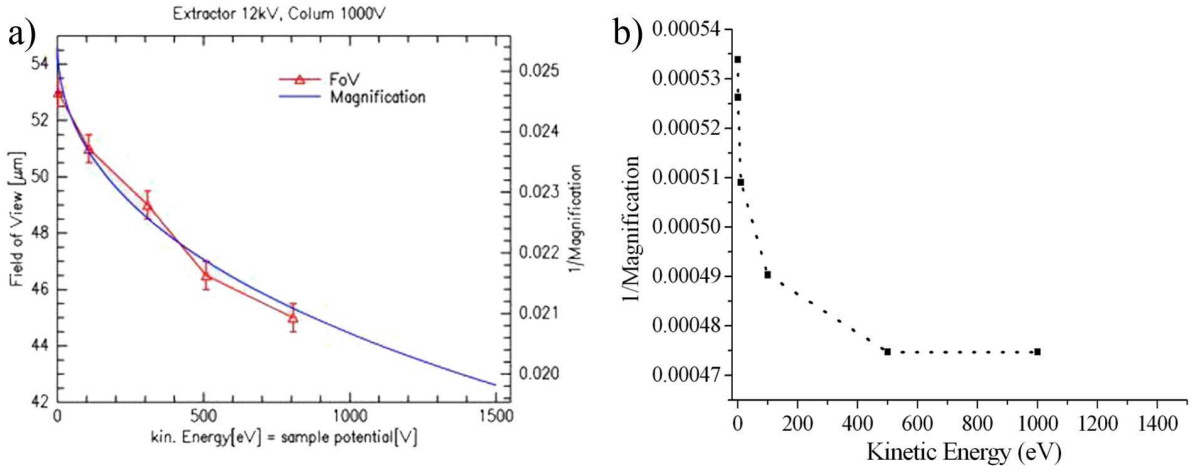

Figure 5.21: *Magnification behavior of the PEEM column: a) NanoESCA real case, b) PEEM simplified SIMION case. The scale in y-coordinates in b) is different than a) due to simplifications, but the behavior is the same.*

or other elements.

5.3.1.2 The particles model

For lighter and faster simulations, we consider here a pn junction in 1D, i.e., that the particles emitted from the surface are emitted from a given plane which crosses the different doped zones of the pn junction modelized.
For the purpose of these analyses, simulated photoelectrons are emitted from point sources on the sample surface with different initial angles and energies. They escape under the shape of bunches: each bunch is composed of seven particles, with initial starting angles in the range from -10° to +10° and an interval of 4°, as can be seen in figure 5.22 a). Their energy can be varied from 0.1 eV to 100 eV. 204 beams are defined in this way, uniformly spaced, in a plane parallel to the sample surface but crossing the pn junction. The focus electrode voltage of the PEEM column is thus adapted to keep the image well focused onto the screen, depending on the particles kinetic energy.

In this simulation, we do not care about electrons in the solid, on their way to the surface. The anisotropy of the SE emission in the vacuum is governed by a refraction effect at the interface sample/vacuum, as presented by Henke *et al.* [165,297] and Cazaux [117]. The angular distribution in vacuum is given by a solid angle emission which depends on the kinetic energy of electrons in the solid, and on the inner angle of incidence at the interface with vacuum, considering an isotropic intern incidence. It can reach large angles, even ± 90° in some particular conditions, before total reflection within the material. We have chosen to use electrons with a restricted cone for small take-off angles. Thus, we do not take into account the full spherical and chromatic aberrations, since angles are small, but this aspect is out of the scope of our study.

Image contrast can be characterized by the current density distribution perpendicularly to the sample surface. This electron density distribution can be extracted from the

direct ray-trace in a given plane. In our case, most of the time, we consider the plane corresponding to the image plane of the PEEM column, i.e., the plane corresponding to the PEEM screen. However, we will also present some electron density distribution taken at the sample surface to observe the distribution on the object plane. These two planes of interest are represented in figure 5.20 b) by red arrows. The position at which each particle crosses this selected plane is computed and recorded in coordinates (y,z) expressed in millimeters and can be localized by red spots in the simulation screen, as shown in figure 5.22 in the vicinity of the sample surface a) or b) on the image plane. Note that, for the simulations, x is perpendicular to the surface.

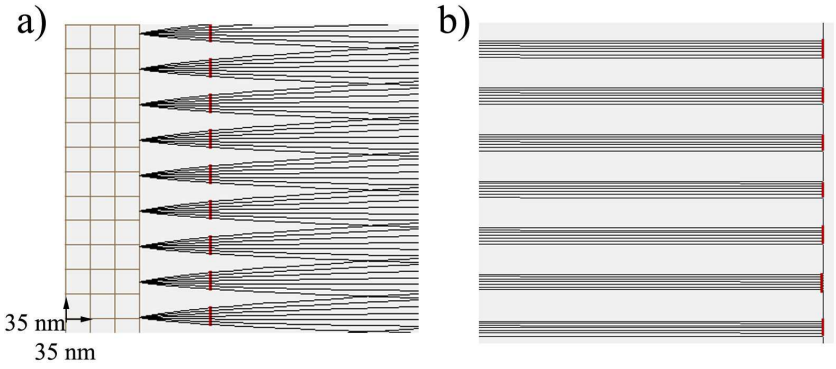

Figure 5.22: *a) Presentation of the photoelectron model adopted at the sample surface, and b) onto the screen.*

Since a finite number of particles is simulated in the form of bunches, some noise in the simulation appears when representing the photoelectron current density, in the guise of undulations. To minimize it, a moving average over the five nearest neighbors was applied on the distribution density data obtained by SIMION simulations.

5.3.1.3 The junction model

Voltage contrast obtained by applying a bias on a sample is not studied here, because only local potential variations due to a difference in work function within the sample are of interest in this chapter. We do not consider either the difference in photoyield regarding the doping type and concentration of each zone of the pn junction. Electrode voltages representing the built-in voltage have been chosen in order to highlight only the effects of the lateral electric field on the image formed in PEEM. In particular, doping concentrations were not considered since as a first step, we are interested in qualitative rather than quantitative simulations.

Since we are interested in the variation of the pn junction position regarding the influence of several factors, we consider two symmetrical pn junctions. We expect from this double junction to observe symmetrical profiles, and thus, we avoid the uncertainty in absolute position of a single junction.
This system is simulated by two linear voltage drops over a section of 3 μm, hence creating a double junction depending on the voltages applied on the structure, as can be seen on figure 5.23: a) either npn, i.e. a p-doped region surrounded by two n-doped regions, or b) pnp, a p-doped region surrounded by two n-doped regions. It is important to notice that

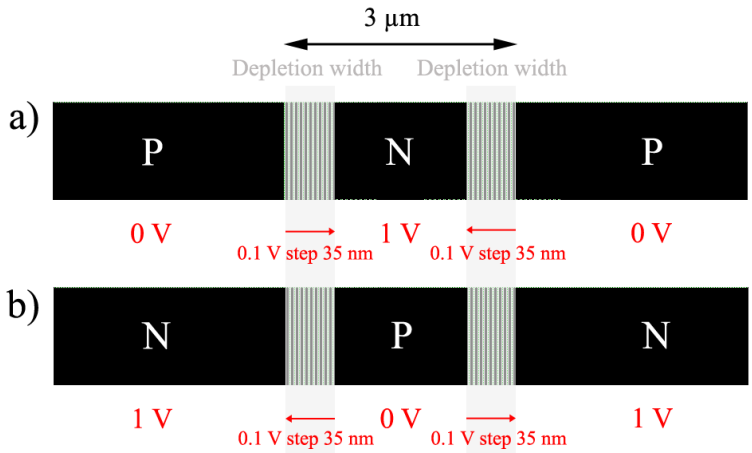

Figure 5.23: *Presentation of the two simulated junctions: a) pnp, b) npn. p-zone is simulated by a potential at 0 V, n-zone by a potential at 1 V.*

in our simulations, we do not take into account the non linear variation of the electrical field within the depletion, as presented in figure 1.1 d).

The space charge zone is sampled in equal sections of 35 nm width each and can be adapted to the desired width. The depletion zone chosen in our case is 350 nm. These devices were realized with a geometric file to facilitate numerical adjustments.

Considering the near-surface region of the sample, as can be seen in figure 5.24, the photoelectrons emitted from the regions where there are no electric field pass through the column without any perturbation. Particles emitted from regions near a junction, where local fields are present, are deviated. Depending on the junction type, either npn in case 5.24 a) or pnp in case b), the photoelectron trajectories are deviated in the opposite and symmetrical direction. The electrical field intensity in the depletion zone is maximal where the particle photocurrent density is the lowest, as presented in black, in figure 5.24 c) for the two types of junction. The symmetry of the two profiles clearly appears.

The red profiles given in right part of figure 5.24 present for the two types of junction, the smoothing improvement when applying an average over the five nearest neighbors to the raw data: the black curve corresponds to the raw data, the red one to the data after noise reduction.

This improvement concerning the noise minimization processing is similar to the one adopted by Sangwan *et al.* [298]. In their publication, they simulate the deflections of the photoelectron trajectories due to voltage contrast when applying a bias on the pn junction within a PEEM without contrast aperture. The simulations are also done with SIMION and figure 5.25 represents a typical result they obtained. More precisely, this graph shows the photoelectron density distribution within the raw data, and after one, or two averages over five nearest neighbors. This averaging method seems coherent and well appropriate.

The profiles showed by Sangwan *et al.* are qualitatively in good agreement with our profiles presented in figure 5.22 c). This agreement supports the methodology we have chosen for simulating the photoelectron trajectories within a simplified PEEM column.

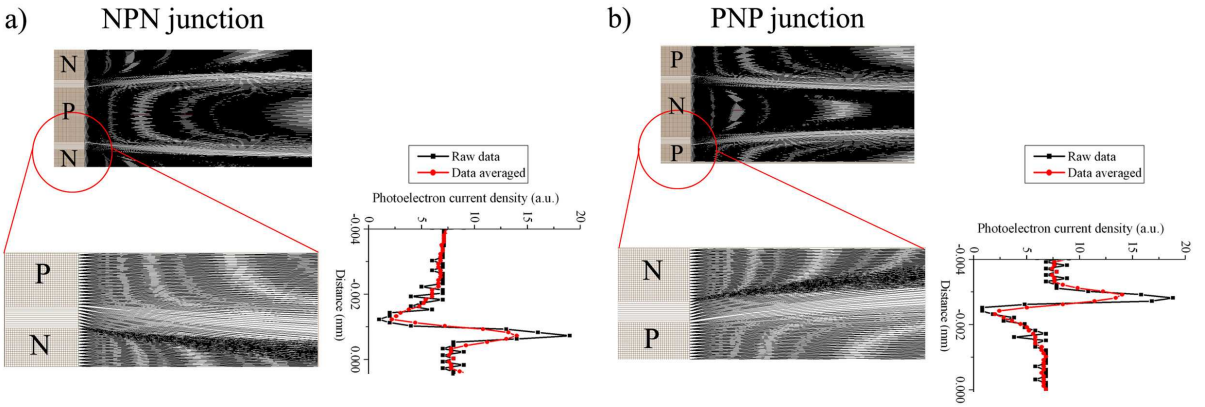

Figure 5.24: *Top: photoelectron trajectories modified due to lateral electric field. Bottom: close-up of the pn junction and the photoelectron trajectories near the surface in case of a) npn junction, and b) pnp junction. Right part of each case: simulation results when plotting the electron current density on the sample plane (black), and the average (red) chosen to minimize the numerical noise.*

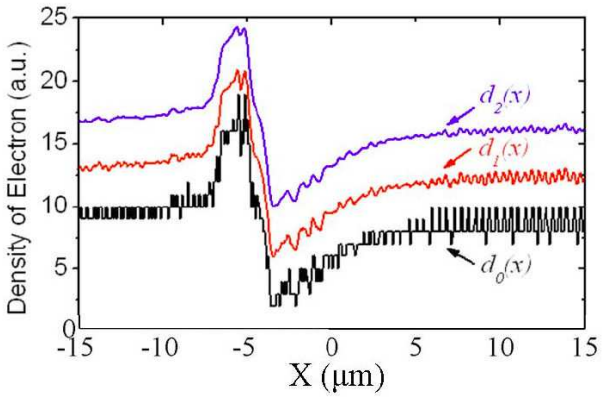

Figure 5.25: *Digitized density of electrons $d_0(x)$ and smoother distributions obtained by doing one running average over five nearest neighbors, $d_1(x)$ and after a second average $d_2(x)$ [298].*

For the following of this chapter, the smooth simulation results are presented under the shape of lines, and not symbols, for reasons of good visibility.

We have chosen to present in figure 5.26 the photoelectrons density distribution at the sample level for two complete types of structure: npn and pnp junctions. The aim is only to understand figure 5.24 in terms of density distribution. A variation in the photoelectrons distribution occurs: particles are deviated, crossing the same trajectories than others non deviated, hence increasing the local density in the vicinity of the sample surface. As it will be presented in this chapter, this behavior is conserved through the PEEM column, leading thus on the screen plane the same variations in the local intensity of the image as those observed in the sample vicinity, with the exception of the magnification factor due to the column.

The photoelectron current density describes a peak whose maximum is reached for the highest potentials across the depletion zone, i.e. when it reaches 1 V. On the contrary, the current distribution is the lowest, representing a dip in the current distribution, for the

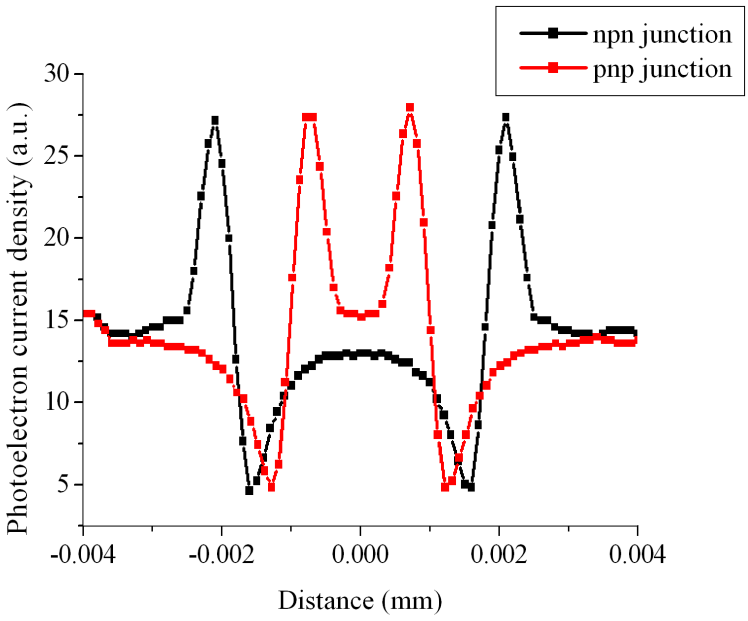

Figure 5.26: *Electron density distribution through the sample in two cases: npn junction (black), and pnp one (red) for photoelectron kinetic energy of 0.1 eV.*

first potential variations next to 0 V. The symmetry in the pattern image in the vicinity of the space charge region is clearly noticed: in the case of npn junction, the peaks are more distant than the two red ones corresponding to the pnp structure junction, since its high potentials are within the centered n-doped zone for the latter.
Another point to mention is the image reversal with respect to the object orientation, that happens in this PEEM configuration, since it only uses one lens for the magnification. In our simulations, since the pn junction object is symmetrical in the vertical axis, and since we consider the pn junction only in one dimension, it can be neglected and the results will not be modified, but it should be important for more sophisticated electron optics simulations.

5.3.2 Influence of electric field on PEEM imaging

There are two ways to simulate a PEEM column, depending on the presence or not, of a contrast aperture (CA):

- The first PEEM model, presented briefly, without contrast aperture, has already been studied by various authors, specially Nepijko *et al.* who have done considerable work on cases we will present in this section [122, 129, 136, 299]. Sangwan *et al.* must also been mentioned [298]. They characterized the voltage contrast in PEEM, and modelize it firstly numerically, thanks to SIMION simulations, and secondly measured it on images, based on the work of Nepijko's calculations.

- The second model, the PEEM column designed with a contrast aperture, is less frequent in the literature. We have only encountered it one time, thanks again to the work led by Nepijko *et al.* [300]. They present the potential mapping of a pn junction using an electron emission microscope and study the image contrast as

a function of beam restriction. They therefore concentrate on dark field imaging. Though the paper is comprehensive, few simulations are presented.

Thus, we have focused our studies on the more realistic PEEM model, i.e. with restriction of the beam due to a contrast aperture. However, we will start this section by briefly presenting the easier case, to validate the PEEM column model, without a contrast aperture.
In the following, we will study the various parameters which have to be taken into account when trying to have a general overview of the factors influencing the photoelectron trajectories. They can be either due to the sample itself, or due to the PEEM column parameters. Most of the time, both parameters contribute to deflect the charged particles. We will thus study the different factor influence separately, before increasing the difficulty by adding them. We intend, for each case where it has been possible, to compare simulations with real experiment, in order to better appreciate the surface physics and electron optics governing the observed images.

5.3.2.1 PEEM without contrast aperture

We consider here a PEEM column without contrast aperture, i.e., *without restriction of the beam* [300]. Adding a contrast aperture is not as easy as it seems, thus, during this thesis, we have started to study the easiest case, to test the particles behavior in the column. We have tuned the photoelectron kinetic energy in a large range of values: from threshold, around 0.1 eV for the lowest values, to core-level typical of 100 eV. The results in the photoelectron current density at the sample surface, and on the image plane are presented respectively in figure 5.27 a) and b) for two kinds of structures: npn or pnp junctions.

Figure 5.27 shows the density of photoelectron distribution resulting a) on the sample plane, and b) on the image plane. As can be seen, this distribution is dependent on the particle kinetic energy: for a given extractor voltage, and for a given lateral electric field across the pn junction, the density distribution varies with the photoelectrons kinetic energy. At high kinetic energy (higher than 10 eV), the distribution of the particles either on both sample and image plane is homogeneous, and no contrast induced by the local electrical field of the junction between the different doped zones is visible. The photoelectron trajectories are more deflected at low kinetic energy: the pn junction appears like a dark and bright stripe.

We observe also that depending on the structure of interest, i.e. the position of the n zone relatively to the p zone, the particles are always deviated towards the n-doped zone: the dark stripe is always on the p side of the junction. In npn (pnp) case, this tends to enlarge (shrink) the p (n) pattern in the sample plane a). As a result, for a structure presenting the same pattern with reversed doping, the localization of the pn junction shifts in the opposite direction.
When comparing the photoelectron distribution in the object and the image planes, a central zone broadened in the sample plane, appears smaller on the image plane than the image of a central zone shrunk in the sample plane: the p stripe of the npn junction is smaller than the n stripe of the pnp in the object plane whereas its image is larger. This has to be analyzed in terms of electron distribution: a broadening in the sample plane means that electrons are leaving this zone to strengthen the neighbor zone. As a result,

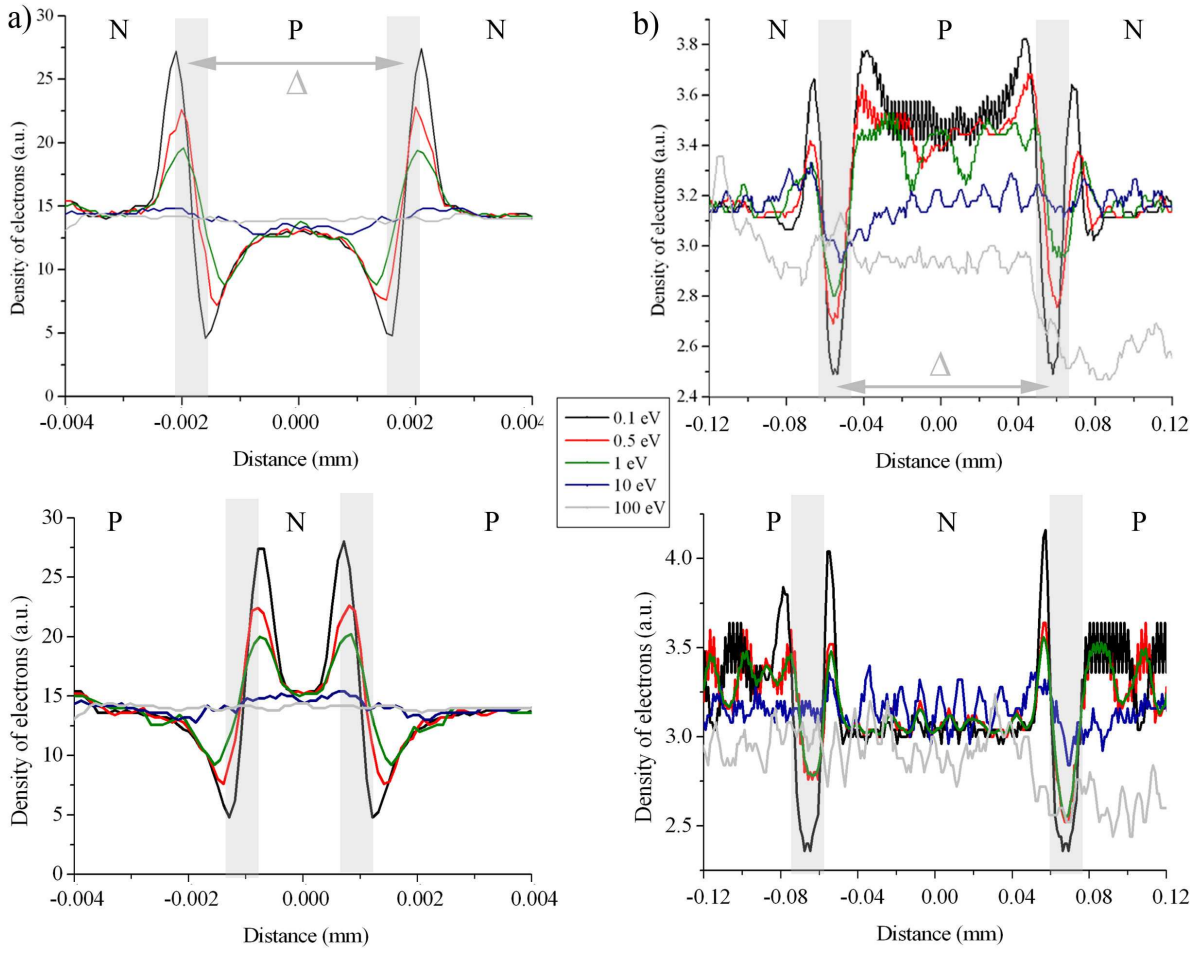

Figure 5.27: *Density of electrons distribution depending on their kinetic energy for npn or pnp structures: a) at their escape of the sample and b) onto the PEEM screen. The PEEM extractor voltage is set constant at 12 kV. The legend in the center of the figure is the same for all the graphs.*

in the image, the pn junction will be shifted relative to the zone where there is a lack of electrons, i.e. shrinking the imaged pattern.

We have measured Δ, the separation between the two junctions in the electron density distribution, as can be seen in figure 5.27 a). We compare it to the expected structure value of 3 nm wide, applying the magnification $\times 44$. However, in such case, the shift is Δ takes into account twice the real position shift due to the influence of the extractor field δx. For photoelectrons having a kinetic energy of 0.1 eV, we find respectively δx values of -3 μm in npn case whereas the shift is the same order of magnitude (measured at $+2.5$ μm) but in the reverse direction in pnp case. This simulation confirms the symmetrical behavior of these two structures.

This trend agrees with the previous studies cited, and qualitatively validates the model we would set up to simulate the PEEM image. Since the difference between simulations of npn or pnp structures is only the direction of the junction shift, we present only the case of the npn structure in the following of this section.

5.3.2.2 PEEM with contrast aperture

When a contrast aperture is inserted in the back focal plane of the immersion lens, photoelectrons deviated by local electric field presented in figure 5.28 a) are stopped by this new element, as showed in b). The redistribution of the photoelectron current density, still present, is modified in c) and implies a change of brightness in the image in d). In terms of 2D imaging, the junction is localized by a dark stripe surrounded by bright zones corresponding to the doped zones. Since we study a symmetrical pattern, the image is symmetrical relative to the central doped zone, with two dark stripes on each side of this zone, as schematically represented in d).

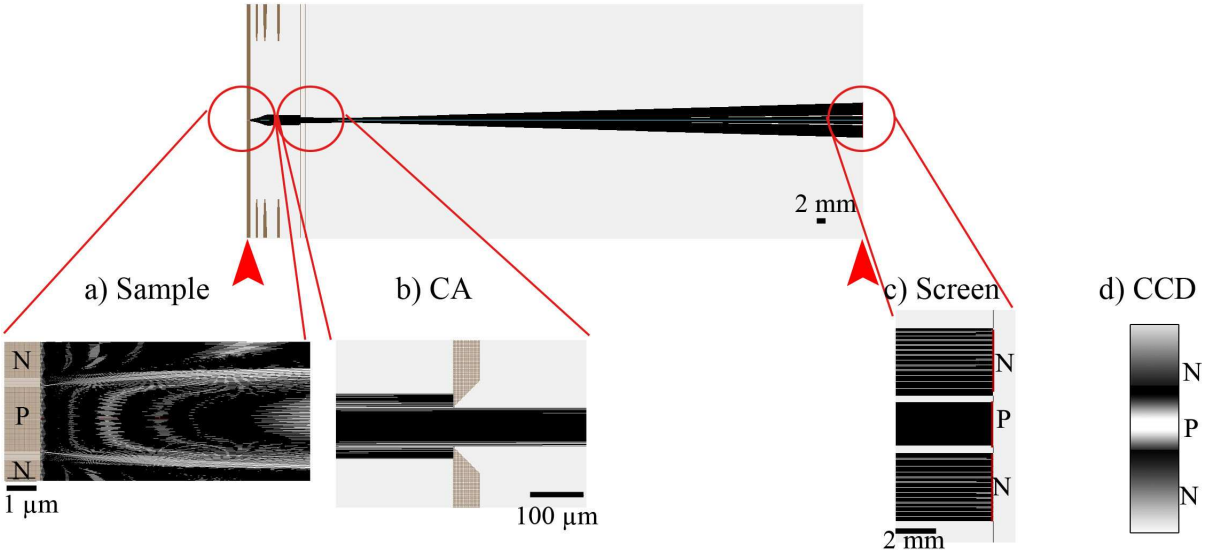

Figure 5.28: *Photoelectron trajectories at different planes through the PEEM column: a) on the sample surface, b) at the contrast aperture, c) on the screen. Figure d) represents the resulting 2D image of the pn junction expected on the CCD camera. The planes of interest where the electron density distribution is analysed are given by red arrows and corresponds to the sample surface and the screen plane.*

On the screen, the peaks in the photoelectron density distribution present due to the presence of local electric field when there are no restrictions of the beam disappear. The more deviated photoelectrons are stopped by the contrast aperture, and the density on the screen stays low. This explains why the structure observed when there are no restriction of the beam (peak+dip) is replaced by deeper and larger well. Without contrast aperture, the black intensity profile in figure 5.29 is the one expected in the vicinity of the depletion zones. When a contrast aperture is inserted in the PEEM column, a larger well, in red profile, highlights the localization of the junction.

5.3.2.3 Varying the extractor voltage

Simulations In order to check whether there is an influence of the accelerating voltage of the PEEM column on the profiles, the extractor voltage has been tuned on a range reaching nearly the double of the lowest value, here 8 kV. The focus electrode voltage is also shifted to keep the image focal plane constant. We have considered the case where

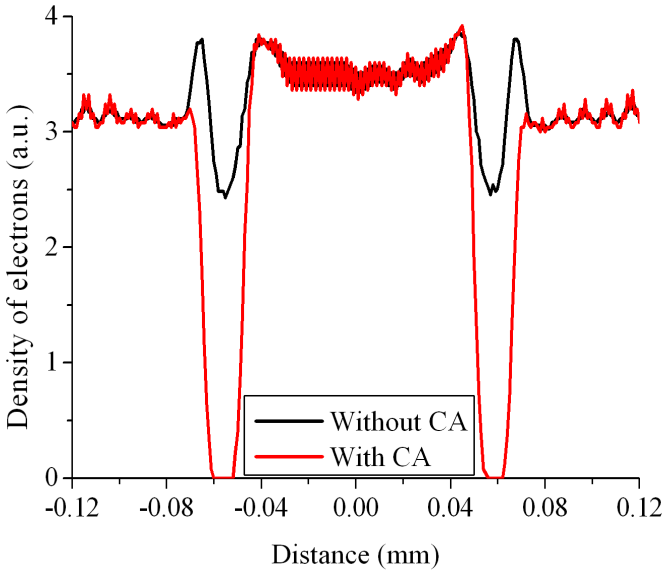

Figure 5.29: *Electron density distribution of a npn junction onto the PEEM screen in two cases: with and without contrast aperture. The photoelectrons kinetic energy is chosen to be 0.1 eV.*

the photoelectrons are the most sensitive to the perturbation of local electric field, i.e. when their kinetic energy is the lowest, at 0.1 eV.
This perturbation includes:

- the influence of the PEEM extractor lens field $E_{ext} = U_{ext}/d$, where d is the distance between the cathode and the extractor lens of the PEEM column.
- the influence of the electric field arising from the junction $E_j = \frac{-dV}{dx}$.

The combination of these two fields gives rise to a resulting vector $E_{res} = E_{ext} + E_j$.

As mentioned previously, to avoid the uncertainty on the position of a pn junction, we consider two symmetrical junctions. For several extractor voltage values, we have measured Δ, the separation between the two junctions in the electron density distribution, as can be seen in figure 5.30 a). However, in such case, a shift of Δ takes into account twice the real junction shift δx due to the influence of the extractor field. Results presented in table 5.5 are corrected from this effect, presenting the position shift for a single pn junction.

U_{ext}	8 kV	10 kV	12 kV	15 kV
Δ (μm)	2.52	2.68	2.80	2.86
δx (μm)	-0.24	-0.16	-0.10	-0.07

Table 5.5: *Lateral measurements of the separation between the two junctions Δ and position shift δx of a single junction deduced from the screen plane and simulated for different extractor voltages.*

The shift of the double pn junction profile resulting varies significantly, as can be seen in figure 5.30 a). The separation between the two junctions Δ has to be compared with the size of the junction simulated, and expected to be 3 μm wide (see section 5.3.1.3).

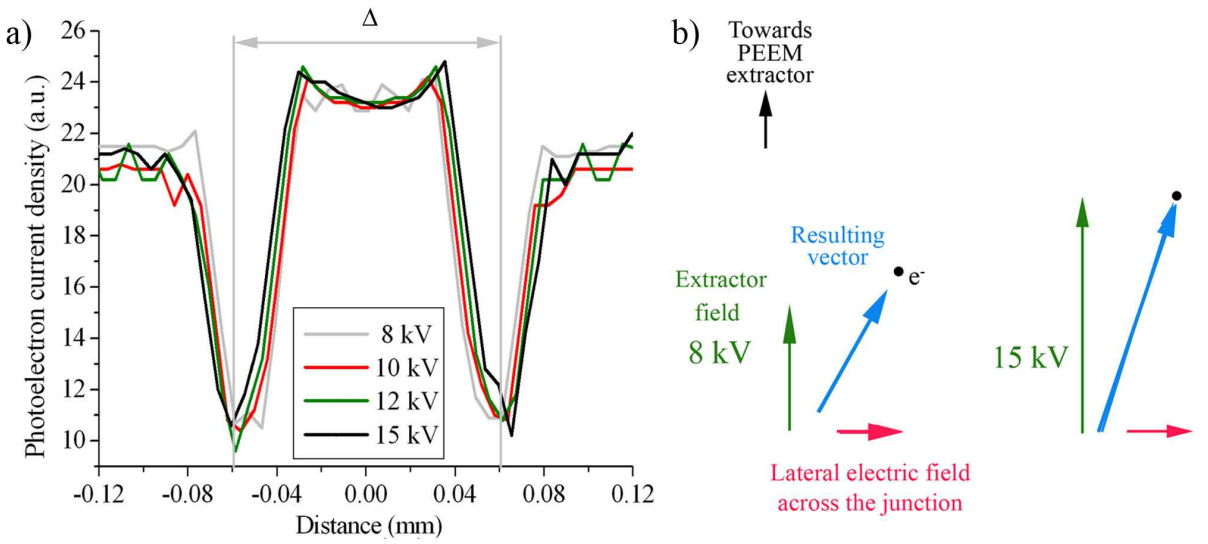

Figure 5.30: *a) Density of electron distribution at the sample surface depending on the extractor voltage of the PEEM column. b) Scheme showing the influence on the photoelectrons of lateral electric field across a pn junction (red) and of extractor voltage (green) depending on its value. The vector sum of these forces is represented in blue.*

Figure 5.31, shows that the real position shift due to the influence of the junction electric field δx decreases with increasing the extractor voltage. At 15 kV, it is nearly nil.

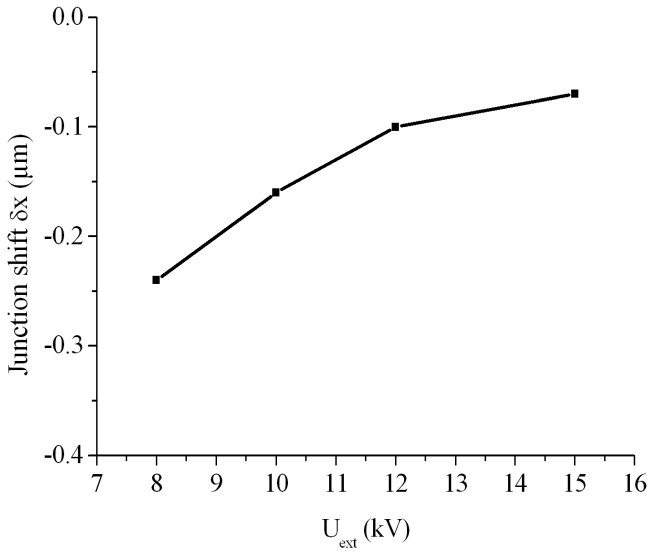

Figure 5.31: *Junction width simulated for different extractor voltages.*

We can summarize this explanation: the low photoelectrons emitted from the surface are sensitive to both fields, the one emitted from the junction, and the other created by the extractor lens. At 15 kV, they are more influenced by the high extractor field and are deviated by the local electric field present across the junction. The behavior which can be deducted from this simulation, is that the higher the extractor field, the less deviated the photoelectrons by the local electric field across the junction (being equal to

2.86 kV.mm^{-1}), and the more accurate the image acquired.
For a low extractor voltage at 8 kV, the electric field applied by the extractor is 4.44 kV.mm^{-1}, the particles are more influenced by the lateral electric field across the junction, than at 15 kV, where the electric field is 8.33 kV.mm^{-1}. Figure 5.30 b) shows the resultant electric field vector for the two extreme values of extractor voltages 8 kV and 15 kV. Green arrows represent the force applied on the particles by the electric field across the depletion zone, which is kept constant, and red ones represent the force applied by the extractor voltage. The resulting vector corresponding to the combination of both fields is represented in blue. Its deviation is obviously the least for the highest PEEM extractor voltage.

Experiments We can now focus on pn junction images obtained at threshold for two extractor voltages: 12 kV and 15 kV which correspond to the experimental used values. For a kinetic energy of $(E - E_F)$=4.75 eV, we have been able to extract the intensity profile of the zero shape presented in the left part of figure 5.32.
The measured dimensions of the pattern vary with the extractor voltage: the results presented at the right part show the difficulty in localizing the pn junction: the pattern profile obtained with an extractor voltage of 12 kV (black) seems slightly shrunk relative to the profile obtained at 15 kV (red) by 0.9 %. This is the same conclusion we have extracted from our simulations.

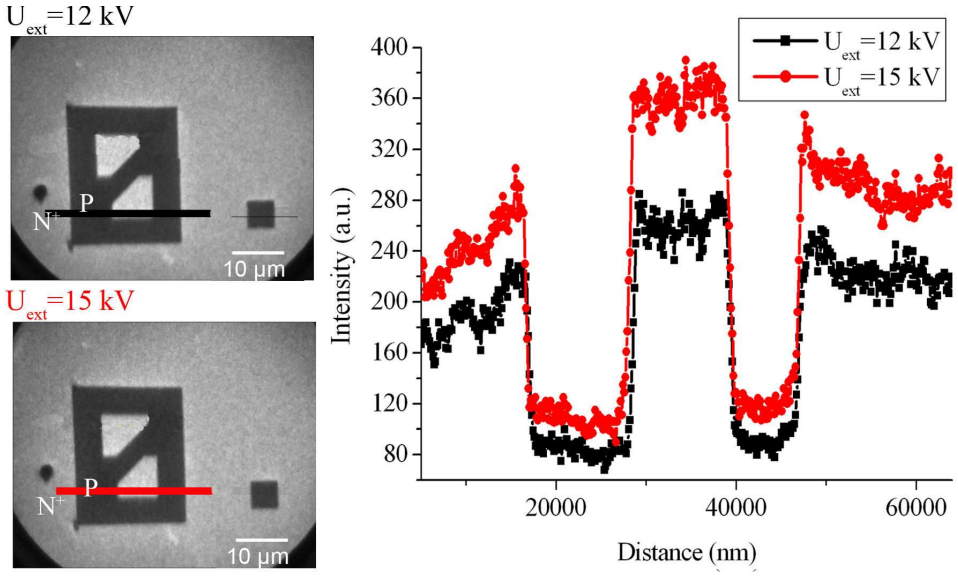

Figure 5.32: *Intensity profile of a pn junction taken at threshold ($(E - E_F)$=4.75 eV) for two extractor voltages: 12 kV (black) and 15 kV (red).*

The pattern size found is 29.89 μm at 12 kV against 30.15 μm at 15 kV: for a high extractor voltage it reaches values closer than the one expected obtained using an optical microscope (31.79 μm, see figure 3.16). Thus, the pattern sizes extracted from image at low kinetic energy are closer to the ones obtained using an optical microscope, when using a high extractor voltage.

It is interesting to compare patterns with such important lateral electrical fields, and patterns with no significant electrical fields. We can thus compare pn junctions with

SiGe structures, presented in chapter 2. A good evidence of the difference between these two samples is obviously via lateral resolution measurement. Table 5.6 summarizes the different measurements obtained at threshold, for the two structures shown in figure 5.33, for a given energy, a contrast aperture diameter of 70 μm, and for the two extractor voltages 12 kV and 15 kV.

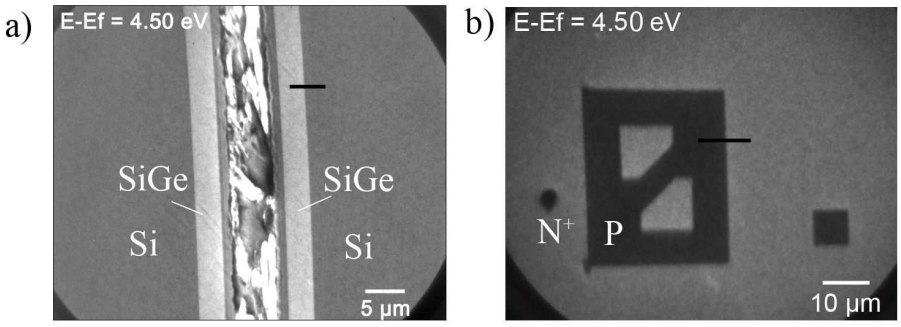

Figure 5.33: *Images at threshold $(E - E_F)$=4.5 eV for the two samples of interest: a) SiGe structure, b) pn junction. The lateral resolution is measured from the intensity profile extracted along the line cut across the patterns.*

Structure type	Electric field E_j	Lateral resolution at 12 kV E_{ext}=6.66 kV.mm^{-1}	Lateral resolution at 15 kV E_{ext}=8.33 kV.mm^{-1}
SiGe	$E_j << E_{ext}$	107.4±21.8	88.4±17.8
pn junction	$E_j \approx E_{ext}$	484.2±50.6	353.7±40.2

Table 5.6: *Lateral resolution measurements given in nanometers at threshold for two structures.*

- When the structure does not present a significant lateral electrical field, the lateral resolution measured is, as expected, the same order of magnitude as the PEEM contrast aperture expressed in nanometers [236]. In our case, we are close to 70 nm when observing the SiGe structure.

- On the contrary, when the electrical fields are non negligible compared to the extractor voltage, as in the pn junction case, the lateral resolution is four time bigger than expected. Thus lateral electrical field across a structure can significantly limit the spatial resolution in PEEM.

5.3.2.4 Varying the photoelectron kinetic energy

Simulations The previous section has already demonstrated the influence of the photoelectron kinetic energy for given PEEM conditions on their trajectory, specially when considering a PEEM column without restriction of the beam, as seen in figure 5.27 on both sample and screen planes.

Here we confirm the validity of our more complete PEEM column model, including the contrast aperture in the back focal plane of the extractor lens. These density of electron distributions are presented for an extractor voltage of 12 kV and a npn junction, varying the photoelectron kinetic energy between 0.1 eV to 100 eV.

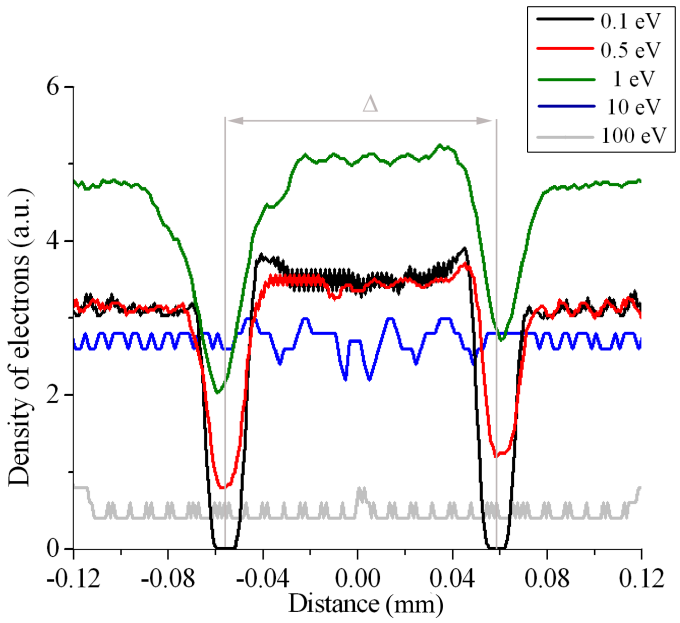

Figure 5.34: *Photoelectron current density distribution on the PEEM image, depending on the particles kinetic energy.*

- The junction position shifts with the photoelectron kinetic energy lower than 1 eV: the higher the kinetic energy, the larger the width Δ between the two wells, and the lower the shift due to local electrical field. These shifts are in the same order of magnitude than those found with previous simulations 5.5. We present in table 5.7 the junction shift evolution δx with the photoelectrons kinetic energy.

Kinetic Energy	0.1 eV	0.5 eV	1 eV	10 eV	100 eV
Δ (μm)	2.55	2.64	2.80	-	-
δx (μm)	-0.23	-0.18	-0.12	-	-

Table 5.7: *Lateral measurements of the separation between the two junctions Δ and position shift δx of a single junction deduced from the screen plane and simulated for different extractor voltages.*

- Particles with very low kinetic energy, from 0.1 eV to 1 eV are strongly deflected inducing an highly contrasted image of the depletion width of the junction: the wells corresponding to a lack of photoelectron current density distribution are very deep. In such cases, the deviation means the junction localisation is not possible without knowing the model to deduce its position.

- When the particles are far from photoemission threshold, for example between 10 eV and 100 eV, they are less depleted by the lateral electric field. They pass through

the PEEM column and the characteristic wells of the npn structure at low kinetic energy are no longer visible on the simulated curves. In this case, the position of the junction may be accurately determined from the doping contrast with a spatial resolution close to that of the PEEM.

The same behavior than the one observed in figure 5.27 b) is indeed observed on the simulations of figure 5.34: the faster the particles, the less important the well, the less deviated the particles.

Experiments We present lateral measurements obtained near threshold for two kinetic energies, visible in figure 5.35. They were performed at different localization of the pattern to better average the experimental value, and also to check the influence of the pattern itself due to the presence or not of several electric field directions, in the vicinity of the measurement.

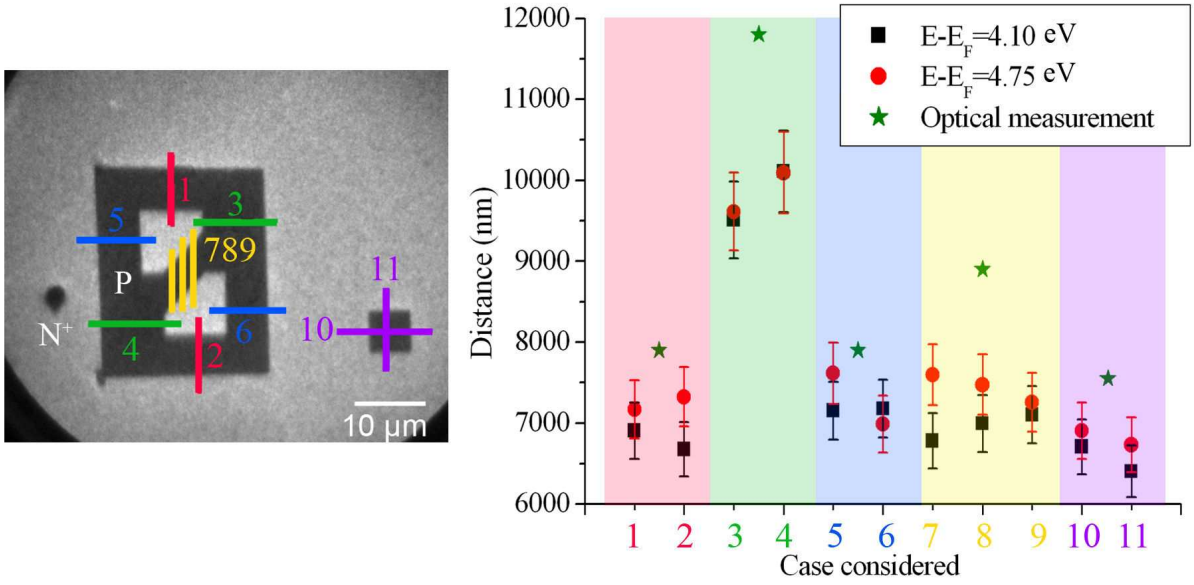

Figure 5.35: *Images obtained for an extractor voltage of 12 kV, at threshold: a) $(E - E_F)$=4.10 eV, b) $(E - E_F)$=4.75 eV. The lateral measurements are determined from the intensity profile extracted along the coloured line cut across the patterns.*

The difference between experimental values and measured optical ones are important. We can assume that this is not only due to the presence of a local lateral electrical field across the junction (due to a difference in work function between the two doped zones of 0.13 eV), but we have to deal with physical topography that can be tenth of nanometers. However, since, during the image series acquisition, these topographies do not have changed, we assume that the relative shift between the two measurements is due to the local electrical field across the junction. No difference in lateral measurement is found regarding the zone chosen for the measurement. The average difference in the pattern size between the images taken at two kinetic energies is 1.2 μm.

Thus the pattern image taken at a kinetic energy of 4.75 eV is larger than the one obtained at 4.10 eV, and closer to the values obtained optically. Thus, we can confirm the dependence of the pattern size measurement to the particles kinetic energy for a constant extractor voltage: the higher the particles, the less deviated by the electric field.

5.3.2.5 Varying the lateral electrical fields through the depletion zone

Simulations In the pn junction configuration considered, with a built-in voltage of 1 V, we expect a lateral field of 2.86 kV.mm^{-1} on the surface, non negligible with the perpendicular field in the PEEM, which is 6.66 kV.mm^{-1} for an extractor voltage of 12 kV. The resulting field vector influencing the photoelectron trajectories represented in blue in figure 5.36 shows the extent of the lateral electric field across the junction.

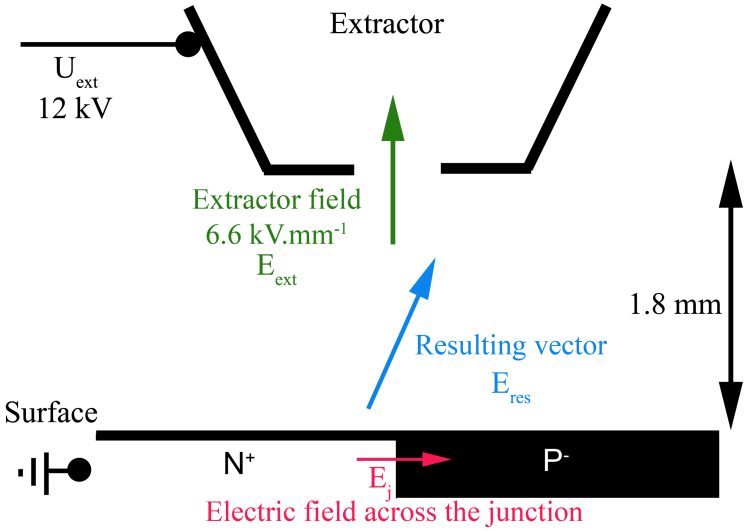

Figure 5.36: *Scheme of the different electric field contributions in a PEEM, at the cathode level.*

Table 5.8 shows the calculated lateral electric field strength across the pn junction depending on the built-in voltage simulated for a constant depletion width of 350 nm. When the built-in potential difference over the depletion width is low, the electric field is low, and has less influence on the photoelectron trajectories compared to the electric field due to the extractor electrode.

Built-in voltage V	Lateral electric field E_j kV.mm^{-1}	E_{ext}/E_j
0.05	0.14	47.6
0.5	1.43	4.70
1	2.86	2.30
1.5	4.29	1.55

Table 5.8: *Lateral electric field E_j and E_{ext}/E_j ratio as a function of built-in voltage considered through the depletion zone of a pn junction.*

Figure 5.37 a) presents simulations of the photoelectron current density distribution at the sample surface for several built-in voltages varying between 0.05 V to 1.5 V. We

observe that the photoelectrons emitted from a surface where the built-in voltage is faint, i.e. the electric field across the junction is low, the particles are not deviated by this latter.

Figure 5.37 b) shows the evolution between the maximum current density relative to the E_{ext}/E_j ratio given in table 5.8 in order to characterize the influence of the built-in voltage. Since no contrast occurs in the density of electron distribution for a low built-in voltage of 0.05 eV, we do not present it. However, a trend is clearly visible: the smaller the ratio between the electric field of the extractor lens and the junction, the more deviated the particles, and the more important the density distribution variations.

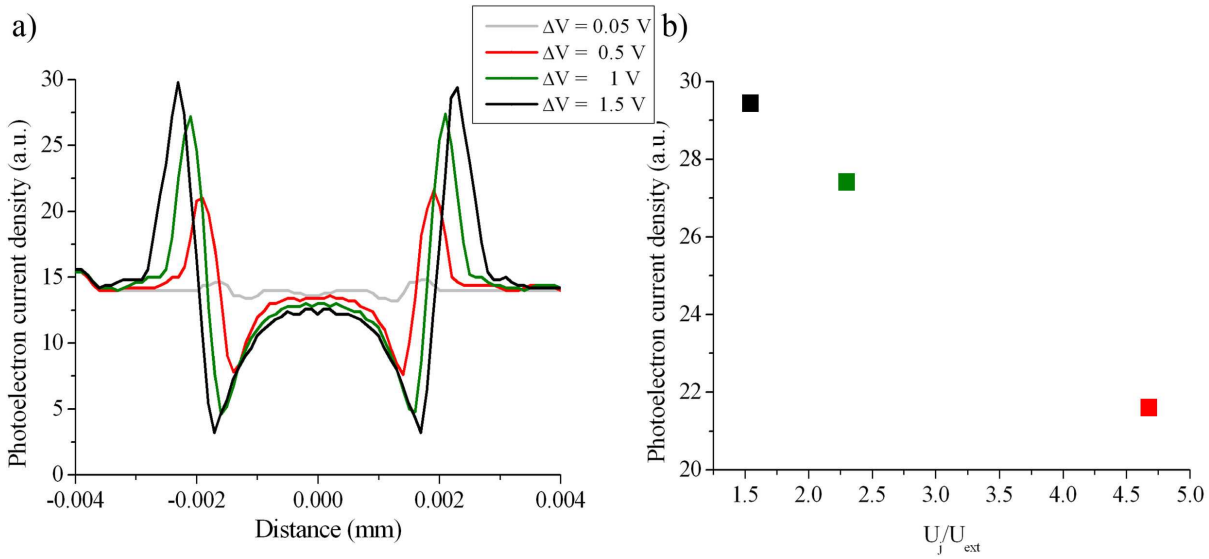

Figure 5.37: *a) Density of electrons distribution at their escape of the sample depending on the potential gradient through the depletion zone. b) Representation of the evolution between maximal current density and E_{ext}/E_j ratio.*

To finish this section, one has to consider the resulting image on the PEEM screen, as presented in figure 5.38.

The depletion zone represented by the wells in the photoelectron current density is only visible for high built-in potentials, more than 0.5 V in the simulated cases. This means that for low potential through the depletion zone, the photoelectrons pass through the PEEM column without any cut-off due to the presence of the contrast aperture. On the screen, the distribution is homogeneous. On the contrary, when the built-in potential is stronger, the photoelectrons are deviated by the electric field across the junction,producing an inhomogeneous current density distribution on the screen. To go further with this idea: the well width in the image increases with the built-in potential, 1 V and 1.5 V, whereas no contrast is seen for other built-in value. We note also particularly that an in-built potential of 0.05 V is very close to the limiting case of no pn junction.

Experiments We can illustrate this behavior taking images at threshold for two silicon doped samples presenting different built-in potential. We have chosen the samples presented in figure 5.39 a) P^+/P and b) P^+/N since the work function difference $\Delta\Phi$

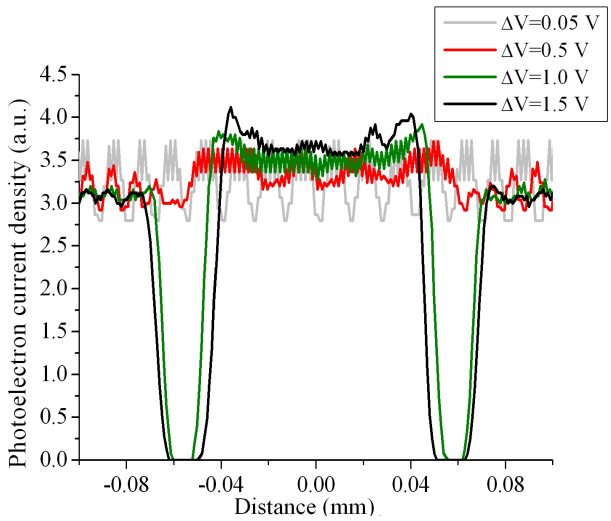

Figure 5.38: *Density of electrons distribution on the screen, depending on the potential gradient across the depletion zone.*

between the two doped zones are faint at 128.9 eV, respectively 0.05 eV and 0.03 eV for P^+/P and P^+/N (see table 4.8). This consideration is particularly of interest since it validates that the shift measured is not influenced by an electrical topography due to potential variations across the junction, but is only due to the presence of a local lateral electric field across this junction.
The images were taken from image series at threshold, with a photon excitation source at 128.9 eV. The energy $(E - E_F)$=4.45 eV has been chosen to allow a good contrast between the different doped zones. The intensity profiles have been extracted along the black (red) line cut on P^+/P sample (P^+/N), across the doped pattern.

The width Ψ measured for the two samples is different: the red pattern, corresponding to the sample P^+/N where the built-in potential is the highest, is larger than the black one.

The effect of the lateral electric field can be quantified, though the signal intensity is noisy, when measuring one pattern side called Ψ:

- $\Psi_{P^+/N}$=8.86 μm,
- $\Psi_{P^+/P}$=8.36 μm.

In comparison, the measurement obtained with the optical microscope $\Psi_{optical}$, which is not influenced by the local electric field across the junction, is 7.9 μm.

The same analysis was performed for images series taken at threshold using laboratory X-ray source (photon energy: 1486.7 eV) on N^+/P and P^+/N samples. The work function difference $\Delta\Phi$ between the two doped zones was faint, respectively 0.07 eV and 0.05 eV for N^+/P and P^+/N samples. Table 5.9 summarizes the pattern size difference with PEEM measurement and optical one, the junction shift δx and recalls the ratio E_{ext}/E_j for the analysis conditions (see table 3.3).

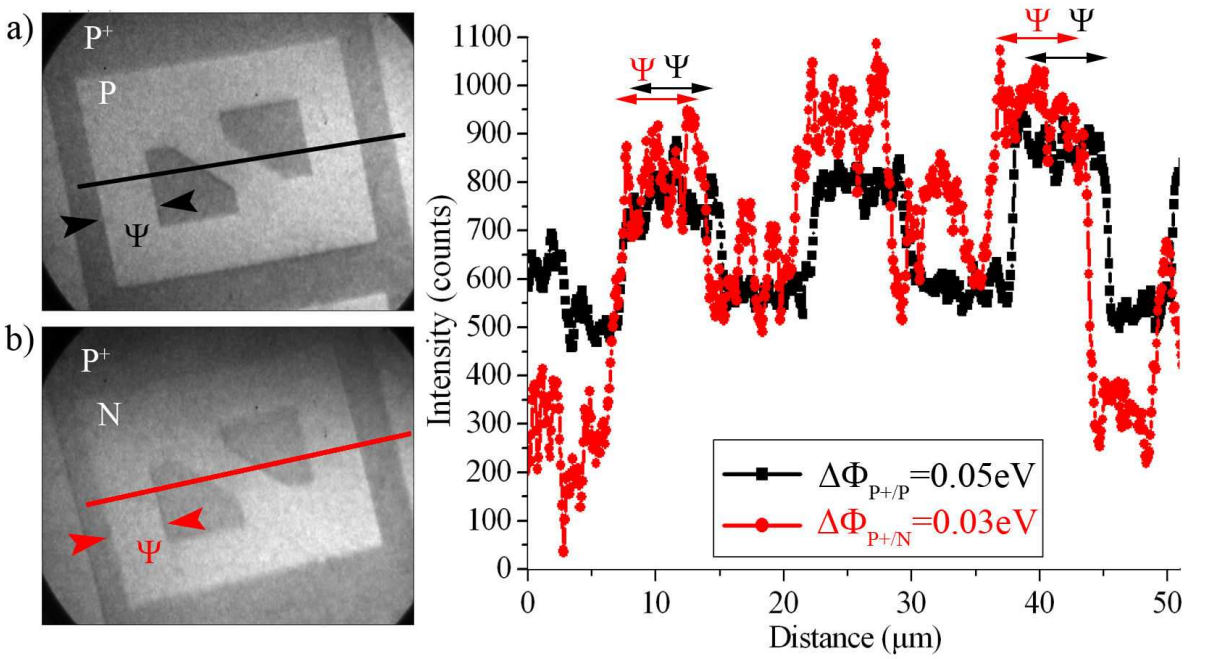

Figure 5.39: *Images of a) P^+/P and b) P^+/N taken at threshold $(E - E_F)$=4.45 eV and intensity profile extracted across the linecuts.*

Photon source	1486.7 eV		128.9 eV	
Sample considered	N^+/P	P^+/N	P^+/P	P^+/N
$\Delta\Phi$ (eV)	0.07	0.05	0.05	0.03
$\Psi_{optical}$-Ψ (μm)	0.69	1.12	-0.46	-0.96
δx	0.34	0.56	-0.23	-0.48
E_{ext}/E_j	4.06	0.33	4.09	0.33

Table 5.9: *Lateral shift δx measured on silicon doped patterns depending on the E_{ext}/E_j ratio, as a function of work function difference $\Delta\Phi$ considered through the depletion zone of a pn junction for two photon energies.*

For a given kinetic energy, and for a given extractor voltage, if we consider a work function difference across the junction, the pn junction shifts measured are an evidence of the presence of this electrical field across the junction. Moreover, for the two photon energies, the shift of the junction position measured is in good agreement when comparing values for lateral electrical fields in the same order of magnitude. Thus, we find a good agreement with what should be expected: the sample presenting a lower electric field across the junction presents a width closer to that of optical microscopy.

5.3.2.6 Conclusion

We have shown that it is not possible to determine accurately the localisation of a pn junction since several factors influence the photoelectron trajectories.
Depending on the PEEM imaging conditions, the particles are influenced by both the extractor field of the immersion lens and the local lateral electric field across a pn junction,

resulting in a shift of the pn junction. Hence, the highest the extractor voltage, the less deviated the photoelectrons by the local electrical field. On the contrary, for a constant extractor voltage, the highest the work function difference between the two doped zones, the more deviated the particles.
The kinetic energy is also an important factor to take into account: whatever the fields strength, the higher the kinetic energy, the less deviated the particles.
The image resulting can be interpreted by local photoelectron current density distribution. The more homogeneous it is, the less the influence of the junction electric field.

The point of interest now is to find a way to experimentally highlight the presence of the lateral electric field due to the built-in potential of the junction in PEEM imaging. This can be done thanks to the dark field imaging technique detailed in the next section.

5.3.3 Dark field PEEM imaging

5.3.3.1 Principle

The dark field imaging technique, based on the restriction of the photoelectron beam, is more sensitive to the presence of electric field and uses the partial cut-off of the electron trajectories to obtain the distribution of these fields across the junction.

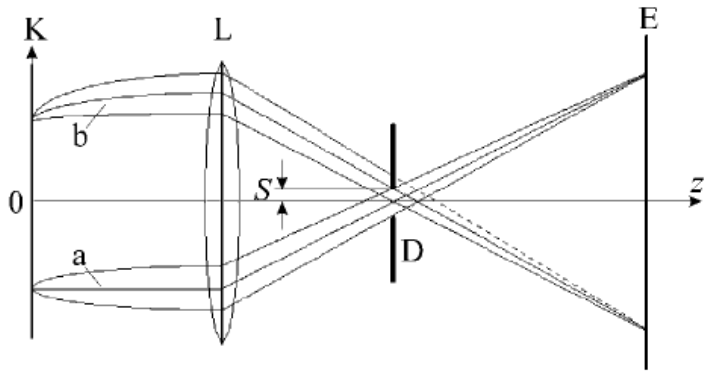

Figure 5.40: *Diagram of the image contrast formation caused by the local fields under restriction of the electron beam. a, undeflected electron beam; b, deflected electron beam due to local fields; K, object plane; L, objective lens; E, screen [300].*

The principle of this technique is well described by Nepijko *et al.* [300]. A contrast aperture situated in the back focal plane of the immersion lens can be shifted off-axis, hence restricting partially the electron beam.
Figure 5.40 represents the schematic diagram of dark field imaging in a PEEM: in absence of electric field coming from the surface, the photoelectrons are not deviated a) and all the particles pass through the diaphragm. On the contrary, under local electric field in b), the particles deviated can be blocked by the contrast aperture D which is not centered on the optical axis. The resulting image on the screen appears darker than a zone where the particles are not deflected. This dark contrast highlights the presence of local fields.

This subsection models the dark field phenomena using SIMION simulations. It is important to distinguish the influence of the photoelectron deviation due to the local electrical field across the pn junction from those due to the sample topography. We have chosen to present electron optical simulations for both factors separately, before completing the section by simulating the influence on particles under the combination of these two effects.

5.3.3.2 Dark field when only presence of lateral electric field

Figure 5.41 presents the SIMION simulations for a npn junction: the photoelectron current density on the screen is plotted for several shifts of 10 μm of the contrast aperture from the optical axis. To better appreciate the deviation of the particles, their kinetic energy is chosen the lowest: 0.1 eV. Central figure in dark reminds the case where the contrast aperture is centered on the optical axis: one recognizes the two wells corresponding to the localization of both side of the p-doped pattern. The simulation results are similar when the contrast aperture was shifted on the one side from the optical axis a), or when it was shifted on the other side b).

The more the contrast aperture is shifted, the more one junction side appears brighter whereas the other seems to disappear. For sample regions where the photoelectron rays are deviated by the local electric field, some of them are stopped by the contrast aperture, which decreases the particles distribution, hence limiting the current density observed. On the other side of the junction, all the photoelectrons deviated can pass through the PEEM column and the current density observed on the screen seems more important.

For larger shifts, more than 40 μm, half the order of magnitude of the contrast aperture diameter, the darkening occurs not only on the depletion zone on one side of the junction: the totality of the photoelectron density indeed decreases, this is why the distribution on the screen seems nearly nil.

5.3.3.3 Influence of topography

The local electrostatic microfields appearing across a pn junction due to a potential variation through the depletion zone are not the only effect to consider: it is also important to consider microfields created by the topography of the sample surface. These microfields can deviate the particles with low kinetic energy, in the same way as the microfields coming from the electrical contrast, as presented by Siegrist *et al.* [130]. The electrons passing through this microfield region are deviated, hence creating several areas with higher or lower electron current density in the image plane. The surface roughness of the sample thus leads to a topographical image contrast which can be considered equivalent to a smooth surface with an electric potential distribution.

In the next subsection, the contrast induced by topography is simulated to understand in which proportions it can have a role on dark field imaging, compared to the electrical contrast. Figure 5.42 validates the PEEM model used when simulating a sample whose surface is not flat, but composed by a step of 1 μm height, from left to right, firstly the simulation of the photoelectron trajectories deviated by the topography, and secondly the current density distribution in the image plane: a) corresponds to Nepijko's results, and b) our simulation results. Since these simulations are both realized considering a PEEM

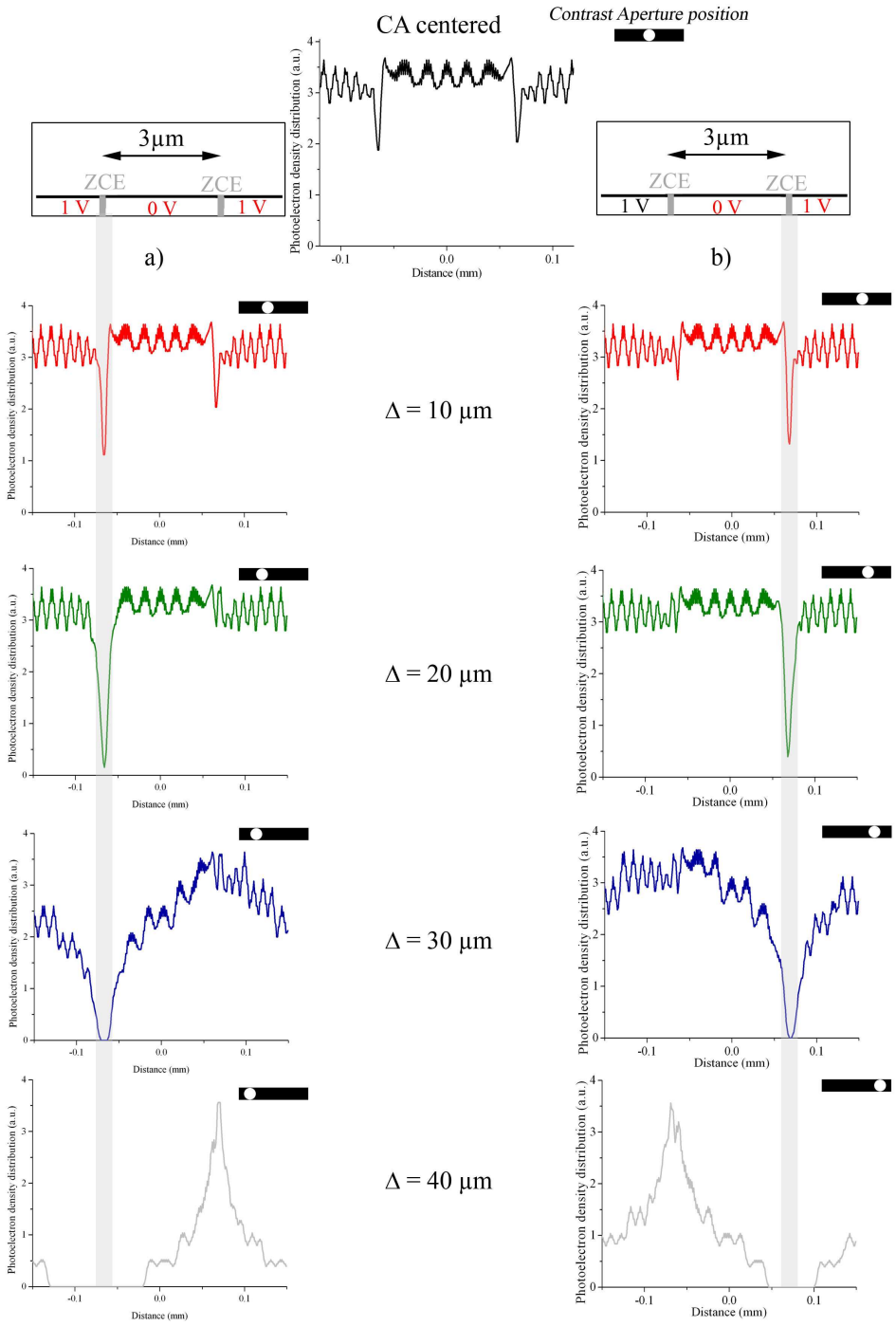

Figure 5.41: *Case of a npn junction. Intensity distribution on the screen for dark field imaging for different CA shifts: a) negative and b) positive. Inset: Sample simulated with dimensions, and potential applied to the npn junction model. The black and white drawings are guide line for the CA position.*

without contrast aperture, one observes in the vicinity of the sample both peak and well in the current distribution, characteristic of the presence of local fields.

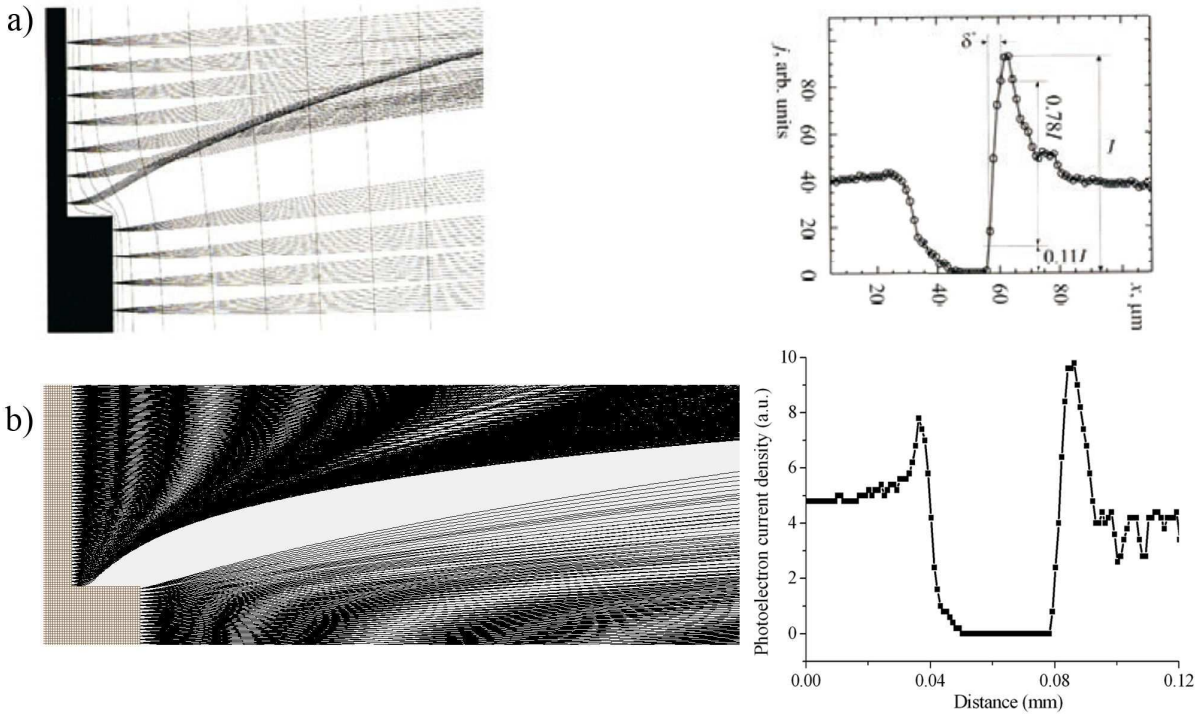

Figure 5.42: *Trajectory distribution and intensity distribution simulated on the screen in a) Nepijko PEEM model [129] and in b) our NanoESCA model to confirm its validity.*

Without lateral electric field - Simulations The situation of a geometrical step of 1 μm height on a smooth surface has already been studied by both computer simulation and analytical theory by Nepijko *et al.* [129]. The step height used here is the same order of magnitude than the one which can be encountered on our samples presented in chapter 3. SSRM shows indeed a topography at the junction between the two doped regions which can attain 70 nm. No voltage is applied to the sample electrodes forming the junction. The photoelectron kinetic energy is chosen to be still 0.1 eV to allow the comparison with figure 5.41.

A change in the brightness due to redistribution of the electron current density again occurs, as seen in figure 5.43. A shift of the contrast aperture within the backfocal plane of the immersion lens highlights the topography influence on the photoelectron deviation on one side of the raised pattern.

The simulations when shifting the diaphragm towards the other direction could have been presented, but they correspond to the same symmetrical results as those presented in figure 5.41. For reasons of clarity, we have chosen to simplify the figure.
In conclusion, within this simulation model, a sample without voltage contrast but topography infers the same influence on the photoelectron trajectories than a flat sample with electric field. When realizing dark field imaging with PEEM the results are quite similar. In a real case, one has to consider both contrasts: topographical and electrical one. Next subsection shows what kind of results one can expects from dark field imaging

with such topographies.

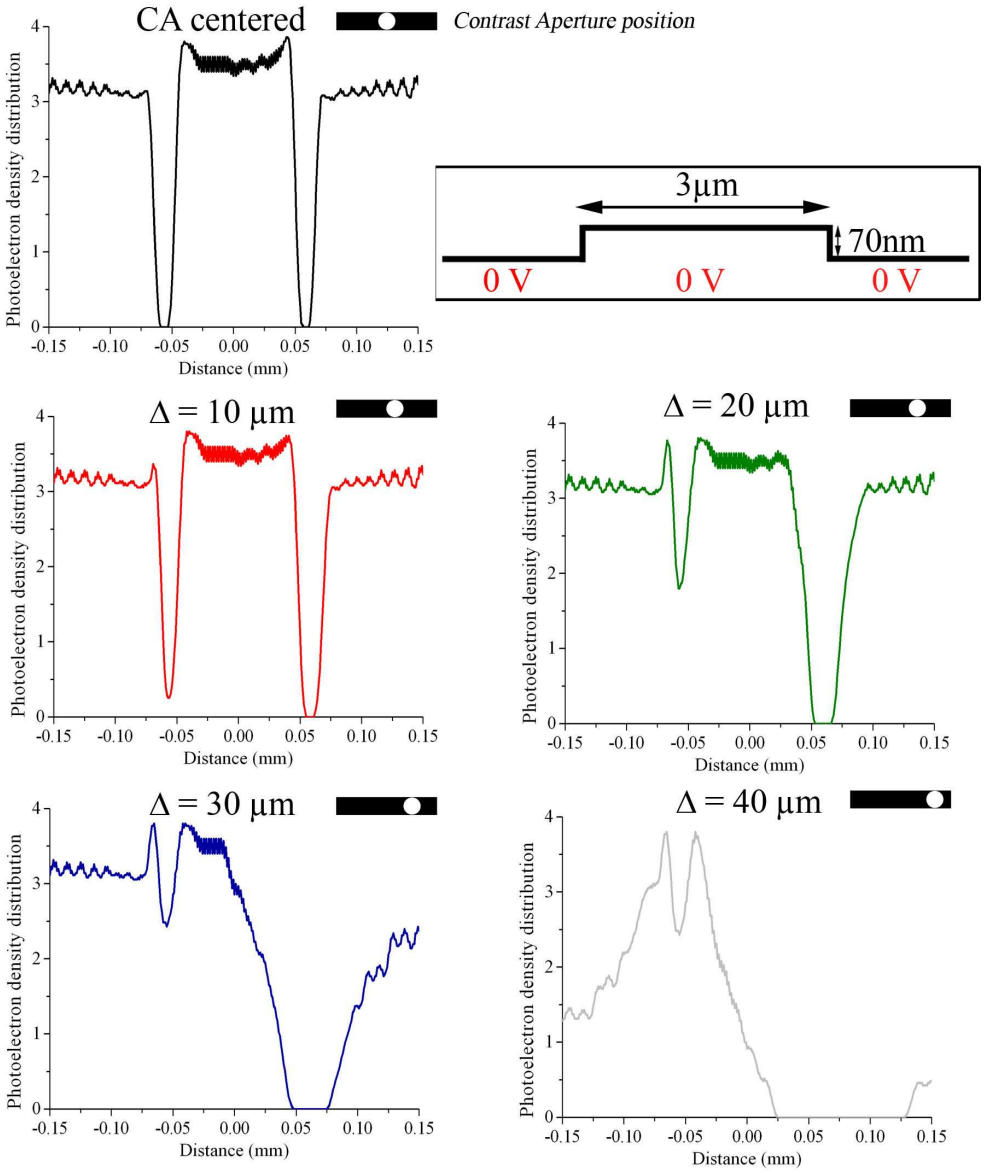

Figure 5.43: *Intensity distribution simulated on the screen for dark field imaging and different CA shifts Δ. Inset: Sample simulated with dimensions, topography, and potential applied to the model. The black and white drawings are guide line for the CA position.*

With lateral electric field - Simulations This subsection shows the simulations the most realistic of microfields which interfere with the photoelectrons emitted from the sample surface. It takes into account not only the electric topography present at a pn junction, but also the physical topography of the sample. The results concern photoemitted electrons with a kinetic energy of 0.1 eV and transmitted through the PEEM column. The point of interest is the distribution of these particles on the image plane when considering dark field imaging.

The data simulated looks like the ones already obtained in previous sections 5.3.3.2 and 5.3.3.3 when shifting the contrast aperture off-axis. To avoid repetition, the only graph presented in this section on figure 5.44 compares the electron current density depending on the origin of the electric field in two cases: a) with a centered contrast aperture, and b) with a contrast aperture having a certain shift, chosen to be half its diameter, i.e. $\pm$ 30 μm.

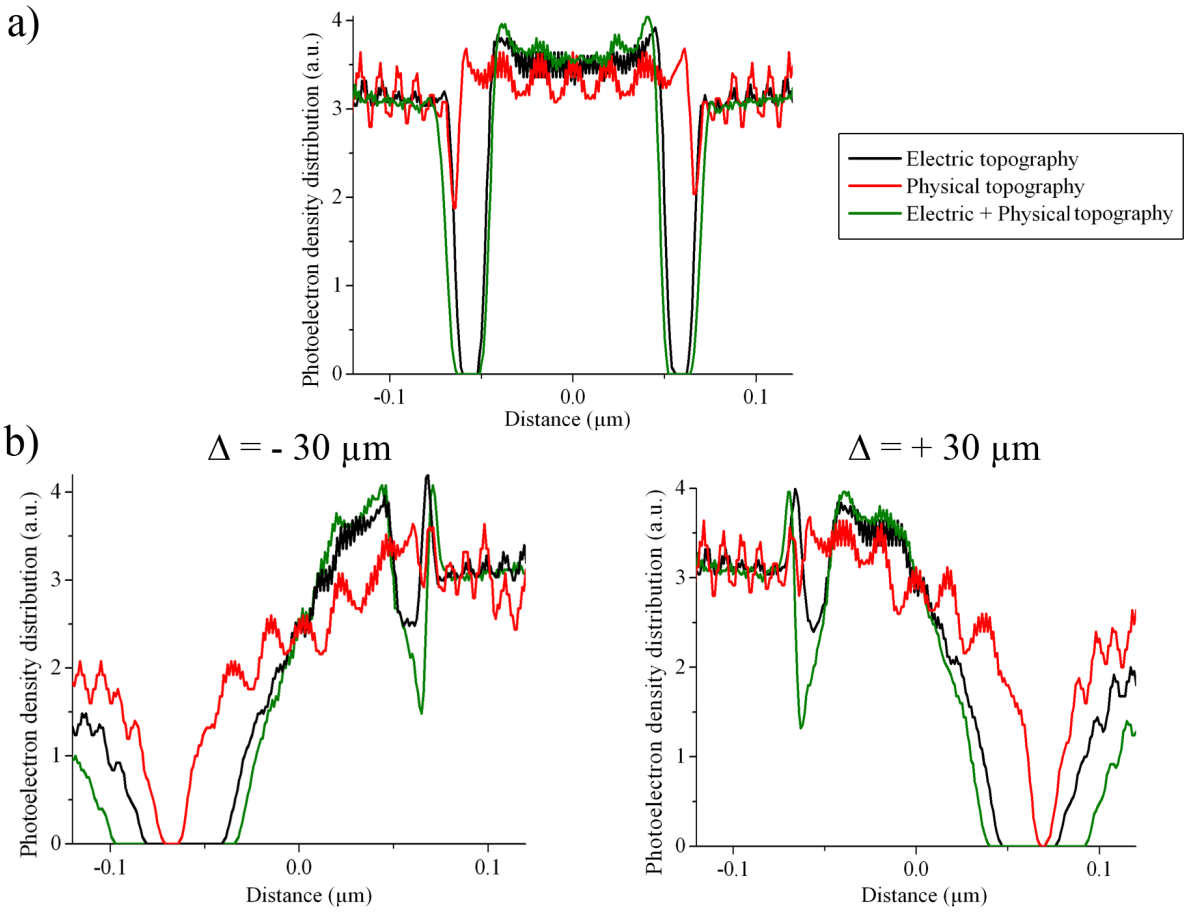

Figure 5.44: *Influence of topography on PEEM imaging, for cases of electric topography alone, lateral one alone, and the both combined with: a) CA centered and b) CA shifted by* $\Delta = \pm$ *30 μm.*

What appears is that the three possibilities of the origin of photoelectron deviation, either electric topography alone, physical one, or both, give a similar results. The difference is only the well width which increases: it is at its maximum for the whole topography influence, electric and physical one. Indeed, the combined effect deviates more the photoelectrons by more than the sum of the deviations calculated separately.

Given the simulation conditions, the physical topography of 70 nm has the lowest influence on the particle trajectories, followed by the electric topography of 1 V due to the junction built-in voltage, the highest effect being due to the two topographies bound together.

Without lateral electric field - Experiments These simulations lead to the conclusion that when realizing dark field imaging on real conditions, it is impossible to determine the origin of the photoelectron current density perturbation more precisely. Thus, observing our silicon doped samples at threshold, we are just able to visualize the presence of these two fields which change the signal from a side of the junction to the other depending on the contrast aperture shift and direction. The edges of our patterns are preferentially darkened, as can be seen on figure 5.45: those from the left, when the contrast aperture is shifted towards negative values (-49 μm), and the right ones, when the shift is positive (+48 μm). The graph in this figure well presents the difference, and above all, the complementarity in dark field imaging between these two contrast aperture positions.

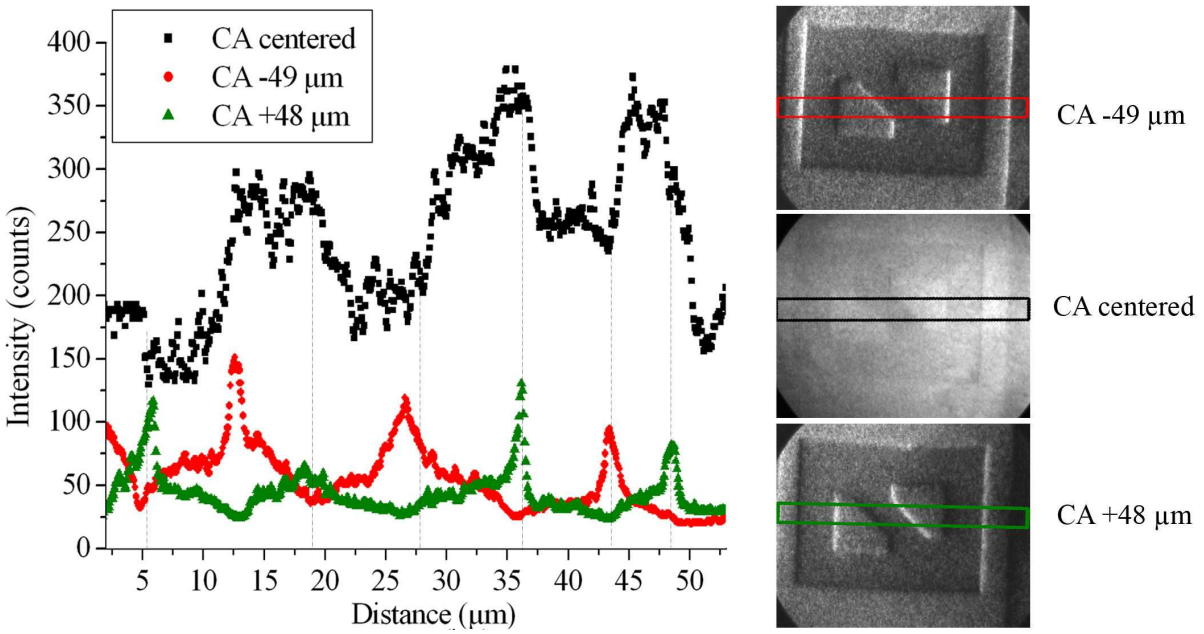

Figure 5.45: *Dark field imaging on P^+/N sample at threshold with a photon source of 128.9 eV. The intensity profile across the lines is represented on the graph.*

We have acquired indeed three images:

- a first image with a contrast aperture well centered on the optical axis,
- two other images with a contrast aperture shifted symmetrically on each side of the optical axis.

From these images, we have extracted the intensity profile across a line cut, for each position of the contrast aperture. The absence of peak corresponds to pattern edges where the presence of lateral electric field is verified. Combining the two profiles helps in determining the complete profile of the pattern, as obtained when the contrast aperture is well centered on the optical axis. This means that the dark field images helps is localizing the position of these electrical fields, without distortion.

To finish this section, we have chosen to show in figure 5.46 a more complete set of dark field images obtained in synchrotron environment on P^+/P sample, for the two photon energies 700.3 eV and 128.9 eV.

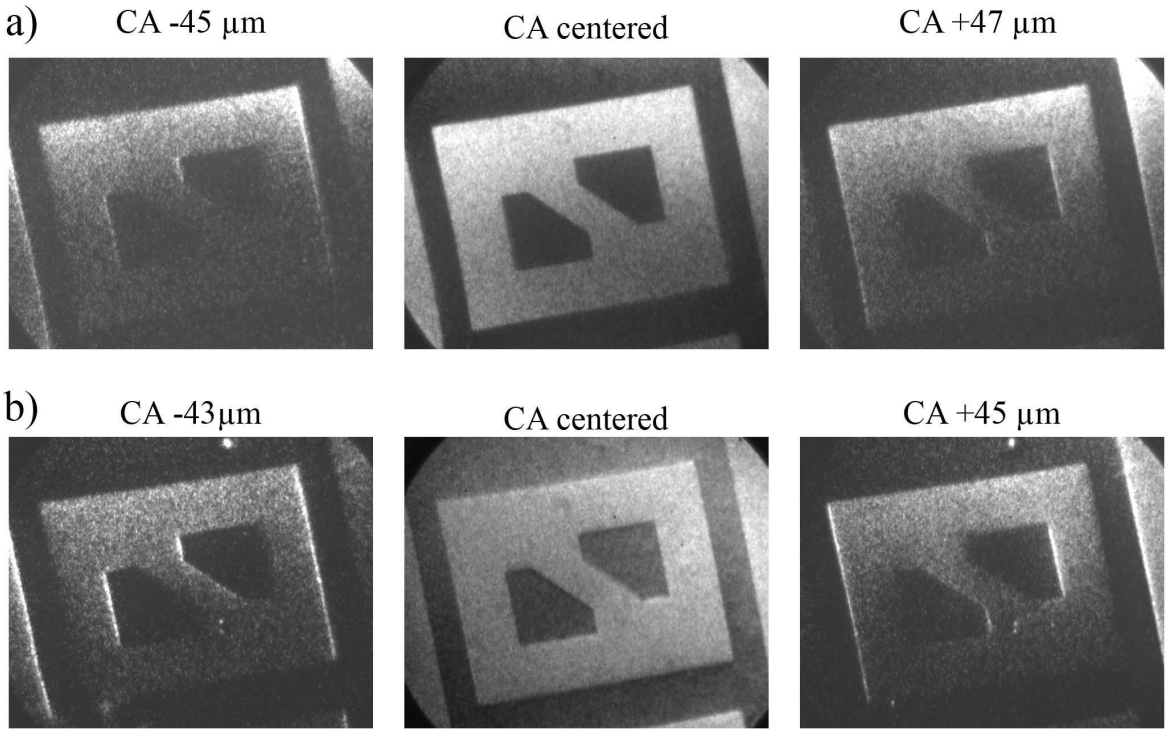

Figure 5.46: *Dark field imaging on passivated P^+/P sample at threshold with a photon source of a) 700.3 eV and b) 128.9 eV.*

- At 128.9 eV, the contrast on the edges is more pronounced than at 700.3 eV. We can deduce that the secondary electrons photoemitted from the first atomic layers of the sample are sensitive to the combination of the fields created by both the sample roughness and the electrical fields across the junction. It may be linked to the contribution electron-hole pairs coming from deeper in the sample, which are more numerous at 128.9 eV than at 700.3 eV.
- With a photon energy of 700.3 eV, electrons come from deeper in the sample. The intensities are lower, but the effect of local fields deflecting the particles trajectories is still present.

5.3.4 Conclusion

SIMION simulations are well adapted to understand the image formation within a PEEM column. Contrast in PEEM imaging is due to the redistribution of the photoelectron density due to a shift of the particle trajectories emitted from the sample surface with very low kinetic energy and influenced by the local electric field across a pn junction.

The two first parts of this section were dedicated to the origin of the contrast formation in a PEEM column with a contrast aperture, and its validation. This has been done on a pn junction model in 1D. When focusing on pn junction imaging, one has to take into account different factors that influence the photoelectron trajectories: the extractor field voltage and the photoelectron kinetic energy. The higher the particles kinetic energy, the

less deviated since they will be less influenced by the local electric field. On the same way, the stronger the extractor electric field, the less deviated the particles since this latter compensates the lateral deviation of the electrical field due to the junction. For these reasons, the true position of the junction is unknown. These conclusions have been obtained by simulations, in good agreement with examples taken from experimental results.

PEEM can be utilized for visualizing the distribution of electric field across the junction thanks to dark field imaging. This technique is based on the principle of shifting the contrast aperture towards two symetrical directions relative to the optical axis of the PEEM column to stop the photoelectrons deflected by the local electrical field, so that the junction image will be modified. Though this dark field imaging helps in highlighting photoelectron deviations due to microlocal fields, it is not possible to clearly distinguish the physical or electric origin of these fields. When considering pn junctions, dark field helps in indirectly localizing the physical junction.

5.4 Conclusion

Energy filtered XPEEM appears to be a powerful tool for contrast imaging at threshold. We have shown that contrast between two doped zones is enhanced when observing passivated samples. Since the contrast is influenced not only by the secondary electron distribution, but also by the difference in threshold between the two doped zones, we can not deduce that one doping is brighter than another when varying the photon energy when acquiring energy-filtered image series. However, we also have studied contrast evolution for two silicon doped zones P^+ and N^+ using as reference the intensity of the P substrate, and integrating the contrast at threshold. We have just determined that the contrast between the P^+ zone and the P substrate was higher than the one between the N^+ zone and the same subtrate, whatever the photon energy considered.

In a second part we have focused on the contrast obtained on N^+/P sample, since, a triple contrast appears on image series acquired at threshold whatever the photon energy considered: the closed doped zone presents a contrast different from the open zone, relative to the substrate. We have performed core-level analysis, and have determined the work-function mapping of this sample. The same observations were done on a sample fabricated by implantation, with close N^+/P doping concentrations than those of the N^+/P sample fabricated by localized epitaxy to check that it was not a problem of fabrication process.
We have also observed this triple contrast with excitation source of different nature, ions by FIB and electrons by SEM. KFM measurement performed have shown that the potential variations observed in the work-function mapping with image series acquired by PEEM were not artifacts: we still observe an inversion in the work functions values, the N^+ zone one being higher than the P one. Moreover, the N^+ work function of the closed zone is always higher of 0.1 eV than the large N^+ zone. ToF SIMS analysis have shown the homogeneity between the open and the closed N^+ doped zones in terms of doping concentration. All these analysis have allowed us to consider the origin of this triple contrast to be due to charging effect in the N^+ zone, since one has to consider this zone

isolated from the substrate by the depletion zone surrounding the pattern.

Last part has shown that the photoelectrons emitted from the sample surface are deviated by the local lateral electric field existing across a pn junction. Thus, when imaging silicon doped pattern, one has to take into account the influence of the device itself on PEEM imaging: we are not able to determine the real position of the junction. Several factors can improve the acquisition conditions, specially an increase of the extractor voltage and imaging photoelectrons at high kinetic energies. Regarding the sample itself, a low difference of work function between the two doped zones induces less influence on the particles trajectories. All these observations have been obtained by SIMION simulations, and confirmed by experimental data observed in the several cases considered.

Studying devices such as pn junction presenting local lateral electric field remains a problem to determine accurately the localization of the junction, since the particles trajectory is strongly influenced by the electric fields in their vicinity. However, we have used this effect to determine qualitatively the presence of local fields on our samples surface thanks to dark field imaging applied to the PEEM technique. An improvement of this study could have been to quantitatively characterize these fields: Nepijko *et al.* have studied the relation between the shift of electrons due to local electric fields and the current density distribution [122, 300]. They interpret in this way the theory of contrast formation to extract qualitative distribution of electric fields from true images acquired with PEEM. The computer simulations are processed considering an analytical model based on an electron emission microscope *without contrast aperture*.
Since the NanoESCA configuration does not allow the application of a bias voltage on the sample surface, we cannot estimate the distribution of the electric fields strength in the way described by Nepijko [300] and Giesen [135]. However, studying the redistribution in intensity from analysis of photoemission image series, we should be able to determine the microscopic distribution of surface potential between two doped zones.

Conclusion and outlooks

This thesis addresses the problem of spatially resolved spectroscopic imaging of model systems semiconductor devices, planar silicon pn junctions, using energy filtered X-ray photoelectron emission microscopy (XPEEM). In the light of increasing demands on device performance at all scales (as specified, for example, in the ITRS - the International Technology Roadmap for Semiconductors) there is an ever increasing need for non-destructive, spatially resolved analysis tools. Energy-filtered PEEM, combining deca-nanometric spatial resolution with full spectroscopic sensitivity may be very complementary to other existing methods (holographic TEM, SEM and near-field techniques). In particular the sensitivity of the photoelectron emission, and thus the contrast in PEEM imaging, to the electronic and chemical states of the surface and near surface region, makes it ideal for the study of devices like patterned silicon pn junctions. The depletion width on either side of the junction varies from a few nm to microns as a function of the doping level which is precisely the spatial resolution covered by PEEM, making it an ideal technique for imaging. However, in this context, understanding role of the built-in lateral electric field across a pn junction in PEEM imaging is a major challenge.

The different contributions to the PEEM contrast observed at a pn junction have been identified and described. Generally, the traditional method and process used for creating doped patterns can condition the surface electronic states. Scanning electron and atomic force microscopy have shown that ion implantation through a mask can lead to ill-defined junctions on the sensitivity level of spatially resolved photoemission and important physical topography. Ion implantation induced damage can also condition the effective doping level obtained. For these reasons localized epitaxial growth, performed in six technological steps in pre-etched pits and channels to form highly P^+ and N^+ doped patterns on either P or N substrates, was preferred and characterized.
The effective doping levels obtained using standard clean room techniques showed depth profiles with significant variations from the nominal doping values. In fact, standard techniques fail to produce homogeneous doping up to the sample surface, in particular for high doping levels. Variations of half a decade for the patterns (N^+ and P^+ doping) and two decades for N doping (P doping concentration could not be reliably determined for sensitivity reasons) were measured. Thus, the doping levels used for the interpretation of the XPEEM results were those determined using SIMS.

The native oxide over the silicon surface is dependent on both doping type and level. Band bending at the oxide/silicon interface masks to a large extent the band line-up at the junction. In order to isolate and identify the role of the built-in electric field at the junction on the PEEM contrast, we have developed a three step passivation protocol

which can yield a surface electronically close to flat band conditions. First, the native oxide is suitably etched, then a chemical oxide is grown, forming a sharper interface with the silicon, finally this chemical oxide is etched leaving a surface with a higher degree of passivation. However, even this optimized process, following characterization on full wafers by X-ray photoelectron spectroscopy (XPS), is sample and laboratory dependent. In the Si $2p$ core-level spectra, a pronounced shoulder at lower binding energy was found on all samples. This was tentatively assigned to the so-called S_1 and S_2 states of silicon atoms reported in the literature of mainly (but not exclusively) reconstructed Si(100) surfaces studied by high-resolution photoelectron spectroscopy. A third surface state, S_3, at high binding energies is also observed. The true origins of such a component, however, are still matter of debate and various interpretations are suggested, including dimer surface states and dangling bonds. We clearly observe variations in the passivation as a function of the doping type and level, and there is evidence that from one chemistry laboratory to another the passivation efficiency varies.

Under photon irradiation, the creation of electron-hole pairs leads to a surface photovoltage (SPV) which always acts to reduce the band bending. The SPV depends on the photon intensity and the effective mass and type of charge carriers. The magnitude of the SPV therefore changes under laboratory X-ray irradiation and synchrotron radiation and, consequently, must be taken into account when interpreting photoemission results.

We have therefore studied the silicon patterns with PEEM using three different photon energies (1486.7 eV, 700.3 eV and 128.9 eV) providing three different probing depths: 8.8 nm, 4.8 nm and 2.3 nm, respectively. It is preferable in PEEM imaging to have structures in both dimensions on the sample surface in order to optimize alignment. Thus although the customized samples presented arrays of doped patterns we have used mainly the numerical labels, done with the same mask since they provide pn junctions with a variety of orientations within the PEEM field of view.

XPEEM imaging of the work function and Si $2p$ core levels, as well as Si $2p$ and valence band micro-spectroscopy have been carried out with both laboratory photon sources and synchrotron radiation. The lower photon intensity in laboratory conditions allows a precise determination of the electronic levels as a function of doping, although the energy resolution is lower than that obtained using more intense synchrotron radiation. Spectromicroscopy with secondary electrons enabled us to generate work function maps of the doped silicon patterns by a pixel-to-pixel fitting of the photoemission threshold. We confirm the overall electronic structure expected from the measured doping levels, the deviations from the theoretically expected results are discussed mainly in the light of possible residual band bending. A systematic sample-dependent work function contrast behaviour is observed in the close doped zones : for both P^+/P and P^+/N samples, both close and opened zones had the same work function ; however, in the particular case of the N^+/P sample, the work function of the close zone is higher than in the opened zone, yielding a 'triple contrast' in the image.
We show that the contrast observed in core level laboratory XPEEM can be principally attributed to the energy levels of the silicon surface atoms. From a quantitative point of view, we observed sample-dependent differences of the measured work function with

respect to the expected value determined from the doping level measured by SIMS at a depth of 3 nm and for flat band conditions. With laboratory excitation, the differences are minimal for N doping, but are in the 0.8-1 eV range for both P and P^+ doping. Therefore, for the patterned zones with high N and P doping, flat band conditions are not reached. Defective silicon surface states evidenced from the fitting of the Si $2p$ core level micro-spectra, are present in proportions depending on both the sample and the pattern/substrate zone (between 13% and nearly 50% the Si^0 intensity). However, it remains difficult to make a systematic quantitative correlation to relate the magnitude of the band bending and the overall quantity of defect states.

Any pn junction has a built-in electric field due to the band line-up across the junction. The built-in fields in our junctions have been evaluated using numerical computations. These values can then be used as input to numerical simulations of the PEEM contrast to be expected from a simple pn junction array. The simulations have been done using the SIMION package. A basic PEEM column is simulated with, notably, the inclusion of a contrast aperture in the focal plane. The effective electron emission angle is determined by the vector sum of the orthogonal extractor and the built-in lateral fields. In order to identify the specific contribution of the lateral field, the contrast induced by the energy position of the electron emission on either side of the junction is not taken into account. A semi-quantitative comparison of this electrical topography with the experimental results obtained in threshold PEEM is presented. The model confirms the observed experimental tendencies. The lateral field shifts the apparent position of the junction in PEEM. This shift depends on the photoelectron kinetic energy. Dark field imaging of the junction has also been simulated. Comparison with the experimental results shows that it can be used to localize the real junction position by measuring the deviation of the emergent electron beams.

Micron-sized heavily doped n-type closed domains surrounded by a p-type substrate (N^+/P sample) show an unusual triple contrast, confirmed by SEM and SSRM measurements. We show experimentally that it is not due to doping variations during epitaxy but may be explained by analogy with a diode, created by the thin oxide wall observed in the etched trenches used for patterning. Thus the finite n-type region charges under the photon beam illumination. Short-circuiting the closed and open regions removes the effect.

Three potential axes of research emerge from this work.

- Firstly, the hitherto used doping and passivation procedures do not necessarily produce sample surfaces compatible with surface analysis techniques such as photoelectron spectroscopy. Given the demand for device performance optimization, it appears necessary to dedicate considerable efforts in understanding the finer ultra-surface mechanisms of passivation, particularly for higher doping levels.

- Secondly, the modeling of PEEM contrast over pn junctions is only in its infancy and also corresponds to actual trends as seen from the recent literature. High resolution experimental PEEM analysis, using established protocols, such as those in the patented method developed during this thesis, require a theoretical understanding in order to enable reliable data interpretation. The next step is to include

contrast due to the initial state electronic energy levels in the simulated contrasts.

- Thirdly, the behaviour of highly n-doped micron scale patterns as diodes potentially paves the way to applications, and is worth pursuing both from a fundamental and technological point of view.

Finally, an interesting way of pursuing this work is to extend the experimental method to pn junctions fabricated in individual semidonducting nanostructures such as nanowires, as these latter are becoming widely studied due to their potential applications in devices.

The difficulty in obtaining fully consistent results using both laboratory sources and synchrotron radiation underlines the extent to which XPEEM is a surface science technique. The combination of laboratory based PEEM and synchrotron radiation extends considerably the depth sensitivity, spatial and spectroscopic resolutions available. Sample standards suitable for bulk sensitive analysis may not be sufficiently stringent to permit reproducible PEEM measurements. On the other hand, it is precisely this extreme surface sensitivity which may allow some analytical breakthroughs in the further optimization of silicon-based and other semiconductor technologies. PEEM is not, as yet, suitable for in-line characterization, however, it appears necessary for indispensable high quality off-line studies using various techniques in a complementary way.

Chapter 6

Résumé

Contents

6.1 Introduction

Cette thèse porte sur l'analyse de motifs de silicium dopé, sous forme de jonctions pn planaires, à l'aide d'un microscope à émission de photoélectrons filtré en énergie (XPEEM). Elle se concentre sur deux aspects principaux :

- Caractérisation électrique et chimique de ces motifs en fonction de l'état de surface.
- Influence des échantillons sur les conditions d'imagerie PEEM.

Une nouvelle génération de microscopes à émission de photoélectrons filtrés en énergie a été utilisée pour la caractérisation de ces dispositifs, à la fois en laboratoire et en environnement synchrotron. La complémentarité en terme de gamme d'énergie accessible, grâce à une brillante source X de laboratoire d'une part, et au rayonnement synchrotron d'autre part, nous a permis d'améliorer notre compréhension des jonctions pn. Utilisant une imagerie électronique de surface plein-champ, cet instrument mesure directement, en fonction des types de dopage et de la concentration de part de d'autre de la jonction, mais également en fonction de l'état de surface des échantillons étudiés, les variations spatiales du travail de sortie, des niveaux électroniques de cœur et des états de valence.

Tout d'abord, nous avons conçu, produit et caractérisé une série de jonctions pn planaires, afin de sonder les niveaux électroniques de part et d'autre de la jonction, au niveau de la zone de déplétion. Cependant, la présence d'un oxyde natif à la surface des échantillons empêchant une analyse en conditions de bandes plates, nous avons au préalable optimisé un protocole de passivation afin de remédier à ce problème.

La seconde partie de notre étude est dédiée aux conditions d'imagerie elles-mêmes, car observer des structures telles que les jonctions pn nécessite de prendre en compte leur influence sur l'imagerie 2D des dopants en XPEEM. Nous nous intéressons ainsi plus particulièrement au champ électrique latéral présent au niveau des jonctions pn qui dévie les trajectoires des photoélectrons émis de la surface, altérant les mesures de résolution latérale en imagerie PEEM. Afin de mieux comprendre son influence ainsi que celle d'autres facteurs, nous illustrons les simulations par des résultats expérimentaux.

6.2 Positionnement de la technique XPEEM dans la caractérisation 2D de dopants

Alors que l'industrie de la microélectronique s'applique à concevoir des dispositifs de plus en plus performants, un besoin de caractérisation électrique et chimique à différentes échelles se développe : on souhaite pouvoir observer des structures sur plusieurs microns (systèmes HFET pour les applications de puissance, micro-systèmes) mais également descendre à quelques nanomètres (transistors CMOS pour le noeud 22 nm). Il est ainsi nécessaire de développer des techniques de caractérisation complémentaires pour satisfaire ces différents besoins : elles doivent être capables non seulement d'imager les distributions des dopants, mais également de pouvoir fournir une analyse quantitative de ces derniers à partir du contraste obtenu. Il est ainsi important d'avoir une bonne compréhension

des mécanismes de contraste lorsqu'on cherche à déterminer une mesure quantitative du contraste obtenu sur des semi-conducteurs dopés.
La jonction pn est une bonne structure de base pour valider les interprétations du contraste en imagerie et nous nous sommes focalisés sur cette dernière pour notre étude.

Différentes techniques d'analyse sont dédiées à la cartographie 2D des dopants et regroupent des méthodes très variées qui peuvent être classées en fonction du type de sonde utilisée [16] :

- Les techniques de faisceaux d'ions, telles que la spectrométrie de masse SIMS et l'imagerie ToF-SIMS.
- Les techniques de champ proche, parmi elles les microscopies KFM, SCM et SSRM.
- Les techniques de microscopie électronique telles que le microscope électronique à balayage (MEB) et l'holographie électronique.
- Les techniques de microscopie ionique type sonde atomique.
- Les techniques basées sur la microscopie de photoémission, comme le SPEM et le PEEM.

Nous avons mis en avant les complémentarités entre ces différentes techniques en termes de préparation d'échantillon, résolution latérale, capacités de quantification des dopants, gamme de sensibilité aux concentrations de dopants et sensibilité en profondeur de l'analyse.

Parmi les techniques de microscopie électronique, la méthode basée sur l'utilisation d'une colonne de microscope à émission de photoélectrons (PEEM) est particulièrement intéressante grâce à sa grande sensibilité de surface et grâce aux mécanismes de contraste spécifiques qu'elle est capable d'étudier, tel le contraste de travail de sortie. Nous avons constaté au cours d'une étude bibliographique que les expériences menées sur l'interprétation du contraste en imagerie PEEM sur des échantillons de silicium depuis une dizaine d'années étaient limitées à cause d'une absence de filtrage en énergie sur les instruments, et de l'utilisation de sources souvent réduites à l'ultraviolet basse énergie. De plus, nous avons vu que le contrôle de l'état de surface des échantillons est également important, et qu'il est préférable d'éviter un oxyde natif en surface ou une contamination carbonnée. Nous avons conclu qu'une étude en imagerie spectroscopique, c'est-à-dire filtrée en énergie, était nécessaire pour mieux comprendre les mécanismes de contraste sur des motifs de silicium dopés.

La particularité de notre étude est ainsi l'utilisation de technique XPEEM filtrée en énergie, qui correspond à de la spectroscopie de photoélectrons (XPS) résolue spatialement. Combiné à l'utilisation de sources X à haute énergie de photons, plus particulièrement une source X à haute énergie de photon, et le rayonnement synchrotron, notre instrument est en mesure d'imager le contraste correspondant aux vrais électrons secondaires, en évitant l'influence de transitions indirectes. Son système de filtrage en énergie permet d'acquérir des informations spectroscopiques de la surface de l'échantillon pour toutes les

gammes d'énergie de photoélectrons (niveau de cœur et bande de valence). Nous pouvons donc étudier le contraste obtenu sur des jonctions pn en fonction de la position en énergie relative des niveaux électroniques étudiés.

6.3 XPEEM filtré en énergie : le NanoESCA

6.3.1 Principe

Cet instrument de dernière génération est composé tout d'abord d'une colonne électronique (le PEEM), constituée de lentilles électrostatiques et d'une ouverture de contraste placée dans le plan focal image de la lentille objectif. L'échantillon est à un potentiel proche de zéro, la lentille d'extraction est portée à une haute tension, jusqu'à 15 kV. Le détecteur, permettant d'obtenir une image de la surface après grandissement de l'objet dans la colonne PEEM, est composé de trois éléments : une galette de microcanaux (MCP) pour amplifier le signal électronique, un écran fluorescent pour convertir les électrons en photons, et une caméra CCD qui image l'écran.
Le NanoESCA utilise comme filtre en énergie un analyseur de type hémisphérique. Ce dernier se comporte comme un filtre passe-bande qui permet d'effectuer une analyse PEEM spectroscopique. La figure 6.1 montre les trois modes d'opération du NanoESCA : imagerie directe non filtrée (1), spectroscopie localisée (2) et imagerie filtrée en énergie (3).

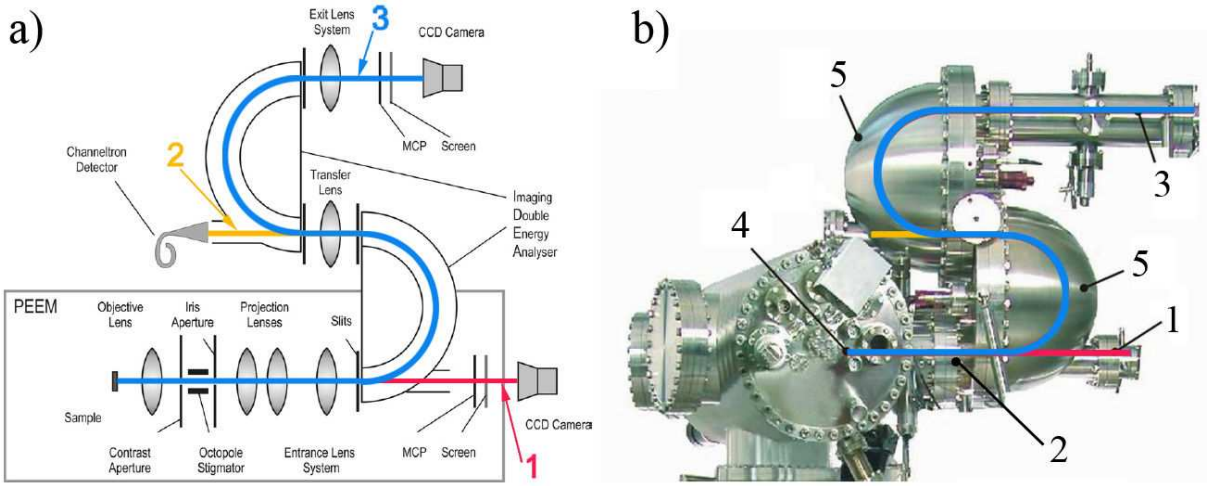

Figure 6.1: *a) Représentation schématique des différents modes d'opération du NanoESCA [209]. b) Photographie de l'instrument : 1 et 3 : MCP, 2 : colonne PEEM, 4 : source X, et 5 : IDEA [201].*

Les électrons dans la colonne PEEM sont à basse énergie cinétique, environ 1 keV, ce qui confère à l'instrument une transmission importante, même pour les faibles énergies de passage. Mais la réelle particularité du NanoESCA est son filtrage en énergie qui est, non pas basé sur un seul analyseur hémisphérique, mais sur un double analyseur dont les deux hémisphères sont couplés par une lentille de transfert (IDEA). La symétrie du filtrage en énergie élimine les aberrations chromatiques et sphériques du système, ce qui d'une part permet l'emploi de fentes d'entrée et de sortie réduites améliorant la transmis-

sion, et d'autre part, réduit les aberrations de l'instrument à celles de la lentille extracteur.

Les sources de rayonnement disponibles sur un tel système sont variées : elles peuvent aller de l'ultraviolet (UV) (grâce à des sources mercure ou deutérium), à l'UV plus lointain (avec des sources He I and He II), en passant par les rayons X (AlKα optimisée en laboratoire ou faisceau de lumière synchrotron).

Ce spectromicroscope permet ainsi d'imager :

- la région du seuil de photoémission afin d'accéder aux variations spatiales du travail de sortie,
- la distribution latérale des espèces et états chimiques en présence grâce aux niveaux de cœur,
- la cartographie des variations spatiales dans la densité d'états, grâce à la région de la bande de valence et du niveau de Fermi.

Un changement de la polarisation de l'échantillon dans la colonne PEEM permet de faire varier l'énergie cinétique ($E-E_F$) et d'enregistrer une séquence d'images en fonction de l'énergie des électrons secondaires. Cette série d'images se présente sous la forme de données en 3D : I(x,y,$E-E_F$), comme schématiquement représenté sur la figure 6.2 a). Il est possible d'extraire des informations au seuil, niveau de cœur ou bande de valence pixel par pixel si l'intensité du signal dans l'image est suffisante.

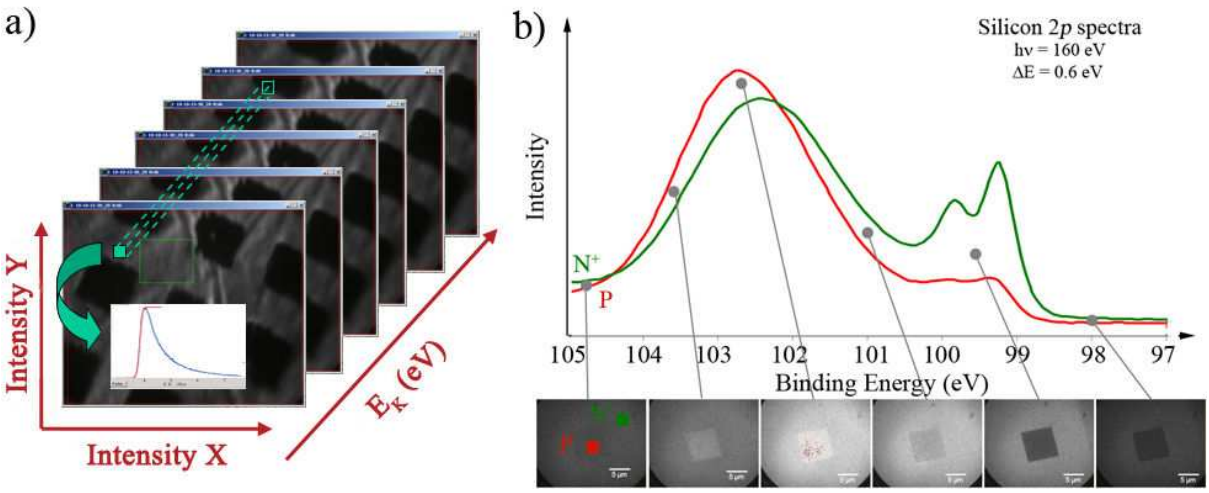

Figure 6.2: *a) Représentation 3D de la série d'images acquise : I(x,y,E). b) Contraste en imagerie de cœur sur la transition Si 2p de zones fortement dopées N sur un substrat dopé P. L'épaisseur d'oxyde est fonction du dopage.*

La force de cette technique est ainsi d'observer les variations des espèces chimiques en présence à la surface de notre échantillon. La figure 6.2 b) montre ainsi une série d'images acquises au niveau de cœur 2p du silicium de surfaces dopées N^+ sur un substrat dopé P. Ces images ont été acquises au synchrotron avec une énergie de photons de 160 eV. Des microspectres ont été extraits de la série d'images sur les deux types de dopage.
On note ainsi une variation de la forme du spectre Si 2p en fonction du type de dopage :

bien que présentant une composante oxyde similaire située vers les hautes énergies de liaisons, le pic Si^0 est très différent selon le dopage P (rouge) ou le dopage N^+ (vert). De plus, le contraste visible en imagerie sur les zones dopées se traduit par une variation au niveau de l'intensité du pic Si^0 : le spectromicroscope permet de déterminer les variations d'épaisseur d'oxyde au niveau des zones dopées. Le signal Si^0 étant plus atténué sur la zone P que sur la zone N^+, l'oxyde y est plus épais.

6.3.2 Optimisation des conditions d'imagerie et mesure de résolution latérale

Un premier travail de cette thèse a consisté à optimiser les conditions d'imagerie, plus particulièrement au niveau de la correction d'astigmatisme de la colonne PEEM. Il a donné lieu au dépôt d'un brevet et a également permis d'obtenir des mesures de résolution latérale au niveau de cœur avec une source X de laboratoire à l'état de l'art. Un protocole de prétraitement des images pour enlever les bruits dus aux défauts du capteur (pixels chauds, offset, non uniformité du CCD) a été mis en place afin d'améliorer la qualité de l'information obtenue.

Grâce au prétraitement des images, nous avons ainsi pu augmenter le rapport signal sur bruit de séries d'images acquises sur une structure de Si/SiGe épitaxié, observée en coupe au niveau $2p_{3/2}$ du germanium. Après correction du bruit de fond de Shirley, nous avons obtenu une image XPS du niveau de cœur $Ge2p_{3/2}$, présenté en figure 6.3 (source X monochromatique à 1486.7 eV). Nous avons ainsi atteint une résolution latérale à l'état de l'art mondial : (477 ± 110) nm avec une résolution en énergie de 0.56 eV [221, 235].

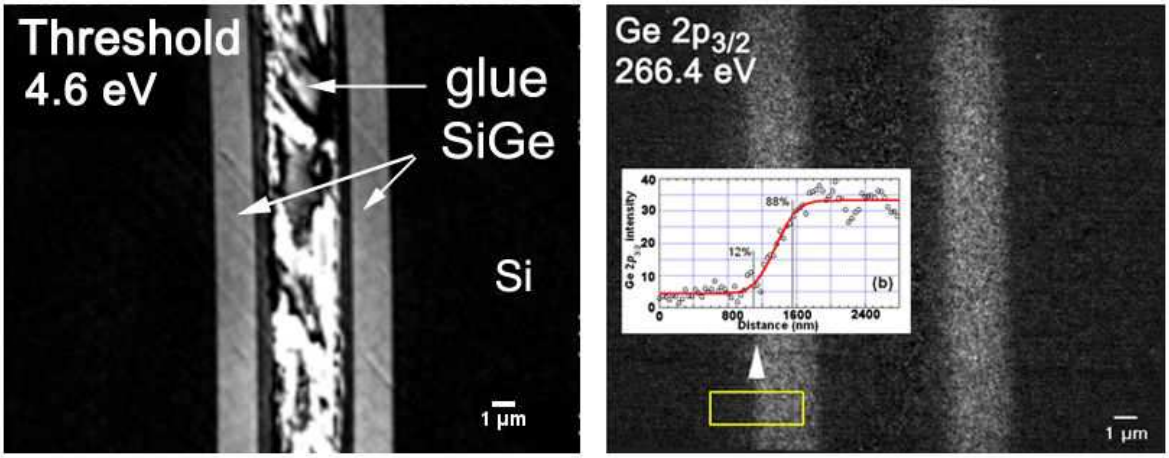

Figure 6.3: *Couches épitaxiées de Si/SiGe observées en coupe a) au seuil et b) à l'énergie de cœur 266.4 eV, corrigée du bruit de fond de photoémission. Encart : profil d'intensité extrait de la région encadrée dans l'image et fit obtenu à partir d'une fonction erreur complémentaire [221].*

6.4 Etude de motifs de silicium dopés

6.4.1 Fabrication des échantillons

Afin de caractériser au mieux les jonctions pn par spectromicroscopie, nous avons fait réaliser spécialement un lot d'échantillons dans les salles blanches du LETI. Les critères de choix technologiques ont été pensés afin de répondre au mieux aux besoins de cette thèse. Nous avons ainsi privilégié un dopage par épitaxie localisée ne nécessitant pas de hautes températures afin d'éviter le maximum de diffusion des dopants au niveau de la jonction.
Quatre combinaisons de dopants, représentées schématiquement sur la figure 6.4, ont été réalisées. Seulement trois seront étudiées par la suite et nommées: P^+/P, N^+/P et P^+/N.

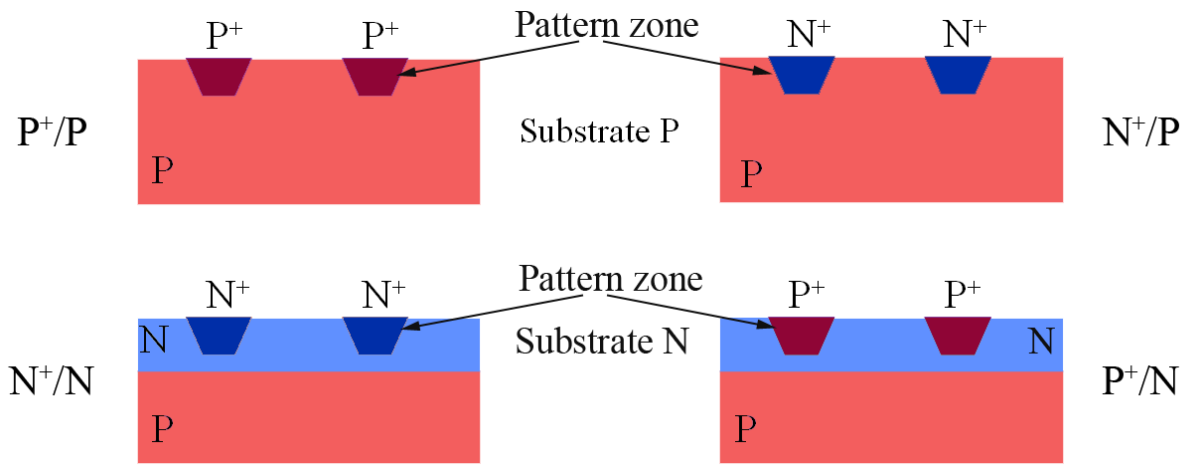

Figure 6.4: *Présentation des différents échantillons créés dans ce lot de plaques : P^+/P, N^+/P, N^+/N, P^+/N.*

La mesure de concentration des dopants a été extraite de profils SIMS à 3 nm sous la surface, ce qui correspond à une intensité dans le spectre XPS émise par 65% du signal d'intérêt pris à un angle de collection de 90°. Nous avons par la suite utilisé ces valeurs pour déterminer quantitativement la courbure de bande résiduelle des données spectroscopiques acquises.
Une topographie résiduelle de la surface des échantillons a été mesurée par AFM : une marche au niveau de la jonction de hauteur comprise entre 20 nm et 75 nm a été trouvée en fonction de l'échantillon considéré.

La particularité de ces échantillons réside dans les champs électriques latéraux :

- Deux échantillons P^+/P et N^+/P présentent des zones de déplétion de largeur importante (environ 500 nm) et un champ électrique latéral maximal au niveau de cette jonction comparables, respectivement environ 3.26 $kV.mm^{-1}$ et 3.29 $kV.mm^{-1}$.

- Un échantillon, P^+/N qui présente une zone de déplétion beaucoup plus étroite (50 nm) ce qui entraîne une valeur maximale du champ électrique latéral au niveau de cette jonction dix fois plus importante (41.7 $kV.mm^{-1}$).

Nous présentons par la suite les résultats obtenus avec deux jeux de trois échantillons, les premiers en laboratoire et les seconds au synchrotron. Ces études combinent des résultats obtenus avec une source X à 1486.7 eV d'énergie de photons, et avec un rayonnement synchrotron à deux énergies : 128.9 eV et 700.3 eV (après calibration sur un échantillon d'argent). Les profondeurs sondées à ces différentes énergies sont résumées dans le tableau 6.1.

Energie de photons (eV)	Profondeur sondée (nm)
128.9	2.3
700.3	4.8
1486.7	8.8

Table 6.1: *Profondeurs sondées en fonction de l'énergie de photons utilisée.*

6.4.2 Préparation des surfaces : passivation des échantillons

Afin de déterminer l'alignement des bandes au niveau de la jonction pn, il faut auparavant s'affranchir d'une courbure de bande existante à l'interface surface de l'échantillon/oxyde natif dû à la présence d'états de surface, comme représenté sur la figure 6.5 afin de se rapprocher de conditions de bandes plates.

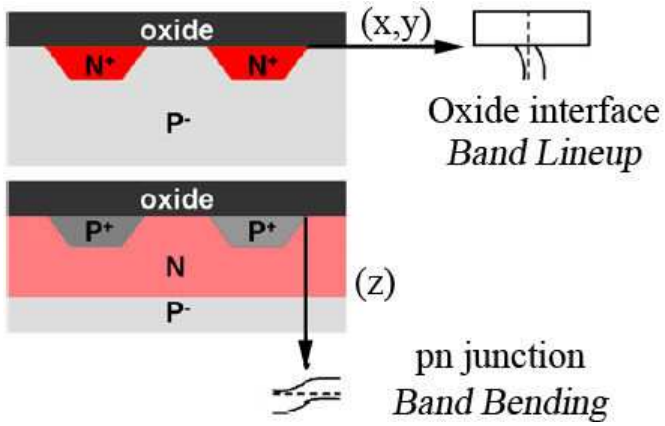

Figure 6.5: *Courbure de bande en 3D représentée schématiquement dans deux plans, respectivement (x,y) et (z) [222].*

Une passivation des échantillons par acide fluoridrique (HF) est ainsi nécessaire [244, 247, 250]. Nous avons choisi un mélange de gravure BOE composé de HF à 49% et de fluorure d'ammonium NH_4F à 40% dans les proportions 1:7. Le protocole de traitement choisi est celui proposé par Higashi *et al.* [251, 257]. Il a été optimisé au cours de cette thèse et comporte trois étapes :

- Dégraissage de l'échantillon par thrichloréthylène,
- Gravure/oxidation chimique de la surface par cycles de HF et de solution piranha (H_2SO_4 à 96% et H_2O_2 à 30% dans les proportions 2/3-1/3) chauffée à 135°C,

- Gravure finale avec solution BOE.

Nous avons caractérisé de façon approfondie la qualité de la passivation réalisée sur nos échantillons. Pour ce faire, nous avons étudié des échantillons de silicium dopé pleine plaque avec un instrument permettant de réaliser des mesures spectroscopiques résolues en angle. Ces échantillons ont été fabriqués par épitaxie localisée, avec des concentrations de dopants proches des valeurs obtenues sur les échantillons présentant des motifs, comme vu en section 3.2.1.1.

Avant passivation, nous avons mesuré un oxyde natif à la surface de ces échantillons pleine plaque, dont l'épaisseur était comprise entre 1.15 nm et 1.8 nm (en prenant une incertitude sur la mesure correspondant à celle du libre parcours moyen des photoélectrons dans le silicium de 20 %).
Après passivation, des spectres Si $2p$ acquis à différentes zones de la surface ont montré une homogénéité globale du procédé. De plus, même pour des conditions d'acquisition sensibles à la surface (pour un angle de collection de 15°, correspondant à une profondeur sondée de 2.3 nm), aucun pic d'oxyde n'est visible.
Des microspectres locaux au niveau de coeur Si $2p$ ont également été acquis pour un angle de collection de 90°, correspondant à une profondeur sondée de 8.8 nm. Nous nous sommes focalisés par la suite sur leur déconvolution.

Des analyses FTIR ont confirmé la présence de liaisons Si-H à la surface du silicium, ce qui nous a permis d'intégrer une composante dans notre déconvolution du spectre Si $2p$ située à une énergie de liaison 0.44 eV au-dessus de la composante Si^0.

La déconvolution du spectre Si $2p$ présentée en partie gauche de la figure 6.6 a également permis de mettre en évidence une composante caractéristique de l'état de surface après passivation, située à une énergie de liaison 0.7 eV inférieure à celle du Si^0 et dont de nombreuses observations ont été confirmées par une étude bibliographique 3.7. Ces études ont pour la plupart été réalisées sur des échantillons de silicium passivé avec un rayonnement synchrotron.

Nous pouvons séparer deux contributions dans les énergies de liaisons inférieures à celles du pic Si^0, à savoir S_1 (-0.5 eV;-0.7 eV), S_2 (-0.2 eV) et une contribution S_3 (+0.2 eV) au-dessus du pic Si^0. Nous retiendrons que la litterature donne à ces pics des origines variées, mais toujours impliquant des changements subtils des premières couches de la surface de silicium. Nous pouvons citer : des défauts dans la matrice, un réarrangement de la structure du silicium en dimères (symétriques ou assymétriques), des liaisons pendantes, des atomes silicium intersticiels, mais également des effets dus aux deuxièmes et troisièmes couches sous la surface.

Dans notre étude en laboratoire, nous supposons que la composante Si^* observée à Si^0-0.7 eV correspond à S_1. Nous ne sommes pas en mesure de résoudre les composantes S_2 et S_3 à cause du manque de résolution en énergie de l'expérience. Nous avons constaté que plus la proportion de Si-H dans le spectre était importante, plus on observait des échantillons dans les conditions proches des bandes plates. En revanche, si la proportion de Si^* était importante, on s'en éloignait. Nous n'avons cependant pas été en

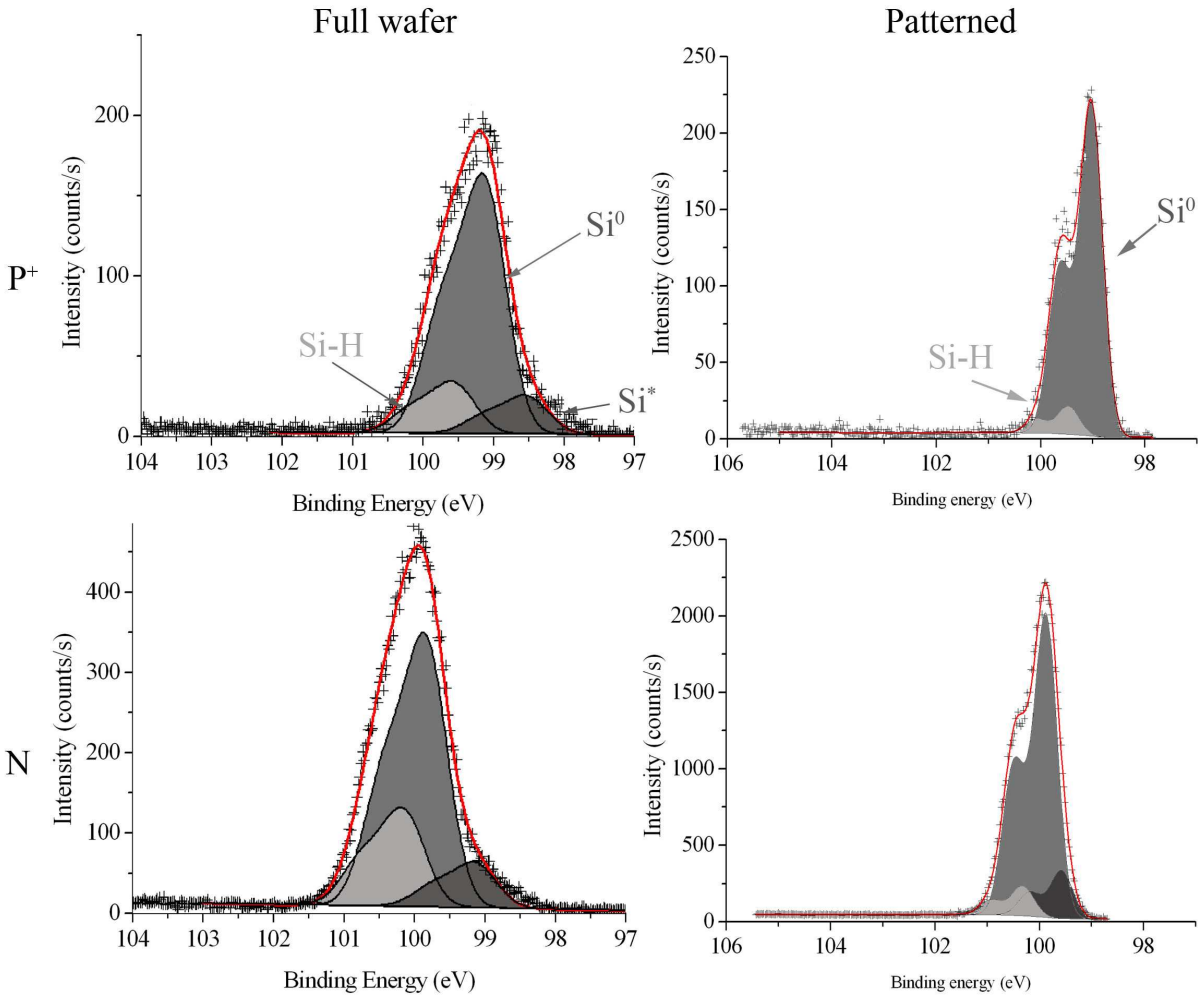

Figure 6.6: *Micro-spectres niveau de cœur Si 2p sur les zones P^+ et N^+ acquis sur les échantillons pleine plaque et les échantillons présentant des motifs. Les spectres obtenus sur les zones P et N ne sont pas présentés car très similaires à ceux des zones fortement dopées.*

mesure de corréler quantitativement la courbure de bande résiduelle avec la variation de la porportion de Si-H par rapport à Si*.

Nous avons poursuivi notre étude sur la qualité du procédé de passivation en réalisant cette fois l'étude sur les échantillons de silicium à motifs avec le NanoESCA. Ces derniers présentaient avant passivation une épaisseur d'oxyde légèrement inférieure à celle des échantillons pleine plaque, à savoir dans des valeurs comprises entre 0.66 nm et 0.86 nm. Les spectres Si $2p$ présentés en partie droite de la figure 6.6 sont très similaires à ceux obtenus sur les pleines plaques, c'est-à-dire qu'aucune composante d'oxyde n'est visible. Cependant, en nous penchant sur la déconvolution de ces spectres, nous constatons d'importantes variations de l'intensité relative des composantes Si-H et S_1 dans le spectre Si $2p$, ce qui suggère une variabilité dans la qualité de la surface après passivation.

De plus, nous avons obtenu des microspectres niveau de cœur Si $2p$ en utilisant le rayonnement synchrotron à deux énergies. A 128.9 eV, qui correspond à une analyse

extrêmement sensible à la surface (nous considérons pour une énergie de photon de 130 eV un libre parcours moyen des photoélectrons de 0.3 nm) un oxyde résiduel est observé. A 700.3 eV, cet oxyde est quasiment indétectable, ce qui signifique la faible épaisseur de ce dernier, inférieur à une mono-couche. Ainsi, ce procédé, même maîtrisé, est trop complexe pour être facilement reproductible. Pour les analyses en laboratoire (hν=1486.7 eV) aucune composante d'oxyde n'apparaît alors qu'elle est visible sur les spectres obtenus en synchrotron: la passivation réalisée dans le laboratoire de chimie du synchrotron SOLEIL a été moins efficace que celle en laboratoire.

Le procédé de passivation ne permet pas d'atteindre les conditions idéales de bandes plates :

- D'un point de vue chimique, ce procédé permet de s'affranchir de l'oxyde natif à la surface de l'échantillon.
- D'un point de vue électronique, il paraît difficile de supprimer tous les états de surface résiduels. Ces derniers sont responsables d'un ancrage du niveau de Fermi donnant lieu à une courbure de bande résiduelle à la surface du semi-conducteur.

6.4.3 Analyse spectromicroscopique des échantillons

Nous avons réalisé une étude spectromicroscopique complète de motifs de silicium passivés, en étudiant toutes les gammes d'énergie accessibles avec le NanoESCA, à savoir électrons secondaires, photoélectrons de cœur et de la bande de valence. Nous avons réalisé cette étude en laboratoire avec une source X à 1486.7 eV et en utilisant le rayonnement synchrotron aux énergies 128.9 eV et 700.3 eV.
Dans les différentes expériences, les conditions d'acquisition sont restées relativement similaires. La plus grande différence est au niveau des temps d'acquisition des séries d'images. Ces paramètres sont présentés dans le tableau 6.2.

Paramètres	En laboratoire	Au synchrotron	
	1486.7 eV	700.3 eV	128.9 eV
Tension d'extracteur	12 kV	12 kV	12 kV
Ouverture de contraste	70 μm	70 μm	70 μm
Diamètre champ de vue	62 μm	62 μm	62 μm
Energie de passage	50 eV	50 eV	50 eV
Seuil			
Largeur fente d'entrée	1 mm	0.5 mm	0.5 mm
Temps acquisition et tension MCP	120 s (900 V)	1 s (900 V)	5 s (900 V)
Résolution énergétique	0.33 eV	0.1 eV	0.1 eV
Niveau de cœur			
Largeur fente d'entrée	1 mm	1 mm	1 mm
Temps acquisition et tension MCP	600 s (950 V)	120 s (930 V)	60 s (930 V)
Résolution énergétique	0.33 eV	0.244 eV	0.202 eV

Table 6.2: *Conditions générales d'acquisition du NanoESCA en laboratoire et au synchrotron.*

6.4.3.1 Analyse spectroscopique complète

Au seuil La cartographie du travail de sortie, obtenue à partir des séries d'images corrigées de la dispersion en énergie dans le champ de vue a été réalisée en laboratoire et au synchrotron. Elle a été obtenue en extrayant pixel par pixel le profil d'intensité au seuil, et en déterminant de ce dernier une mesure locale du travail de sortie, comme présenté en figure 6.7 a). De cette cartographie, nous traçons l'histogramme des valeurs, visible en figure 6.7 b), pour en déduire les valeurs moyennes du travail de sortie des différentes zones d'intérêt, dont l'incertitude est donnée par la largeur à mi-hauteur (FWHM) des différents pics.

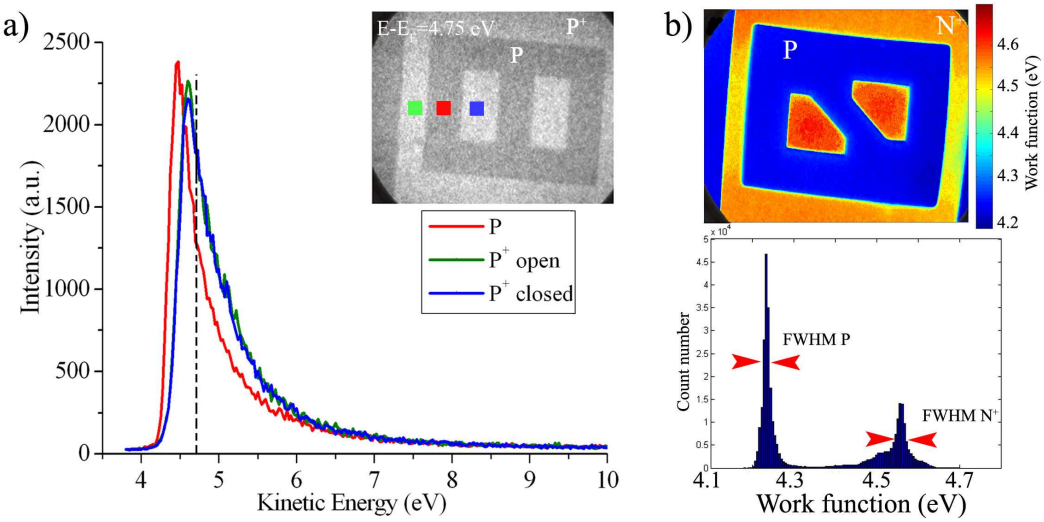

Figure 6.7: *a) Image XPEEM de l'échantillon P^+/P au seuil et microspectres extraits de différentes zones d'intérêt. b) Cartographie du travail de sortie pour l'échantillon N^+/P et histogramme déduit des valeurs de travail de sortie dans le champ de vue. (Champ de vue :62 µm)*

D'un point de vue qualitatif, nous avons tout d'abord observé que les valeurs de travail obtenues étaient dans une gamme réaliste et étroite de valeurs. De plus la cartographie du travail de sortie reflétait bien le motif original des structures observées, ce qui nous a permis de valider l'uniformité du dopage au niveau microscopique.
Nous avons constaté que quelle que soit l'énergie de photon utilisée, le contraste de travail de sortie obtenu au niveau de la zone fermée (entourée par le substrat) dépendait du dopage considéré : pour les échantillons P^+/P et P^+/N, les zones fortement dopées (respectivement P^+ et N^+) présentent le même travail de sortie. En revanche, dans le cas de l'échantillon N^+/P, le travail de sortie de la zone ouverte est plus grand que celui de la zone fermée. Ce phénomène, déjà visible sur les images individuelles prises dans les basses énergies au seuil est appelé 'triple contraste' et sera étudié de façon plus approfondie dans la partie 6.5.3.

D'un point de vue quantitatif, la cartographie du travail de sortie nous a permis d'observer des mesures de travail de sortie reflétant une courbure de bande à l'interface semi-conducteur/vide due à des états de surface résiduels après passivation des échantillons.

Nous avons observé en laboratoire une bonne corrélation avec ce que nous attendions, à savoir un travail de sortie qui diminue lorsque l'énergie de photons augmente, et pour le dopage P un travail de sortie qui augmente lorsque l'énergie de photons augmente. Les écarts de mesure pour les dopages N sont faibles mais peuvent varier dans une gamme de 0.8-1 eV pour les dopages P et P^+. Ainsi, nous n'avons pas observé les échantillons dans les conditions de bandes plates.
En utilisant le rayonnement synchrotron, nous avons également trouvé des différences entre les valeurs de travail de sortie mesurées et celles attendues à partir des mesures de dopage SIMS prises à 3 nm en conditions de bandes plates confirmant une courbure de bandes résiduelle après passivation. De plus, nous avons noté une différence plus importante pour un flux de photons faible (à 128.9 eV) que pour un flux important (à 700.3 eV) : nous avons attribué cet effet au photopotentiel de surface (SPV) qui tend à aplatir la courbure de bande résiduelle, d'autant plus que le flux de photons à la surface de l'échantillon est important.

Analyse niveau de cœur et bande de valence Nous avons par la suite réalisé une étude complète au niveau de cœur Si $2p$ par microspectroscopie en laboratoire et spectromicroscopie au synchrotron.

Les spectres acquis en laboratoire sont semblables à ceux présentés en partie droite de la figure 6.6. Ils présentent les composantes Si-H et S_1 dans des proportions très variables mais sans trace de sous oxyde.
Les spectres acquis au synchrotron ont montré des variations en terme d'état de la surface après passivation : les spectres acquis à 128.9 eV présentent même différentes composantes d'oxyde et de sous-oxydes. De plus, nous avons observé une désoxydation non uniforme en fonction du dopage considéré dans le champ de vue. Les densités d'états de surface sont ainsi très variables et nous n'observons pas les échantillons dans des conditions de bandes plates.

Nous avons réalisé des déconvolutions de ces spectres, telles que présentées en figure 6.8 pour lesquelles nous faisons apparaître les trois composantes S_1, S_2 et S_3 (cf tableau 3.7). Nous avons constaté que les spectres à 128.9 eV étaient moins bien résolus qu'à 700.3 eV : nous relions cette différence à la profondeur d'analyse sondée à ces deux énergies, et à la proportion relative des composantes de surface Si-H, S_1, S_2 et S_3 qui sont en plus grand nombre à 128.9 eV qu'à 700.3 eV. De la même façon, nous avons constaté que les spectres Si $2p$ acquis sur le substrat étaient plus résolus que ceux acquis sur les zones fortement dopées, à cause de la présence de ces mêmes composantes dans des proportions variées.

- Pour les dopages N, l'énergie de liaison augmente avec l'augmentation de l'énergie de photons.

- Pour les dopages P, l'énergie de liaison diminue avec l'augmentation de l'énergie de photons.

L'extrapolation des seuils de bandes permet de déterminer le maximum de la bande de valence (VBM) en fonction du dopage. Nous avons pu le corréler avec les résultats obtenus sur les niveaux de cœur Si $2p$. Nous avons observé le comportement suivant :

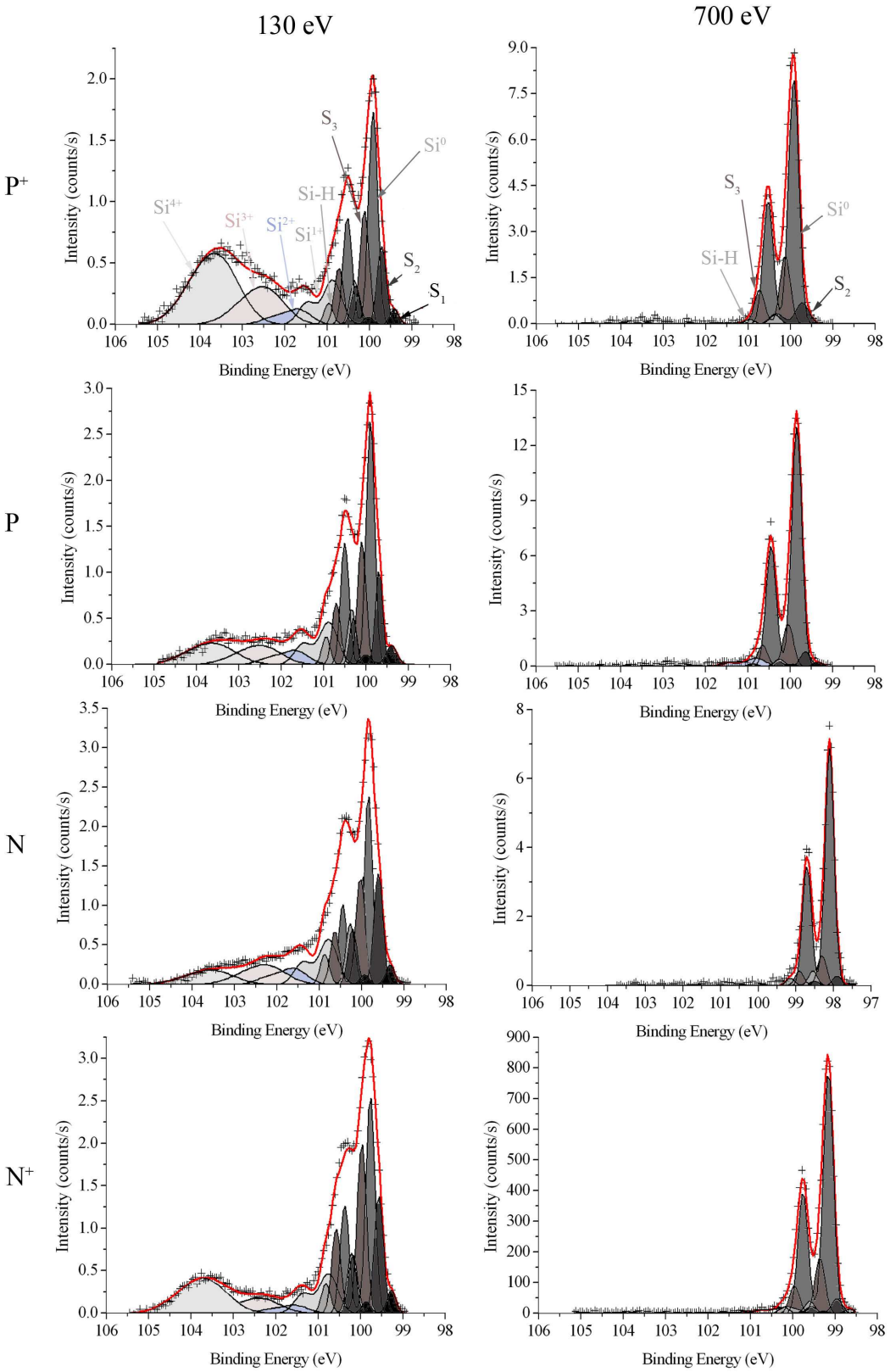

Figure 6.8: *Déconvolution des spectres Si 2p obtenus à deux énergies de photons.*

- Pour les dopages N, le VBM augmente avec l'augmentation de l'énergie de photons.
- Pour les dopages P, le VBM diminue avec l'augmentation de l'énergie de photons.

Cependant, nous n'avons pas pu relier quantitativement les écart de courbure de bande mesurés et les proportions relatives mesurées des éléments S_1, S_2 et S_3.

6.4.4 Contraste en XPEEM en imagerie niveau de cœur sur pic Si 2*p*

Nous avons réalisé des séries d'images niveau de cœur sur chaque échantillon en laboratoire et en environnement synchrotron. Nous nous sommes focalisés sur le pic Si 2*p* entre 98 eV et 101.5 eV, sans prendre en compte les composantes aux plus hautes énergies correspondant à de l'oxyde résiduel à la surface des échantillons. Nous avons intégré l'intensité du niveau de cœur sur la totalité du pic et corrigé l'image résultante du bruit de fond de Shirley à l'aide du logiciel Multipak. Les images sont présentées en figure 6.9. Nous notons le triple contraste visible sur les images intégrées pour l'échantillon N^+/P, qui sera étudié plus en détail en partie 6.5.3.

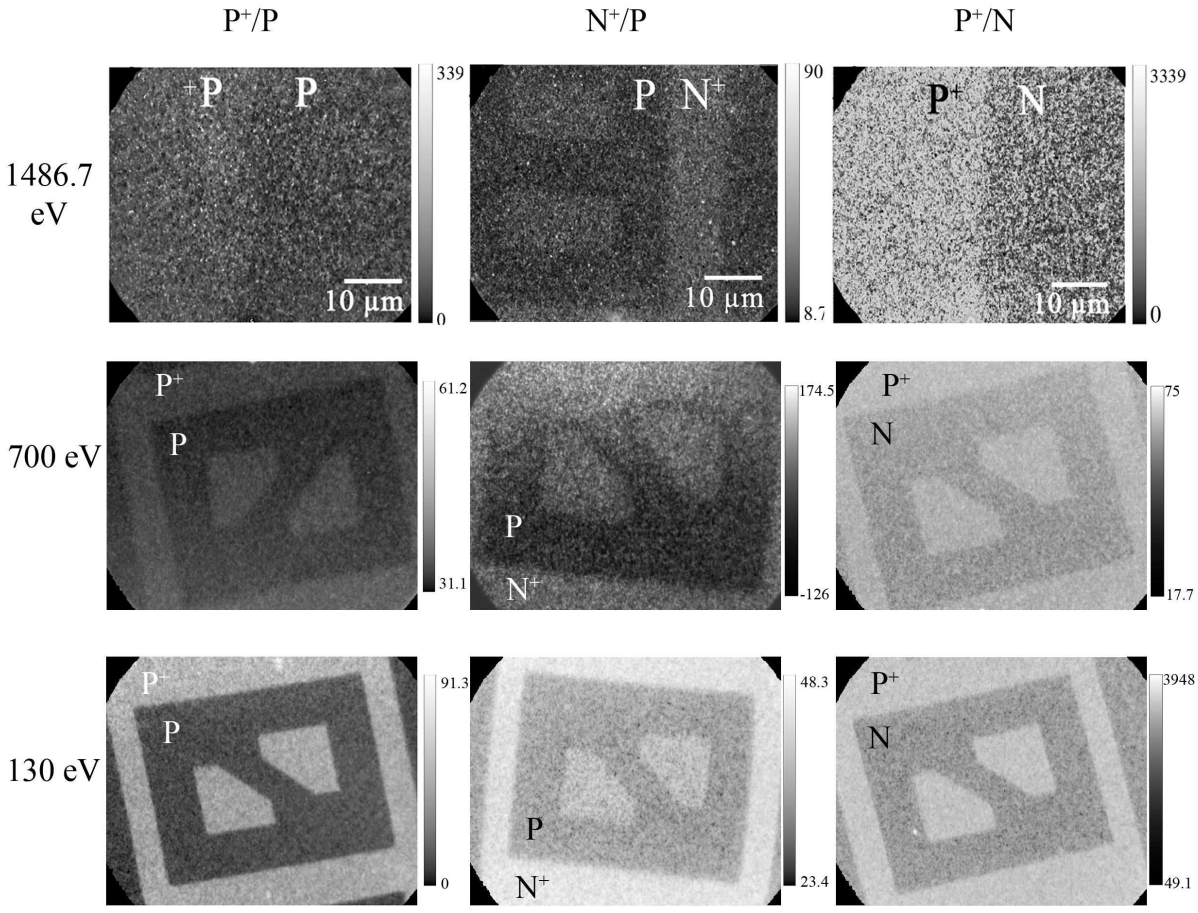

Figure 6.9: *Imagerie niveau de cœur intégrée sur le pic Si 2p (gamme d'énergie considérée : 98 eV à 101.5 eV) sur les échantillons P^+/P, N^+/P et P^+/N pour les trois énergies de photon considérées.*

Concernant les champs de vue choisis, nous avons conservé les motifs 'zéro' pour les études au synchrotron grâce au bon rapport signal sur bruit obtenu de part le flux important du faisceau synchrotron. Au laboratoire, le flux de la source X étant plus faible, nous avons choisi pour les deux échantillons (P^+/P et P^+/N) pour lesquelles le signal sur bruit était minimal, à savoir un champ de vue dans lequel les deux zones dopées étaient équitablement réparties dans les proportions 50-50. L'échantillon N^+/P présentant quant à lui un rapport signal sur bruit suffisamment important, nous sommes restés sur le champ de vue présentant le motif 'huit'.

Nous remarquons que la zone la plus brillante, quelle que soit l'énergie de photons et quel que soit le type de dopage considéré, correspond toujours à la zone la plus dopée, le substrat étant toujours plus sombre. Nous avions vérifié à 1486.7 eV qu'il n'y avait pas d'oxyde résiduel présent à la surface de l'échantillon et que sur les analyses synchrotron, l'oxyde résiduel était inférieur à une monocouche : le contraste ne peut pas être interprété en terme de différences d'atténuation du signal du susbtrat atténué par l'oxyde en surface. Nous observons bien un contraste même si la surface est désoxydée, alors que la densité de silicium pour les différents dopages est la même.

En observant la forme des spectres Si $2p$ acquis en laboratoire et au synchrotron, nous avons constaté que la largeur du pic Si^0, et donc son intensité intégrale variait en fonction de la zone considérée. La figure 6.10 illustre bien cette remarque en présentant les spectres obtenus en laboratoire sur les deux types de dopage de l'échantillon P^+/N.

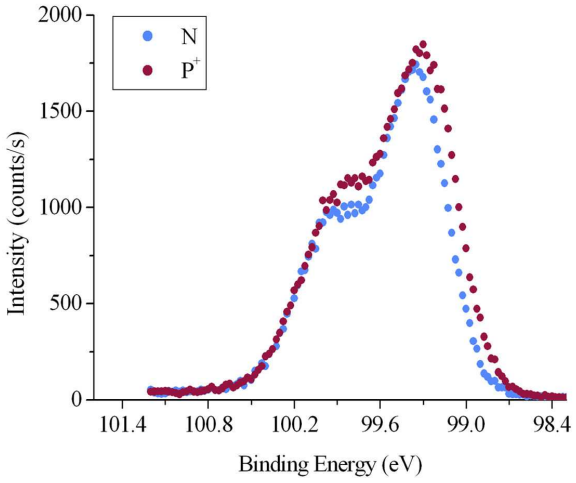

Figure 6.10: *Spectres Si 2p (gamme d'énergie considérée : 98 eV à 101.5 eV) obtenus sur les deux types de dopage de l'échantillon P^+/N ($h\nu$=1486.8 eV).*

Grâce à une déconvolution détaillée du pic Si $2p$ à 128.9 eV et 700.3 eV pour déterminer les composantes spectrales et leurs proportions dans l'intensité globale du spectre, nous avons mis en évidence que :

- En laboratoire, la composante S_1 est responsable de l'élargissement du pic Si $2p$ et du contraste observé : plus la proportion de S_1 est élevée dans une zone et plus cette dernière paraît brillante sur l'image intégrée.

- Au synchrotron, c'est la proportion de la composante S_3 qui détermine réellement la zone la plus brillante.

D'après Jolly *et al.*, l'une des origines possibles de S_2 et S_3 pourrait être liée à l'influence d'atomes d'oxygène second voisins résiduels avec les atomes de silicium de la surface. Nous supposons donc que le contraste au niveau de cœur dépend de l'état de la surface après passivation. Nous avons vu que cet état varie d'un nettoyage chimique à l'autre, entraînant la prédominance de l'une des deux composantes S_1 ou S_3 au signal Si^0 qui influence alors le contraste en imagerie niveau de cœur intégrée.

6.5 Imagerie XPEEM filtrée en énergie de jonctions pn

6.5.1 Contraste en XPEEM au seuil de photoémission

La cartographie 2D de dopants obtenue en électrons secondaires à l'aide d'un microscope électronique reste une technique très utilisée de nos jours, mais le contraste obtenu peut avoir des origines variées qui limitent la résolution spatiale des images. Nous distinguons ainsi :

- Contraste matériel et de travail de sortie [126],
- Contraste d'absorption,
- Contraste magnétique [95],
- Contraste topographique et effet d'ombrage [129, 130],
- Contraste électrique [134, 135].

Nous dressons maintenant plus particulièrement un état de l'art des interprétations avancées pour expliquer le contraste obtenu en microscopie électronique sur les jonctions de silicium pn. Les variations du rendement des électrons secondaires peuvent être causées par différents facteurs :

- Des effets de courbure de bande dus à des changements d'affinité électronique relative à la barrière de potentiel V_{bi} existant dans la zone de déplétion au travers de la jonction [106, 107]
- Un changement de la hauteur de la barrière Schottky à la surface de l'échantillon dû à la présence d'états de surface dans le gap créés par une contamination carbonée [112, 115, 116] ou un oxyde natif [94, 103, 108, 119].
- Un changement dans la profondeur d'échappement dû à un taux d'atténuation des électrons photoexcités, diffusés et réabsorbés qui créent des paires électron-trou avec des rendements dépendant du dopage [75, 79, 113].
- Des effets causés par des champs électriques présents à la surface des jonctions pn qui perturbent les trajectoires de certains électrons photoémis [83, 84, 122].

6.5.2 Contraste au seuil de photoémission

Nous considérons dans cette étude des séries d'images acquises au seuil, corrigées de la dispersion en énergie et du bruit. Nous avons étudié l'évolution du paramètre contraste C défini à partir de l'intensité du substrat I_{sub} et celle de la zone dopée I_{dep}, par :

$$C = \frac{I_{dep} - I_{sub}}{I_{dep} + I_{sub}} \, . \tag{6.1}$$

Influence de la passivation sur le contraste au seuil de photoémission Nous avons comparé en laboratoire le rendement de photoémission de la zone dopée et du substrat pour les trois types d'échantillons, en gardant des conditions d'acquisition constantes. Nous ne présentons en figure 6.11 que le résultat obtenu pour l'échantillon P/P^+ mais des remarques similaires ont été faites sur les autres échantillons dans le manuscrit :

- Le contraste extrait de ces séries d'images est plus important après passivation. Il apparaît légèrement décalé vers les hautes énergies cinétiques. Une inversion de contraste est même visible sur les images filtrées en bas de la figure 6.11, prises arbitrairement à 4.375 eV et 5.225 eV.

- Le contraste diminue avec l'énergie cinétique des électrons secondaires.

Influence de l'énergie de photons sur le contraste au seuil de photoémission Nous avons observé deux tendances en fonction de l'énergie de photons utilisée :

- Lorsque la source de photons est faible, de l'ordre de 128.9 eV, le contraste est élevé et diminue avec l'augmentation de l'énergie de photons. C'est le cas de l'échantillon N^+/P.

- A faible énergie de photons, le contraste est faible, puis augmente avec l'augmentation de celle-ci. C'est le cas des échantillons P^+/P and P^+/N.

Etude du rendement de photoémission Nous terminé cette étude en comparant le rendement de photoémission des dopages N^+ et P^+ en prenant le substrat P pour référence. En nous basant sur le travail réalisé par Hovorka, nous utilisons ici une définition de contraste modifiée [138] :

$$C = \frac{(I_{dep} - I_{sub})}{I_{sub}} \, . \tag{6.2}$$

Le contraste étant influencé non seulement par la distribution des électrons secondaires, mais également par la différence entre les seuils de photoémission des deux zones dopées, nous n'avons pas pu déterminer de cette étude quelle zone avait le rendement le meilleur [138].

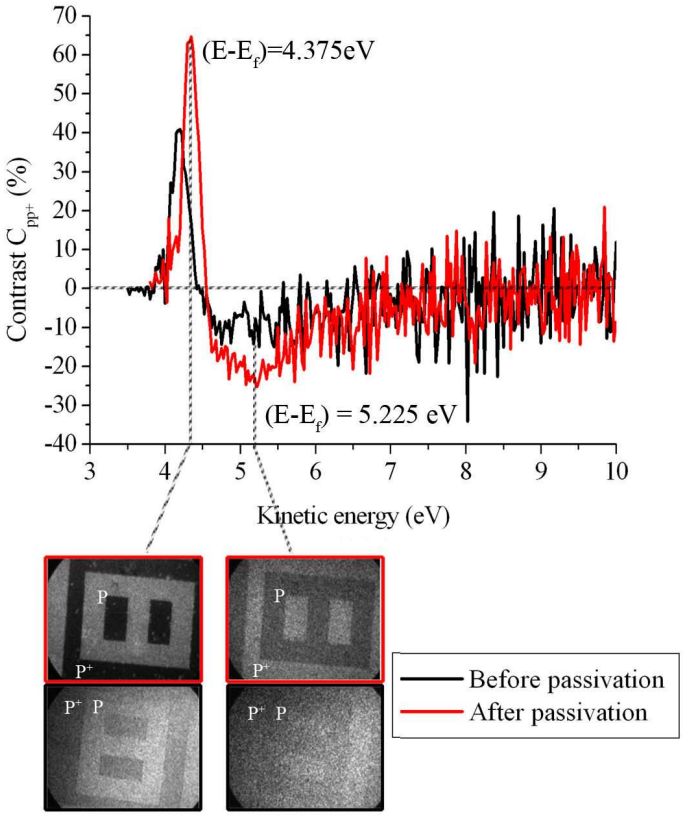

Figure 6.11: *Evolution du contraste C_{P/P^+} en fonction de l'énergie cinétique des électrons secondaires avant et après passivation. Les images présentées ont été extraites des séries à deux énergies cinétiques : (E-E_f)=4.375 eV and 5.225 eV.*

6.5.3 Triple contraste en imagerie PEEM

Les résultats de la section précédente mettent en valeur les possibilités du NanoESCA en terme d'évaluation du contraste sur des images au seuil en fonction du type et de la concentration des dopants dans des motifs de silicium dopés. Cependant, nos études nous ont permis de nous pencher sur un cas atypique de triple contraste. Celui-ci n'apparaît que dans le cas de l'échantillon N^+/P.

Imagerie PEEM au seuil Nous avons observé une différence de contraste au seuil entre la zone dopée large et celle plus petite entourée par le substrat. Ce triple contraste visible en XPEEM avec une source de photons X à différentes énergies a également été observé avec des faisceaux d'excitation de différentes natures, à savoir électronique par MEB et ionique par FIB (ions Ga^+ à 30 KeV et 28 pA), comme présenté respectivement en figure 6.12 b) et c).

Cette observation a déjà été faite par Hovorka dans la litérature, pour deux études [137,138]. Il suggère que ce phénomène peut être dû à des états de surface qui augmentent le rendement de photoémission.

Nous avons extrait des séries d'images au seuil, pour les trois énergie de photons, les spectres de photoémission pour trois zones : le substrat, la zone dopée N^+ ouverte et la zone dopée N^+ fermée. Nous avons ainsi constaté des variations dans le seuil de

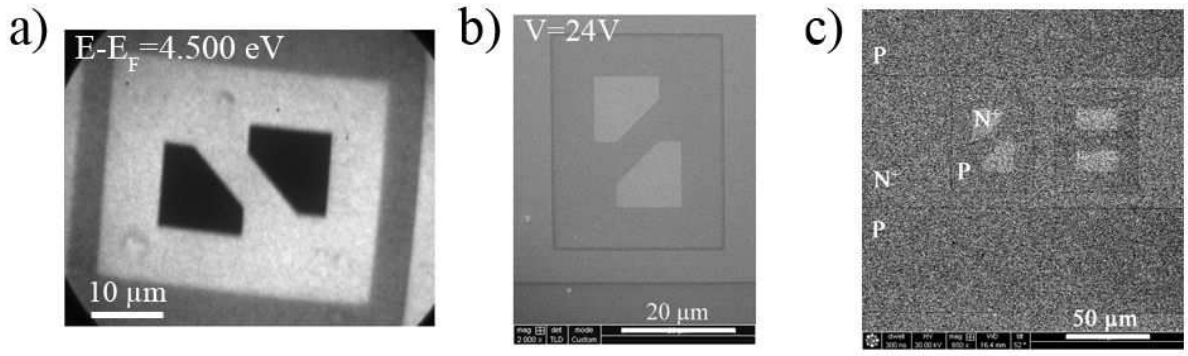

Figure 6.12: *Image de l'échantillon N$^+$/P en : a) XPEEM, b) SEM, c) FIB.*

photoémission :

- Pour la zone ouverte dopée N$^+$, un décalage progressif du seuil de photoémission apparaît à 700.3 eV.
- Pour la zone fermée N$^+$, ce décalage progressif du seuil est déjà présent à 128.9 eV, mais apparaît plus marqué à 700.3 eV.
- Ce décalage seuil n'est pas un artéfact car il n'est pas visible sur le spectre extrait du substrat P, quelle que soit l'énergie de photons.

Imagerie PEEM niveau de cœur La figure 6.13 représente les microspectres localisés extraits d'une série d'images au niveau de cœur Si $2p$. Le spectre de la zone dopée N$^+$ ouverte présente les caractéristiques combinées de celles de la zone fermée et du substrat. Comme pour la zone N$^+$ ouverte, il a un oxyde natif à sa surface, mais la position du Si^0 correspond à l'énergie de celle du substrat. Cette remarque a été vérifiée aux deux énergies 128.9 eV et 700.3 eV par des déconvolutions précises.

Préparation de l'échantillon Nous avons dans un premier temps vérifié par ToF-SIMS que le dopage était uniforme dans les deux zones N$^+$ ouvertes et fermées. Nous avons également vérifié que ce phénomène n'était pas dû au procédé de fabrication par épitaxie de l'échantillon. Nous avons ainsi comparé deux échantillons non passivés : l'un réalisé par épitaxie et l'autre faisant partie d'une étude précédente [222] réalisée par implantation avec la même gamme de dopage : $1\times10^{20}/1\times10^{16}$ at.cm^{-3} contre $1.8\times10^{19}/4\times10^{15}$ at.cm^{-3} par épitaxie. Les cartographies du travail de sortie obtenues à partir de séries d'images au seuil acquises a) au synchrotron à 265 eV pour l'échantillon implanté et b) en laboratoire pour l'échantillon épitaxié sont présentées en figure 6.14.

Nous constatons que le travail de sortie de la zone N$^+$ fermée est supérieur à celui de la zone ouverte qui reste proche de celui du substrat P. Dans les deux cas, les valeurs restent très supérieures à celles attendues pour un dopage N$^+$. La présence d'un bourrelet brillant à l'extérieur du motif présentant un travail de sortie inférieur est toujours visible.

Analyses complémentaires KFM et SCM Nous avons étudié l'échantillon N$^+$/P épitaxié et présentant un oxyde natif par SSRM. Les mesures ont confirmé un potentiel

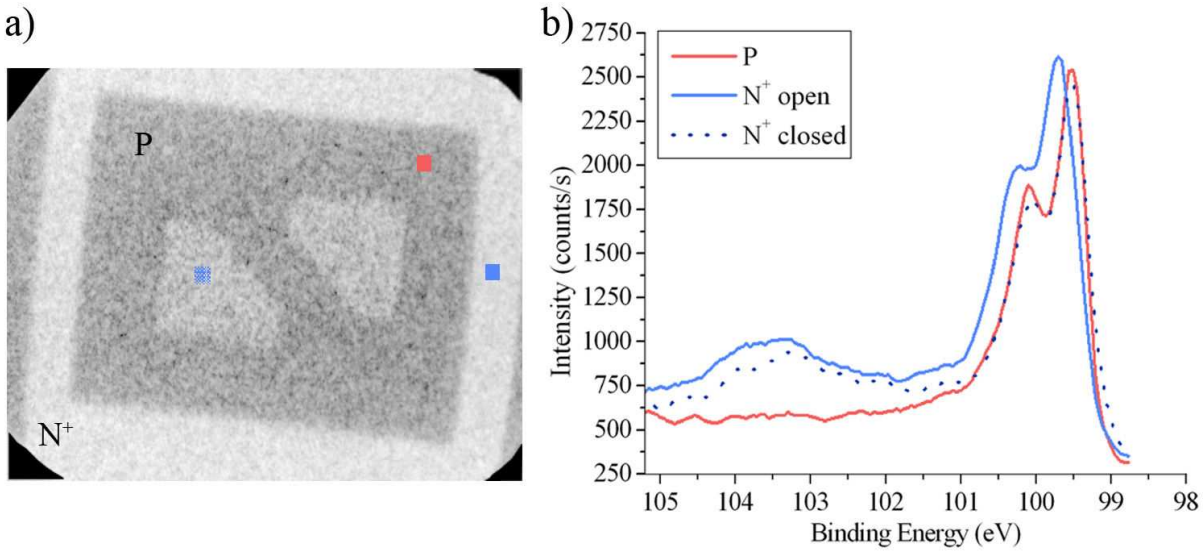

Figure 6.13: *a) Imagerie Si 2p de l'échantillon N^+/P à 103.5 eV après soustraction du bruit de Shirley. b) Spectres Si 2p extraits de la série en énergie pour les trois zones d'intérêt. (Energie de photons : 128.9 eV)*

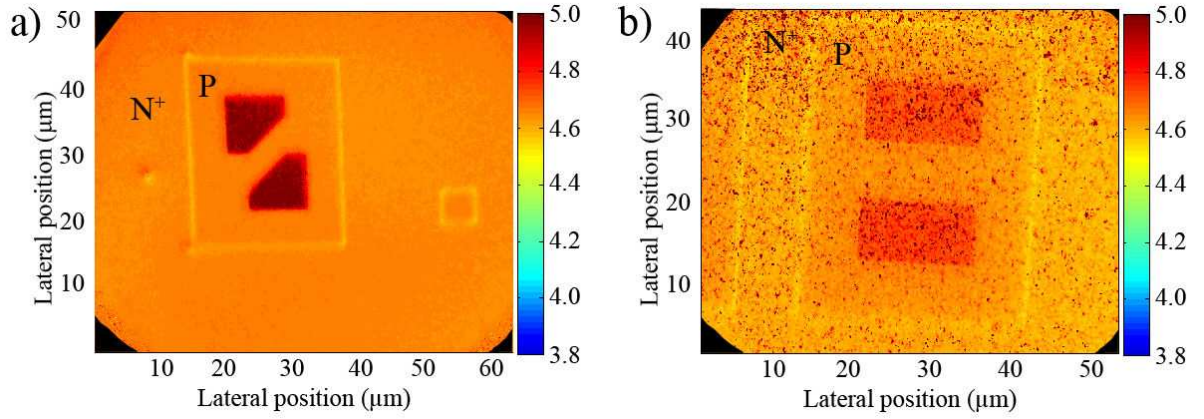

Figure 6.14: *Cartographie du travail de sortie sur l'échantillon N^+/P réalisé par : a) implantation (energy de photons : 265 eV) et b) épitaxie (énergie de photons : 1486.7 eV).*

de surface très différent entre la zone dopée ouverte et la zone fermée, d'environ 140 mV. De plus, nous observons une inversion de type sur le profil issu de l'image 6.15 a).

Nous avons mesuré des valeurs locales de travail de sortie par deux techniques, XPEEM et KFM, comparables, ce qui nous a permis de rejeter un problème de mesure avec le NanoESCA.

Une analyse SCM a quant à elle permis de mettre en évidence une variation du signal SCM dans la zone externe du motif P lorsque le potentiel V_{dc} varie entre -1 V et +1 V.

Discussion Pour expliquer ce phénomène, nous avons choisi de privilégier une explication basée sur un effet de charge.

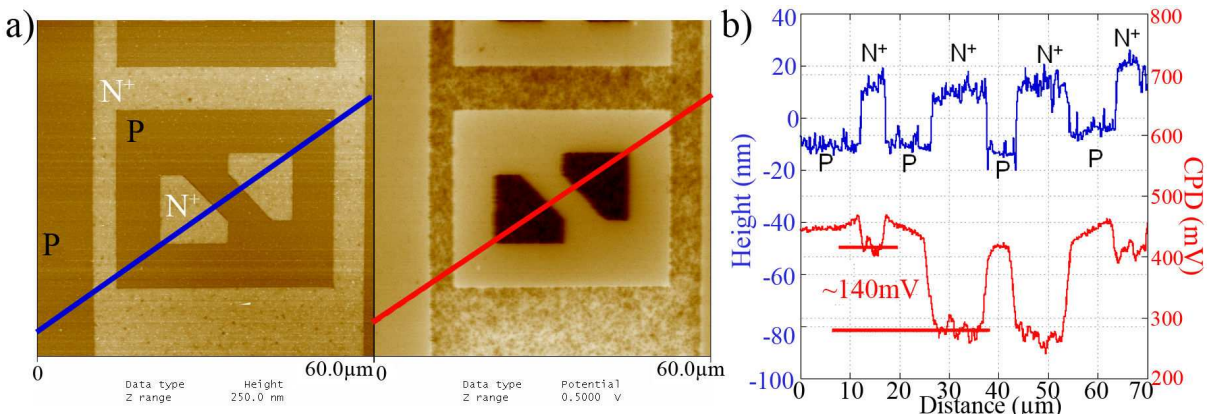

Figure 6.15: *Image SSRM de l'échantillon N^+/P : a) topographie et b) potentiel. $V_{AC} = 5V$.*

Ainsi, nous considérons la zone dopée N^+ fermée comme une diode en 3D entourée par un substrat P. La zone de déplétion joue un rôle d'isolant tout autour de la zone N^+ qui se comporte alors comme une capacité. Les électrons arrachés par effet photoélectrique des zones fortement dopées ne sont pas remplacés car la zone dopée est isolée du susbtrat (à cause de la zone de charge d'espace en 3D tout autour de la zone épitaxiée). Le champ électrique existant, dirigé de N vers P empêche les charges de passer et l'on se retrouve donc avec une accumulation de trous dans la zone N^+. Cet effet peut expliquer l'abaissement progressif du niveau de Fermi, et la variation des valeurs de travail de sortie et d'énergie de liaison Si^0 plus proches de mesures que l'on obtiendrait dans le cas d'un dopage P.

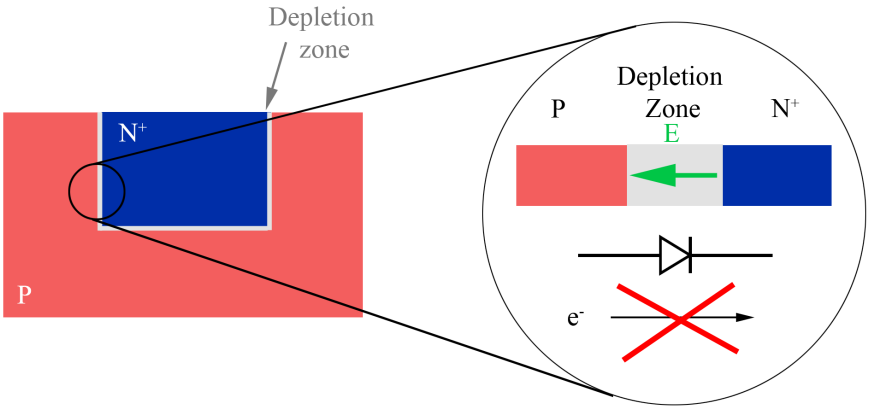

Figure 6.16: *Représentation schématique de l'échantillon N^+/P en tant que diode.*

Le fait que la zone ouverte N^+ présente également une inversion en terme de travail de sortie, mais inférieure à celle de la zone fermée est dû à un effet de géométrie. En effet, il faut regarder le problème sur une surface de quelques centaines de microns : la zone qui semble ouverte à faible champ de vue est en réalité fermée elle aussi par le substrat mais à une plus grande échelle. Le phénomène de charge est également présent dans cette zone, mais est masqué par le nombre d'électrons qui permet de trouver un meilleur équilibre.

Cette hypothèse explique le fait que ce phénomène de triple contraste ne soit pas

visible dans l'échantillon P^+/N : bien que la diode soit en mode bloqué, le champ électrique étant dirigé de N vers P permet une bonne conductivité entre les deux zones. Nous pouvons également donner une explication partielle sur l'origine de la zone brillante extérieure du substrat P. Puisque les charges ne peuvent pas traverser la zone de déplétion, elles se retrouvent stockées dans le substrat, au voisinage avec la zone dopée N^+. Cependant, cela n'explique pas pourquoi le phénomène n'apparaît qu'entre l'interface P et la zone N^+ ouverte.

Pour terminer, et afin de valider notre hypothèse de transfert de charges affectant le contraste, nous avons réalisé par FIB sur ces mêmes motifs des ponts permettant un bon contact électrique entre zone dopée et substrat. Les résultats KFM présentés en figure 6.17 montrent que le potentiel de surface de la zone fermée reliée par court-circuit au substrat se rapproche de celui de la zone ouverte N^+. Cependant, la différence résiduelle peut être attribuée au fait que le pont créé n'est pas assez large pour permettre à la totalité des charges de s'écouler.

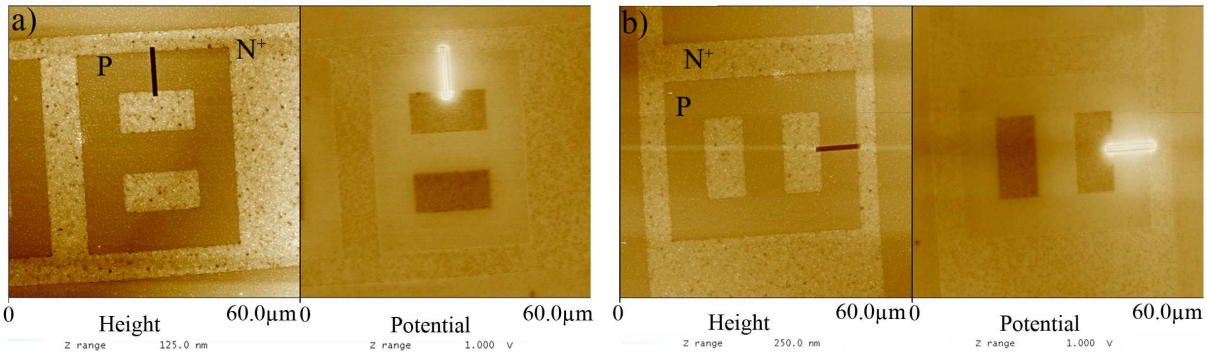

Figure 6.17: *Cartographie AFM de la topographie et du potentiel sur deux motifs 'zéro' présentant pour chacun d'entre eux une zone fermée dopée N^+ connectée au substrat : analyse a) verticale et b) horizontale pour vérifier que la variation de potentiel mesurée n'était pas un artefact. Zone gravée (Ga^+/30kV/28pA, profondeur : 50 nm, mesurée à 40 nm. V_{AC}= 5 V.)*

6.6 Simulations SIMION

6.6.1 Méthodologie

Afin d'évaluer au mieux l'influence des champs électriques latéraux au travers de la jonction pn sur les conditions d'imagerie PEEM, nous avons décidé de simuler les trajectoires des photoélectrons émis d'une telle structure. Nous avons utilisé le logiciel SIMION version 8 [131] qui permet de simuler des champs électrostatiques et magnétiques et de tracer les trajectoires de particules chargées en utilisant une méthode d'intégration de Runge-Kutta d'ordre 4.

La colonne PEEM simulée est semblable à celle du NanoESCA, comme visible sur le schéma 6.18 : l'échantillon est positionné sur la cathode de la colonne PEEM située à 1.8 mm devant la lentille objectif, à un potentiel proche de zéro. Cette dernière est composée de trois électrodes : l'extracteur, qui peut être porté à une tension de 15 kV,

l'électrode de focalisation et l'électrode définissant le potentiel de la colonne. Une ouverture de contraste de 70 μm de diamètre est située sur l'axe optique, dans le plan focal image de la lentille à immersion. Les potentiels des différentes électrodes sont réglés de façon à assurer une image focalisée au niveau de l'écran de la colonne PEEM. Le pouvoir de grandissement tel que défini par notre modèle est de $\times 44$.

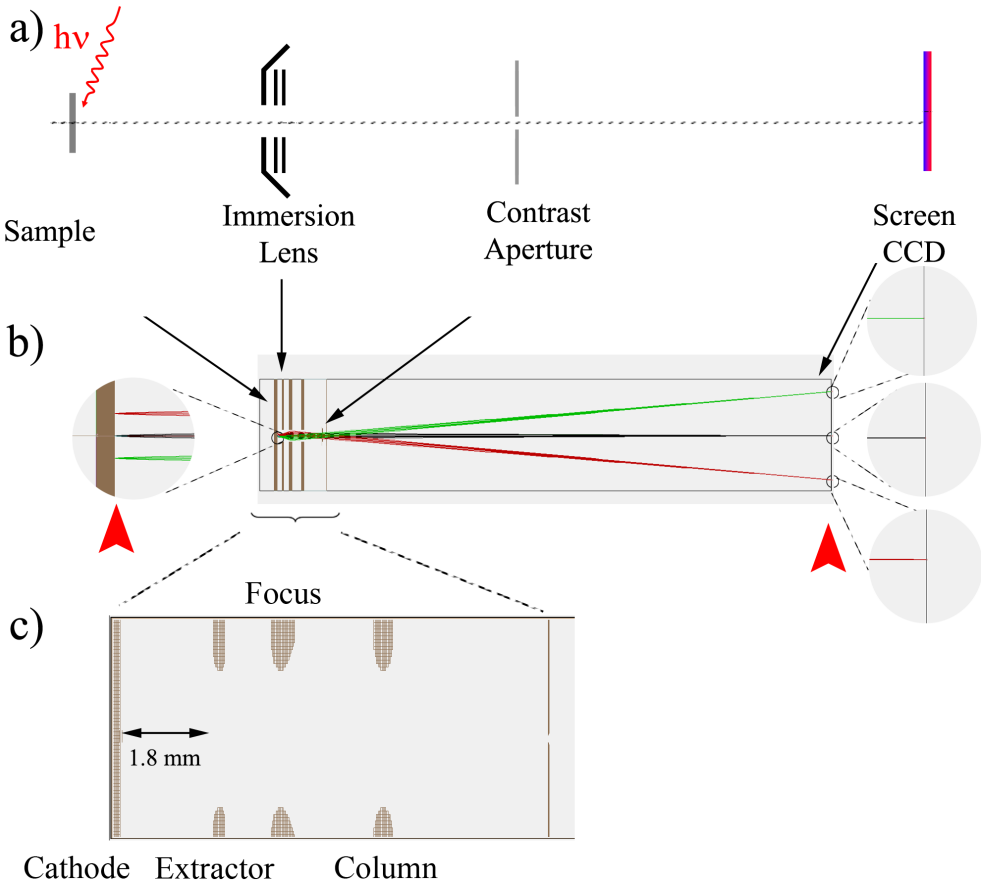

Figure 6.18: *Présentation du modèle simplifié d'une colonne PEEM : a) éléments optiques de la colonne PEEM, b) vue générale de SIMION, c) Grandissement des premiers éléments PEEM simulés sous SIMION.*

Nous considérons une structure symétrique composée de deux jonctions pn afin de nous affranchir des problèmes de positionnement absolu d'une unique jonction. L'échantillon est simulé par des électrodes dont le potentiel varie en fonction du potentiel de barrière choisi entre les deux zones dopées. Nous le fixons arbitrairement à 0 V pour la zone dopée P et à +1 V pour la zone dopée N. La structure telle que présentée en figure 6.19 consiste en deux jonctions séparées par une distance de 3 μm. La zone de déplétion est échantillonnée par des électrodes espacées de 35 nm. En fonction des potentiels appliqués, nous considérons une structure npn a) ou pnp b). Les résultats étant symétriques, nous nous sommes focalisés par la suite sur l'étude du cas npn.

Les photoélectrons émis par la surface de l'échantillon sont simulés sous la forme de faisceaux composés de sept particules ayant des angles d'émission allant de -10° à +10°

par pas de 4°. Leur énergie peut être changée entre 0.1 eV et 100 eV. Nous avons ainsi défini 204 faisceaux, répartis le long d'une ligne, intersectant le modèle de la jonction simulée nous permettant ainsi de simuler une jonction pn en 1D.

Lorsque les particules sont déviées par des champs électriques, leurs trajectoires se retrouvent modifiées dans une direction définie par le champ électrique latéral au niveau de la jonction, comme présenté en figure 6.19 a) pour une structure npn et en b) pour une structure pnp. Cela entraîne un renforcement de la concentration de photoélectrons par endroit et une déplétion de la zone dans laquelle se trouve le champ électrique. Nous étudions la distribution spatiale de la densité d'électrons au niveau d'un plan défini: soit l'échantillon, soit l'écran (schématiquement représentés par les deux flèches rouges en figure 6.18 b)) comme présenté dans le graphe par la courbe noire sur la partie droite des parties a) et b) en figure 6.19. Afin de minimiser au maximum de bruit dû au nombre fini de particules simulées, nous avons appliqué une moyenne glissante sur les 5 premiers voisins, comme visible en rouge sur le même graphe. Cette méthode de moyennage a également été utilisée par d'autres auteurs tels que Sangwan *et al.* [298].

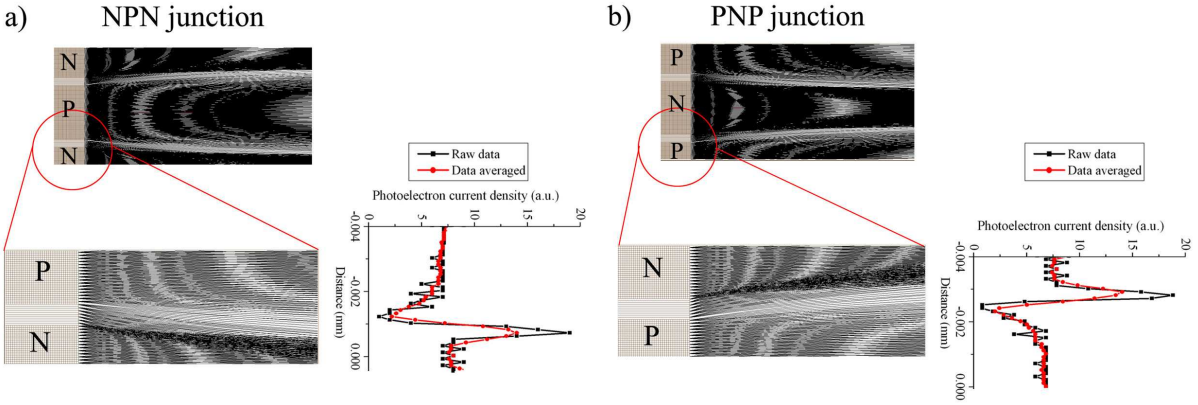

Figure 6.19: *Haut : trajectoires des photoélectrons modifiées par le champ électrique latéral au niveau de la jonction. Bas : agrandissement de la jonction pn et des trajectoires des particules dans la zone proche de l'échantillon dans le cas d'une structure a) npn et b) pnp. Partie droite de chaque cas : résultats des simulations présentant la distribution de la densité électronique au niveau d'un plan choisi proche de la surface de l'échantillon (noir) et sa moyenne (rouge) choisie pour minimiser le bruit.*

6.6.2 Influence de divers paramètres sur les conditions d'imagerie PEEM

Nous avons dans un premier temps considéré une colonne PEEM sans ouverture de contraste afin de tester pour un champ électrique latéral au niveau de la jonction E_j donné, l'influence de divers paramètres tels que l'énergie cinétique des photoélectrons, et la tension d'extraction de la colonne. Ces simulations, illustrées par des résultas expérimentaux nous ont permis de vérifier qu'il n'était pas possible de déterminer réellement la position de la jonction :

- Plus l'énergie cinétique des photoélectrons est élevée, moins ces particules sont déviées par le champ électique latéral de la jonction.

- De la même façon, plus le champ électrique créé par la lentille d'extraction est élevé, plus il compense celui créé par la jonction, et les particules sont moins déviées.

Nous nous sommes également intéressés à l'influence de la barrière de potentiel au niveau de la jonction sur la déviation des particules que nous présentons ci-après de façon plus détaillée. Les simulations ont montré que pour une tension d'extraction donnée E_{ext} plus la barrière de potentiel V_{bi} était importante plus, le rapport E_{ext}/E_j est faible et plus les électrons photoémis sont déviés.

Nous avons expérimentalement vérifié ce phénomène en considérant deux échantillons passivés dans les mêmes conditions expérimentales, pour lesquelles nous avons mesuré la différence de travail de sortie $\Delta\Phi$ entre les deux zones dopées. Nous avons extrait un profil d'intensité en noir (en rouge) d'une image avec un rayonnement synchrotron à 128.9 eV à une énergie de $(E - E_F)$=4.45 eV pour les échantillons de silicium dopés P^+/P (P^+/N), comme représenté en figure 6.20.

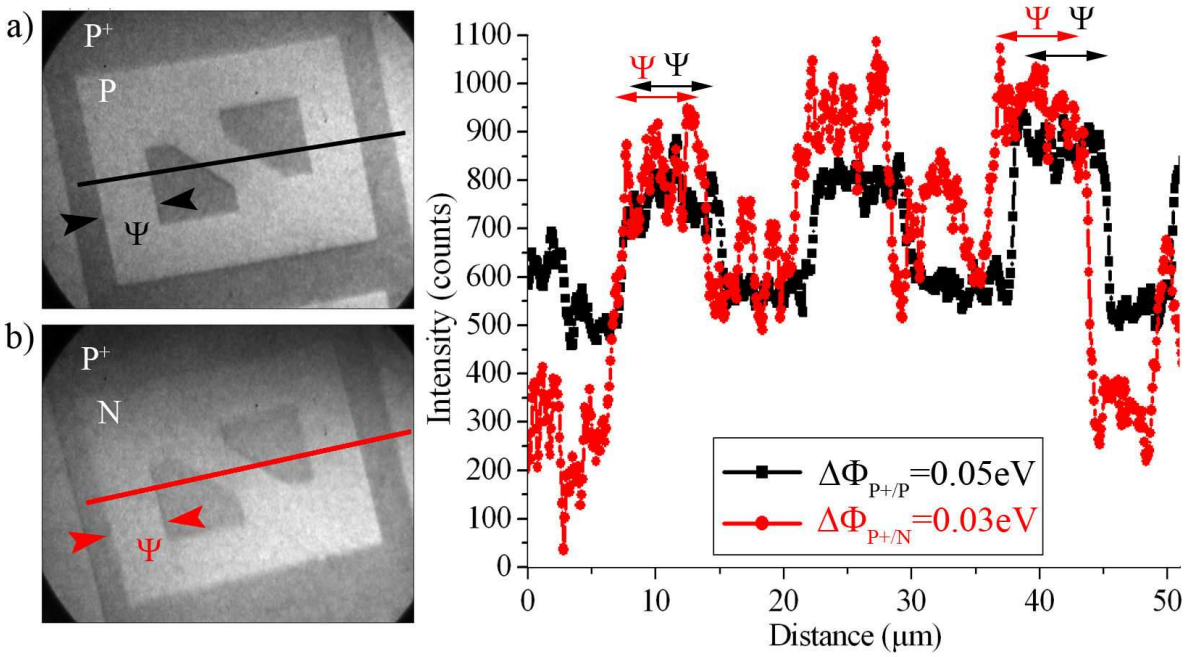

Figure 6.20: *Images des échantillons a) P^+/P et b) P^+/N au seuil $(E - E_F)$=4.45 eV et profil d'intensité extrait des coupes.*

Nous avons réalisé la même analyse pour une énergie de photon à 1486.7 eV sur les échantillons N^+/P et P^+/N dont les différences de travail de sortie pour un échantillon donné étaient différentes des cas précédents. Nous avons mesuré la largeur Ψ correspondant à l'écart entre deux jonctions et en avons déduit le décalage d'une unique jonction δx en prenant comme référence les mesures latérales $\Psi_{optical}$ obtenues avec un microscope optique, qui ne sont pas influencées par le champ électrique au travers de la jonction.

Les motifs observés ont des dimensions plus proches de celles mesurées en microscopie optique lorsque l'échantillon présente un faible champ électrique au niveau de la jonction (dû à une faible différence de travail de sortie entre les deux zones dopées). Pour une

énergie cinétique des particules et une tension d'extraction données, une différence de travail de sortie entre les deux dopages va entraîner un décalage de la position de la jonction.

Il convient maintenant de trouver un moyen de mettre en évidence facilement la présence de ce champ électrique latéral au niveau de la jonction pn : cela est possible en appliquant à l'imagerie PEEM le principe de la méthode en champ sombre, détaillée dans la partie suivante 6.6.3.

6.6.3 Imagerie PEEM en champ sombre

Le principe de la technique d'imagerie en champ sombre, bien expliqué par Nepijko *et al.* [300], consiste à décaler dans la colonne PEEM l'ouverture de contraste placée dans le plan focal image de la lentille extraction : si l'on considère une zone dans laquelle les particules sont déviées par un champ électrique latéral, ces dernières vont être bloquées par l'ouverture de contraste et la zone depuis laquelle elles ont été émises apparaîtra sombre dans l'image résultante.

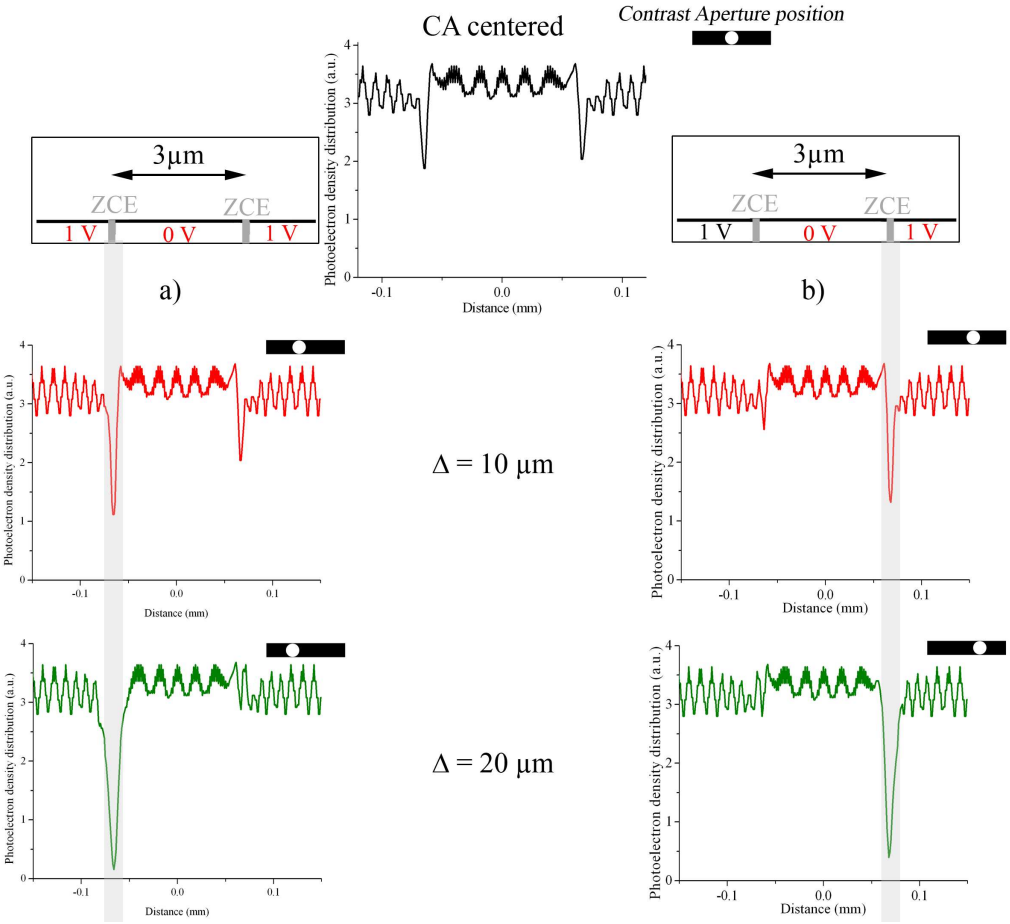

Figure 6.21: *Cas d'une structure npn. Distribution de l'instensité sur l'écran pour l'imagerie champ sombre à différents décalages de l'ouverture de contraste : a) négatifs et b) positifs. Encart : échantillon simulé avec dimensions, et potentiel appliqué au modèle. Les schémas blancs et noirs sont des représentations schématiques de la position de l'ouverture de contraste.*

Nous détaillons en figure 6.21 les simulations SIMION montrant le principe du champ sombre dans le cas d'une topographie électrique sur le modèle de la structure npn présentée précédemment. La distribution des photoélectrons sur l'écran est présentée pour des décalages successifs de l'ouverture de contraste de 10 μm par rapport à l'axe optique. Afin de mieux visualiser ce principe, nous choisissons une énergie cinétique des particules faibles pour les rendre le plus sensibles au champ électrique latéral au niveau de la jonction : 0.1 eV. La figure centrale montre la distribution de photoélectron attendue lorsque l'ouverture de contraste est centrée sur l'axe optique : nous y reconnaissons les deux puits correspondant à la localisation de la jonction. Les simulations présentent des résultats similaires, symétriques, suivant le sens de décalage de l'ouverture de contraste d'un côté a), ou de l'autre b) de l'axe optique. Nous observons ainsi que plus l'ouverture de contraste est décalée, plus l'un des côtés de la structure apparaît clairement alors que l'autre semble disparaître.

Nous avons vu que les photoélectrons pouvaient être déviés non seulement par la topographie électrique des échantillons, existant au niveau d'une jonction pn, mais également par la topographie physique, par exemple une marche de 75 nm. Dans la pratique, il n'est pas possible de distinguer indépendamment l'influence de l'un de ces deux facteurs sur l'imagerie dark field obtenue. Nous devons considérer la combinaison de ces deux phénomènes. Nous avons simulé l'influence sur la distribution des photoélectrons en imagerie champ sombre de ces deux paramètres séparément puis en les combinant. Les résultats obtenus sont similaires, mais la combinaison des deux phénomènes engendre une déviation plus importante des photoélectrons.

Nous terminons cette section en illustrant en figure 6.22 la simulation par une expérience menée à 128.9 eV d'énergie de photons au seuil pour laquelle nous pouvons visualiser au seuil la présence d'un champ électrique latéral au niveau des jonctions pn. Nous avons ainsi décalé l'ouverture de contraste symétriquement de part et d'autre de l'axe optique, les jonctions opposées des motifs s'assombrissant en fonction de la direction choisie. Le graphe présenté dans la partie gauche de la figure 6.22 montre bien la complémentarité des deux décalages de l'ouverture de contraste pour localiser sans distortion la position du champ électrique au niveau du motif. Nous retrouvons en combinant les deux profils, le profil noir obtenu lorsque l'ouverture de contraste est centrée sur l'axe optique.

6.7 Conclusion

Cette thèse a démontré le potentiel de l'XPEEM filtré en énergie pour l'interprétation du contraste au seuil et en niveau de coeur sur des motifs de silicium dopé en utilisant ses capacités de spectromicroscopie résolue spatialement.
Nous avons déduit de cette étude quelques axes de recherche à approfondir :

- Les procédures de réalisation d'échantillons dopés ainsi que de passivation des surfaces actuelles utilisées ne sont pas parfaitement adaptées à des techniques d'analyse de surface aussi sensibles que la spectroscopie de photoélectrons. Il paraît nécessaire d'approfondir les connaissances des mécanismes de passivation sur l'extrême surface des échantillons, mais également celles concernant la maîtrise des concentrations de

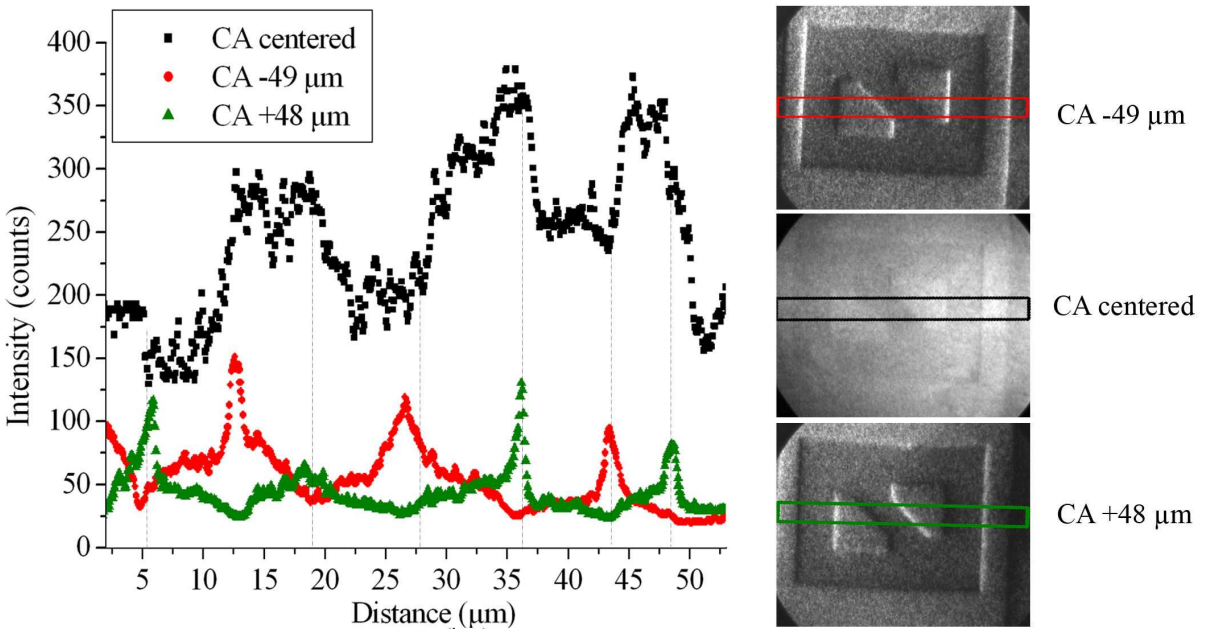

Figure 6.22: *Imagerie en champ sombre réalisée sur l'échantillon P^+/N au seuil avec une source de 128.9 eV. Les profils extraits des images sont présentés sur le graphe de gauche.*

dopants sur la profondeur d'intérêt en XPS concernant les dix premiers nanomètres sous la surface.

- La modélisation numérique du contraste obtenu sur des jonctions pn avec une colonne PEEM afin d'aider à son interprétation fine n'en est qu'à ses balbutiements. Des simulations approfondies mettant en jeu un contraste au niveau de la jonction dû à une différence des niveaux électroniques initiaux des photoélectrons seraient un apport supplémentaire.

- Pour terminer, la sensibilité de la technique XPEEM couplée à l'utilisation du rayonnement synchrotron permet d'élargir l'étendue des profondeurs sondées et des résolutions spatiales et énergétiques atteignables. Son extrême sensibilité à la surface en fait une technique indispensable pour la caractérisation d'échantillons semi-conducteurs dans les années à venir.

Bibliography

[1] L. Pelaz, L. A. Marqués, M. Aboy, Y. Santos, and P. Lopez. Simulation of pn junctions: present aud future challenges for technologies beyond 32 nm. *Journal of Vacuum Science and Technology B : Microelectronics and Nanometer Structures*, 28(1):1–6, 2010.

[2] W. Schottky and E. Spenke. *Wiss Veröffentl Siemens-Werken*, 18(3), 1939.

[3] N. F. Mott. *Proc. Roy. Soc.*, A171, 1939.

[4] C. G. B. Garrett and W. H. Brattain. Physical theory of semiconductor surfaces. *Physical Review*, 99(2):376, 1955.

[5] R. Subrahmanyan. Methods for the measurement of two-dimensional doping profiles. *Journal of Vacuum Science and Technology B: Microelectronics and Nanometer Structures*, 10:358, 1992.

[6] F. A. Stevie and D. P. Griffis. Quantification in dynamic SIMS: current status and future needs. *Applied Surface Science*, 255:1364–1367, 2008.

[7] C. A. Evans. Recent advances and applications of SIMS to electronic materials, 1984.

[8] R. J. Blattner and C. A. Evans. High-performance Secondary Ion Mass Spectrometry. *Scanning Electron Microscopy*, pages 55–68, 1980.

[9] H. F. Arlinghaus. Possibilities and limitations of high-resolution mass spectrometry in life sciences. *Applied Surface Science*, 255(4):1058–1063, 2008.

[10] V. A. Ukraintsev, P. J. Chen, J. T. Gray, C. F. Machala, L. K. Magel, and M.-C. Chang. High-resolution two-dimensional dopant characterization using Secondary Ion Mass Spectrometry. *Journal of Vacuum Science and Technology B: Microelectronics and Nanometer Structures*, 18(1):580–585, 2000.

[11] X. Liu, S. Goodwin-Johansson, J. D. Jacobson, M. A. Ray, and G. E. McGuire. On the spatial resolution of two dimensional doping profiles as measured using Secondary Ion Mass Spectrometry tomography. *Journal of Vacuum Science and Technology B: Microelectronics and Nanometer Structures*, 12(1):116–124, 1994.

[12] P. Chakraborty. Ultra-high depth resolution SIMS for the interface analysis of complex low-dimensional structures. *Nuclear Instruments and Methods in Physics*

Research Section B: Beam Interactions with Materials and Atoms, 266(8):1858 1865, 2008.

[13] M. G. Dowsett and G. A. Cooke. Two dimensional profiling using Secondary Ion Mass Spectrometry. *Journal of Vacuum Science and Technology B: Microelectronics and Nanometer Structures*, 10(1), 1992.

[14] R. A. Oliver. Advances in AFM for the electrical characterization of semiconductors. *Reports on Progress in Physics*, 71(076501):1–37, 2008.

[15] G. Benstetter, R. Biberger, and D. Liu. A review of advanced scanning probe microscope analysis of functional films and semiconductor devices. *Thin Solid Films*, 517:5100–5105, 2009.

[16] N. Duhayon, P. Eyben, M. Fouchier, T. Clarysse, W. Vandervorst, D. Alvarez, S. Schoemann, M. Ciappa, M. Stangoni, W. Fichtner, P. Formanek, M. Kittler, V. Raineri, F. Giannazzo, D. Goghero, Y. Rosenwaks, R. Shikler, S. Saraf, S. Sadewasser, N. Barreau, T. Glatzel, M. Verheijen, S. A. Mentink, M. von Sprekelsen, T. Maltezopoulos, R. Wiesendanger, and L. Hellemans. Assessing the performance of two-dimensional dopant profiling techniques. *Journal of Vacuum Science and Technology B: Microelectronics and Nanometer Structures*, 22(1):385–393, 2004.

[17] P. De Wolf, R. Stephenson, T. Trenkler, T. Clarysse, T. Hantschel, and W. Vandervorst. Status and review of two-dimensional carrier and dopant profiling using Scanning Probe Microscopy. *Journal of Vacuum Science and Technology B : Microelectronics and Nanometer Structures*, 18(1):361–368, 2000.

[18] M. L. Hildner, R. J. Phaneuf, and E. D. Williams. Imaging the depletion zone in a si lateral pn junction with Scanning Tunneling Microscopy. *Applied Physics Letters*, 72(25):3314–3316, 1998.

[19] J. Y. Park, R. J. Phaneuf, and E. D. Williams. Conductance imaging of the depletion region of biaised silicon pn junction device. *Material Research Society Symposium Proceedings*, 669:J2.3.1–J2.3.5, 2001.

[20] H. Fukutome, Y. Momiyama, T. Kubo, Y. Tagawa, T. Aoyama, and H. Arimoto. Direct evaluation of gate line edge roughness impact on extension profiles in sub 50nm n-MOSFETs. *Electron Devices, IEEE Transactions on*, 53(11):2755–2763, 2006.

[21] H. Fukutome, S. Hasegawa, K. Takano, H. Nakashima, T. Aoyama, and H. Arimoto. Visualization of the depleted layer in nanoscaled pn junctions on Si(001) surfaces with the use of scanning tunneling microscopy. *Applied Surface Science*, 144-145:554 563, 1999.

[22] H. Fukutome. Two-dimensional carrier profiling by Scanning Tunneling Microscopy and its application to advanced device development. *FUJISTU Sci. Tech. J.*, 46(3):237 242, 2010.

[23] J. Y. Park, R. J. Phaneuf, D. F. Ogletree, and M. Salmeron. Direct measurement of forces during Scanning Tunneling Microscopy imaging of silicon pn junctions. *Applied Physics Letters*, 86:172105–1 – 172105–3, 2005.

[24] J. A. Stroscio, R. M. Feenstra, and A. P. Fein. Electronic structure of the Si(111) 2x1 surface by Scanning Tunneling Microscopy. *Physical Review Letters*, 57(20):2579, 1986.

[25] L. D. Bell, W. J. Kaiser, M. H. Hecht, and F. J. Grunthaner. Direct control and characterization of a Schottky barrier by Scanning Tunneling Microscopy. *Applied Physics Letters*, 52(4):278–280, 1988.

[26] J. S. McMurray, J. Kim, C. C. Williams, and J. Slinkman. Direct comparison of two-dimensional dopant profiles by Scanning Capacitance Microscopy with small-caps TSUPREM4 process simulation. *Journal of Vacuum Science Technology B: Microelectronics and Nanometer Structures*, 16(1):344–348, 1998.

[27] J. Adrian, N. Rodriguez, F. Essely, G. Haller, C. Grosjean, A. Portavoce, and C. Girardeaux. Investigation of a new method for dopant characterization. *Microelectronics Reliability*, 47:1599 1603, 2007.

[28] M. Stangoni, M. Ciappa, and W. Fichtner. Assessment of the analytical capabilities of scanning capacitance and Scanning Spreading-Resistance Microscopy applied to semiconductor devices. *Microelectronics and Reliability*, 45(9-11):1532–1537, 2005.

[29] F. Giannazzo, V. Raineri, S. Mirabella, E. Bruno, G. Impellizzeri, and F. Priolo. Scanning Capacitance Microscopy two-dimensional carrier profiling for ultra-shallow junction characterization in deep submicron technology. *Materials Science and Engineering: B*, 124-125:54–61, 2005.

[30] N. Rodriguez, J. Adrian, C. Grosjean, G. Haller, C. Girardeaux, and A. Portavoce. Evaluation of Scanning Capacitance Microscopy sample preparation by Focused Ion Beam. *Microelectronics Reliability*, 46:1554 1557, 2006.

[31] G. Zimmermann, A. Born, B. Ebersberger, and C. Boit. Application of SCM for the microcharacterization of semiconductor devices. *Applied Physics A: Materials Science and Processing*, 76:885–888, 2003.

[32] D. Goghero, F. Giannazzo, and V. Raineri. Improved reproducibility in Scanning Capacitance Microscopy for quantitative 2D carrier profiling on silicon. *Materials Science and Engineering B*, 102(1-3):152–155, 2003.

[33] O. Jeandupeux, V. Marsico, A. Acovic, P. Fazan, H. Brune, and K. Kern. Use of Scanning Capacitance Microscopy for controlling wafer processing. *Microelectronics Reliability*, 42(2):225–231, 2002.

[34] R. Stephenson, A. Verhulst, P. De Wolf, M. Caymax, and W. Vandervorst. Contrast reversal in Scanning Capacitance Microscopy imaging. *Applied Physics Letters*, 73(18):2597–2599, 1998.

[35] D. Goghero, V. Raineri, and F. Giannazzo. Study of interface states and oxide quality to avoid contrast reversal in Scanning Capacitance Microscopy. *Applied Physics Letters*, 81(10):1824–1826, 2002.

[36] Y.D. Hong, J. Yan, K.M. Wong, Y.T. Yeow, and W.K. Chim. Dopant profile extraction by inverse modeling of Scanning Capacitance Microscopy using peak dc/dv. In *Solid-State and Integrated Circuits Technology, 2004. Proceedings. 7th International Conference on*, volume 2, pages 954 – 957, 2005.

[37] M. Buzzo, M. Leicht, T. Schweinböck, M. Ciappa, M. Stangoni, and W. Fichtner. 2D dopant profiling on 4H silicon carbide P+N junction by Scanning Capacitance and Scanning Electron Microscopy. *Microelectronics and Reliability*, 44:1681–1686, 2004.

[38] L. Zhang, H. Tanimoto, K. Adachi, and A. Nichiyama. 1-nm spatial resolution in carrier profiling of ultrashallow junctions by Scanning Spreading-Resistance Microscopy. *IEEE Electron Device Letters*, 29(7):799–801, 2008.

[39] L. Zhang, K. Ohuchi, K. Adachi, K. Ishimaru, M. Takayanagi, and A. Nishiyama. High-resolution characterization of ultrashallow junctions by measuring in vacuum with Scanning Spreading-Resistance Microscopy. *Applied Physics Letters*, 90(19):192103, 2007.

[40] D. À lvarez, M. Fouchier, J. Kretz, J. Hartwich, S. Schoemann, and W. Vandervorst. Fabrication and characterization of full diamond tips for Scanning Spreading-Resistance Microscopy. *Microelectronic Engineering*, 73-74:910–915, 2004.

[41] P. Eyben, D. Alvarez, M. Jurczak, R. Rooyackers, A. De Keersgieter, E. Augendre, and W. Vandervorst. Analysis of the 2D dopant profile in a 90 nm complementary Metal Oxide Semiconductor technology using Scanning Spreading Resistance Microscopy. *Journal of Vacuum Science and Technology B: Microelectronics and Nanometer Structures*, 22(1):364–368, 2004.

[42] P. Eyben, S. Denis, T. Clarysse, and W. Vandervorst. Progress towards a physical contact model for Scanning Spreading Resistance Microscopy. *Materials Science and Engineering B*, 102(1-3):132–137, 2003.

[43] P. Eyben, T. Janssens, and W. Vandervorst. Scanning Spreading Resistance Microscopy (SSRM) 2D carrier profiling for ultra-shallow junction characterization in deep-submicron technologies. *Materials Science and Engineering B*, 124-125:45–53, 2005.

[44] P. Eyben, D. Vanhaeren, T. Janssens, T. Hantschel, W. Vandervorst, K. Adachi, and K. Ishimaru. Evaluation of the junction delineation accuracy and reproducibility with the SSRM technique. *Microelectronic Engineering*, 84(3):437–440, 2007.

[45] S. Saraf and Y. Rosenwaks. Local measurement of semiconductor band bending and surface charge using Kelvin probe Force Microscopy. *Surface Science*, 574(2-3):L35–L39, 2005.

[46] B.-Y. Tsui, C.-M. Hsieh, P.-C. Su, S.-D. Tzeng, and S. Gwo. Two-dimensional carrier profiling by Kelvin-probe Force Microscopy. *Japanese Journal of Applied Physics*, 47(6):4448–4453, 2008.

[47] S. Magonov and J. Alexander. Advanced Atomic Force Microscopy: Exploring measurements of local electric properties. *Agilent Technologies: application notes*, 2008.

[48] S.-C. Chin, Y.-C. Chang, C.-C. Hsu, W.-H. Lin, W.-I. Wu, C.-S. Chang, T. T. Tsong, W.-Y. Woon, L.-T. Lin, and H.-J. Tao. Two-dimensional dopant profiling by Electrostatic Force Microscopy using carbon nanotube modified cantilevers. *Nanotechnology*, 19:1–7, 2008.

[49] S. Duguay, M. Ngamo, P. F. Fazzini, F. Cristiano, K. Daoud, and P. Pareige. Atomic scale study of a MOS structure with an ultra-low energy boron-implanted silicon substrate. *Thin Solid Films*, 58:2398 2401, 2010.

[50] G. Da Costa, F. Vurpillot, A. Bostel, M. Bouet, and B. Deconihout. Design of a delay-line position-sensitive detector with improved performance. *Review of Scientific Instruments*, 76(013304):1–8, 2005.

[51] M. K. Miller and R. G. Forbes. Atom Probe Tomography - tutorial review. *Materials Characterization*, 60:461 469, 2009.

[52] M. A. Kelly and M. K. Miller. Invited review article: Atom Probe Tomography. *Review of Scientific Instruments*, 78:031101, 2007.

[53] D. J. Larson and M. A. Kelly. Nanoscale analysis of materials using a local-electrode atom probe. *Microscopy and analysis*, pages 59–62, 2006.

[54] T. F. Kelly. LEAP tomography and the rapidly expanding world of microelectronic applications. In *International Conference on Frontiers of Characterization and Metrology for Nanoelectronics (ICFCMN)*, 2007.

[55] S. Kölling and W. Vandervorst. Failure mechanisms of silicon-based atom-probe tips. *Ultramicroscopy*, 109:486–491, 2009.

[56] G.B. Thompson, M.K. Miller, and H.L. Fraser. Some aspects of atom probe specimen preparation and analysis of thin film materials. *Ultramicroscopy*, 100:25–34, 2004.

[57] B. Gault, A. La Fontaine, M. P. Moody, S. P. Ringer, and E. A. Marquis. Impact of laser pulsing on the reconstruction in an Atom Probe Tomography. *Ultramicroscopy*, 110(9):1215–1222, 2010.

[58] A. Lenk, H. Lichte, and U. Muehle. 2D-mapping of dopant distribution in deep sub micron CMOS devices by electron holography using adapted FIB-preparation. *Journal of Electron Microscopy*, 54(4):351–359, 2005.

[59] A. C. Twitchett-Harrison, T. J. V. Yates, S. B. Newcomb, R. E. Dunin-Borkowski, and P.A. Midgley. High-resolution three-dimensional mapping of semiconductor dopant potentials. *Nano Letters*, 7(7):2020–2023, 2007.

[60] W.-D. Rau and A. Orchowki. Mapping of process-induced dopant redistributions by electron holography. *Microscopy and Microanalysis*, 10:462–469, 2004.

[61] J. H. Yoo, J.-M. Yang, S. Ulugbek, C. W. Ahn, W.-J. Hwang, J. K. Park, C. M. Park, S. B. Hong, J. J. Kim, and D. Shindo. Electron holography study for two-dimensional dopant profile measurement with specimens prepared by backside ion milling. *Journal of Electron Microscopy*, 57(1):13–18, 2008.

[62] N. Ikarashi, A. Toda, K. Uejima, T. Yako, M. Hane, and M. Sato. Electron holography for analysis of deep submicron devices: present status and challenges. *Journal of Vacuum Science and Technology B: Microelectronics and Nanometer Structures*, 28(1):C1D5–C1D10, 2010.

[63] P.A. Midgley and R. E. Dunin-Borkowski. Electron tomography and holography in materials science. *Nature Materials*, 8:271–280, 2009.

[64] D. Cooper, R. Truche, F. Laugier, F. Bertin, and A. Chabli. *Dopant Profiling of Silicon Calibration Specimens by Off-Axis Electron Holography*, volume 120 of *Microscopy of Semiconducting Materials 2007*. Springer Proceedings Physics, springer netherlands edition, 2008.

[65] W. D. Rau, P. Schwander, F. H. Baumann, W. Höppner, and A. Ourmazd. Two-dimensional mapping of the electrostatic potential in transistors by electron holography. *Physical Review Letters*, 82(12):2614, 1999.

[66] D. Cooper, J.-P. Barnes, J.-H. Hartmann, and F. Bertin. Off-axis electron holography of Si semiconductors prepared using FIB milling. *Journal of physics: conference series*, 209(1):012062, 2010.

[67] P.A. Midgley. An introduction to off-axis electron holography. *Micron*, 32:167–184, 2001.

[68] P. Formanek and E. Bugiel. Specimen preparation for electron holography of semiconductor devices. *Ultramicroscopy*, 106:365 375, 2006.

[69] M. Rommel, G. Spoldi, V. Yanev, S. Beuer, B. Amon, J. Jambreck, S. Petersen, A. J. Bauer, and L. Frey. Comprehensive study of Focused Ion Beam induced lateral damage in silicon by scanning probe microscopy techniques. *Journal of Vacuum Science and Technology B: Microelectronics and Nanometer Structures*, 28(3):595–607, 2010.

[70] D Cooper, J.-P. Barnes, J. M. Hartmann, A. Beche, and J.-L. Rouviere. Dark field electron holography for quantitative strain measurements with nanometer-scale spatial resolution. *Applied Physics Letters*, 95(5):053501, 2009.

[71] A. C. Twitchett-Harrison, R. E. Dunin-Borkowski, and P.A. Midgley. Mapping the electrical properties of semiconductor junctions: the electron holographic approach. *Scanning*, 30:299–309, 2008.

[72] P. F. Fazzini, P. G. Merli, G. Pozzi, and F. Ubaldi. Effects of beam specimen interaction on the observation of reverse-biased pn junctions by electron interferometry. *Physical Review B*, 72(8):85312–0 85312–8, 2005.

[73] D. Cooper, C. Ailliot, R. Truche, J.-P. Barnes, J.-M. Hartmann, and F. Bertin. Experimental off-axis electron holography of focused ion beam-prepared Si pn junctions with different dopant concentrations. *Journal of Applied Physics*, 104(6):064513, 2008.

[74] D. D. Perovic, M. R. Castell, A. Howie, C. Lavoie, T. Tiedje, and J. S. W. Cole. *Ultramicroscopy*, 58(104), 1995.

[75] S. L. Elliott, R. F. Broom, and C. J. Humphreys. Dopant profiling with the Scanning Electron Microscope: a study of Si. *Journal of Applied Physics*, 91(11):9116–9122, 2002.

[76] D. Venables, H. Jain, and D. C. Collins. Secondary electron imaging as a two-dimensional dopant profiling technique: review and update. *Journal of Vacuum Science and Technology B: Microelectronics and Nanometer Structures*, 16(1):362–366, 1997.

[77] P. Kazemian, C. Rodenburg, and C. J. Humphreys. Effect of experimental parameters on doping contrast of Si pn junctions in a FEG-SEM. *Microelectronic Engineering*, 73 74:948 953, 2004.

[78] A. K. W. Chee, R. F. Broom, C. J. Humphreys, and E. G. T. Bosch. A quantitative model for doping contrast in the scanning electron microscope using calculated potential distributions and monte carlo simulations. *Journal of Applied Physics*, 109(1):013109, 2011.

[79] P. Kazemian, A. C. Twitchett-Harrison, C. J. Humphreys, and C. Rodenburg. Site-specific dopant profiling in a Scanning Electron Microscope using Focused Ion Beam prepared specimens. *Applied Physics Letters*, 88(212110):1–3, 2006.

[80] C. Schönjahn, C. J. Humphreys, and M. Glick. Energy-filtered imaging in a Field-Emission Scanning Electron Microscope for dopant mapping in semiconductors. *Journal of Applied Physics*, 92(12):7667–7671, 2002.

[81] P.-T. Liu, J.-H. Lee, Y. S. Huan, and D. Su. Application of secondary electron potential contrast on junction leakage isolation. *Applied Physics Letters*, 95:122105, 2009.

[82] P. Kazemian, S. A. Mentink, C. Rodenburg, and C. J. Humphreys. Quantitative Secondary Electron energy filtering in a Scanning Electron Microscope and its applications. *Ultramicroscopy*, 107:140–150, 2007.

[83] M. Buzzo, M. Ciappa, J. Millan, P. Godignon, and W. Fichtner. Two-dimensional dopant imaging of silicon carbid devices by secondary electron potential contrast. *Microelectronic Engineering*, 84:413–418, 2007.

[84] M. Buzzo, M. Ciappa, and W. Fichtner. Imaging and dopant profiling of silicon carbide devices by secondary electron dopant contrast. *IEEE Transactions on device and materials reliability*, 6(2):203–212, 2006.

[85] I. Müllerovà and M. Lenc. Some approaches to low-voltage Scanning Electron Microscopy. *Ultramicroscopy*, 41(4):399–410, 1992.

[86] I. Müllerovà, L. Frank, and W. H. Peter. Scanning low-energy Electron Microscopy. In *Advances in Imaging and Electron Physics*, volume Volume 128, pages 309–443. 2003.

[87] I. Müllerovà and L. Frank. Contrast mechanisms in the Scanning Electron Microscopy. *Microscopy and Microanalysis*, 9(SupplementS03):120–121, 2003.

[88] I. Müllerovà and L. Frank. Very Low Energy Scanning Electron Microscopy. In *Modern Research and Educational Topics in Microscopy*. 2007.

[89] J. Cazaux. About the role of the various types of secondary electrons (SE_1; SE_2; SE_3) on the performance of LVSEM. *Journal of Microscopy*, 214(3):341 347, 2003.

[90] S. Günther, A. Kolmakov, J. Kovac, and M. Kiskinova. Artefact formation in scanning photoelectron emission microscopy. *Ultramicroscopy*, 75(1):35, 1998.

[91] S. Günther, B. Kaulich, L. Gregoratti, and M. Kiskinova. Photoelectron microscopy and applications in surface and materials science. *Progress in Surface Science*, 70(4-8):187 – 260, 2002.

[92] A. Locatelli and A. Bauer. Recent advances in chemical and magnetic imaging of surfaces and interfaces by XPEEM. *Journal of Physics: Condensed Matter*, 20:1–22, 2008.

[93] A. Barinov, P. Dudin, L. Gregoratti, A. Locatelli, T. O. Mentes, M. Angel Niño, and M. Kiskinova. Synchrotron-based photoelectron microscopy. *Nuclear Instruments and Methods in Physics Research Section A: Accelerators, Spectrometers, Detectors and Associated Equipment*, 601(1-2):195–202, 2009.

[94] R. J. Phaneuf, H. C. Kan, M. Marsi, L. Gregoratti, S. Günther, and M. Kiskinova. Imaging the variation in band bending across a silicon pn junction surface using spectromicroscopy. *Journal of Applied Physics*, 88(2):863–868, 2000.

[95] C. M. Schneider and G. Schönhense. Investigating surface magnetism by means of photoexcitation electron emission microscopy. *Reports on Progress in Physics*, 65(12):1785–1839, 2002.

[96] G. De Stasio, B. Gilbert, B. H. Frazer, K. H. Nealson, P. G. Conrad, V. Livi, M. Labrenz, and J. F. Banfield. The multidisciplinarity of spectromicroscopy: from geomicrobiology to archaeology. *Journal of Electron Spectroscopy and Related Phenomena*, 114-116:997–1003, 2001.

[97] R. Könenkamp, Robert C. Word, G. F. Rempfer, T. Dixon, L. Almaraz, and T. Jones. 5.4 nm spatial resolution in biological photoemission electron microscopy. *Ultramicroscopy*, 110(7):899–902, 2010.

[98] N. Weber, M. Escher, M. Merkel, A. Oelsner, and G. Schönhense. Energy- and time-resolved microscopy using PEEM: recent developments and state-of-the-art. *Journal of physics: conference series*, 100, 2008.

[99] G. Margaritondo. Photoelectron spectromicroscopy and spectronanoscopy at synchrotrons: Growing impact on life sciences and materials science. *Journal of Electron Spectroscopy and Related Phenomena*, 178-179:273–291, 2010.

[100] O. Renault and A. Chabli. Energy-filtered photoelectron emission microscopy (EF-PEEM) for imaging nanoelectronic materials. *AIP Conference Proceedings*, 931(1):502–506, 2007.

[101] N. Barrett, L. F. Zagonel, O. Renault, and A. Bailly. Spatially resolved, energy-filtered imaging of core level and valence band photoemission of highly p and n doped silicon patterns. *Journal of Physics: Condensed Matter*, 21(31):314015, 2009.

[102] A. Bailly, Renault O., Barrett N., Zagonel L. F., Gentile P., Pauc N., Dhalluin F., Baron T., Chabli A. Cezar J. C. B., and Brookes N. Aspects of lateral resolution in energy-filtered core level photoelectron emission microscopy. *Journal of Physics: Condensed Matter*, 21(31):314002, 2009.

[103] V. W. Ballarotto, K. Siegrist, R. J. Phaneuf, E. D. Williams, and S. Mogren. PEEM imaging of dopant contrast in Si(001). *Surface Science*, 461(1-3):L570–L574, 2000.

[104] T. H. P. Chang and W. C. Nixon. Electron beam induced potential contrast on unbiased planar transistors. *Solid State Electronic*, 10(701), 1967.

[105] C. G. H. Walker, F. Zaggout, and M. M. El-Gomati. The role of oxygen in secondary electron contrast in doped semiconductors using Low Voltage Scanning Electron Microscopy. *Journal of Applied Physics*, 104(12):123713, 2008.

[106] H. Seiler. Secondary electron emission in the Scanning Electron Microscope. *Journal of Applied Physics*, 54(11):R1–R18, 1983.

[107] J. Cazaux. Recent developments and new strategies in Scanning Electron Microscopy. *Journal of Microscopy*, 217(1):16–35, 2005.

[108] V. W. Ballarotto, K. Siegrist, R. J. Phaneuf, and E. D. Williams. Model for doping-induced contrast in photoelectron emission microscopy. *Journal of Applied Physics*, 91(1):469–475, 2002.

[109] F. G. Allen and G. W. Gobeli. Work function, photoelectric threshold, and surface states of atomically clean silicon. *Physical Review*, 127(1):150, 1962.

[110] M. Giesen, Raymond J. Phaneuf, Ellen D. Williams, and Theodore L. Einstein. Photoemission electron microscopy of schottky contacts. *Surface Science*, 396(1-3):411–421, 1998.

[111] A. Howie. *Microscopy and Microanalysis*, 6:291, 2000.

[112] M. Dapor, B. J. Inkson, C. Rodenburg, and J. M. Rodenburg. A comprehensive Monte Carlo calculation of dopant contrast in secondary-electron imaging. *Europhysics Letters*, 82:3006 1–4, 2008.

[113] I. Volotsenko, M. Molotskii, Z. Barkay, J. Marczewski, P. BGrabiec, B. Jaroszewicz, G. Meshulam, E. Grunbaum, and Y. Rosenwaks. Secondary electron doping contrast: theory based on Scanning Electron Microscope and Kelvin probe Force Microscopy measurments. *Journal of Applied Physics*, 107:014510, 2010.

[114] C. P. Sealy, M. R. Castell, and P. R. Wilshaw. Mechanism for secondary electron dopant contrast in the SEM. *Journal of Electron Microscopy (Tokyo)*, 49(2):311–321, 2000.

[115] M. El Gomati, F. Zaggout, H. Jayacody, S. Tear, and K. Wilson. Why is it possible to detect doped regions of semiconductors in low voltage sem: a review and update. *Surface and Interface Analysis*, 37:901–911, 2005.

[116] I. Müllerovà, M. M. El-Gomati, and L. Frank. Imaging of the boron doping in silicon using low energy SEM. *Ultramicroscopy*, 93(3-4):223–243, 2002.

[117] J. Cazaux. Calculated influence of work function on SE escape probability and secondary electron emission yield. *Applied Surface Science*, 257(3):1002–1009, 2010.

[118] J. Cazaux. Material contrast in SEM: Fermi energy and work function effects. *Ultramicroscopy*, 110(3):242–253, 2010.

[119] F. N. Zaggout, C. G. H. Walker, and M. M. El Gomati. The chemisorption of oxygen and its effect on the secondary electron emission from doped semiconductors. *Journal of physics: conference series*, 209(1):012055, 2010.

[120] V. W. Ballarotto, M. Breban, K. Siegrist, R. J. Phaneuf, and E. D. Williams. Photoelectron emission microscopy of ultrathin oxide covered devices. *Journal of Vacuum Science and Technology B: Microelectronics and Nanometer Structures*, 20(6):2514, 2002.

[121] L. Frank, I. Müllerovà, D. A. Valdaitsev, A. Gloskovskii, S. A. Nepijko, H.-J. Elmers, and G. Schönhense. The origin of contrast in the imaging of doped areas in silicon by slow electrons. *Journal of Applied Physics*, 100(9), 2006.

[122] S. A. Nepijko, A. Gloskovskii, N. N. Sedov, and G. Schönhense. Measurement of the electric field distribution and potentials on the object surface in an emission electron microscope without restriction of the electron beams. *Journal of Microscopy*, 211(1):89–94, 2003.

[123] E. Mutoro, B. Luerssen, S. Gunther, and J. Janek. Photoelectron microscopy : Imaging tools for the study of surfac reactions with temporal and spatial resolution. *Bunsen-Magazin*, 9(18), 2007.

[124] B.J. Tielsch and J.E. Fulghum. Differential charging in XPS. part I: Demonstration of lateral charging in a bulk insulator using imaging XPS. *Surface and Interface Analysis*, 24(1):28–30, 1996.

[125] B. Gilbert, R. Andres, P. Perfetti, G. Margaritondo, G. Rempfer, and G. De Stasio. Charging phenomena in PEEM imaging and spectroscopy. *Ultramicroscopy*, 83(1-2):129, 2000.

[126] M. D. v Przychowski, G. K. L. Marx, G. H. Fecher, and G. Schönhense. A spatially resolved investigation of oxygen adsorption on polycrystalline copper and titanium by means of photoemission electron microscopy. *Surface Science*, 549(1):37–51, 2004.

[127] O. Renault, R. Brochier, A. Roule, P.H. Haumesser, B. Krömker, and D. Funnemann. Work-function imaging of oriented copper grains by photoemission. *Surface and Interface Analysis*, 38:375–377, 2006.

[128] J. Stöhr, H.A. Padmore, S. Anders, T. Stammler, and M. R. Scheinfein. Principles of X-ray Magnetic Dichroism spectromicroscopy. *Surface Review and Letters*, 5(6):1297 – 1308, 1998.

[129] S.A. Nepijko, N. N. Sedov, G. Schönhense, M. Escher, X. Bao, and W. Huang. Resolution deterioration in emission electron microscopy due to object roughness. *Annalen der Physik*, 9(6):441–451, 2000.

[130] K. Siegrist, E. D. Williams, and V. W. Ballarotto. Characterizing topography-induced contrast in photoelectron emission microscopy. *Journal of Vacuum Science and Technology A: Vacuum, Surfaces, and Films*, 21(4):1098–1102, 2003.

[131] SIMION 3D Version 8.0 S.I.S. Inc. Industry standard charged particle optics simulation software.

[132] J. Stöhr and S. Anders. X-ray spectromicroscopy of complex materials and surfaces. *IBM journal of research and development*, 44(4):535, 2000.

[133] G-F. Rempfer, K. Nadakavukaren, and O. H. Griffith. Depth of field in emission microscopy. *Ultramicroscopy*, 5(1-3):449–457, 1980.

[134] K. Siegrist, V. Ballarotto, and E. D. Williams. Quantifying field-induced contrast effects in photoelectron emission microscopy, 2004.

[135] M. Giesen, R. J. Phaneuf, E. D. Williams, T. L. Einstein, and H. Ibach. Characterization of p-n junctions and surface-states on silicon devices by photoemission electron microscopy. *Applied Physics A: Materials Science and Processing*, 64(5):423–430, 1997.

[136] S. A. Nepijko, N. N. Sedov, O. Schmidt, G. Schönhense, X. Bao, and W. Huang. Imaging of three-dimensional objects in emission electron microscopy. *Journal of Microscopy*, 202(3):480–487, 2001.

[137] M. Hovorka, F. Mika, and L. Frank. *Profiling of N-type dopants in silicon structures*, volume Vol. 1: Instrumentation and Methodology. Verlag der TU Graz 2009, 2009.

[138] M. Hovorka, L. Frank, D. Valdaitsev, S. A. Nepijko, H. S. Elmers, and G. Schönhense. High-pass energy-filtered photoemission electron microscopy imaging of dopants in silicon. *Journal of Microscopy*, 230(1):42–47, 2008.

[139] L. Frank, F. Mika, M. Hovorka, D. Valdaitsev, G. Schönhense, and I. Müllerovà. Dopant contrast in semiconductors as interpretation challenge at imaging by electrons. *Material Transactions*, 48(5):936–939, 2007.

[140] L. Votocek and J. Tousek. Surface photovoltaic effect and its applications to Si wafers and monocrystalline Si solar cells diagnostics. In *WDS'05*, pages 595–600, 2005.

[141] L. Kronik and Y. Shapira. Surface photovoltage phenomena: theory, experiment, and applications. *Surface Science Reports*, 37(1-5):1–206, 1999.

[142] D.K. Schroder. Surface voltage and surface photovoltage: history, theory and applications. *Measurement Science and Technology*, 12(3):R16, 2001.

[143] L. Kronik and Y. Shapira. Surface photovoltage spectroscopy of semiconductor structures: at the crossroads of physics, chemistry and electrical engineering. *Surface and Interface Analysis*, 31(10):954–965, 2001.

[144] M. Alonso, R. Cimino, and K. Horn. Surface photovoltage effects in photoemission from metal-GaP(110) interfaces: importance for band-bending evalution. *Physical Review Letters*, 64(16):1947–1950, 1990.

[145] M. H. Hecht. Role of photocurrent in low-temperature photoemission studies of Schottky-barrier formation. *Physical Review B*, 41(11):7918–7921, 1990.

[146] C. J. Powell. Growth and trends in Auger-electron spectroscopy and X-ray photoelectron spectroscopy for surface analysis. *Journal of Vacuum Science and Technology A: Vacuum, Surfaces, and Films*, 21(5):S42–S53, 2003.

[147] P. Coxon, J. Krizek, M. Humpherson, and I. R. M. Wardell. Escascope - a new imaging photoelectron spectrometer. *Journal of Electron Spectroscopy and Related Phenomena*, 52:821–836, 1990.

[148] A. Einstein. *Ann Phys*, 322:132–148, 1905.

[149] N. Barrett and O. Renault. La spectromicroscopie XPEEM avec le rayonnement synchrotron. *Matériaux et Techniques*, 97:101–122, 2009.

[150] J. H. Scofield. Hartree-Slater subshell photoionization cross-sections at 1254 eV and 1487 eV. *Journal of Electron Spectroscopy and Related Phenomena*, 8(2):129–137, 1976.

[151] J. J. Yeh and I. Lindau. Atomic subshell photoionization cross sections and asymmetry parameters: 1 <= Z <= 103. *Atomic Data and Nuclear Data Tables*, 32(1):1–155, 1985.

[152] C. R. Brundle. Elucidation of surface structure and bonding by photoelectron spectroscopy? *Surface Science*, 48(1):99–136, 1975.

[153] M. P. Seah and W. A. Dench. Quantitative electron spectroscopy of surfaces: A standard data base for electron inelastic mean free paths in solids. *Surface and Interface Analysis*, 1(1):2–11, 1979.

[154] C. J. Powell and A. Jablonski. Progress in quantitative surface analysis by X-ray photoelectron spectroscopy: Current status and perspectives. *Journal of Electron Spectroscopy and Related Phenomena*, 178-179:331–346, 2009.

[155] S. Tanuma, C. J. Powell, and D. R. Penn. Calculations of electron inelastic mean free paths. iii. data for 15 inorganic compounds over the 50-2000 ev range. *Surface and Interface Analysis*, 17(13):927–939, 1991.

[156] G. Gergely, S. Gurban, M. Menyhard, A. Jablonski, L. Zommer, and K. Goto. The inelastic mean free path of electrons. past and present research. *Vacuum*, 84(1):134–136, 2009.

[157] Ebel. 1985.

[158] M. P. Seah. Reference data for Auger electron spectroscopy and X-ray photoelectron spectroscopy combined. *Applied Surface Science*, 144-145:161–167, 1999.

[159] C. J. Powell and A. Jablonski. Surface sensitivity of X-ray photoelectron spectroscopy. *Nuclear Instruments and Methods in Physics Research Section A: Accelerators, Spectrometers, Detectors and Associated Equipment*, 601(1-2):54–65, 2009.

[160] A. Jablonski and C. J. Powell. Practical expressions for the mean escape depth, the information depth, and the effective attenuation length in Auger-electron spectroscopy and X-ray photoelectron spectroscopy. *Journal of Vacuum Science and Technology A: Vacuum, Surfaces, and Films*, 27(2):253–264, 2009.

[161] M. G. Helander, M. T. Greiner, Z. B. Wang, and Z. H. Lu. Pitfalls in measuring work function using photoelectron spectroscopy. *Applied Surface Science*, 256(8):2602–2605, 2010.

[162] S. Halas and T. Durakiewicz. Work functions of elements epressed in terms of the Fermi energy and the density of free electrons. *Journal of Physics: Condensed Matter*, 10:10815–10826, 1998.

[163] S. Halas. 100 years of work function. *Materials Science-Poland*, 24(4):951–968, 2006.

[164] S. Halas and T. Durakiewicz. Is work function a bulk or a surface property? *Vacuum*, 85(4):486–488, 2010.

[165] B. L. Henke, J. A. Smith, and D. T. Attwood. 0.1-10 keV X-ray-induced electron emissions from solids - models and secondary electron measurements. *Journal of Applied Physics*, 48(5):1852–1866, 1977.

[166] K. Takeuchi, A. Suda, and S. Ushioda. Local variation of the work function of Cu(111) surface deduced from the low energy photoemission spectra. *Surface Science*, 489(1-3):100–106, 2001.

[167] N. Pauly and S. Tougaard. Surface and core-hole effect in X-ray photoelectron spectroscopy. *Surface Science*, 604(13-14):1193–1196, 2010.

[168] D. A. Shirley. High-resolution X-ray photoemission spectrum of the valence bands of gold. *Physical Review B*, 5(12):4709, 1972.

[169] C. J. Powell and J. M. Conny. Evaluation of uncertainties in X-ray photoelectron spectroscopy intensities associated with different methods and procedures for background subtraction. I. spectra for monochromatic Al X-ray. *Surface and Interface Analysis*, 41(4):269–294, 2009.

[170] O. Sise, T. J. M. Zouros, M. Ulu, and M. Dogan. First-order focusing and energy resolution optimization of a biased paracentric hemispherical spectrograph. *Physics Procedia*, 1(1):467–472, 2008.

[171] P. Ruffieux, P. Schwaller, O. Groning, L. Schlapbach, P. Groning, Q. C. Herd, D. Funnemann, and J. Westermann. Experimental determination of the transmission factor for the Omicron EA 125 electron analyzer. *Review of Scientific Instruments*, 71(10):3634–3639, 2000.

[172] A. Herrera-Gomez, J. T. Grant, P. J. Cumpson, M. Jenko, F. S. Aguirre-Tostado, C. R. Brundle, T. Conard, G. Conti, C. S. Fadley, J. Fulghum, K. Kobayashi, L. Kövér, H. Nohira, R. L. Opila, S. Oswald, R. W. Paynter, R. M. Wallace, W. S. M. Werner, and J. Wolstenholme. Report on the 47^{th} IUVSTA workshop lsqoangle-resolved XPS: the current status and future prospects for angle-resolved XPS of nano and subnano filmsrsquo. *Surface and Interface Analysis*, 41(11):840–857, 2009.

[173] E. Brüche and H. Johansson. Einige neue kathodenuntersuchungen mit dem elektrischen elektronenmikroskop. *Phys. Z*, 33:898 899, 1932.

[174] E. Brüche. *Zeitschrift für Physik*, 86:448, 1933.

[175] H. Niedrig and T. Mulvey. *2.6A The Early History of Electron Microscopy in Germany*, volume 96. Advances in Imaging and Electron Physics, 1996.

[176] E. Bauer. The possibilities for analytical methods in photoemission and low-energy microscopy. *Ultramicroscopy*, 36(1-3):52–62, 1991.

[177] H. Bethge and M. Klaua. Photo-electron emission microscopy of work function changes. *Ultramicroscopy*, 11(2-3):207–214, 1983.

[178] Oswald Benka and Peter Zeppenfeld. Secondary electron images obtained with a standard photoelectron emission microscope set-up. *Journal of Physics: Condensed Matter*, 17(16):S1311–S1318, 2005.

[179] B. H. Frazer, M. Girasole, L. M. Wiese, T. Franz, and G. De Stasio. Spectromicroscope for the photoelectron imaging of nanostructures with x-rays (sphinx): performance in biology, medicine and geology. *Ultramicroscopy*, 99(2-3):87–94, 2004.

[180] S. Anders, H. A. Padmore, R. M. Duarte, T. Renner, T. Stammler, A. Scholl, M. R. Scheinfein, J. Stöhr, L. Sève, and B. Sinkovic. Photoemission electron microscope for the study of magnetic materials. *Review of Scientific Instruments*, 70(10):3973–3981, 1999.

[181] J. Ladislas Wiza. Microchannel Plate Detectors. *Nuclear Instruments and Methods*, 162(1-3):587–601, 1979.

[182] G. Moldovan, J. Matheson, G. Derbyshire, and A. Kirkland. Characterisation of a detector based on Microchannel Plates for electrons in the energy range 10-20 keV. *Nuclear Instruments and Methods in Physics Research Section A: Accelerators, Spectrometers, Detectors and Associated Equipment*, 596(3), 2008.

[183] H. Yasufuku, Y. Ohminami, T. Tsutsumi, H. Niimi, N. Matsudaira, K. Asakura, M. Kato, Y. Sakai, Y. Kitajima, and Y. Iwasawa. Observation of element-specific energy-filtered X-ray photoemission electron microscopy images of Au on Ta using a Wien filter type energy analyzer. *Japanese Journal of Applied Physics*, 43(11 A):7682;7688, 2004.

[184] G. K. L. Marx, V. Gerheim, and G. Schönhense. Multipole Wien-filter for a high-resolution X-PEEM. *Journal of Electron Spectroscopy and Related Phenomena*, 84(1-3):251–261, 1997.

[185] H. Niimi, W.-J. Chun, S. Suzuki, K. Asakura, and M. Kato. Aberration-corrected multipole Wien filter for energy-filtered X-ray photoemission electron microscopy. *Review of Scientific Instruments*, 78:1–8, 2007.

[186] Y. Sakai, M. Kato, S. Masuda, Y. Harada, and T. Ichinokawa. Development of a Low Energy Electron Microscope with an energy analyzer. *Surface Review and Letters*, 5(6):1199–1211, 1998.

[187] T. Tsutsumi, T. Miyamoto, H. Niimi, Y. Kitajima, Y. Sakai, M. Kato, T. Naito, and K. Asakura. Energy-filtered X-ray photoemission electron microscopy and its applications to surface and organic materials. *Solid-State Electronics*, 51(10):1360–1366, 2007.

[188] T. Tsutsumi, H. Yasufuku, H. Matsudaira, H. Niimi, S. Suzuki, W. J. Chun, K. Asakura, Y. Kitajima, and Y. Iwasawa. Development of EXPEEM system. *Photon Factory Activity Report*, 20:70, 2003.

[189] R. Fink, M. R. Weiss, E. Umbach, D. Preikszas, H. Rose, R. Spehr, P. Hartel, W. Engel, R. Degenhardt, and R. Wichtendahl. SMART: a planned ultrahigh-resolution spectromicroscope for BESSY II. *Journal of Electron Spectroscopy and Related Phenomena*, 84(1-3):231–250, 1997.

[190] R. Wichtendahl, R. Fink, H. Kuhlenbeck, D. Preikszas, H. Rose, R. Spehr, P. Hartel, R. Schlogl, H. J. Freund, A. M. Bradshaw, G. Lilienkamp, T. Schmidt, A. Bauer, G. Benner, and E. Umbach. SMART: An aberration-corrected XPEEM/LEEM with energy filter. *Surface Review and Letters*, 5(6):1249–1256, 1998.

[191] H. Spiecker, O. Schmidt, Ch Ziethen, D. Menke, U. Kleineberg, R. C. Ahuja, M. Merkel, U. Heinzmann, and G. Schönhense. Time-of-flight photoelectron emission microscopy TOF-PEEM: first results. *Nuclear Instruments and Methods in Physics Research Section A: Accelerators, Spectrometers, Detectors and Associated Equipment*, 406(3):499–506, 1998.

[192] A. Oelsner, O. Schmidt, M. Schicketanz, M. Klais, G. Schönhense, V. Mergel, O. Jagutzki, and H. Schmidt-Bocking. Microspectroscopy and imaging using a delay line detector in time-of-flight photoemission microscopy. *Review of Scientific Instruments*, 72(10):3968–3974, 2001.

[193] A. Oelsner, M. Rohmer, C. Schneider, D. Bayer, G. Schönhense, and M. Aeschlimann. Time- and energy resolved photoemission electron microscopy-imaging of photoelectron time-of-flight analysis by means of pulsed excitations. *Journal of Electron Spectroscopy and Related Phenomena*, 178-179:317–330, 2010.

[194] G. Schönhense, A. Oelsner, O. Schmidt, G. H. Fecher, V. Mergel, O. Jagutzki, and H. Schmidt-Bocking. Time-of-flight photoemission electron microscopy - a new way to chemical surface analysis. *Surface Science*, 480(3):180–187, 2001.

[195] G. Schönhense. Time-resolved photoemission electron microscopy. In *EMC 2008 14th European Microscopy Congress 1 to 5 September 2008, Aachen, Germany*, volume 1 : Instrumentation and Methods, pages 689–690. 2008.

[196] M. Merkel, M. Escher, J. Settemeyer, D. Funnemann, A. Oelsner, Ch Ziethen, O. Schmidt, M. Klais, and G. Schönhense. Microspectroscopy and spectromicroscopy with photoemission electron microscopy using a new kind of imaging energy filter. *Surface Science*, 480(3):196–202, 2001.

[197] M. Kotsugi, W. Kuch, F. Offi, L. I. Chelaru, and J. Kirschner. Microspectroscopic two-dimensional Fermi surface mapping using a photoelectron emission microscope. *Review of Scientific Instruments*, 74(5):2754–2758, 2003.

[198] B. P. Tonner, D. Dunham, T. Droubay, and M. Pauli. A photoemission microscope with a hemispherical capacitor energy filter. *Journal of Electron Spectroscopy and Related Phenomena*, 84(1-3):211–229, 1997.

[199] O. Schmidt, Ch Ziethen, G. H. Fecher, M. Merkel, M. Escher, D. Menke, U. Kleineberg, U. Heinzmann, and G. Schönhense. Chemical microanalysis by selected-area ESCA using an electron energy filter in a photoemission microscope. *Journal of Electron Spectroscopy and Related Phenomena*, 88-91:1009–1014, 1998.

[200] M. Escher, N. Weber, M. Merkel, B. Kromker, D. Funnemann, S. Schmidt, F. Reinert, F. Forster, S. Hufner, P. Bernhard, Ch Ziethen, H. J. Elmers, and G. Schönhense. NanoESCA: imaging UPS and XPS with high energy resolution. *Journal of Electron Spectroscopy and Related Phenomena*, 144-147:1179–1182, 2005.

[201] M. Escher, K. Winkler, O. Renault, and N. Barrett. Applications of high lateral and energy resolution imaging XPS with a double hemispherical analyser based spectromicroscope. *Journal of Electron Spectroscopy and Related Phenomena*, 178-179:303–316, 2010.

[202] O. Renault, N. Barrett, A. Bailly, L. F. Zagonel, D. Mariolle, J. C. Cezar, N. B. Brookes, K. Winkler, B. Kromker, and D. Funnemann. Energy-filtered XPEEM with NanoESCA using synchrotron and laboratory X-ray sources: Principles and first demonstrated results. *Surface Science*, 601(20):4727–4732, 2007.

[203] A. Bailly, O. Renault, N. Barrett, L. F. Zagonel, P. Gentile, N. Pauc, F. Dhalluin, T. Baron, A. Chabli, J. C. Cezar, and N. B. Brookes. Direct quantification of Gold along a single Si nanowire. *Nano Letters*, 8(11):3709–3714, 2008.

[204] F. U. Hillebrecht, D. Spanke, J. Dresselhaus, and V. Solinus. Imaging of magnetic domains by photoemission microscopy. *Journal of Electron Spectroscopy and Related Phenomena*, 84(1-3):189–200, 1997.

[205] L. J. Heyderman, S. Czekaj, F. Nolting, E. Muller, P. Fischer, Ph Gasser, and L. Lopez-Diaz. Photoemission electron microscopy study of remanent magnetic domain states in ferromagnetic wedge films deposited on substrates with micrometer-sized square plateaus. *Journal of Applied Physics*, 99(6):063904–9, 2006.

[206] A. Gloskovskii, J. Barth, B. Balke, G. H. Fecher, C. Felser, F. Kronast, R. Ovsyannikov, H. Durr, W. Eberhard, and G. Schönhense. A spatially resolved investigation of the local, micro-magnetic domain structure of single and polycrystalline Co_2/FeSi. *Journal of Physics D: Applied Physics*, 40(6):1570–1575, 2007.

[207] P. Bernhard, J. Maul, T. Berg, F. Wegelin, U. Ott, Ch. Sudek, H. Spiecker, S. Merchel, and G. Shönhense. Nondestructive full-field imaging XANES-PEEM analysis of cosmic grains. *Physical Review B: Condensed Matter and Materials Physics*, 74:075401–1 – 075401–8, 2006.

[208] P. Bernhard, J. Maul, U. Ott, Ch Sudek, M. Escher, N. Weber, M. Merkel, B. Kromker, D. Funnemann, and G. Schönhense. Trace element analysis in presolar stardust grains via full-field imaging XPS (NanoESCA). *Nuclear Instruments and Methods in Physics Research Section B: Beam Interactions with Materials and Atoms*, 246(1):275–280, 2006.

[209] M. Escher, N. Weber, M. Merkel, C. Ziethen, P. Bernhard, G. Schönhense, S. Schmidt, F. Forster, F. Reinert, B. Krömker, and D. Funnemann. NanoESCA: a novel energy filter for imaging X-ray photoemission spectroscopy. *Journal of Physics: Condensed Matter*, 17(16):S1329 – S1338, 2005.

[210] D. Funnemann and M. Escher. Energy filter image generator for electrically charges particles and the use of thereof, 2007.

[211] R. M. Tromp. Measuring and correcting aberrations of a cathode objective lens. *Ultramicroscopy*, In Press, Uncorrected Proof, 2011.

[212] G. F. Rempfer and O. H. Griffith. The resolution of photoelectron microscopes with UV, X-ray, and synchrotron excitation sources. *Ultramicroscopy*, 27(3):273–300, 1989.

[213] G. F. Rempfer and O. H. Griffith. Emission microscopy and related techniques: resolution in photoelectron microscopy, low electron microscopy and mirror electron microscopy. *Ultramicroscopy*, 47:35–54, 1992.

[214] C SOLEIL-JF Santarelli-EPSIM.

[215] E. Bauer. Photoelectron microscopy. *Journal of Physics: Condensed Matter*, 13(49):11391 11404, 2001.

[216] W. Y. Li, K. Goto, and R. Shimizu. PEEM is a suitable tool for absolute work function measurements. *Surface and Interface Analysis*, 37(2):244–247, 2005.

[217] L.-F. Zagonel, N. Barrett, O. Renault, A. Bailly, M. Bäurer, M. Hoffmann, S.-J. Shih, and D. Cockayne. Orientation-dependent surface composition of in situ annealed strontium titanate. *Surface and Interface Analysis*, 40(13):1709–1712, 2008.

[218] N. Barrett, M. Lavayssière, L. F. Zagonel, A. Bailly, and O. Renault. X-ray photoelectron spectromicroscopy of doped silicon patterns. volume 1173, pages 99–103, 2009.

[219] Class for Physics of the Royal Swedish Academy of Sciences. Scientific background on the Nobel prize in physics 2009 : Two revolutionary optical technologies. *Nobel Prize 2009*, 2009.

[220] J. R. Janesick. *Scientific charge-coupled devices*. SPIE - The International Society for Optical Engineering, Washington, 2001.

[221] O. Renault, M. Lavayssière, A. Bailly, D. Mariolle, and N. Barrett. Core level photoelectron spectromicroscopy with Al Kα_1 excitation at 500 nm spatial resolution. *Journal of Electron Spectroscopy and Related Phenomena*, 171:68–71, 2009.

[222] F. de la Peña, N. Barrett, L. F. Zagonel, M. Walls, and O. Renault. Full field chemical imaging of buried native sub-oxide layers on doped silicon patterns. *Surface Science*, 604:1628–1636, 2010.

[223] A. Locatelli, T. O. Mentes, M. A. Niño, and E. Bauer. Image blur and energy broadening effects in xpeem. *Ultramicroscopy*, In Press, Corrected Proof, 2011.

[224] H. Rose and W. Wan. Aberration correction in electron microscopy, 2005.

[225] C. Weissbäcker and H. Rose. Electrostatic correction of the chromatic and of the spherical aberration of charged-particle lenses (Part I). *Japanese Journal of Applied Physics*, 50(5):383–390, 2001.

[226] G. Schönhense and H. Spiecker. Correction of chromatic and spherical aberration in electron microscopy utilizing the time structure of pulsed excitation sources. *Journal of Vacuum Science and Technology B: Microelectronics and Nanometer Structures*, 20(6):2526–2534, 2002.

[227] J. Wolstenholme. Summary of ISO/TC 201 standard: ISO 18516:2006.Surface chemical analysis:Auger electron spectroscopy and X-ray photoelectron spectroscopy.Determination of lateral resolution. *Surface and Interface Analysis*, 40:966, 2008.

[228] M. Senoner, T. Wirth, W. Unger, W. Osterle, I. Kaiander, R. L. Sellin, and D. Bimberg. BAM-L002: a new type of certified reference material for length calibration and testing of lateral resolution in the nanometre range. *Surface and Interface Analysis*, 36(10):1423–1426, 2004.

[229] M. Senoner, T. Wirth, W. E. S. Unger, M. Escher, N. Weber, D. Funnemann, and B. Krömker. Testing of lateral resolution in the nanometer range using the BAML002 certified reference material: Application of TOF-SIMS and NanoESCA instruments. *Journal of Surface Analysis*, 12(2):78–82, 2005.

[230] J. Westermann. Imaging XPS with 650 nm resolution. *Pico*, 10(2):2–3, 2006.

[231] F. Ratto, F. Rosei, A. Locatelli, S. Cherifi, S. Fontana, S. Heun, P.-D. Szkutnik, A. Sgarlata, M. De Crescenzi, and N. Motta. Composition of Ge(Si) islands in the growth of Ge on Si(111). *Applied Physics Letters*, 84(22):4526–4528, 2004.

[232] F. Ratto, A. Locatelli, S. Fontana, S. Kharrazi, S. Ashtaputre, S. K. Kulkarni, S. Heun, and F. Rosei. Chemical mapping of individual semiconductor nanostructures. *Small*, 2(3):401–405, 2006.

[233] O. Renault, M. Lavayssière, and D. Mariolle. Procédé de correction d'astigmatisme en imagerie par spectromicroscopie à émission d'électrons, 2010.

[234] H. Hiromi. *Electron microscope*, volume 10/951,892. Patent US 7,126,120,B2, 2006.

[235] D. E. Peebles, J. A. Ohlhausen, P. G. Kotula, S. Hutton, and C. Blomfield. Multivariate statistical analysis for X-ray photoelectron spectroscopy spectral imaging: Effect of image acquisition time. *Journal of Vacuum Science and Technology A: Vacuum, Surfaces, and Films*, 22(4):1579–1586, 2004.

[236] R. N. Watts, S. Liang, Z. H. Levine, T. B. Lucatorto, F. Polack, and M. R. Scheinfein. A transmission X-ray microscope based on secondary-electron imaging. *Review of Scientific Instruments*, 68(9):3464–3476, 1997.

[237] F. J. Himpsel, B. S. Meyerson, F. R. McFeeley, J. F. Morar, A. Taleb-Ibrahimi, and J. A. Yarmoff. *Core Level Spectroscopy at Silicon Surfaces and Interfaces.* Proceedings of the 1988 Enrico Fermi School on Photoemission and Absorption Spectroscopy of Solids and Interfaces with Synchrotron Radiation. Varenna: North Holland, 1988.

[238] S. Nepijko, A. Oelsner, A. Krasyuk, A. Gloskovskii, N. N. Sedov, C. M. Schneider, and G. Schönhense. Lateral resolving power of a time-of-flight photoemission electron microscope. *Applied Physics A: Materials Science and Processing*, 78(1):47–51, 2004.

[239] E. G. Seebauer and K. W. Noh. Trends in semiconductor defect engineering at the nanoscale. *Materials Science and Engineering: R: Reports*, 70(3-6):151–168, 2010.

[240] K. Yamamoto and H. Itoh. XPS study of silicon surface after ultra-low-energy ion implantation. *Surface Science*, 600(18):3753–3756, 2006.

[241] D. Cooper, A. Beche, J.-M. Hartmann, V. Carron, and J.-L. Rouvière. Strain mapping for the semiconductor industry by dark-field electron holography and nanobeam electron diffraction with nm resolution. *Semiconductor Science and Technology*, 25(9):095012, 2010.

[242] A. Abbadie, J. M. Hartmann, P. Holliger, M. N. Séméria, P. Besson, and P. Gentile. Low thermal budget surface preparation of Si and SiGe. *Applied Surface Science*, 225(1-4):256–266, 2004.

[243] F. Gonzatti, J.-H. Hartmann, and K. Yckache. Low and high temperature boron and phosphorous doping of Si for junctions and MEMS purposes. *ECS Transactions*, 16(10):485–493, 2008.

[244] W. Kern and D. A. Puotinen. Cleaning solution based on hydrogen peroxide for use in semiconductor technology. *RCA review*, 31, 1970.

[245] B. R. Weinberger, G. G. Peterson, T. C. Eschrich, and H. A. Krasinski. Surface chemistry of HF passivated silicon: X-ray photoelectron and ion scattering spectroscopy results. *Journal of Applied Physics*, 60(9):3232–3234, 1986.

[246] H. Ubara, T. Imura, and A. Hiraki. *Solid State Communications*, 50:673, 1984.

[247] E. Yablonovitch, D. L. Allara, C. C. Chang, T. Gmitter, and T. B. Bright. Unusually low surface-recombination velocity on silicon and germanium surfaces. *Physical Review Letters*, 57(2):249, 1986.

[248] G. W. Trucks, K. Raghavachari, G. S. Higashi, and Y. J. Chabal. Mechanism of HF etching of silicon surfaces: A theoretical understanding of hydrogen passivation. *Physical Review Letters*, 65(4):504, 1990.

[249] L. J. Huang and W. M. Lau. Effects of HF cleaning and subsequent heating on the electrical properties of silicon (100) surfaces. *Applied Physics Letters*, 60(9):1108–1110, 1992.

[250] Y. J. Chabal, G. S. Higashi, K. Raghavachari, and V. A. Burrows. Infrared spectroscopy of Si(111) and Si(100) surfaces after HF treatment: Hydrogen termination and surface morphology. *Journal of Vacuum Science and Technology A: Vacuum, Surfaces, and Films*, 7(3):2104–2109, 1989.

[251] G. S. Higashi, Y. J. Chabal, G. W. Trucks, and K. Raghavachari. Ideal hydrogen termination of the Si(111) surface. *Applied Physics Letters*, 56(7):656–658, 1990.

[252] G. S. Higashi, R. S. Becker, Y. J. Chabal, and A. J. Becker. Comparison of Si(111) surfaces prepared using aqueous solutions of NH_4F versus HF. *Applied Physics Letters*, 58(15):1656–1658, 1991.

[253] C. P. Wade and C. E. D. Chidsey. Etch-pit initiation by dissolved oxygen on terraces of H-Si(111). *Applied Physics Letters*, 71(12):1679–1681, 1997.

[254] L. J. Webb and N. S. Lewis. Comparison of the electrical properties and chemical stability of crystalline silicon(111) surfaces alkylated using grignard reagents or olefins with lewis acid catalysts. *The Journal of Physical Chemistry B*, 107(23):5404–5412, 2003.

[255] B. Stegemann, D. Sixtensson, T. Lussky, U. Bloeck, and M. Schmidt. Ultrahigh vacuum preparation and passivation of abrupt SiO_2/Si interfaces. *Chimia*, 61(12):826–830, 2007.

[256] L. Baraton. *Fabrication et étude d une diode moléculaire à résistance différentielle négative greffé sur silicium terminé hyrogène.* PhD thesis, 2004.

[257] H. Angermann, Th Dittrich, and H. Flietner. Investigation of native-oxide growth on HF-treated Si(111) surfaces by measuring the surface-state distribution. *Applied Physics A: Materials Science and Processing*, 59(2):193–197, 1994.

[258] H. Angermann. Characterization of wet-chemically treated silicon interfaces by surface photovoltage measurements. *Analytical and Bioanalytical Chemistry*, 374(4):676–680, 2002.

[259] A. Illiberi, K. Sharma, M. Creatore, and M. C. M. van de Sanden. Role of a-Si:H bulk in surface passivation of c-si wafers. *Physica status solidi (RRL) - Rapid Research Letters*, 4(7):172–174, 2010.

[260] M. Kolibal, J. Cechal, M. Bartosik, and T. Sikola. Stability of hydrogen-terminated vicinal Si(111) surface under ambient atmosphere. *Applied Surface Science*, 256:3423–3426, 2010.

[261] E. Romano, G. F. Cerofolini, D. Narducci, C. Galati, and L. Renna. Comparing the IR spectra of H-terminated inner and outer silicon surfaces. *Surface and Interface Analysis*, 42:1321–1325, 2010.

[262] A. Orduña Diaz, C. G. Treviño Palacios, M. Rojas-Lopez, R. Delgado-Macuil, V. L. Gayou, and A. Torres-Jacome. FTIR and electrical characterization of a-Si:H layers deposited by PECVD at different boron ratios. *Materials Science and Engineering: B*, 174(1-3):93–96, 2010.

[263] M. Niwano. In-situ IR observation of etching and oxidation processes of Si surfaces. *Surface Science*, 427-428:199–207, 1999.

[264] H. Noda and T. Urisu. Assignments of bending and stretching vibrational spectra and mechanisms of thermal decomposition of SiH_2 on Si(100) surfaces. *Chemical Physics Letters*, 326(1-2):163–168, 2000.

[265] C. Mazzara, J. Jupille, W. Q. Zheng, M. Tanguy, A. Tadjeddine, and P. Dumas. Hydrogen-terminated Si(111) and Si(100) by wet chemical treatment: linear and non-linear infrared spectroscopy. *Surface Science*, 427-428:208–213, 1999.

[266] M. P. Seah and S. J. Spencer. Ultrathin SiO_2 on Si IV. intensity measurement in XPS and deduced thickness linearity. *Surface and Interface Analysis*, 35:515–524, 2003.

[267] M. P. Seah and S. J. Spencer. Ultrathin SiO_2 on Si II. issues in quantification of the oxide thickness. *Surface and Interface Analysis*, 33:640–652, 2002.

[268] M. P. Seah and R. White. Ultrathin SiO_2 on Si: III. Mapping the layer thickness efficiently by XPS. *Surface and Interface Analysis*, 33:960–963, 2002.

[269] F. Liu, Z. Zhao, L. Zhao, and H. Wang. Considerations of the intermediate oxides via XPS elemental quantitative analysis for the thickness measurements of ultrathin SiO_2 on Si. *Surface and Interface Analysis*, page In press, 2010.

[270] D. Aureau. *Interface silicium/couche organique : Maîtrise des propriétés et fonctionnalisation*. PhD thesis, 2008.

[271] W. B. Ying, Y. Mizokawa, Y. Kamiura, K. Kawamoto, and W. Y. Yang. The chemical composition changes of silicon and phosphorus in the process of native oxide formation of heavily phosphorus doped silicon. *Applied Surface Science*, 181(1-2):1–14, 2001.

[272] W. B. Ying, Y. Mizokawa, K. Tanahashi, Y. Kamiura, M. Iida, K. Kawamoto, and W. Y. Yang. Evaluation of the initial oxidation of heavily phosphorus doped silicon surfaces using angle-dependent X-ray photoelectron spectroscopy. *Thin Solid Films*, 343-344:393–396, 1999.

[273] E. Landemark, C. J. Karlsson, Y. C. Chao, and R. I. G. Uhrberg. Core-level spectroscopy of the clean Si(001) surface: Charge transfer within asymmetric dimers of the 2x1 and c(4x2) reconstructions. *Physical Review Letters*, 69(10):1588, 1992.

[274] T. Kakiuchi, S. Hashimoto, N. Fujita, M. Tanaka, K. Mase, and S.-I. Nagaoka. Topmost-surface-sensitive Si $2p$ photoelectron spectra of clean Si(100)-2x1 measured with photoelectron Auger coincidence spectroscopy. *Surface Science*, 604(9-10):L27–L30, 2010.

[275] F. J. Himpsel, F. R. McFeely, A. Taleb-Ibrahimi, J. A. Yarmoff, and G. Hollinger. Microscopic structure of the SiO_2/Si interface. *Physical Review B*, 38(9):6084, 1988.

[276] C. J. Karlsson, F. Owman, E. Landemark, Y. C. Chao, aring, P. rtensson, and R. I. G. Uhrberg. Si 2*p* core-level spectroscopy of the Si(111)-(1x1):H and Si(111)-(1x1):D surfaces: Vibrational effects and phonon broadening. *Physical Review Letters*, 72(26):4145, 1994.

[277] C. J. Karlsson, E. Landemark, Y. C. Chao, and R. I. G. Uhrberg. Atomic origins of the surface components in the Si 2*p* core-level spectra of the Si(111) 7x7 surface. *Physical Review B*, 50(8):5767, 1994.

[278] Y. C. Chao, L. S. O. Johansson, C. J. Karlsson, E. Landemark, and R. I. G. Uhrberg. Adsorption of K on Si(100) 2x1 at room temperature studied with photoelectron spectroscopy. *Physical Review B*, 52(4):2579, 1995.

[279] G. F. Cerofolini, E. Romano, G. Giorgi, and P. Belanzoni. Counterintuitive assignment of the lines observed by X-ray photoelectron spectroscopy at the hydrogen-terminated (100) surface of silicon. *Journal of Physics D: Applied Physics*, 42(22):225301, 2009.

[280] Y. Mizokawa, W. B. Ying, Y. B. Yu, Y. Kamiura, M. Iida, and K. Kawamoto. Phosphorus redistribution in the surface region of heavily phosphorus doped silicon. *Applied Surface Science*, 100-101:561–565, 1996.

[281] Y. Yamashita, M. Nagao, S. Machida, K. Hamaguchi, F. Yasui, K. Mukai, and J. Yoshinobu. High resolution Si 2*p* photoelectron spectroscopy of unsaturated hydrocarbon molecules adsorbed on Si(100) c(4x2): the interface bonding and charge transfer between the molecule and the Si substrate. *Journal of Electron Spectroscopy and Related Phenomena*, 114-116:389–393, 2001.

[282] Y. Enta, H. Nakazawa, S. Sato, H. Kato, and Y. Sakisaka. Silicon thermal oxidation and its thermal desorption investigated by Si 2*p* core-level photoemission. *Journal of physics: conference series*, 235(1):012008, 2010.

[283] F. Jolly, F. Rochet, G. Dufour, C. Grupp, and A. Taleb-Ibrahimi. Oxidized silicon surfaces studied by high resolution Si 2*p* core-level photoelectron spectroscopy using synchrotron radiation. *Journal of Non-Crystalline Solids*, 280(1-3):150–155, 2001.

[284] M. V. Gomoyunova and I. I. Pronin. Photoelectron spectroscopy of atomic core levels on the silicon surface: a review. *Technical physics*, 49(10):1249–1279, 2004.

[285] D. S. Lin, T. Miller, and T. C. Chiang. Dimer charge asymmetry determined by photoemission from epitaxial Ge on Si(100)-(2x1). *Physical Review Letters*, 67(16):2187, 1991.

[286] T. W. Pi, I. H. Hong, C. P. Cheng, and G. K. Wertheim. Surface photoemission from Si(100) and inelastic electron mean-free-path in silicon. *Journal of Electron Spectroscopy and Related Phenomena*, 107(2):163–176, 2000.

[287] C. Grupp and A. Taleb-Ibrahimi. Core-level broadening mechanisms at silicon surfaces. *Journal of Electron Spectroscopy and Related Phenomena*, 101-103:309–313, 1999.

[288] Y. Yamashita, S.-I. Machida, M. Nagao, S. Yamamoto, Y. Kakefuda, K. Mukai, and J. Yoshinobu. Direct evidence for asymmetric dimer on Si(100) at low temperature by means of high-resolution Si $2p$ photoelectron spectroscopy. *Japanese Journal of Applied Physics*, 41:L272–L274, 2002.

[289] R. Schlaf, R. Hinogami, M. Fujitani, S. Yae, and Y. Nakato. Fermi level pinning on HF etched silicon surfaces investigated by photoelectron spectroscopy. *Journal of Vacuum Science and Technology A: Vacuum, Surfaces, and Films*, 17(1):164–169, 1999.

[290] L. Gregoratti, T. O. Mentes, A. Locatelli, and M. Kiskinova. Beam-induced effects in soft x-ray photoelectron emission microscopy experiments. *Journal of Electron Spectroscopy and Related Phenomena*, 170(1-3):13–18, 2009.

[291] P. Eyben. *Scanning spreading resistance microscopy: high resolution 2*D *carrier profiling of semiconductor structures*. PhD thesis, 2004.

[292] T.J.M. Zouros and E.P. Benis. Ultimate energy resolution of a hemispherical analyzer using a cylindrically symmetric injection lens and virtual entry aperture. *Applied Physics Letters*, 86:094105, 2005.

[293] T. J. M. Zouros, F. M. Spiegelhalder, and David J. Manura. Modelling SIMION's accuracy for hemispherical deflector analyzers using a spherical capacitor. *Physics Procedia*, 1(1):461–466, 2008.

[294] O. Sise, M. Ulu, M. Dogan, G. Martinez, and Th. J. M. Zouros. Fringing field optimization of hemispherical deflector analyzers using BEM and FDM. *Journal of Electron Spectroscopy and Related Phenomena*, 177(1):42–51, 2010.

[295] J. Feng, H. Padmore, D. H. Wei, S. Anders, Y. Wu, A. Scholl, and D. Robin. Modeling the acceleration field and objective lens for an aberration corrected photoemission electron microscope. In *Papers from the 12th National Synchrotron Radiation Instrumentation Conference*, volume 73, pages 1514–1517, 2002.

[296] O. Sise, M. Ulu, and M. Dogan. Multi-element cylindrical electrostatic lens systems for focusing and controlling charged particles. *Nuclear Instruments and Methods in Physics Research Section A: Accelerators, Spectrometers, Detectors and Associated Equipment*, 554(1-3):114–131, 2005.

[297] B. L. Henke, J. Liesegang, and S. D. Smith. Soft-X-ray-induced secondary-electron emission from semiconductors and insulators: Models and measurements. *Physical Review B*, 19(6):3004, 1979.

[298] V.K Sangwan, V. Ballarotto, K. Siegrist, and E. D. Williams. Characterizing voltage contrast in photoelectron emission microscopy. *Journal of Microscopy*, 238(3):210–217, 2010.

[299] S. A. Nepijko, G. K. L. Marx, and G. Schönhense. Quantitative determination of magnetic fields on object surfaces via photoemission electron microscopy without restriction of the electron beam. *Nuclear Instruments and Methods in Physics Research Section B: Beam Interactions with Materials and Atoms*, 264(1):194–200, 2007.

[300] S. A. Nepijko, N. N. Sedov, G. Schönhense, and M. Escher. Use of emission electron microscope for potential mapping in semiconductor microelectronics. *Journal of Microscopy*, 206(2):132–138, 2002.

Résumé : Ce mémoire de thèse traite de l'étude de jonctions pn silicium planaires, réalisées par épitaxie localisée, avec un nouveau type de microscopie à émission de photoélectrons (XPEEM) filtré en énergie. L'objectif est d'améliorer notre compréhension des facteurs influençant l'imagerie XPEEM de jonctions modèles avec une perspective à plus long terme d'application de cette technique aux cas réels.
Sur les trois types de jonction réalisées présentant des champs électriques variables (P^+/P, N^+/P, P^+/N), nous avons d'abord mis en œuvre un procédé de passivation en trois étapes afin de se rapprocher de conditions en bandes plates en surface. Ce procédé nous a permis d'étudier la position des niveaux électroniques de part et d'autre des jonctions grâce à une imagerie en XPEEM spectroscopique avec électrons secondaires (travail de sortie local), électrons de cœur Si $2p$ et bande de valence, avec à la fois avec des sources X de laboratoire et le rayonnement synchrotron. Un mécanisme de contraste des images en électrons de cœur dû à la toute première couche atomique de surface a été montré. Ensuite, nous avons mis en évidence le rôle du champ électrique au niveau de la zone de déplétion des jonctions qui décale la position apparente de cette dernière dans l'image XPEEM. Nous avons comparé les résultats expérimentaux avec des simulations (logiciel SIMION) afin d'estimer son influence sur les conditions d'imagerie. Enfin, nous avons étudié l'impact de la technique d'imagerie en champ sombre sur la localisation de la jonction réelle au niveau de la surface de l'échantillon.

Mots clés : XPS, XPEEM, spectromicroscopie, silicium dopé, rayonnement synchrotron, travail de sortie, bande de valence, niveaux de cœur, SIMION, champ sombre.

Abstract: This thesis addresses the problem of imaging of model systems planar silicon pn junctions, fabricated by localized epitaxy, using the novel energy-filtered X-ray Photo-Electron Emission Microscope (XPEEM). The objective is to improve the understanding of the phenomena influencing the XPEEM images of the junctions, with as long-term perspective, a possible application of this method in a complementary way to existing techniques of 2D dopant mapping.
The studies were carried out over three types of junction realized to this purpose and presenting variable electrical field (P^+/P, N^+/P, P^+/N). We firstly developed and optimized a passivation protocol in three-steps which yielded a surface close to flat band conditions. This process allowed us to deduce band alignments as a function of doping level and type on both side of the junction thanks to spectroscopic XPEEM imaging of secondary electrons (to determine local work function), Si $2p$ core-level and valence band with both laboratory photon sources and synchrotron radiation. Contrast in core-level imaging due to the first atomic layer of the surface was also shown.
Then, we highlighted the role of the lateral electric field across the depletion zone of a pn junction which shifts the apparent position of the latter in PEEM imaging. We compared experimental results and simulations performed with SIMION software to estimate the influence of pn junctions on PEEM imaging. Dark field imaging of the junction was also simulated. Comparison with the experimental results showed that it can be used to localize the real junction.

Keywords: XPS, XPEEM, spectromicroscopy, silicon doped, synchrotron radiation, work function, valence band, core-level, SIMION, dark-field.

Résumé : Ce mémoire de thèse traite de l'étude de jonctions pn silicium planaires, réalisées par épitaxie localisée, avec un nouveau type de microscopie à émission de photoélectrons (XPEEM) filtré en énergie. L'objectif est d'améliorer notre compréhension des facteurs influençant l'imagerie XPEEM de jonctions modèles avec une perspective à plus long terme d'application de cette technique aux cas réels.
Sur les trois types de jonction réalisées présentant des champs électriques variables (P^+/P, N^+/P, P^+/N), nous avons d'abord mis en œuvre un procédé de passivation en trois étapes afin de se rapprocher de conditions en bandes plates en surface. Ce procédé nous a permis d'étudier la position des niveaux électroniques de part et d'autre des jonctions grâce à une imagerie en XPEEM spectroscopique avec électrons secondaires (travail de sortie local), électrons de cœur Si $2p$ et bande de valence, avec à la fois avec des sources X de laboratoire et le rayonnement synchrotron. Un mécanisme de contraste des images en électrons de cœur dû à la toute première couche atomique de surface a été montré. Ensuite, nous avons mis en évidence le rôle du champ électrique au niveau de la zone de déplétion des jonctions qui décale la position apparente de cette dernière dans l'image XPEEM. Nous avons comparé les résultats expérimentaux avec des simulations (logiciel SIMION) afin d'estimer son influence sur les conditions d'imagerie. Enfin, nous avons étudié l'impact de la technique d'imagerie en champ sombre sur la localisation de la jonction réelle au niveau de la surface de l'échantillon.

Mots clés : XPS, XPEEM, spectromicroscopie, silicium dopé, rayonnement synchrotron, travail de sortie, bande de valence, niveaux de cœur, SIMION, champ sombre.

Abstract: This thesis addresses the problem of imaging of model systems planar silicon pn junctions, fabricated by localized epitaxy, using the novel energy-filtered X-ray Photo-Electron Emission Microscope (XPEEM). The objective is to improve the understanding of the phenomena influencing the XPEEM images of the junctions, with as long-term perspective, a possible application of this method in a complementary way to existing techniques of 2D dopant mapping.
The studies were carried out over three types of junction realized to this purpose and presenting variable electrical field (P^+/P, N^+/P, P^+/N). We firstly developed and optimized a passivation protocol in three-steps which yielded a surface close to flat band conditions. This process allowed us to deduce band alignments as a function of doping level and type on both side of the junction thanks to spectroscopic XPEEM imaging of secondary electrons (to determine local work function), Si $2p$ core-level and valence band with both laboratory photon sources and synchrotron radiation. Contrast in core-level imaging due to the first atomic layer of the surface was also shown.
Then, we highlighted the role of the lateral electric field across the depletion zone of a pn junction which shifts the apparent position of the latter in PEEM imaging. We compared experimental results and simulations performed with SIMION software to estimate the influence of pn junctions on PEEM imaging. Dark field imaging of the junction was also simulated. Comparison with the experimental results showed that it can be used to localize the real junction.

Keywords: XPS, XPEEM, spectromicroscopy, silicon doped, synchrotron radiation, work function, valence band, core-level, SIMION, dark-field.